frontiers | Research Topics

Incorporation of texture analysis in diagnosing and characterizing cancer

Edited by
Chuanming Li and Usha Dutta

Published in
Frontiers in Oncology

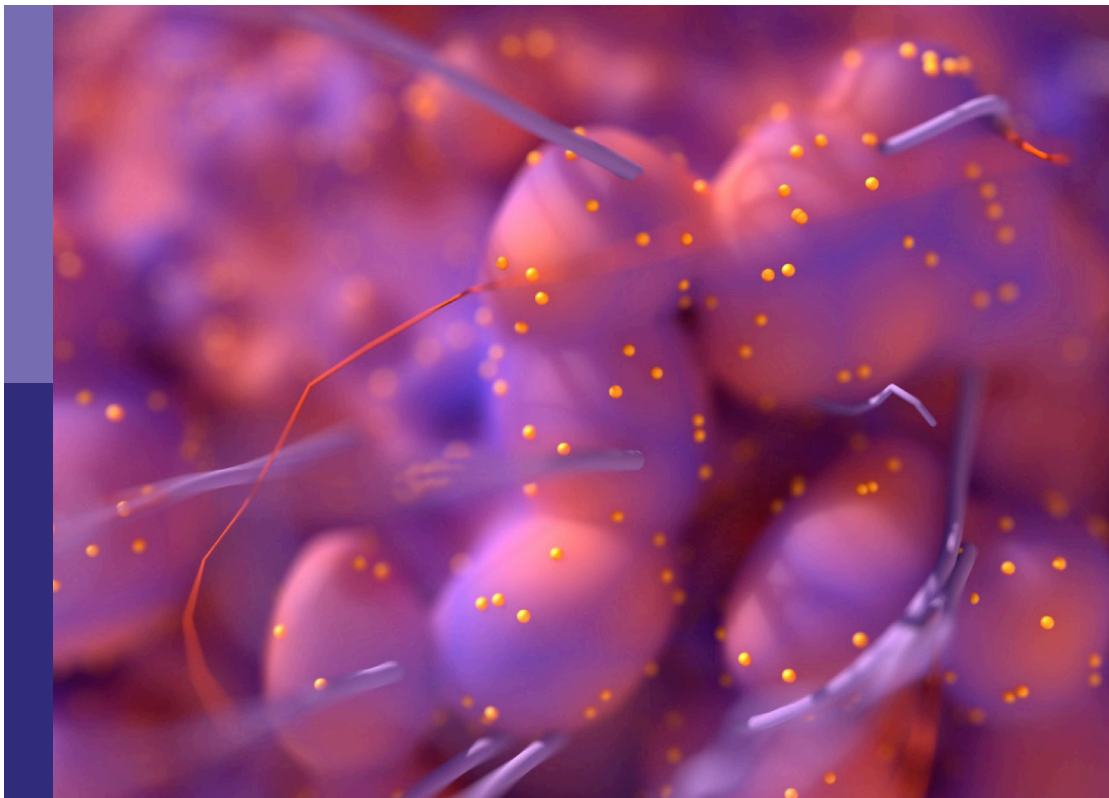

ISSN 1664-8714
ISBN 978-2-8325-2766-5
DOI 10.3389/978-2-8325-2766-5

About Frontiers

Frontiers is more than just an open access publisher of scholarly articles: it is a pioneering approach to the world of academia, radically improving the way scholarly research is managed. The grand vision of Frontiers is a world where all people have an equal opportunity to seek, share and generate knowledge. Frontiers provides immediate and permanent online open access to all its publications, but this alone is not enough to realize our grand goals.

Frontiers journal series

The Frontiers journal series is a multi-tier and interdisciplinary set of open-access, online journals, promising a paradigm shift from the current review, selection and dissemination processes in academic publishing. All Frontiers journals are driven by researchers for researchers; therefore, they constitute a service to the scholarly community. At the same time, the *Frontiers journal series* operates on a revolutionary invention, the tiered publishing system, initially addressing specific communities of scholars, and gradually climbing up to broader public understanding, thus serving the interests of the lay society, too.

Dedication to quality

Each Frontiers article is a landmark of the highest quality, thanks to genuinely collaborative interactions between authors and review editors, who include some of the world's best academicians. Research must be certified by peers before entering a stream of knowledge that may eventually reach the public - and shape society; therefore, Frontiers only applies the most rigorous and unbiased reviews. Frontiers revolutionizes research publishing by freely delivering the most outstanding research, evaluated with no bias from both the academic and social point of view. By applying the most advanced information technologies, Frontiers is catapulting scholarly publishing into a new generation.

What are Frontiers Research Topics?

Frontiers Research Topics are very popular trademarks of the *Frontiers journals series*: they are collections of at least ten articles, all centered on a particular subject. With their unique mix of varied contributions from Original Research to Review Articles, Frontiers Research Topics unify the most influential researchers, the latest key findings and historical advances in a hot research area.

Find out more on how to host your own Frontiers Research Topic or contribute to one as an author by contacting the Frontiers editorial office: frontiersin.org/about/contact

Incorporation of texture analysis in diagnosing and characterizing cancer

Topic editors

Chuanming Li — Chongqing University Central Hospital, China

Usha Dutta — Post Graduate Institute of Medical Education and Research (PGIMER), India

Citation

Li, C., Dutta, U., eds. (2023). *Incorporation of texture analysis in diagnosing and characterizing cancer*. Lausanne: Frontiers Media SA.

doi: 10.3389/978-2-8325-2766-5

Table of contents

frontiers | Frontiers in Oncology

TYPE Editorial
PUBLISHED 06 June 2023
DOI 10.3389/fonc.2023.1224644

OPEN ACCESS

EDITED AND REVIEWED BY
Zaver Bhujwalla,
Johns Hopkins University, United States

*CORRESPONDENCE
Chuanming Li
li_chuanming@yeah.net

RECEIVED 18 May 2023
ACCEPTED 30 May 2023
PUBLISHED 06 June 2023

CITATION
Feng J and Li C (2023) Editorial: Incorporation of texture analysis in diagnosing and characterizing cancer. *Front. Oncol.* 13:1224644. doi: 10.3389/fonc.2023.1224644

Editorial: Incorporation of texture analysis in diagnosing and characterizing cancer

Junbang Feng[1,2] and Chuanming Li[1,2]*

[1]Chongqing University Central Hospital, Chongqing, China, [2]Chongqing Emergency Medical Center, Chongqing, China

KEYWORDS

texture analysis, radiomics, CT, MRI, cancer

Editorial on the Research Topic
Incorporation of texture analysis in diagnosing and characterizing cancer

Cancer is a group of diseases which are aggressive, invasive, and sometimes metastatic. It can affect people of all ages, even fetuses, and the risk increases with age. According to the statistics of the American Cancer Society, it is estimated that there will be more than 600000 cancer deaths in the United States in 2023. Currently, *in vivo* diagnosis and evaluation of cancer mainly rely on methods of medical imaging such as MRI and CT. However, many small and hidden information in MRI and CT can not be detected by naked eye observation. Radiomics is a new technology that can be used to automatically mine large amounts of high-throughput data features from medical images. Although many studies have reported the use of radiomics and texture analysis in the diagnosis of cancer in recent years, further exploration of their potential in early cancer discrimination and prognosis is still worth exploring.

In this Research Topic, the application of radiomics and texture analysis in the diagnosis, differentiation, and prognostic evaluation of various cancers was focused. Texture analysis could reflect the physiological and pathological changes of cancer by extracting a large number of potential image features. The signal intensity features could reflect the composition of a tissue, while texture features could reflect the consistency of internal components within the tissue. Sun et al. investigated the potential of CT imaging features and texture analysis to distinguish bronchiolar adenoma from adenocarcinoma *in situ* and minimally invasive adenocarcinoma. They found that the multiple logistic regression model based on six key texture features extracted from non-enhanced CT could accurately identify them with the AUC of 0.977 and 0.976, respectively. The Six key texture features were GLCMEntropy, LongRunLowGreyLevelEmphasis, GLCMEnergy, ShortRunEmphasis VoxelValueSum, and Quantile. Q. Some pulmonary nodules may gradually/grow and develop into lung cancer, while others may remain stable for many years. Accurately predicting the growth of pulmonary nodules in advance is of great clinical significance for early treatment (Shen et al.). The SVM, RF, MLP and AdaBoost models developed by Yang et al. based on age and radiomic features demonstrated high accuracy in predicting the growth of pulmonary nodules in the future next year, with AUCs of 0.81, 0.77, 0.81 and 0.71 respectively in the validation group. The rearrangement state of anaplastic lymphoma kinase (ALK) plays a key role in targeted therapy of non-small cell

lung cancer. However, how to accurately detect them is a great challenge. Hao et al. proved that ALK rearrangement status could be accurately predicted using a machine learning-based classification model based on CT textural features and clinical data. This study provided a non-invasive solution for accurately identifying ALK gene status, which was an efficient and rapid new method for clinical genetic diagnosis. Pancreatic ductal adenocarcinoma (PDAC) accounts for more than 90% of pancreatic cancer and is the seventh leading cause of cancer-related death worldwide. Early identification of lymph node metastasis around PDAC is very important for surgical treatment. Li et al. successfully constructed a logistic regression model to detect lymph node metastasis using radiomics features of enhanced CT, and the AUC of the training group and the validation group were 0.937 and 0.851, respectively. This model may help clinicians accurately assess the risk of lymph node metastasis before surgery. Liver cancer is the sixth most common cancer in the world and poses a serious threat to human health. Artificial intelligence and radiomics has undergone rapid development and has a wide application in the diagnosis and treatment of liver diseases. Xiong et al. compiled a relative comprehensive and quantitative report on the research of liver disease using artificial intelligence by employing bibliometrics. They summarized the current research progress, hotspots, and emerging trends of cancer artificial intelligence. The microvascular invasion (MVI) refers to the tumor invasion in small intrahepatic vessels, covering portal veins, hepatic vessels, and lymphatic vessels. Zhang et al. developed a nomogram to predict preoperative MVI of HCC with an AUC of 0.884 by combining clinicoradiological factors and radiomics features. This was crucial for accurately identifying the malignancy of HCC and developing appropriate treatment plans. Endometrial cancer (EC) is one of the three most common malignant tumors in the female reproductive system. Its incidence rate and mortality are on the rise and spread to young people. Ki-67 and p53 are closely related to the proliferation and apoptosis of tumor cells. Jiang et al. established a logistic regression model based on the textural features and apparent diffusion coefficient values of multimodal MRI to predict the expression levels of Ki-67 and p53 before surgery. In the verification group, the AUCs were 0.938 and 0.922, which had high auxiliary diagnostic value for clinical application. Their method could non-invasive evaluate the levels of Ki 67 and p53 in EC, and had important potential in evaluating the malignancy of EC and guiding appropriate treatment plans. Prostate cancer (PCa) occurs in middle-aged men aged 45-60 years and is the most common malignant tumor of the male reproductive system. High-risk prostate cancer (PCa) is often treated by prostate-only radiotherapy (PORT) owing to its favourable toxicity profile compared to whole-pelvic radiotherapy. Unfortunately, more than 50% patients still developed disease progression following PORT. Ching et al. developed a Ridge regression model based on radiomics and clinical characteristics of preoperative planned computed tomography, which could predict the progression of high-risk PCa patients at 5 years after prostate-only radiotherapy with an AUC of 0.797. This study might help clinicians for the personalized treatment of high-risk prostate cancer patients in the future.

Through this Research Topic, the important role of texture analysis in cancer imaging was clearly presented, which provided quantitative and objective support for various cancer detection and treatment decision. Although there are still many difficulties in achieving a complete cure for cancer, new treatment methods such as targeted drugs have brought many new hopes. Radiomics and texture analysis can greatly assist in the diagnosis, gene prediction, and prognosis evaluation of tumors, and have the hope of being used as a decision-making tool in future clinical applications.

Author contributions

CL and JF: conceptualization; data curation; manuscript drafting; manuscript editing. All authors approved the submitted version.

Conflict of interest

The authors declare that the research was conducted in the absence of any commercial or financial relationships that could be construed as a potential conflict of interest.

Publisher's note

frontiers in Oncology

ORIGINAL RESEARCH
published: 26 April 2021
doi: 10.3389/fonc.2021.634564

CT Texture Analysis for Differentiating Bronchiolar Adenoma, Adenocarcinoma *In Situ*, and Minimally Invasive Adenocarcinoma of the Lung

Jinju Sun[1†], Kaijun Liu[2†], Haipeng Tong[3], Huan Liu[4], Xiaoguang Li[3], Yi Luo[1], Yang Li[3], Yun Yao[1], Rongbing Jin[1], Jingqin Fang[3,5] and Xiao Chen[1,5*]*

[1] Department of Nuclear Medicine, Daping Hospital, Army Medical University, Chongqing, China, [2] Department of Gastroenterology, Daping Hospital, Army Medical University, Chongqing, China, [3] Department of Radiology, Daping Hospital, Army Medical University, Chongqing, China, [4] GE Healthcare, Shanghai, China, [5] Chongqing Clinical Research Center for Imaging and Nuclear Medicine, Chongqing, China

OPEN ACCESS

Edited by:
Chuanming Li,
Chongqing Medical University, China

Reviewed by:
Yi Xiao,
Shanghai Changzheng Hospital, China
Lian-Ming Wu,
Shanghai JiaoTong University, China

***Correspondence:**
Xiao Chen
xiaochen229@foxmail.com
Jingqin Fang
jingqin0405@163.com

[†] These authors have contributed equally to this work

Specialty section:
This article was submitted to Cancer Imaging and Image-directed Interventions, a section of the journal Frontiers in Oncology

Received: *30 November 2020*
Accepted: *22 February 2021*
Published: *26 April 2021*

Citation:
Sun J, Liu K, Tong H, Liu H, Li X, Luo Y, Li Y, Yao Y, Jin R, Fang J and Chen X (2021) CT Texture Analysis for Differentiating Bronchiolar Adenoma, Adenocarcinoma In Situ, and Minimally Invasive Adenocarcinoma of the Lung. Front. Oncol. 11:634564. doi: 10.3389/fonc.2021.634564

Purpose: This study aimed to investigate the potential of computed tomography (CT) imaging features and texture analysis to distinguish bronchiolar adenoma (BA) from adenocarcinoma *in situ* (AIS)/minimally invasive adenocarcinoma (MIA).

Materials and Methods: Fifteen patients with BA, 38 patients with AIS, and 36 patients with MIA were included in this study. Clinical data and CT imaging features of the three lesions were evaluated. Texture features were extracted from the thin-section unenhanced CT images using Artificial Intelligence Kit software. Then, multivariate logistic regression analysis based on selected texture features was employed to distinguish BA from AIS/MIA. Receiver operating characteristics curves were performed to determine the diagnostic performance of the features.

Results: By comparison with AIS/MIA, significantly different CT imaging features of BA included nodule type, tumor size, and pseudo-cavitation sign. Among them, pseudo-cavitation sign had a moderate diagnostic value for distinguishing BA and AIS/MIA (AUC: 0.741 and 0.708, respectively). Further, a total of 396 quantitative texture features were extracted. After comparation, the top six texture features showing the most significant difference between BA and AIS or MIA were chosen. The ROC results showed that these key texture features had a high diagnostic value for differentiating BA from AIS or MIA, among which the value of a comprehensive model with six selected texture features was the highest (AUC: 0.977 or 0.976, respectively) for BA and AIS or MIA. These results indicated that texture analyses can effectively improve the efficacy of thin-section unenhanced CT for discriminating BA from AIS/MIA.

Conclusion: CT texture analysis can effectively improve the efficacy of thin-section unenhanced CT for discriminating BA from AIS/MIA, which has a potential clinical value and helps pathologist and clinicians to make diagnostic and therapeutic strategies.

Keywords: bronchiolar adenoma, texture analysis, computed tomography, lung adenocarcinoma, ground glass nodule

INTRODUCTION

Bronchiolar adenoma (BA) is a recently recognized rare benign tumor with good prognosis that corresponds to the anatomic epithelial cellular component of bronchioles (1). According to the proportion of mucous cells and ciliated cells on the luminal surface, BA is divided into proximal type and distal type. On computed tomography (CT) images, BA often presents as a peripheral irregular-shaped small solid nodule, ground-glass nodule (GGN), or subsolid GGN with a central cavity (2, 3), which could be easily misdiagnosed as adenocarcinoma *in situ* (AIS) or minimally invasive adenocarcinoma (MIA) (4). As subtypes of lung adenocarcinomas, AIS or MIA requires surgery and is not expected to recur if removed completely (5–7). However, BA, a benign tumor, does not need surgery and just needs follow-up observation. Thus, it is important to accurately differentiate BA from AIS and MIA before operation. However, conventional CT characteristics of pulmonary nodules such as tumor size, density, shape, and margin are often insufficient for evaluation.

Clinically, biopsy is used to preoperatively confirm the diagnosis when lung cancer is suspected. This process requires an invasive procedure, which has risks including bleeding, pneumothorax, and infection (8, 9). And the pathological diagnosis through biopsy is inherently prone to sampling error due to tumor heterogeneity. Moreover, with the small size and peripheral nature of BA, preoperative diagnosis with transbronchial or percutaneous biopsy could be difficult. In addition, previous studies reported that it was extremely challenging to distinguish BA from adenocarcinoma on frozen sections, even for experienced thoracic pathologists, which results in overtreatment of patients (10). Thus, it is urgent to develop non-invasive complementary approaches to accurately discriminate BA from AIS and MIA prior to operation, which could help pathologists and clinicians to make diagnostic and therapeutic strategies.

Texture analysis is a novel imaging post-processing technique used for the quantification of image grayscale distribution features, pixel interrelationships, and spectral properties of images (11–13). Compared with conventional imaging methods, texture analysis can measure tumor heterogeneity that may not be perceptible to the human eye. Recent studies have shown potential clinical value of computer-aided texture analysis in the field of oncology, primarily preoperative diagnosis, grading, assessing progression, and response to therapy of cancer patients (14–16). In particular, CT texture analysis has shown promising results in lung cancer for subsolid/solid nodules and lung masses (17–19). However, to our knowledge, no data is available concerning the application of CT texture analysis to the BA. Therefore, we aimed to identify quantitative texture features for further evaluation as non-invasive biomarkers. Such biomarkers could potentially be used to distinguish BA from AIS and MIA.

MATERIALS AND METHODS

Patients

This study was approved by the ethics committee of Daping Hospital, and the informed consent requirement was waived. In this retrospective study, from October 2017 to June 2020, 86 patients underwent surgical resection of tumors presenting as solitary pulmonary nodule, including solid nodule, GGN, or subsolid GGN, on CT images and pathologically diagnosed as BA, AIS, or MIA. AIS and MIA were diagnosed according to the World Health Organization 2015 criteria as confirmed by surgery (20). BA was diagnosed based on morphologically identifying a continuous basal cell layer, which was followed by immunohistochemical confirmation using the basal cell markers p40, p63, and CK5/6 (1, 21, 22). Tissue specimens were reviewed by pathologists with 10 years of experience in lung pathology. The inclusion criteria were as follows: (a) thin-section CT scans were performed before surgery; (b) lesions presented as solitary pulmonary nodule on thin-section CT images; (c) biopsy, surgery, chemotherapy, and radiotherapy were not performed for lesions before CT examination; (d) there was surgical resection and histopathological confirmation as BA, AIS or MIA; (e) the interval between CT scanning and surgery was within 30 days. The exclusion criteria were as follows: (a) tumor diameter was larger than 3 cm; (b) there were severe respiratory artifacts on CT images. In total, 15 BA, 38 AIS, and 36 MIA were enrolled. The clinical data including age, gender, smoking history, and surgical extent were collected. Patient demographics are summarized in **Table 1**.

CT Image Acquisition and Analysis

All CT images were obtained on a 64-detector CT scanner (LightSpeed VCT, GE Healthcare) with a breath-held helical acquisition of the entire thorax. CT parameters were as follows: tube voltage = 120 kVp; tube current = 150 mAs; detector collimation = 0.5 mm × 64; pitch = 0.625; rotation time = 0.5 s; reconstruction slice thickness = 1 mm; matrix = 512 × 512; field of view = 407 mm. All CT images were analyzed by two radiologists (JF and XL, with 13 and 9 years of experience in chest radiology, respectively) independently. Both radiologists were informed of the location of each lesion but were blinded to the pathological diagnosis. Lung nodules were divided into three types, containing pure GGNs, subsolid GGNs, and solid nodules based on thin-section unenhanced CT images. A pure GGN was defined as a nodule occupied by ground-glass opacity without solid regions. A subsolid GGN was defined as a nodule that obscured underlying vascular signs and where <50% of the nodule was observed at the mediastinal window. When more than 50% of a nodule was seen at the mediastinal window, a solid nodule was defined (3). At the lung window, we assessed the tumor size, shape (round to oval or irregular), margin (smooth, lobulated, or spiculated), tumor–lung interface (clear or fuzzy), pseudo-cavitation, and distance to pleura of the lesion. The tumor size was defined as the maximum length of the lesion in any axis (23). Pseudo-cavitation presented as an oval or round area of low attenuation in lung nodules, masses, or areas of consolidation that represent spared parenchyma, normal or ectatic bronchi, or focal emphysema rather than cavitation (24). Any interobserver discordance resulted in the radiologists reevaluating the image together and reaching a consensus.

TABLE 1 | Demographic and clinical data of the subjects.

Variable		BA ($n = 15$)	AIS ($n = 38$)	MIA ($n = 36$)	F-value (t/χ^2)	P-value
Age (years)		52.27 ± 15.91	55.95 ± 8.92	58.69 ± 11.70	1.728	0.184
Sex	Male	5/15 (33.33%)	7/38 (18.42%)	11/36 (30.56%)	1.949	0.377[a]
	Female	10/15 (66.67%)	31/38 (81.58%)	25/36 (69.44%)		
Smoking	Never	1/15 (6.67%)	2/38 (5.26%)	4/36 (11.11%)	0.908	0.635[a]
	Former or current	14/15 (93.33%)	36/38 (94.74%)	32/36 (88.89%)		
	Wedge resection	2/15 (13.33%)	4/38 (10.53%)	2/36 (5.56%)	6.538	0.162[a]
Surgery	Segmentectomy	0/15 (0%)	7/38 (18.42%)	2/36 (5.56%)		
	Lobectomy	13/15 (86.67%)	27/38 (71.05%)	32/36 (88.88%)		

Quantitative variables are expressed as mean ± standard deviation. Qualitative variables are expressed as proportion. [a]Chi-square test for sex, smoking, and surgery. The comparison of age among three groups was performed with ANOVA. The level of significance for intergroup differences was set at $P < 0.05$. BA, bronchiolar adenoma; AIS, adenocarcinoma in situ; MIA, minimally invasive adenocarcinoma.

Volume of Interest (VOI) Segmentation and Texture Feature Extraction

The lesions were delineated on the thin-section unenhanced CT images using the ITK-SNAP software (available at www.itksnap.org) at the lung window. Two experienced radiologists (JS and HT, both with 9 years of experience in imaging) blinded to the clinical outcomes were involved in region of interest (ROI) segmentation. The whole tumor volume was determined by manually drawing an ROI along the border of the tumor on each consecutive slice covering the whole lesion. Therefore, a three-dimensional VOI was finally obtained. The texture features were automatically calculated by the AK software (Artificial Intelligence Kit, GE Healthcare). A total of 396 texture features were extracted, including six types: histogram, gray-level co-occurrence matrix (GLCM), gray-level size zone matrix (GLSZM), gray-level run-length matrix (GLRLM), form factor features, and Haralick features. The extracted texture features were standardized to remove the unit limits of each feature. The histogram described the distribution of voxel intensities within the image region defined by the mask through commonly used and basic metrics. GLRLM depicts the amount of homogeneity in specific directions. GLCM and Haralick features provide information about the gray-level value distribution of pixel pairs in all directions. GLSZM is efficient for characterizing texture homogeneity, non-periodicity, or a speckle-like texture (25).

Statistical Analysis

Statistical analyses were performed using the SPSS software (version 20.0, IBM Corp., Armonk, NY). Kolmogorov–Smirnov and Levene tests were used for the assessment of normal distribution and equal variance. With regard to the reproducibility of volumetric and texture analysis, inter-observer reliability was assessed by an intraclass correlation coefficient (ICC) test. In general, an ICC <0 indicates no agreement, 0–0.20 slight agreement, 0.21–0.40 fair agreement, 0.41–0.60 moderate agreement, 0.61–0.80 substantial agreement, and 0.81–1 almost perfect agreement. A one-way analysis of variance (ANOVA) test was applied to assess the ability of CT imaging features to differentiate between BA and AIS/MIA. The level of significance for intergroup differences was set at $P < 0.05$. *Post-hoc* tests with Bonferroni correction were performed after observing statistical differences among the three groups. $P < 0.017$ (0.05/3) was considered significant after Bonferroni correction. Feature dimension reduction was performed as follows: first, a t-test or Mann–Whitney U-test was performed; second, univariate logistic analysis was conducted, and statistically significant features ($P < 0.05$) were chosen; third, the minimal-redundancy maximal-relevance method (mRMR) was used to remove the redundant and less-relevant features. Multivariate logistic regression analyses were performed to establish a comprehensive model with the most valuable parameters to distinguish BA from AIS or MIA. The diagnostic accuracy of different CT imaging features, textural features, and comprehensive models were evaluated by a receiver operating characteristic (ROC) analysis to obtain area under curves (AUCs), sensitivity, and specificity. The MedCalc Statistical Software (version 19.3.1, MedCalc Software Ltd, Ostend, Belgium) was used to compare differences in AUCs. Two-tailed P-values were calculated with a 0.05 significance level.

RESULTS

Patients' Clinical Characteristics

The clinical characteristics of 15 BA, 35 AIS, and 38 MIA patients are summarized in **Table 1**. No significant differences were found in age, sex, smoking status, and surgery among the three groups. In our study, women (66/89, 74.16%) and patients who had smoking history (82/89, 92.13%) were more common. Lobectomy was performed in the majority of the patients (72/89, 80.90%).

Comparison of CT Imaging Features Between BA and AIS/MIA

CT features of BA, AIS, and MIA are summarized in **Table 2**, and examples of BA, AIS, and MIA are shown in **Figure 1**. BA presented as pure GGN (2/15, 13.33%), subsolid GGN (3/15, 20.00%), or solid nodule (10/15, 66.67%), among which a solid nodule was more common in this study, whereas subsolid GGN was the common nodule type in AIS and MIA. Tumor size was larger in MIA than in BA (16.11 ± 6.07 vs. 10.53 ± 4.50, $P < 0.001$), but no significant difference was found

TABLE 2 | Differences in CT findings among BA, AIS, and MIA.

Variable		BA	AIS	MIA	*F*-value (t/χ^2)	*P*-value
Diameter (mm)		10.53 ± 4.50	11.26 ± 3.54	16.11 ± 6.07	11.685	<0.001*#
Nodule type	Pure GGN	2/15 (13.33%)	2/38 (5.26%)	8/36 (22.22%)	25.99	<0.001a*$
	Subsolid GGN	3/15 (20.00%)	27/38 (71.05%)	26/36 (72.22%)		
	Solid nodule	10/15 (66.67%)	9/38 (23.69%)	2/36 (5.56%)		
Shape	Round to oval	1/15 (6.67%)	11/38 (28.95%)	8/36 (22.22%)	3.067	0.216a
	Irregular	14/15 (93.33%)	27/38 (71.05%)	28/36 (77.78%)		
Margin	Smooth	9/15 (60.00%)	13/38 (34.21%)	12/36 (33.33%)	4.375	0.358a
	Lobulated	5/15 (33.33%)	20/38 (52.63%)	17/36 (47.22%)		
	Spiculated	1/15 (6.67%)	5/38 (13.16%)	7/36 (19.45%)		
Tumor–lung interface	Clear	9/15 (60.00%)	25/38 (65.79%)	17/36 (47.22%)	2.658	0.265a
	Fuzzy	6/15 (40.00%)	13/38 (34.21%)	19/36 (52.78%)		
Pseudo-cavitation	Absent	5/15 (33.33%)	31/38 (81.58%)	27/36 (75.00%)	12.624	0.002a*$
	Present	10/15 (66.67%)	7/38 (18.42%)	9/36 (25.00%)		
Distance to pleura		6.18 ± 7.47	8.26 ± 8.41	8.57 ± 8.26	0.475	0.623

*Quantitative variables are expressed as mean ± standard deviation. Qualitative variables are expressed as proportion. [a]Chi-square test for nodule type, shape, margin, tumor–lung interface, and pseudo- cavitation. The comparison of tumor maximum diameter and distance to pleura among three groups was performed with ANOVA. The level of significance for intergroup differences was set at $P < 0.05$. [$]$P < 0.017$ (0.05/3) BA vs. AIS, with post-hoc test, Bonferroni corrected. *$P < 0.017$ (0.05/3) BA vs. MIA, with post-hoc test, Bonferroni corrected. [#]$P < 0.017$ (0.05/3) AIS vs. MIA, with post-hoc test, Bonferroni corrected. BA, bronchiolar adenoma; AIS, adenocarcinoma in situ; MIA, minimally invasive adenocarcinoma; GGN, ground-glass nodules.*

between BA and AIS (10.53 ± 4.50 vs. 11.26 ± 3.54, $P = 0.624$). Notably, a pseudo-cavitation sign was observed more frequently in BA (10/15, 66.67%), compared to AIS (7/38, 18.42%) or MIA (9/36, 25.00%) ($P = 0.002$). No statistically significant differences with respect to tumor shape ($P = 0.216$), margin ($P = 0.358$), tumor–lung interface ($P = 0.265$), and distance to pleura ($P = 0.623$) were observed among BA, AIS, and MIA. Furthermore, ROC analysis was performed to ascertain relevant CT imaging features in differentiating BA from AIS/MIA. The results showed that the pseudo-cavitation sign had a moderate diagnostic value (AUC: 0.741, sensitivity: 81.6%, specificity: 66.7%, **Supplementary Table 1**) for distinguishing BA and AIS, while others demonstrated no significance ($P > 0.05$). For BA and MIA, the nodule type, tumor size, and pseudo-cavitation sign had moderate diagnostic values (AUC: 0.780, 0.763, and 0.708, respectively, **Supplementary Table 2**). Overall, the pseudo-cavitation sign was the CT imaging feature which had a moderate diagnostic value for differentiating BA from AIS/MIA.

Comparison of CT Texture Analysis Between BA and AIS/MIA

To improve the diagnostic value for BA and AIS/MIA, we performed the CT texture analysis of these lesions. A total of 396 texture features were extracted from unenhanced CT images. The ICC values of the inter-observer of our research were 0.82–0.98, which suggests great accordance between two readers and the reliability of VOI sketching. Three representative sets of CT texture features of patients with BA, AIS, and MIA are shown in **Figure 2**, which have similar CT imaging features but different characteristics of CT texture features. The histogram showed that the gray distribution of BA is more concentrated than that of AIS/MIA. The variation of GLRLM of BA is smaller than that of AIS/MIA. And the distribution of GLCM indicated that the heterogeneity of lesions in AIS/MIA was greater than that in BA. The top six texture features showing the most significant difference, namely, GLCMEntropy_AllDirection_offset1_SD ($P < e^{-4}$), LongRunLowGreyLevelEmphasis_angle45_offset7 ($P = 0.00028$), GLCMEnergy_AllDirection_offset1_SD ($P = 0.00042$), ShortRunEmphasis_angle0_offset1 ($P < e^{-4}$), VoxelValueSum ($P = 0.00310$), and Quantile0.975 ($P = 0.00348$), were calculated between BA and AIS (**Figure 3**). The diagnostic performance of each texture is shown in **Figure 5A**. Generally, an AUC > 0.9 indicates excellent diagnostic efficacy, and between 0.8 and 0.9 good diagnostic efficacy. The ROC results showed that three of these six texture features had high diagnostic values for differentiating BA from AIS (AUC > 0.8, **Supplementary Table 3**), among which the value of GLCMEntropy_AllDirection_offset1_SD was the highest (AUC: 0.912, sensitivity: 93.3%, specificity: 78.9%, cutoff value: 0.0018). Moreover, for BA vs. MIA, ClusterShade_AllDirection_offset1 ($P < e^{-4}$), ClusterShade_angle0_offset1 ($P < e^{-4}$), LongRunLowGreyLevelEmphasis_angle0_offset7 ($P < e^{-4}$), ClusterShade_angle45_offset1 ($P < e^{-4}$), VoxelValueSum ($P < e^{-4}$), and ClusterShade_angle90_offset7 ($P < e^{-4}$) were the top six texture features showing the most significant difference (**Figure 4**). The ROC results showed that all these six texture features had high diagnostic values for differentiating BA from MIA (AUC > 0.85, **Supplementary Table 4** and **Figure 5B**), among which the value of ClusterShade_AllDirection_offset1 was the highest (AUC: 0.876, sensitivity: 80.0%, specificity: 91.7%, cutoff value: 28,505.6). Notably, among these features, VoxelValueSum was the texture feature showing the most significant difference in common for BA vs. AIS and BA vs. MIA. This feature was significantly greater in AIS/MIA patients than in BA patients, which had a high diagnostic value for differentiating

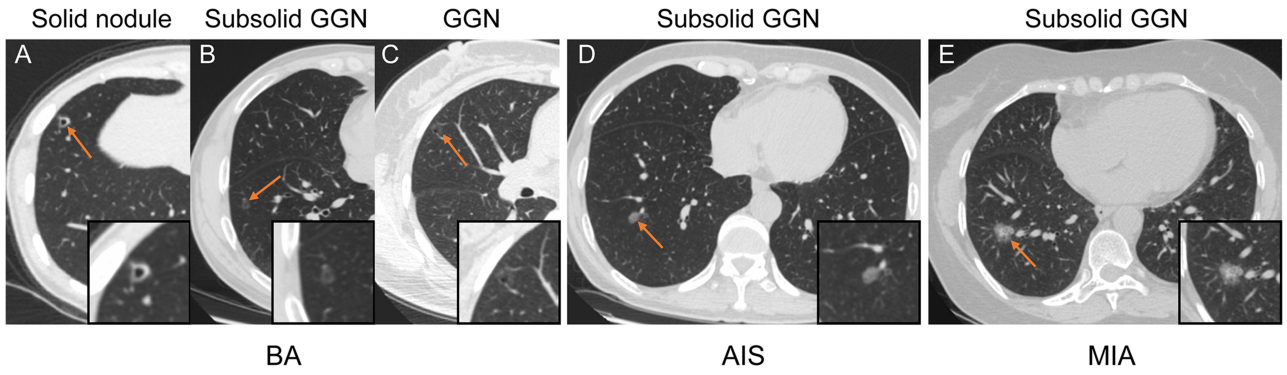

FIGURE 1 | Representative CT images of patients with BA **(A–C)**, AIS **(D)**, and MIA **(E)**. **(A–C)** Axial CT image of BA presenting as a solid nodule **(A)**, subsolid GGN **(B)**, and GGN **(C)** with round to oval shape, pseudo-cavitation, smooth margins, and clear tumor–lung interface. **(D)** Axial CT image of AIS that presents as a subsolid GGN with an oval shape, smooth margins, and clear tumor–lung interface. **(E)** Axial CT image of MIA appearing as a subsolid GGN with an oval shape, small spiculated margin, shallow lobulation, and clear tumor–lung interface.

BA from AIS/MIA simultaneously (**Supplementary Tables 3**, **4**). Furthermore, there was no significant difference between the AUC of pseudo-cavitation and the maximum AUC of texture feature for distinguishing BA from AIS ($Z = 1.885$, $P = 0.0595$) or MIA ($Z = 1.628$, $P = 0.1035$). However, a pseudo-cavitation sign had a moderate diagnostic value for distinguishing BA and AIS (AUC: 0.741) or MIA (AUC: 0.708), while texture features had a high diagnostic value for differentiating BA from AIS (highest AUC: 0.912) or MIA (highest AUC: 0.876). These results indicate that the diagnostic values of texture features are higher than those of CT imaging features for differentiating BA from AIS/MIA.

Model Development and Analysis

Multivariate logistic regression analyses were performed to establish a comprehensive model with six selected texture features to distinguish BA from AIS or MIA. The sensitivity, specificity, and AUC for differentiating BA from AIS were 93.3, 92.1, and 0.977 (95% CI 0.893–0.999), respectively (**Figure 6A**). While the sensitivity, specificity, and AUC for differentiating BA from MIA were 99.9, 85.7, and 0.976 (95% CI 0.885–0.999), respectively (**Figure 6B**). Further, the performance of the comprehensive model for distinguishing BA and AIS or MIA was significantly better than that of the pseudo-cavitation sign (BA vs. AIS: $Z = 3.153$, $P = 0.0016$; BA vs. MIA: $Z = 3.508$, $P = 0.0005$).

DISCUSSION

The present study is the first to distinguish BA from AIS/MIA using texture analysis on thin-section unenhanced CT images. In our study, we evaluated the role of CT imaging and texture analysis in differentiating BA from AIS/MIA. Pseudo-cavitation, one of the CT imaging features, could help differentiate BA from AIS and MIA. Key texture features showing the most significant difference between BA and AIS or MIA have a better distinguishing effect on disease than CT imaging features. Our data indicate that CT texture analysis demonstrates great potential in differentiating BA from AIS/MIA pre-operation.

BA, a rare benign tumor appearing as a peripherally solitary small lung nodule, was first reported in 2018 by Chang et al. (1). Although studies of BA have made new progress, some difficulties still exist in its differential diagnosis. Frozen-section diagnosis is especially challenging for BA. Invasive adenocarcinoma and BA are easily misdiagnosed based on frozen sections owing to their irregular adenoid structures and widened stroma (21, 26). Misdiagnosis of BA as invasive adenocarcinoma may lead to unnecessary interventional procedures, which leads to overtreatment of patients with BA (10). A previous study reported some CT imaging features, including pseudo-cavitation and tumor–lung interface, could help differentiate BA from AIS/MIA (2). In our study, the nodule type, tumor size, and pseudo-cavitation sign showed significant differences between BA and AIS/MIA. BA mainly manifested as a solid nodule type (66.67%), which was consistent with previous studies (3, 27–29). The pseudo-cavitation sign, which is a CT imaging feature of BA, can also be seen in adenocarcinoma, bronchioalveolar carcinoma, and infectious pneumonia (24). However, the pseudo-cavitation sign was reported to be more frequently observed in BA than in AIS and MIA (2). In our cohort, the pseudo-cavitation sign was found in 66.67% of BA and 21.62% of AIS/MIA, similar to what has been reported in a previous study. However, no significant differences were found in tumor–lung interface and tumor shape between BA and AIS/MIA, which was inconsistent with the findings of Cao et al. (2). This inconsistency may be explained by the small sample size because of the low morbidity of BA. In future, a multicenter study with a larger sample size is needed. Furthermore, we evaluated the value of nodule type, tumor size, and pseudo-cavitation sign in differentiating BA from AIS and MIA. The ROC results indicated that the pseudo-cavitation sign had a moderate diagnostic value to differentiate BA from AIS and MIA. Thus, it is necessary to develop non-invasive complementary approaches to improve the diagnostic accuracy for BA before surgery, since the diagnostic value of CT imaging features were not sufficient.

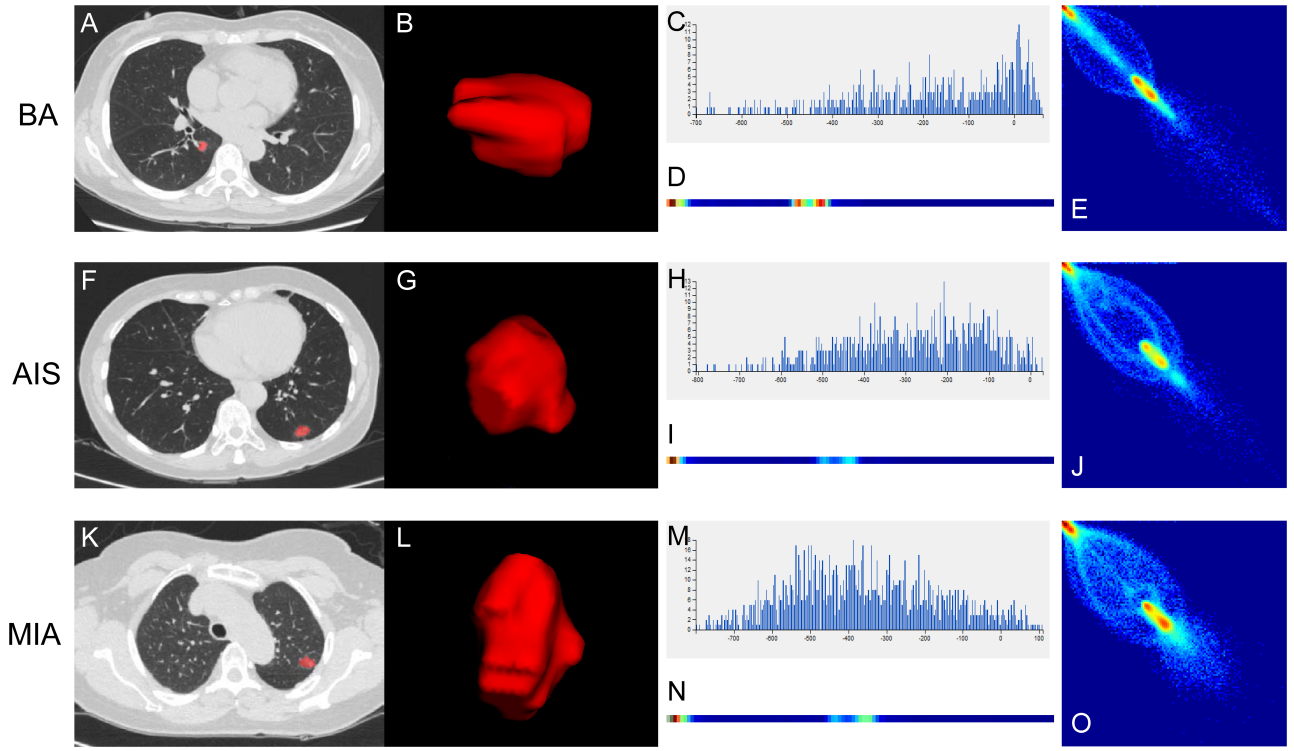

FIGURE 2 | Three representative sets of CT texture features of patients with BA **(A–E)**, AIS **(F–J)**, and MIA **(K–O)**. **(A,F,K)** Thin-section unenhanced CT images. **(B,G,L)** VOIs delineated by the ITK-SNAP software. **(C,H,M)** Histograms of texture parameters of the three lesions showed a marked difference. The distribution of **(H)** and **(M)** were more dispersed than the distribution of **(C)**. **(D,I,N)** GLRLM features of the three lesions. The frequency of grayscale changes of **(D)** was more stable than that of **(I,N)**. **(E,J,O)** GLCM features of the three lesions. The distribution of **(E)** was more concentrated than the distribution of **(J,O)**.

Texture analysis is an emerging imaging-based post-processing method that allows for quantification of tissue heterogeneity (30). There has been a surge in recent years in the research application of CT texture analysis in tumor identification, staging, and therapy response assessment (14–16). However, no studies have demonstrated the value of CT texture analysis in differentiating BA from AIS/MIA. Our data show that GLCMEntropy_AllDirection_offset1_SD, LongRunLowGreyLevelEmphasis_angle45_offset7, GLCM Energy_AllDirection_offset1_SD, ShortRunEmphasis_angle 0_offset1, VoxelValueSum, and Quantile0.975 were the features showing the most significant difference between BA and AIS. Meanwhile, ClusterShade_AllDirection_offset1, ClusterShade_angle0_offset1, LongRunLowGreyLevelEmphasis _angle0_offset7, ClusterShade_angle45_offset1, VoxelValueSum, and ClusterShade_angle90_offset7 were the features showing the most significant difference between BA and MIA. Moreover, to find non-invasive imaging biomarkers for detecting BA patients, we evaluated the discriminative ability of these texture features. Three of these six features had high diagnostic values in discriminating BA from AIS by performing ROC analysis independently, among which the value of GLCMEntropy_AllDirection_offset1_SD was the highest with an AUC of 0.91, sensitivity of 93.3%, and specificity of 78.9%. Meanwhile, for BA vs. MIA, the six obtained features also had high diagnostic values in discriminating BA from MIA, among which the value of ClusterShade_AllDirection_offset1 was the highest with an AUC of 0.88, sensitivity of 80.0%, and specificity of 91.7%. All these AUCs of texture features were higher than those of CT imaging features. Then, we established a comprehensive model with six selected texture features and studied the diagnostic value of the model for distinguishing BA from AIS or MIA by ROC curve analyses. The comprehensive model presented the best diagnostic value, with a significant difference relative to the pseudo-cavitation sign. Moreover, VoxelValueSum was the feature which could well-distinguish BA from AIS and MIA, simultaneously. Therefore, texture analyses can effectively improve the efficacy of thin-section unenhanced CT in discriminating BA from AIS/MIA.

There are some limitations in our study. First, this is a single-institution retrospective analysis, and the sample size is rather small because of the low morbidity of BA. Second, potential selection biases cannot be excluded since this is a retrospective study. Third, manual segmentation of GGN ROIs has a higher risk of observer bias compared to delineation with semi-automatic regression. However, the ICC values of the inter-observer of this study were 0.82–0.98, suggesting great accordance between two readers and the reliability of VOI sketching. Therefore, a multicenter program to include more BA patients may be needed, and a validation

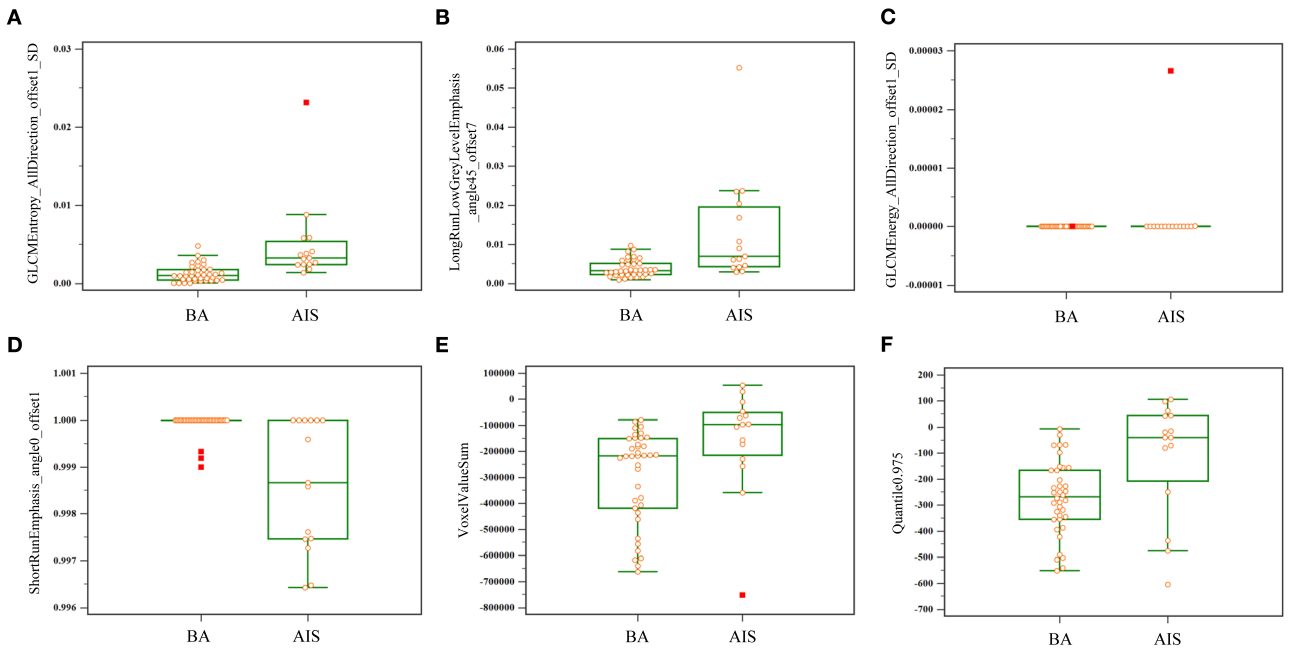

FIGURE 3 | Key texture features of the most significant difference between BA and AIS. Six features, namely, GLCMEntropy_AllDirection_offset1_SD **(A)**, LongRunLowGreyLevelEmphasis_angle45_offset7 **(B)**, GLCMEnergy_AllDirection_offset1_SD **(C)**, ShortRunEmphasis_angle0_offset1 **(D)**, VoxelValueSum **(E)**, and Quantile 0.975 **(F)**, varied significantly between BA and AIS on thin-section unenhanced CT images.

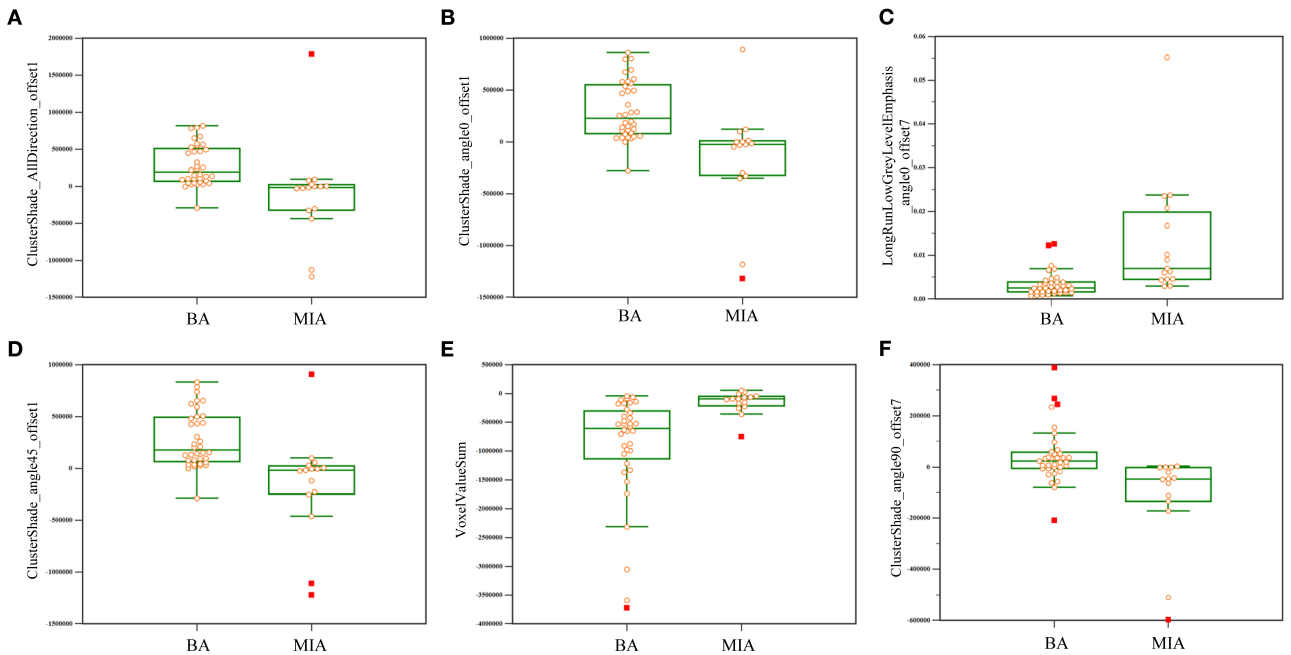

FIGURE 4 | Key texture features showing the most significant difference between BA and MIA. Six features, namely, ClusterShade_AllDirection_offset1 **(A)**, ClusterShade_angle0_offset1 **(B)**, LongRunLowGreyLevelEmphasis_angle0_offset7 **(C)**, ClusterShade_angle45_offset1 **(D)**, VoxelValueSum **(E)**, and ClusterShade_angle90_offset7 **(F)**, varied significantly between BA and MIA on thin-section unenhanced CT images.

to confirm the potential value of CT texture analyses in discriminating BA from AIS/MIA may also be needed in the future.

In conclusion, our study indicated that CT texture analysis can effectively improve the efficacy of thin-section unenhanced CT for discriminating BA from AIS/MIA, which has a potential

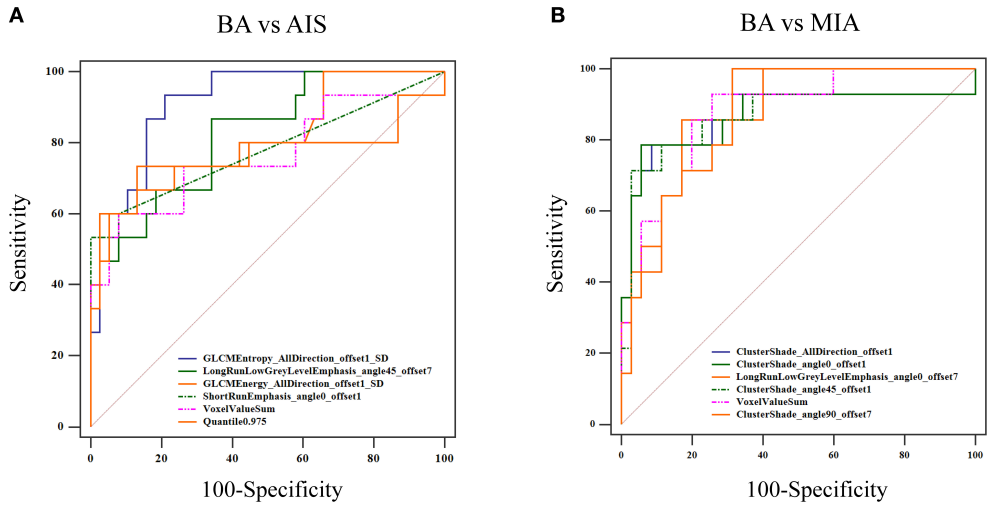

FIGURE 5 | ROC curve for distinguishing BA from AIS/MIA. **(A)** For BA vs. AIS, the AUC values of GLCMEntropy_AllDirection_offset1_SD, LongRunLowGrey LevelEmphasis_angle45_offset7, GLCMEnergy_AllDirection_offset1_SD, ShortRunEmphasis_angle0_offset1, VoxelValueSum, and Quantile 0.975 were 0.912, 0.823, 0.813, 0.779, 0.763, and 0.760, respectively. **(B)** For BA vs. MIA, AUC values of ClusterShade_AllDirection_offset1, ClusterShade_angle0_offset1, LongRunLowGreyLevelEmphasis_angle0_offset7, ClusterShade_angle45_offset1, VoxelValueSum, and ClusterShade_angle90_offset7 were 0.876, 0.876, 0.874, 0.870, 0.865, and 0.857, respectively.

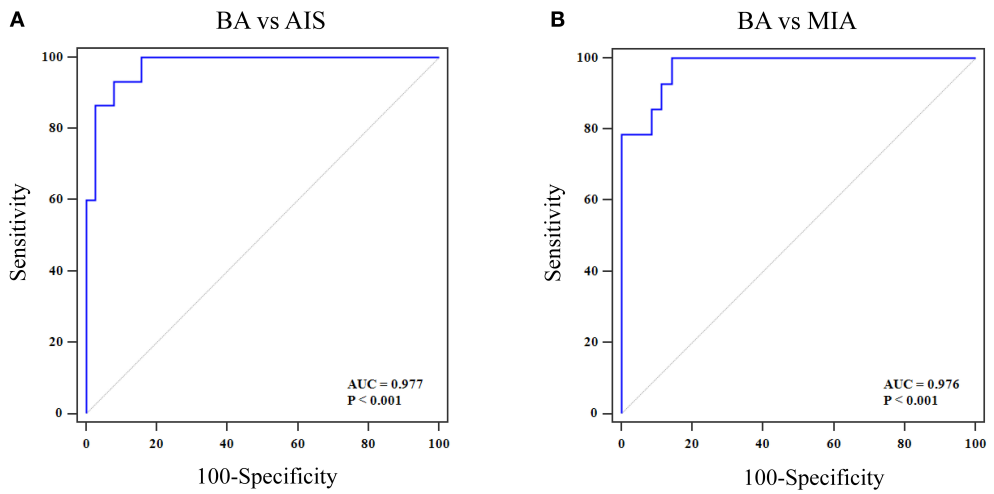

FIGURE 6 | ROC curve of a comprehensive model with six selected texture features for distinguishing BA from AIS/MIA. **(A)** For BA vs. AIS, the AUC value, specificity, and sensitivity were 0.997, 92.1, and 93.3%, respectively. **(B)** For BA vs. MIA, the AUC value, specificity, and sensitivity were 0.976, 85.7, and 99.9%, respectively.

clinical value and helps pathologist and clinicians to make diagnostic and therapeutic strategies.

DATA AVAILABILITY STATEMENT

The original contributions presented in the study are included in the article/**Supplementary Material**, further inquiries can be directed to the corresponding author/s.

ETHICS STATEMENT

The studies involving human participants were reviewed and approved by Research Ethics Committee of Daping Hospital, Army Medical University, Chongqing, China. The ethics committee waived the requirement of written informed consent for participation.

AUTHOR CONTRIBUTIONS

XC and JF conceived and designed the study. JS and YLu collected the CT and clinical data. JF and XL analyzed the CT data. HT and JS extracted the CT texture features. HL analyzed the CT texture data. KL performed the statistics. YLi and YY prepared the figures and tables. XC and KL wrote the manuscript. JF and RJ edited the manuscript. All authors revised the manuscript and read and approved the submitted version.

FUNDING

This work was supported by grants from the National Natural Science Foundation of China (81801672), the Natural Science Foundation of Chongqing (cstc2019jcyj-msxmX0123), Science and Technology Innovation Ability Enhancement Project of Army Medical University (2019XLC3054), Talent Innovation Ability Training Program of Daping Hospital (2019CXLCC010), and Chongqing Clinical Research Center of Imaging and Nuclear Medicine (CSTC2015YFPT-gcjsyjzx0175).

SUPPLEMENTARY MATERIAL

The Supplementary Material for this article can be found online at: https://www.frontiersin.org/articles/10.3389/fonc.2021.634564/full#supplementary-material

REFERENCES

1. Chang JC, Montecalvo J, Borsu L, Lu S, Larsen BT, Wallace WD, et al. Bronchiolar adenoma: expansion of the concept of ciliated muconodular papillary tumors with proposal for revised terminology based on morphologic, immunophenotypic, and genomic analysis of 25 cases. *Am J Surg Pathol*. (2018) 42:1010–26. doi: 10.1097/PAS.0000000000001086
2. Cao L, Wang Z, Gong T, Wang J, Liu J, Jin L, et al. Discriminating between bronchiolar adenoma, adenocarcinoma *in situ* and minimally invasive adenocarcinoma of the lung with CT. *Diagn Interv Imaging*. (2020) 101:831–7. doi: 10.1016/j.diii.2020.05.005
3. Onishi Y, Kusumoto M, Motoi N, Watanabe H, Watanabe SI. Ciliated muconodular papillary tumor of the lung: thin-section CT findings of 16 cases. *AJR Am J Roentgenol*. (2020) 214:761–5. doi: 10.2214/AJR.19.21945
4. Si MJ, Tao XF, Du GY, Cai LL, Han HX, Liang XZ, et al. Thin-section computed tomography-histopathologic comparisons of pulmonary focal interstitial fibrosis, atypical adenomatous hyperplasia, adenocarcinoma *in situ*, and minimally invasive adenocarcinoma with pure ground-glass opacity. *Eur J Radiol*. (2016) 85:1708–15. doi: 10.1016/j.ejrad.2016.07.012
5. Kadota K, Villena-Vargas J, Yoshizawa A, Motoi N, Sima CS, Riely GJ, et al. Prognostic significance of adenocarcinoma *in situ*, minimally invasive adenocarcinoma, and nonmucinous lepidic predominant invasive adenocarcinoma of the lung in patients with stage I disease. *Am J Surg Pathol*. (2014) 38:448–60. doi: 10.1097/PAS.0000000000000134
6. Gu J, Lu C, Guo J, Chen L, Chu Y, Ji Y, et al. Prognostic significance of the IASLC/ATS/ERS classification in Chinese patients-A single institution retrospective study of 292 lung adenocarcinoma. *J Surg Oncol*. (2013) 107:474–80. doi: 10.1002/jso.23259
7. Tsuta K, Kawago M, Inoue E, Yoshida A, Takahashi F, Sakurai H, et al. The utility of the proposed IASLC/ATS/ERS lung adenocarcinoma subtypes for disease prognosis and correlation of driver gene alterations. *Lung Cancer*. (2013) 81:371–6. doi: 10.1016/j.lungcan.2013.06.012
8. Merritt RE, Shrager JB. Indications for surgery in patients with localized pulmonary infection. *Thorac Surg Clin*. (2012) 22:325–32. doi: 10.1016/j.thorsurg.2012.05.005
9. Ozeki N, Iwano S, Taniguchi T, Kawaguchi K, Fukui T, Ishiguro F, et al. Therapeutic surgery without a definitive diagnosis can be an option in selected patients with suspected lung cancer. *Interact Cardiovasc Thorac Surg*. (2014) 19:830–7. doi: 10.1093/icvts/ivu233
10. Guo Y, Shi Y, Tong J. Bronchiolar adenoma: a challenging diagnosis based on frozen sections. *Pathol Int*. (2020) 70:186–8. doi: 10.1111/pin.12901
11. Sharma N, Ray AK, Sharma S, Shukla KK, Pradhan S, Aggarwal LM. Segmentation and classification of medical images using texture-primitive features: application of BAM-type artificial neural network. *J Med Phys*. (2008) 33:119–26. doi: 10.4103/0971-6203.42763
12. Tourassi GD. Journey toward computer-aided diagnosis: role of image texture analysis. *Radiology*. (1999) 213:317–20. doi: 10.1148/radiology.213.2.r99nv49317
13. Gillies RJ, Kinahan PE, Hricak H. Radiomics: images are more than pictures, they are data. *Radiology*. (2016) 278:563–77. doi: 10.1148/radiol.2015151169
14. Ganeshan B, Goh V, Mandeville HC, Ng QS, Hoskin PJ, Miles KA. Non-small cell lung cancer: histopathologic correlates for texture parameters at CT. *Radiology*. (2013) 266:326–36. doi: 10.1148/radiol.12112428
15. Xie T, Chen X, Fang J, Kang H, Xue W, Tong H, et al. Textural features of dynamic contrast-enhanced MRI derived model-free and model-based parameter maps in glioma grading. *J Magn Reson Imaging*. (2018) 47:1099–111. doi: 10.1002/jmri.25835
16. Shu Z, Fang S, Ye Q, Mao D, Cao H, Pang P, et al. Prediction of efficacy of neoadjuvant chemoradiotherapy for rectal cancer: the value of texture analysis of magnetic resonance images. *Abdom Radiol*. (2019) 44:3775–84. doi: 10.1007/s00261-019-01971-y
17. Chen BT, Chen Z, Ye N, Mambetsariev I, Fricke J, Daniel E, et al. Differentiating peripherally-located small cell lung cancer from non-small cell lung cancer using a CT radiomic approach. *Front Oncol*. (2020) 10:593. doi: 10.3389/fonc.2020.00593
18. Gao C, Xiang P, Ye J, Pang P, Wang S, Xu M. Can texture features improve the differentiation of infiltrative lung adenocarcinoma appearing as ground glass nodules in contrast-enhanced CT? *Eur J Radiol*. (2019) 117:126–31. doi: 10.1016/j.ejrad.2019.06.010
19. Gao N, Tian S, Li X, Huang J, Wang J, Chen S, et al. Three-dimensional texture feature analysis of pulmonary nodules in CT images: lung cancer predictive models based on support vector machine classifier. *J Digit Imaging*. (2020) 33:414–22. doi: 10.1007/s10278-019-00238-8
20. Micke P, Mattsson JS, Djureinovic D, Nodin B, Jirstrom K, Tran L, et al. The impact of the fourth edition of the WHO classification of lung tumours on histological classification of resected pulmonary NSCCs. *J Thorac Oncol*. (2016) 11:862–72. doi: 10.1016/j.jtho.2016.01.020
21. Kamata T, Yoshida A, Kosuge T, Watanabe S, Asamura H, Tsuta K. Ciliated muconodular papillary tumors of the lung: a clinicopathologic analysis of 10 cases. *Am J Surg Pathol*. (2015) 39:753–60. doi: 10.1097/PAS.0000000000000414
22. Chuang HW, Liao JB, Chang HC, Wang JS, Lin SL, Hsieh PP. Ciliated muconodular papillary tumor of the lung: a newly defined peripheral pulmonary tumor with conspicuous mucin pool mimicking colloid adenocarcinoma: a case report and review of literature. *Pathol Int*. (2014) 64:352–7. doi: 10.1111/pin.12179
23. Bankier AA, MacMahon H, Goo JM, Rubin GD, Schaefer-Prokop CM, Naidich DP. Recommendations for measuring pulmonary nodules at CT: a statement from the fleischner society. *Radiology*. (2017) 285:584–600. doi: 10.1148/radiol.2017162894
24. Hansell DM, Bankier AA, MacMahon H, McLoud TC, Muller NL, Remy J. Fleischner society: glossary of terms for thoracic imaging. *Radiology*. (2008) 246:697–722. doi: 10.1148/radiol.2462070712
25. Zhang Y, Yu S, Zhang L, Kang L. Radiomics based on CECT in differentiating kimura disease from lymph node metastases in head and neck: a non-invasive and reliable method. *Front Oncol*. (2020) 10:1121. doi: 10.3389/fonc.2020.01121
26. Travis WD, Brambilla E, Noguchi M, Nicholson AG, Geisinger K, Yatabe Y, et al. Diagnosis of lung adenocarcinoma in resected specimens: implications of the 2011 international association for the study of lung cancer/American thoracic society/European respiratory society classification. *Arch Pathol Lab Med*. (2013) 137:685–705. doi: 10.5858/arpa.2012-0264-RA
27. Abe M, Osoegawa A, Miyawaki M, Noda D, Karashima T, Takumi Y, et al. Ciliated muconodular papillary tumor of the lung: a case report and literature review. *Gen Thorac Cardiovasc Surg*. (2020) 68:1344–9. doi: 10.1007/s11748-019-01252-x

28. Onishi Y, Ito K, Motoi N, Morita T, Watanabe SI, Kusumoto M. Ciliated muconodular papillary tumor of the lung: 18F-FDG PET/CT findings of 15 cases. *Ann Nucl Med*. (2020) 34:448–52. doi: 10.1007/s12149-020-01457-8
29. Shao K, Wang Y, Xue Q, Mu J, Gao Y, Wang Y, et al. Clinicopathological features and prognosis of ciliated muconodular papillary tumor. *J Cardiothorac Surg*. (2019) 14:143. doi: 10.1186/s13019-019-0962-3
30. Cannella R, Borhani AA, Minervini MI, Tsung A, Furlan A. Evaluation of texture analysis for the differential diagnosis of focal nodular hyperplasia from hepatocellular adenoma on contrast-enhanced CT images. *Abdom Radiol*. (2019) 44:1323–30. doi: 10.1007/s00261-018-1788-5

Conflict of Interest: HL was employed by company GE Healthcare.

The remaining authors declare that the research was conducted in the absence of any commercial or financial relationships that could be construed as a potential conflict of interest.

frontiers in Oncology

ORIGINAL RESEARCH
published: 23 December 2021
doi: 10.3389/fonc.2021.745001

Pancreatic Serous Cystic Neoplasms and Mucinous Cystic Neoplasms: Differential Diagnosis by Combining Imaging Features and Enhanced CT Texture Analysis

Hai-Yan Chen[1,2], Xue-Ying Deng[1,2], Yao Pan[3], Jie-Yu Chen[1,2], Yun-Ying Liu[2,4], Wu-Jie Chen[1,2], Hong Yang[1,2], Yao Zheng[1,2], Yong-Bo Yang[1,2], Cheng Liu[5], Guo-Liang Shao[1,2,6] and Ri-Sheng Yu[3]**

[1] Department of Radiology, Cancer Hospital of the University of Chinese Academy of Sciences (Zhejiang Cancer Hospital), Hangzhou, China, [2] Institue of Cancer and Basic Medicine (ICBM), Chinese Academy of Sciences, Hangzhou, China, [3] Department of Radiology, Second Affiliated Hospital, Zhejiang University School of Medicine, Hangzhou, China, [4] Department of Pathology, Cancer Hospital of the University of Chinese Academy of Sciences (Zhejiang Cancer Hospital), Hangzhou, China, [5] Research Institute of Artificial Intelligence in Healthcare, Hangzhou YITU Healthcare Technology Co. Ltd., Hangzhou, China, [6] Clinical Research Center of Hepatobiliary and Pancreatic Diseases of Zhejiang Province, Hangzhou, China

OPEN ACCESS

Edited by:
Manisha Aggarwal,
Johns Hopkins University,
United States

Reviewed by:
Shao Zhihong,
Shanghai Zhabei District Shibei Hospital, China
Nguyen Minh Duc,
Pham Ngoc Thach University of Medicine, Vietnam

***Correspondence:**
Guo-Liang Shao
shaogl@zjcc.org.cn
Ri-Sheng Yu
risheng-yu@zju.edu.cn

Specialty section:
This article was submitted to Cancer Imaging and Image-directed Interventions, a section of the journal Frontiers in Oncology

Received: 21 July 2021
Accepted: 29 November 2021
Published: 23 December 2021

Citation:
Chen H-Y, Deng X-Y, Pan Y, Chen J-Y, Liu Y-Y, Chen W-J, Yang H, Zheng Y, Yang Y-B, Liu C, Shao G-L and Yu R-S (2021) Pancreatic Serous Cystic Neoplasms and Mucinous Cystic Neoplasms: Differential Diagnosis by Combining Imaging Features and Enhanced CT Texture Analysis. Front. Oncol. 11:745001. doi: 10.3389/fonc.2021.745001

Objective: To establish a diagnostic model by combining imaging features with enhanced CT texture analysis to differentiate pancreatic serous cystadenomas (SCNs) from pancreatic mucinous cystadenomas (MCNs).

Materials and Methods: Fifty-seven and 43 patients with pathology-confirmed SCNs and MCNs, respectively, from one center were analyzed and divided into a training cohort (n = 72) and an internal validation cohort (n = 28). An external validation cohort (n = 28) from another center was allocated. Demographic and radiological information were collected. The least absolute shrinkage and selection operator (LASSO) and recursive feature elimination linear support vector machine (RFE_LinearSVC) were implemented to select significant features. Multivariable logistic regression algorithms were conducted for model construction. Receiver operating characteristic (ROC) curves for the models were evaluated, and their prediction efficiency was quantified by the area under the curve (AUC), 95% confidence interval (95% CI), sensitivity and specificity.

Results: Following multivariable logistic regression analysis, the AUC was 0.932 and 0.887, the sensitivity was 87.5% and 90%, and the specificity was 82.4% and 84.6% with the training and validation cohorts, respectively, for the model combining radiological features and CT texture features. For the model based on radiological features alone, the AUC was 0.84 and 0.91, the sensitivity was 75% and 66.7%, and the specificity was 82.4% and 77% with the training and validation cohorts, respectively.

Conclusion: This study showed that a logistic model combining radiological features and CT texture features is more effective in distinguishing SCNs from MCNs of the pancreas than a model based on radiological features alone.

Keywords: pancreatic neoplasms, serous cystadenoma, mucinous cystadenoma, texture analysis, tomography

INTRODUCTION

Pancreatic serous cystic neoplasms (SCNs) originate from cuboidal epithelial cells full of glycogen-rich components, and are the only benign tumors of the pancreas, accounting for 10-16% of pancreatic cystic neoplasms (1, 2). The detection of SCNs is increasing, owing to the more widespread use of abdominal imaging (3); typically, however, SCNs only constitutes approximately 30% of all SCNs, presenting with a microcystic appearance with a star-like fibrous central scar with or without calcifications (4). Furthermore, as there is a chanceful spectrum of performances for SCNs in radiology, up to 60% of SCN patients performed surgery with uncertain diagnosis (5); atypical SCNs may misdiagnosed as mucinous cystic neoplasms (MCNs) or intraductal papillary mucinous neoplasms (IPMNs), which have the potential for malignancy, so misdiagnosis can lead to unnecessary surgery (6–8).

There is no consensus regarding the management of SCNs in terms of follow-up and surgery (9, 10). Symptoms, initial tumor size and growth rate are always taken into consideration when determining whether surgery should be performed (11–13). Some studies recommend surgery for SCNs measuring >4 cm regardless of the symptoms due to its rapid growth rate and high risk of symptoms onset (12), while others suggest resection only for SCNs with associated symptoms (10). SCNs are very safe and develop an indolent nature after long-term follow-up, while MCNs should be treated with surgery once a diagnosis is made (14).

Imaging examinations such as CT and MRI, are a mainstay in distinguishing SCNs and MCNs; however, their performance remains unsatisfactory. The accuracy in discriminating certain types of pancreatic cystic neoplasms is between 40-95% for MRI and between 10-81% for CT (10). Texture analysis is a popular technique for quantitatively assessing the heterogeneity of tissues through the extraction, analysis, and interpretation of radiological features and has been widely used in the treatment of pancreatic lesions, such as differential diagnosis, tumor grading, and prognosis prediction (15–18). Several studies related to the discrimination of SCNs and MCNs or that differentiate SCNs from other pancreatic cystic lesions (PCLs) using radiomics have been published (15, 19–24). However, these studies are limited by the use of single center data and small sample sizes, so multicenter studies with larger sample are urgently needed to clarify the role of radiomics. Hence, our study included the largest sample size to date and is the first to incorporate outside data to validate the performance of selected features. Then, we combined imaging features and enhanced CT texture analysis to distinguish SCNs from MCNs.

Abbreviations: SCNs, Serous cystadenomas; MCNs, Mucinous cystadenomas; IPMNs, intraductal papillary mucinous neoplasms; PCLs, Pancreatic cystic lesions; LASSO, Least absolute shrinkage and selection operator; RFE_LinearSVC, Recursive feature elimination linear support vector machine; ROC, Receiver operating characteristic; AUC, Area under the curve; CI, Confidence interval; ROI, Region of interest; ICC, Intraclass correlation coefficient; SD, Standard deviation.

MATERIALS AND METHODS

Patient Population

Ethical approval for this study was approved by the Second Affiliated Hospital of Zhejiang University School of Medicine and Zhejiang Cancer Hospital, and the requirement for informed consent was waived. We retrospectively collected patients diagnosed with pathologically confirmed SCNs (n = 57) or MCNs (n = 43) from the Second Affiliated Hospital of Zhejiang University School of Medicine from January 1, 2010 to October 30, 2019. A cohort to be used solely for external validation was collected from Zhejiang Cancer Hospital from January 1, 2009 to February 20, 2021 (SCN = 19, MCN = 9).

The inclusion criteria were as follows: (1) abdominal contrast-enhanced CT scan performed within 2 months before the operation; and (2) lesion diagnosis confirmed by surgery or biopsy. The exclusion criteria were as follows: (1) incomplete imaging or clinical information; (2) a lesion too small (≤ 5 mm) to draw a region of interest (ROI); and (3) poor image quality or contamination of the ROI by artifacts, preventing analysis.

Image Acquisition

All patients fasted from solid food for approximately 4-6 hours before the examinations. The CT scans were performed with the following equipment: Siemens Somatom definition AS 64、Perspective (Siemens Medical Systems), TOSHIBA Aquilion 320 (TOSHIBA Medical Systems Corporation), and Optima CT680 Series (GE Medical Systems). The imaging parameters were as follows: kVp/effective mA = 120 Kv/160-250 mAs, slice thickness = 5 mm; and field of view = 320-380 mm. A plain scan was performed, followed by intravenous injection of nonionic contrast medium (Omnipaque 300 g/l; GE Healthcare; iopromide; Ultravist 370, Bayer Schering Pharma, 120 mL) at a rate of 3 mL/s. Images were obtained in the arterial phase (23-25 s), portal venous phase (40 s) and equilibrium phase (70 s).

Image Analysis

The imaging features were evaluated by two radiologists (3 and 5 years of experience in pancreatic imaging) who were unaware of the pathology of the lesions. Any arguments were settled by consulting with a third radiologist with 31 years of experience in pancreatic imaging. Demographic data, such as sex, age, symptoms, and tumor markers, were collected. The following radiologic features were included: maximum diameter, location,

central scar, calcification (on the cyst wall or septum vs on the central scar or noncyst wall), the presence of small cysts (extracapsular cystic sign: a small cyst outside the main cyst; intracapsular cystic sign: a small cyst inside the main cyst), cystic wall thickening (≥3 mm), and tumor morphology (single cyst or multiple cysts) (**Figure 1**).

Feature Extraction

CT texture features were extracted from the portal venous phase using MaZda software (version 4.6, www.eletel.p.lodz.pl/programy/mazda) (25). Before extraction, all images were processed with standardized grayscale levels to reduce the impact of changes in imaging contrast and brightness. ROIs were drawn in the maximum diameter of the lesion by consensus of the two evaluating radiologists. The intraclass correlation coefficient (ICC) was calculated to assess the stability and reproducibility of the extracted features. Ten patients (5 SCNs and 5 MCNs) were selected randomly, and the ROI was drawn again two months later by two radiologists. An ICC value of at least 0.9 was considered as stable (26).

Feature Selection

The group of 100 patients from center 1 was randomly divided into a training cohort and an internal validation cohort at a 7:3 ratio, while patients from center 2 were used to construct an external validation cohort (n = 28). The workflow is illustrated in **Figure 2**.

A two-step method was performed for texture features selection.

The training dataset was used to select the texture features. The least absolute shrinkage and selection operator (LASSO) algorithm minimizes the residual sum of squares, sets a bound on the sum of the absolute values of the coefficients, and can be used for reducing the dimensions of high-dimensional data (27). Thus, LASSO was implemented by 10-fold cross-validation for feature reduction, and the minimum λ value was calculated to determine the number of selected features. According to the weighted logistic regression coefficient corresponding to each selected feature, the linear mathematical formula contained the score of the radiomics label for each patient was obtained. The formula is listed as follows:

$$Radiomics\_score = w_0 + w_1x_1 + \ldots w_nx_n$$

where w_n denotes to the respective coefficients and x_n denotes the selected features.

The selected features were analyzed by Student's t-test or the Mann-Whitney U test to eliminate features without significant differences, and then a recursive feature-elimination linear support vector machine (RFE_LinearSVC) was used for further feature selection. RFE_LinearSVC is a powerful method for identifying predictive factors accurately and has consistently outperforms other algorithms in feature selection (28). The internal and external validation cohorts were adopted to verify the performance of the selected features in distinguishing SCNs from MCNs.

Statistical Analysis

Continuous variables were presented as the median (25-75%), and differences between them were assessed using the Mann-Whitney U test. Categorical variables were expressed as frequencies (%), using Chi test. Multivariable logistic regression with 5-fold cross-validation was conducted for training both the mixed model (radiological features combined with extracted texture features) and the radiological model to identify independent factors and establish diagnostic models. The corresponding receiver operating characteristic (ROC) curves were evaluated, and the prediction efficiency of the two models was quantified by the area under the curve (AUC), the 95% confidence interval (95% CI), sensitivity and specificity.

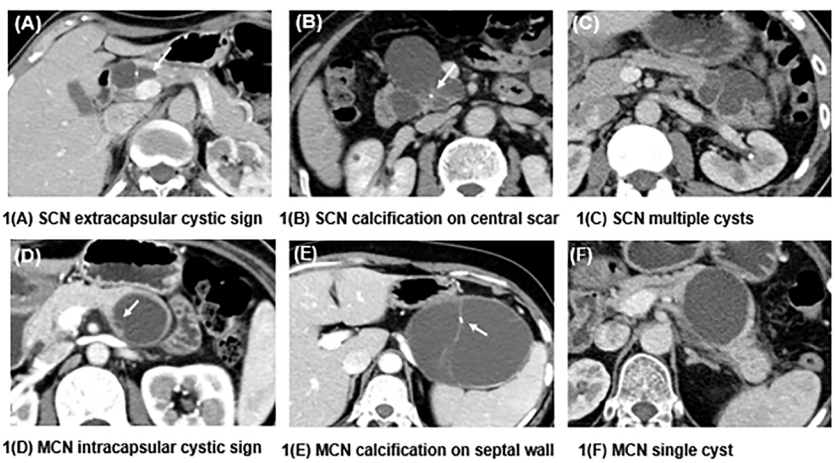

FIGURE 1 | Differences in the characteristics of SCNs and MCNs. **(A)** shows a macrocystic SCN in the head of the pancreas, and a small cyst can be seen outside the mother cyst (white arrow), called the extracapsular cystic sign. **(B)** shows an SCN presenting as a central scar with dotted calcification, which is typical of this kind of neoplasm. **(C)** presents an SCN with multiple cysts that is difficult to diagnose. **(D)** shows a septal wall inside an MCN, which forms a small cyst called the intracapsular cystic sign. **(E)** depicts an MCN with calcification on the septal wall. **(F)** shows an MCN with a single cyst and a smooth contour.

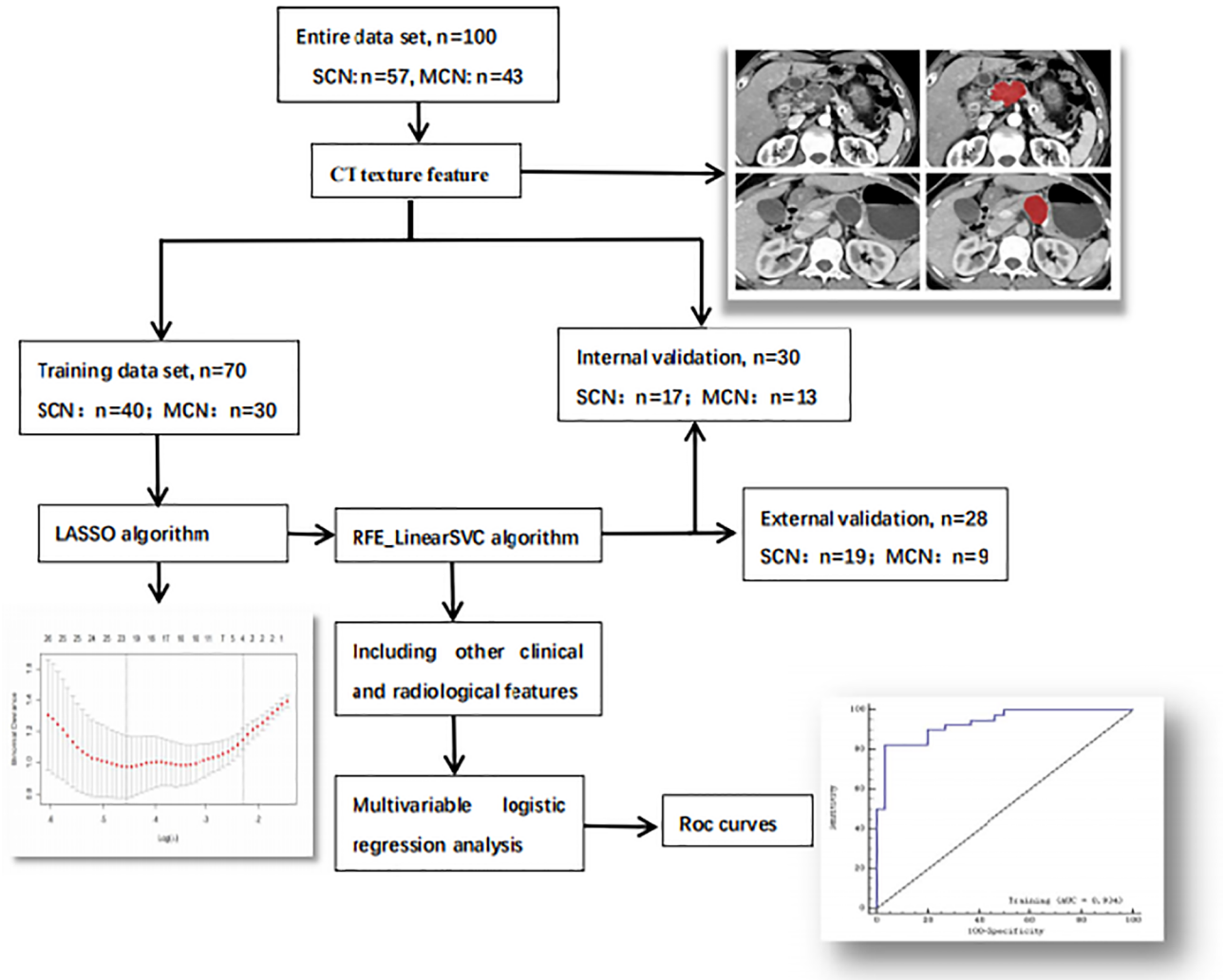

FIGURE 2 | Workflow of the research. The workflow can be divided into four parts: image acquisition, texture feature extraction, texture feature selection and model construction.

Clinical and imaging data were analyzed using SPSS 23.0 software, and $p < 0.05$ was considered as statistically significant. R 3.6.1 software with "glmnet", "Matrix", "foreach" and"ggplot2" packages was used to implement the LASSO algorithm. The YITU AI Enabler was applied to implement the RFE_LinearSVC algorithm, and build models were built using python pyradiomics (version 3.0.1) and the scikit-learn (version 0.22) package.

RESULTS

General Clinical Information and Imaging Features Among SCNs and MCNs

The demographic data of the participants and their imaging features are summarized in **Table 1**. SCNs were more frequently observed among older women than MCNs (median age of 54 vs 47 years, $p < 0.05$). The vast majority of MCNs were found in women (90.7%) and were located in the body/tail (86%), while SCNs could occur anywhere in the pancreas equally ($p < 0.05$). The diameter of the SCNs was generally smaller than that of the MCNs (38.3 mm vs 53.1 mm, $p = 0.009$), and SCNs were often characterized by characteristic central scars, which could have calcifications, while the calcifications of MCNs often occurred on the cyst wall or septum ($p < 0.05$). The most characteristic manifestation of MCNs was the intracapsular cystic sign, while the extracapsular cystic sign was more frequent among SCNs. MCNs were more prone to thickening of the cyst wall (14% vs 1.8%, p=0.024) than SCNs. Finally, there was no significant difference between SCNs and MCNs in terms of symptoms, tumor markers, or tumor morphology ($p > 0.05$).

Feature Extraction and Selection

A total of 271 texture features were extracted: 9 histogram features, 220 gray-level cooccurrence matrix (GLCM) features,

TABLE 1 | Comparison of the clinical information and imaging features between SCNs and MCNs.

Variables	SCNs (n=57)	MCNs (n=43)	P value
Age (years)	54 (44.3-61.3)	47 (33-54)	**0.009***
Gender			**0.042****
Male	14 (24.6)	4 (9.3)	
Female	43 (75.4)	39 (90.7)	
Symptomatic	11 (19.3)	5 (11.6)	0.300
Tumor maker	4 (7.0)	4 (9.3)	0.476
Location			**<0.001****
Head/neck	26 (45.6)	6 (14.0)	
Body/tail	31 (54.4)	37 (86.0)	
Largest diameter (mm)	38.3 (23.9-52.7)	53.1 (32.2-69.5)	**0.009***
Central scar	16 (28.1)	0 (0)	**<0.001****
Calcification			**<0.001****
None	42 (73.7)	34 (79.1)	
On cyst wall	0 (0)	8 (18.6)	
On non-cyst wall	15 (26.3)	1 (2.3)	
Combined with small cyst			**0.003****
None	53 (93.0)	32 (74.4)	
Intracapsular cystic sign	0 (0)	8 (18.6)	
Extracapsular cystic sign	4 (7.0)	3 (7.0)	
Cystic wall thickening			**0.024****
<3mm	56 (98.2)	37 (86.0)	
≥3mm	1 (1.8)	6 (14.0)	
Tumor morphology			0.194
Single cyst	12 (21.1)	14 (32.6)	
Multiple cysts	45 (78.9)	29 (67.4)	

**means P value has significance by using Mann-Whitney U test; **means P value has significance by using Chi test.*

5 gradient features, 5 autoregressive model-based features, 20 run-length matrix features and 12 wavelet features. The ICC value was 0.952 for all features, which was considered stable.

Twenty-three texture features were extracted by the minimum λ value of 0.0106, which was determined through 10-fold cross-validation method using the LASSO algorithm (**Figure 3**). The linear formula contained the score of the radiomics label for each patient was listed in **Supplementary Material 1**. After removing 10 irrelevant statistical variables, 13 texture features were eventually included in the RFE_LinearSVC algorithm as follows: Skewness, S(2,2)DifVarnc, S(2,-2)InvDfMom, S(5,5)InvDfMom, S(4,4)SumEntrp, S(5,5)SumAverg, S(5,5)SumVarnc, Vertl_GLevNonU, 45dgr_GLevNonU, GrNonZeros, Teta1, Teta2, and Teta4. The heat map is shown in **Supplementary Material Figure 1**. Finally, 5 features (Skewness, GrNonZeros, S(2,-2)InvDfMom, S(5,5)InvDfMom, and S(5,5)SumVarnc) were selected with RFE_LinearSVC, and the corresponding decision curve is depicted in **Figure 4**. For the training group, the AUC was 0.934 (95% CI: 0.848-0.980), sensitivity was 90%, and specificity was 76.7%. For the internal and external validation cohorts, the AUCs were 0.855 (95% CI: 0.679-0.956) and 0.892 (95% CI: 0.716-0.977), the sensitivity was 82.4% and 94.7%, and the specificity was 69.2% and 77.8%, respectively (**Figure 5**).

Multivariable Logistic Regression Models

A multivariable logistic regression model combining radiological features and selected texture features was established to differentiate SCNs from MCNs. The AUC was 0.932 (95% CI: 0.845-0.978) and 0.887 (95% CI: 0.0.718-0.973), the sensitivity was 87.5% and 90%, and the specificity was 82.4% and 84.6% with the training and validation cohorts, respectively. Another model based on radiological features alone was also constructed. The AUC was 0.84 (95% CI: 0.732-0.916) and 0.91 (95% CI: 0.747-0.983), the sensitivity was 75% and 66.7%, and the specificity was 82.4% and 77% with the training and validation cohorts, respectively (**Figure 6**).

DISCUSSION

Radiomics appeared to be superior to conventional clinical and radiologic approaches in differentiating the type of PCLs, while the combination of radiomic features and clinical or imaging features may possibly optimize the predictive accuracy of the model (24). Our most compelling result was that we successfully built multiple logistic regression models to differentiate SCNs from MCNs. The logistic model combining radiological features and enhanced CT texture features had an excellent performance, with an AUC of 0.932, compared with the model built with imaging features only, with an AUC of 0.84.

Imaging performance is the most intuitive approach for distinguishing SCNs from MCNs. SCNs can appear in any part of the pancreas, while the vast majority of MCNs (>90%) occur in the body or tail of the pancreas. Since SCNs have always been misdiagnosed as MCNs or other malignant lesions, several special radiologic features have been summarized to help make an accurate diagnosis, such as the typical honeycomb sign (4), petal sign (29), lobulation sign (30) and extracapsular cystic sign (31). External lobulations appear more frequently in SCNs than in MCNs, and the extracapsular cystic sign also suggests an SCN, while the intracapsular cystic sign is a typical presentation of MCNs, which corresponds to other studies (4, 30, 31).

Although radiological manifestations enable an accurate diagnosis in characteristic cases or provide higher priority to less typical cases, SCNs, especially oligocystic types, are difficult to differentiate from MCNs (7, 32). MCNs present as mildly septate, large cystic neoplasms with smooth unilocular contours, and their cystic wall can be thick and enhanced and accompanied by dotted or arcuate calcifications (33). Surgery should be performed when certain MCN diagnoses are made because these lesions have malignant potential (10). Our study successfully established a diagnostic model based on imaging features. After training the model through logistic regression, the resulting AUC values were 0.84 and 0.91 with the training and validation groups, respectively, suggesting good discriminability when distinguishing SCNs from MCNs. Lee et al. (32) described the MRI features of SCNs and MCNs and found that oligocystic SCNs tended to be smaller lesions with a lobulated (85.7%) contour and multiple clustered cystic configurations. Manfredi R et al. (7) included 57 patients with SCNs and 26 patients with MCNs in the body-tail of the pancreas, and they described similar MR imaging features as previous studies. After analysis, they found that a microcystic appearance, central scarring and lack of peripheral wall enhancement were suggestive of SCNs, whereas a macrocystic appearance, enhancement of the peripheral wall and mural nodules were suggestive for MCNs.

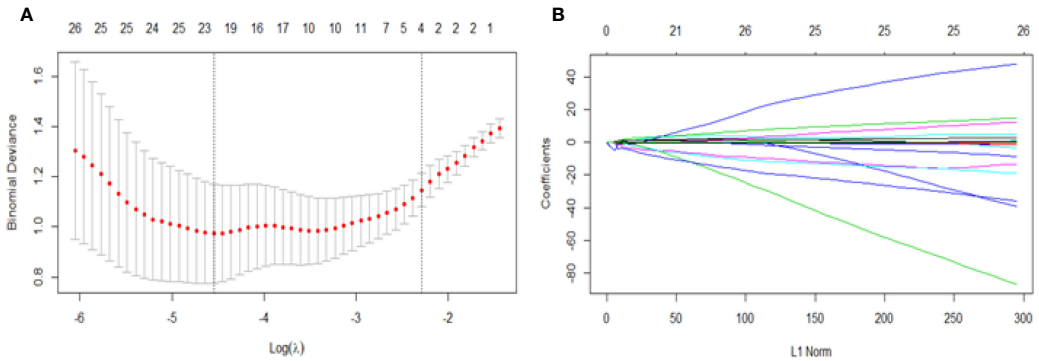

FIGURE 3 | Feature selection for the LASSO algorithm. **(A)** The figure shows binomial deviance (y-axis) plotted against log (λ) (x-axis). The left dotted vertical line is drawn at the optimal value of λ (min λ value = 0.0106, log (λ) = -4.5468), where the model provides the best fit of the data, corresponding to the number of selected features (23). The right vertical dotted line represents the value of λ that yields the best minimum deviation value (minimum λ standard deviation value = 0.1011, log (λ) = - 2.2912). **(B)** LASSO coefficient profiles for all features, which shows that the coefficients of 271 texture features changes with the final selections of different numbers of features.

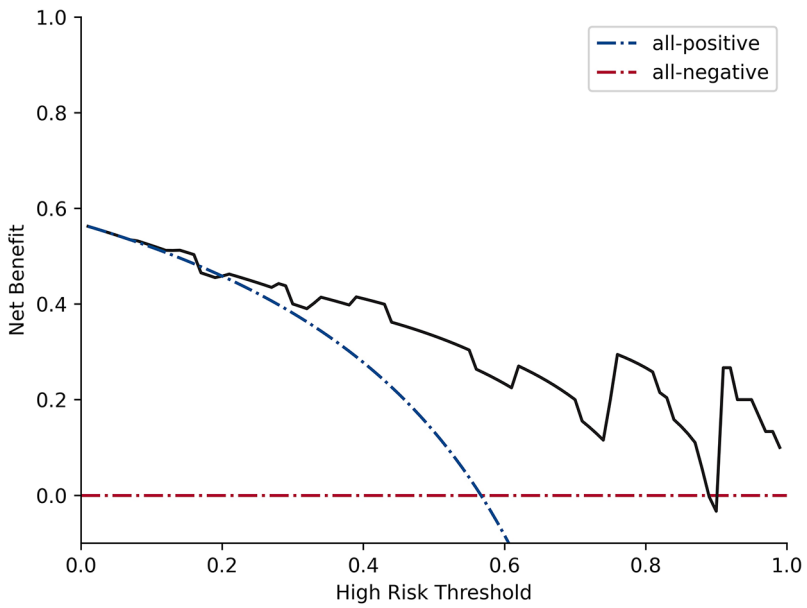

FIGURE 4 | Decision curve analysis for RFE_LinearSVC. The black line represents the true divisional capacity in distinguishing SCNs from MCNs.

However, to overcome diagnostic radiological limitations, radiomics has been recently suggested to differentiate SCNs from MCNs. The combination of radiomics and imaging data may lead to a more precise diagnosis, as described in our study.

Texture analysis has been extensively used for pancreatic tumors as well as PCLs (15–18, 20–22). Yun et al. (17) used CT texture analysis to predict the prognosis of pancreatic cancers and found that texture parameters extracted from preoperative CT images could be used as an independent predictive tool. The grade of pancreatic neuroendocrine tumors could also be predicted accurately; for example, higher skewness and lower kurtosis were identified as risk factors for a higher tumor grade (34). Texture analysis could also identify high-risk disease in patients with IPMNs (35, 36). Xie et al. (22) developed a radiomic model to distinguish macrocystic SCNs (n = 26) from MCNs (n = 31), and their combined model showed better calibration than a single model, as our study showed; however, their sample size was too small and lacked a validation group. Yang et al. (19) included 53 SCNs and 25 MCNs, without external validation, and extracted radiomics features only. After implementing random forest and LASSO methods, they built a diagnostic prediction model to distinguish SCNs from MCNs and obtained AUCs of 0.73 and

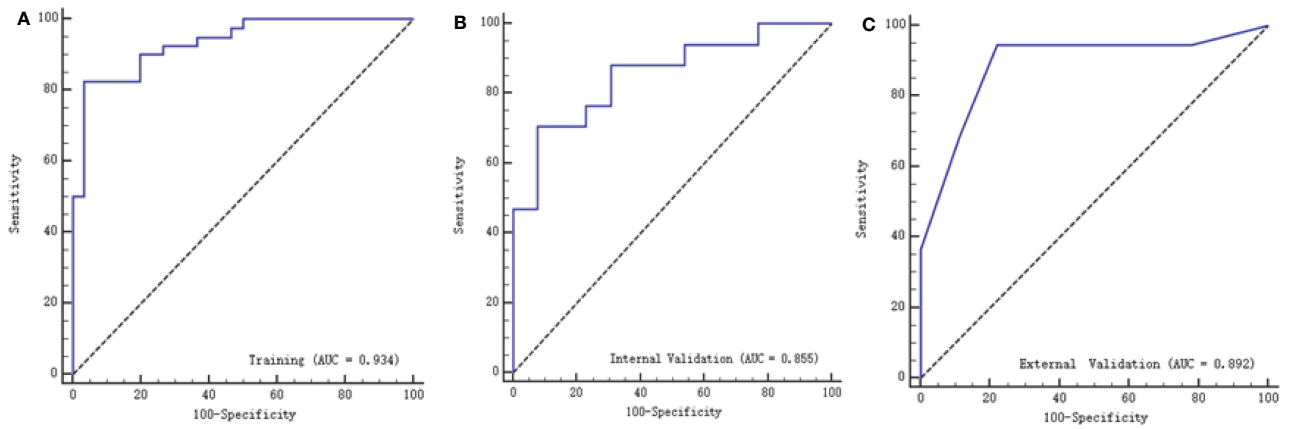

FIGURE 5 | ROC curves of texture features with the training, internal validation and external validation cohorts. **(A)** represents the training group with AUC of 0.934, **(B)** represents the internal validation group with AUC of 0.855, while **(C)** represents with external validation group with AUC of 0.892.

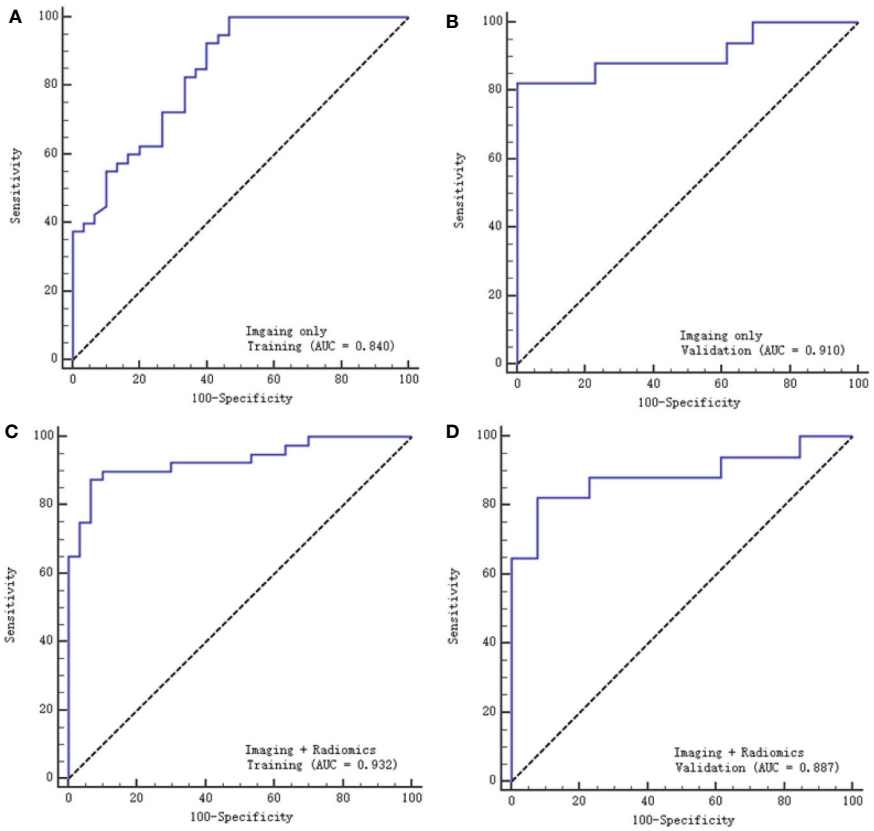

FIGURE 6 | ROC curves of the two models with the training and validation cohorts. **(A, B)** represent the imaging model alone, respectively, and **(C, D)** represent the imaging and radiomics models.

0.70 with the training group and the validation group, respectively. Our study also developed a model based on texture features, which achieved an AUC of 0.934 with the training group and 0.855 and 0.892 with the internal and external validation groups, respectively. Textural features derived from enhanced CT images are useful in differentiating SCNs from MCNs and could provide a noninvasive method to identify whether or not surgery is needed. However, the combination of imaging characteristics and texture features

outperformed morphological features or texture features alone in Yang's study (15), which achieved an AUC of 0.893 for the mixed model. They used the LASSO algorithm to select 15 features, and no further algorithm was applied, as in our study. For further feature selection, we used the RFE_LinearSVC method, a machine learning method with an excellent classification performance that leads to superior discrimination (28). The external validation cohort also demonstrated the remarkable capability of the model to differentiate SCNs from MCNs. A radiomics-based method could differentiate SCNs from other PCLs, with an AUC of 0.767, sensitivity of 0.686 and specificity of 0.709 in Wei's study (23). Shen et al. (20) performed similar work to differentiate SCNs, MCNs and IPMNs, and their random forest classifier achieved the highest accuracy of 84.35 and 79.59% in both the training and validation cohorts. Another study designed an automatic classification algorithm using random forest and conventional neural network ensemble to classify the most common types of PCLs, with an overall accuracy of 83.6% (21).

Several limitations should be emphasized in this study. First, this was a retrospective study with unavoidably inherent selection bias. Second, we only considered the maximal size of the lesion, which may not represent the whole lesion due to tumor heterogeneity. Finally, although the sample size was the largest among similar studies, even larger numbers of patients are required, especially for internal and external validation cohorts, in future investigations.

In conclusion, this study showed that a logistic model combining radiological features and CT texture features is more effective in distinguishing SCNs from MCNs of the pancreas than models built from radiological features alone.

DATA AVAILABILITY STATEMENT

The original data for this manuscript are not publicly available because of patients information privacy. Requests to access the data should be directed to corresponding author R-SY (risheng-yu@zju.edu.cn).

AUTHOR CONTRIBUTIONS

H-YC completed the initial manuscript and designed the whole study; YP and J-YC collected patients and recorded the needed information; X-YD and H-YC collected CT texture features; Y-YL helped collected cases and reviewed the manuscript; W-JC and CL performed the statistics and draw the figure of the manuscript; HY and YZ provided result interpretation; Y-BY performed the control of image quality; G-LS and R-SY revised the manuscript and guaranteed the entire study; All authors did literature research. All authors contributed to the article and approved the submitted version.

FUNDING

This study was supported by funding from the National Natural Science Foundation of China (82072032), Major Medical and Health Science and Technology Projects in Zhejiang Province (WKJ-ZJ-2002), Key R&D Projects in Zhejiang Province (2019C03058), Medical Science and Technology Project of the Health Department of Zhejiang Province of China (2019328554, 2021KY091).

SUPPLEMENTARY MATERIAL

The Supplementary Material for this article can be found online at: https://www.frontiersin.org/articles/10.3389/fonc.2021.745001/full#supplementary-material

REFERENCES

1. Chandwani R, Allen PJ. Cystic Neoplasms of the Pancreas. *Annu Rev Med* (2016) 67:45–57. doi: 10.1146/annurev-med-051914-022011
2. Dababneh Y, Mousa OY. *Pancreatic Serous Cystadenoma*. StatPearls. Treasure Island (FL: StatPearls Publishing Copyright © 2021, StatPearls Publishing LLC (2021).
3. Valsangkar NP, Morales-Oyarvide V, Thayer SP, Ferrone CR, Wargo JA, Warshaw AL, et al. 851 Resected Cystic Tumors of the Pancreas: A 33-Year Experience at the Massachusetts General Hospital. *Surgery* (2012) 152(3 Suppl 1):S4–12. doi: 10.1016/j.surg.2012.05.033
4. Chu LC, Singhi AD, Haroun RR, Hruban RH, Fishman EK. The Many Faces of Pancreatic Serous Cystadenoma: Radiologic and Pathologic Correlation. *Diagn Interv Imaging* (2017) 98(3):191–202. doi: 10.1016/j.diii.2016.08.005
5. Jais B, Rebours V, Malleo G, Salvia R, Fontana M, Maggino L, et al. Serous Cystic Neoplasm of the Pancreas: A Multinational Study of 2622 Patients Under the Auspices of the International Association of Pancreatology and European Pancreatic Club (European Study Group on Cystic Tumors of the Pancreas). *Gut* (2016) 65(2):305–12. doi: 10.1136/gutjnl-2015-309638
6. Kim SY, Lee JM, Kim SH, Shin KS, Kim YJ, An SK, et al. Macrocystic Neoplasms of the Pancreas: CT Differentiation of Serous Oligocystic Adenoma From Mucinous Cystadenoma and Intraductal Papillary Mucinous Tumor. *AJR Am J Roentgenol* (2006) 187(5):1192–8. doi: 10.2214/AJR.05.0337
7. Manfredi R, Ventriglia A, Mantovani W, Mehrabi S, Boninsegna E, Zamboni G, et al. Mucinous Cystic Neoplasms and Serous Cystadenomas Arising in the Body-Tail of the Pancreas: MR Imaging Characterization. *Eur Radiol* (2015) 25(4):940–9. doi: 10.1007/s00330-014-3493-2
8. Postlewait LM, Ethun CG, McInnis MR, Merchant N, Parikh A, Idrees K, et al. Association of Preoperative Risk Factors With Malignancy in Pancreatic Mucinous Cystic Neoplasms: A Multicenter Study. *JAMA Surg* (2017) 152 (1):19–25. doi: 10.1001/jamasurg.2016.3598
9. Dewhurst CE KJM. Cystic Tumors of the Pancreas: Imaging and Management. *Radiol Clin North Am* (2012) 50(3):467–86. doi: 10.1016/j.rcl.2012.03.001
10. European Study Group on Cystic Tumours of the Pancreas. European Evidence-Based Guidelines on Pancreatic Cystic Neoplasms. *Gut* (2018) 67 (5):789–804. doi: 10.1136/gutjnl-2018-316027
11. Lekkerkerker SJ, Besselink MG, Busch OR, Verheij J, Engelbrecht MR, Rauws EA, et al. Comparing 3 Guidelines on the Management of Surgically Removed Pancreatic Cysts With Regard to Pathological Outcome. *Gastrointest Endosc* (2017) 85(5):1025–31. doi: 10.1016/j.gie.2016.09.027

12. Malleo G, Bassi C, Rossini R, Manfredi R, Butturini G, Massignani M, et al. Growth Pattern of Serous Cystic Neoplasms of the Pancreas: Observational Study With Long-Term Magnetic Resonance Surveillance and Recommendations for Treatment. *Gut* (2012) 61(5):746–51. doi: 10.1136/gutjnl-2011-300297
13. Farrell JJ. Pancreatic Cysts and Guidelines. *Dig Dis Sci* (2017) 62(7):1827–39. doi: 10.1007/s10620-017-4571-5
14. Tanaka M, Fernandez-del Castillo C, Adsay V, Chari S, Falconi M, Jang JY, et al. International Consensus Guidelines 2012 for the Management of IPMN and MCN of the Pancreas. *Pancreatol: Off J Int Assoc Pancreatol* (2012) 12 (3):183–97. doi: 10.1016/j.pan.2012.04.004
15. Yang J, Guo X, Zhang H, Zhang W, Song J, Xu H, et al. Differential Diagnosis of Pancreatic Serous Cystadenoma and Mucinous Cystadenoma: Utility of Textural Features in Combination With Morphological Characteristics. *BMC Cancer* (2019) 19(1):1223. doi: 10.1186/s12885-019-6421-7
16. Guo CG, Ren S, Chen X, Wang QD, Xiao WB, Zhang JF, et al. Pancreatic Neuroendocrine Tumor: Prediction of the Tumor Grade Using Magnetic Resonance Imaging Findings and Texture Analysis With 3-T Magnetic Resonance. *Cancer Manage Res* (2019) 11:1933–44. doi: 10.2147/CMAR.S195376
17. Yun G, Kim YH, Lee YJ, Kim B, Hwang J-H, Choi DJ. Tumor Heterogeneity of Pancreas Head Cancer Assessed by CT Texture Analysis: Association With Survival Outcomes After Curative Resection. *Sci Rep* (2018) 8(1):7226. doi: 10.1038/s41598-018-25627-x
18. Sandrasegaran K, Lin Y, Asare-Sawiri M, Taiyini T, Tann M. CT Texture Analysis of Pancreatic Cancer. *Eur Radiol* (2019) 29(3):1067–73. doi: 10.1007/s00330-018-5662-1
19. Yang J, Guo X, Ou X, Zhang W, Ma X. Discrimination of Pancreatic Serous Cystadenomas From Mucinous Cystadenomas With CT Textural Features: Based on Machine Learning. *Front Oncol* (2019) 9:494. doi: 10.3389/fonc.2019.00494
20. Shen X, Yang F, Yang P, Yang M, Xu L, Zhuo J, et al. A Contrast-Enhanced Computed Tomography Based Radiomics Approach for Preoperative Differentiation of Pancreatic Cystic Neoplasm Subtypes: A Feasibility Study. *Front Oncol* (2020) 10:248. doi: 10.3389/fonc.2020.00248
21. Dmitriev K, Kaufman AE, Javed AA, Hruban RH, Fishman EK, Lennon AM, et al. Classification of Pancreatic Cysts in Computed Tomography Images Using a Random Forest and Convolutional Neural Network Ensemble. *Med Image Comput Comput Assist Interv* (2017) 10435:150–8. doi: 10.1007/978-3-319-66179-7_18
22. Xie H, Ma S, Guo X, Zhang X, Wang X. Preoperative Differentiation of Pancreatic Mucinous Cystic Neoplasm From Macrocystic Serous Cystic Adenoma Using Radiomics: Preliminary Findings and Comparison With Radiological Model. *Eur J Radiol* (2020) 122:108747. doi: 10.1016/j.ejrad.2019.108747
23. Wei R, Lin K, Yan W, Guo Y, Wang Y, Li J, et al. Computer-Aided Diagnosis of Pancreas Serous Cystic Neoplasms: A Radiomics Method on Preoperative MDCT Images. *Technol Cancer Res Treat* (2019) 18:1533033818824339. doi: 10.1177/1533033818824339
24. Machicado JD, Koay EJ, Krishna SG. Radiomics for the Diagnosis and Differentiation of Pancreatic Cystic Lesions. *Diagnost (Basel Switzerland)* (2020) 10(7):505. doi: 10.3390/diagnostics10070505
25. Szczypiński PM, Strzelecki M, Materka A, Klepaczko A. MaZda—A Software Package for Image Texture Analysis. *Comput Methods Programs Biomed* (2009) 94(1):66–76. doi: 10.1016/j.cmpb.2008.08.005
26. Dong F, Li Q, Xu D, Xiu W, Zeng Q, Zhu X, et al. Differentiation Between Pilocytic Astrocytoma and Glioblastoma: A Decision Tree Model Using Contrast-Enhanced Magnetic Resonance Imaging-Derived Quantitative Radiomic Features. *Eur Radiol* (2019) 29(8):3968–75. doi: 10.1007/s00330-018-5706-6
27. Vasquez MM, Hu C, Roe DJ, Halonen M, Guerra S. Measurement Error Correction in the Least Absolute Shrinkage and Selection Operator Model When Validation Data Are Available. *Stat Methods Med Res* (2019) 28 (3):670–80. doi: 10.1177/0962280217734241
28. Wang X, Wan Q, Chen H, Li Y, Li X. Classification of Pulmonary Lesion Based on Multiparametric MRI: Utility of Radiomics and Comparison of Machine Learning Methods. *Eur Radiol* (2020) 30(8):4595–605. doi: 10.1007/s00330-020-06768-y
29. Ozaki K, Ikeno H, Kaizaki Y, Maeda K, Higuchi S, Kosaka N, et al. Pearls and Pitfalls of Imaging Features of Pancreatic Cystic Lesions: A Case-Based Approach With Imaging-Pathologic Correlation. *Jpn J Radiol* (2021) 39 (2):118–42. doi: 10.1007/s11604-020-01032-1
30. Kimura W, Moriya T, Hirai I, Hanada K, Abe H, Yanagisawa A, et al. Multicenter Study of Serous Cystic Neoplasm of the Japan Pancreas Society. *Pancreas* (2012) 41(3):380–7. doi: 10.1097/MPA.0b013e31822a27db
31. Chen HY, Zhao J, Lu YF, Lv SY, Chen JY, Pan Y, et al. The "Extracapsular Cystic" Sign in Pancreatic Serous Cystic Neoplasms: A Clinicopathologic Study of 177 Patients With Cystic Pancreatic Lesions. *Eur J Radiol* (2018) 106:167–72. doi: 10.1016/j.ejrad.2018.08.002
32. Lee JH, Kim JK, Kim TH, Park MS, Yu JS, Choi JY, et al. MRI Features of Serous Oligocystic Adenoma of the Pancreas: Differentiation From Mucinous Cystic Neoplasm of the Pancreas. *Br J Radiol* (2012) 85(1013):571–6. doi: 10.1259/bjr/42007785
33. Kalb B, Sarmiento JM, Kooby DA, Adsay NV, Martin DR. MR Imaging of Cystic Lesions of the Pancreas. *RadioGraphics* (2009) 29:1749–65. doi: 10.1148/rg.296095506
34. Choi TW, Kim JH, Yu MH, Park SJ, Han JK. Pancreatic Neuroendocrine Tumor: Prediction of the Tumor Grade Using CT Findings and Computerized Texture Analysis. *Acta Radiol* (2018) 59(4):383–92. doi: 10.1177/0284185117725367
35. Attiyeh MA, Chakraborty J, Gazit L, Langdon-Embry L, Gonen M, Balachandran VP, et al. Preoperative Risk Prediction for Intraductal Papillary Mucinous Neoplasms by Quantitative CT Image Analysis. *HPB (Oxford)* (2019) 21(2):212–8. doi: 10.1016/j.hpb.2018.07.016
36. Chakraborty J, Midya A, Gazit L, Attiyeh M, Langdon-Embry L, Allen PJ, et al. CT Radiomics to Predict High-Risk Intraductal Papillary Mucinous Neoplasms of the Pancreas. *Med Phys* (2018) 45(11):5019–29. doi: 10.1002/mp.13159

Conflict of Interest: Author CL was employed by Hangzhou YITU Healthcare Technology Co. Ltd.

The remaining authors declare that the research was conducted in the absence of any commercial or financial relationships that could be construed as a potential conflict of interest.

Publisher's Note: All claims expressed in this article are solely those of the authors and do not necessarily represent those of their affiliated organizations, or those of the publisher, the editors and the reviewers. Any product that may be evaluated in this article, or claim that may be made by its manufacturer, is not guaranteed or endorsed by the publisher.

frontiers in Oncology

ORIGINAL RESEARCH
published: 20 January 2022
doi: 10.3389/fonc.2021.805545

The Feasibility of Combining ADC Value With Texture Analysis of T_2WI, DWI and CE-T_1WI to Preoperatively Predict the Expression Levels of Ki-67 and p53 of Endometrial Carcinoma

Xueyan Jiang[1†], Haodong Jia[2†], Zhongyuan Zhang[2], Chao Wei[2], Chuanbin Wang[2] and Jiangning Dong[1,2]*

[1] Department of Radiology, Bengbu Medical College, Bengbu, China, [2] Department of Radiology, The First Affiliated Hospital of the University of Science and Technology of China, Anhui Provincial Cancer Hospital, Hefei, China

OPEN ACCESS

Edited by:
Chuanming Li,
Chongqing Medical University, China

Reviewed by:
Caterina Giannitto,
Humanitas Research Hospital, Italy
Jian Shu,
Affiliated Hospital of Southwest Medical University, China

****Correspondence:***
Jiangning Dong
dongjn@163.com

[†]These authors have contributed equally to this work

Specialty section:
This article was submitted to Cancer Imaging and Image-directed Interventions, a section of the journal Frontiers in Oncology

Received: *01 November 2021*
Accepted: *29 December 2021*
Published: *20 January 2022*

Citation:
Jiang X, Jia H, Zhang Z, Wei C, Wang C and Dong J (2022) The Feasibility of Combining ADC Value With Texture Analysis of T_2WI, DWI and CE-T_1WI to Preoperatively Predict the Expression Levels of Ki-67 and p53 of Endometrial Carcinoma. Front. Oncol. 11:805545. doi: 10.3389/fonc.2021.805545

Purpose: To evaluate the feasibility of apparent diffusion coefficient (ADC) value combined with texture analysis (TA) in preoperatively predicting the expression levels of Ki-67 and p53 in endometrial carcinoma (EC) patients.

Methods: Clinical, pathological and MRI findings of 110 EC patients were analyzed retrospectively. The expression levels of Ki-67 and p53 in EC tissues were detected by immunohistochemistry. ADC value was calculated, and three-dimensional (3D) texture features were measured on T_2-weighted images (T_2WI), diffusion-weighted images (DWI), and contrast-enhanced T_1-weighted images (CE-T_1WI). The univariate and multivariate logistic regression and cross-validations were used for the selection of texture features. The receiver operating characteristic (ROC) curve was performed to estimate the diagnostic efficiency of prediction model by the area under the curve (AUC) in the training and validation cohorts.

Results: Significant differences of the ADC values were found in predicting Ki-67 and p53 (P=0.039, P=0.007). The AUC of the ADC value in predicting the expression levels of Ki-67 and p53 were 0.698, 0.853 and 0.626, 0.702 in the training and validation cohorts. The AUC of the TA model based on T_2WI, DWI, CE-T_1WI, and ADC value combined with T_2WI + DWI + CE-T_1WI in the training and validation cohorts for predicting the expression of Ki-67 were 0.741, 0.765, 0.733, 0.922 and 0.688, 0.691, 0.651, 0.938, respectively, and for predicting the expression of p53 were 0.763, 0.805, 0.781, 0.901 and 0.796, 0.713, 0.657, 0.922, respectively.

Conclusion: ADC values combined with TA are beneficial for predicting the expression levels of Ki-67 and p53 in EC patients before surgery, and they provide higher auxiliary diagnostic values for clinical application.

Keywords: endometrial carcinoma, p53, Ki-67, apparent diffusion coefficient, texture analysis

INTRODUCTION

Endometrial carcinoma (EC) is one of the most common malignancies of the female reproductive system worldwide (1), and the morbidity and mortality of EC have been rising with a trend towards a younger age (2). It has been suggested that the occurrence and development of EC are related not only to estrogen levels but also to the proliferation and apoptosis of tumor cells (3). A necessary condition for normal functioning of the body is to maintain the dynamic balance between cell proliferation and apoptosis (4, 5). If this balance is broken, it will promote the occurrence of tumors. Ki-67 and p53 are closely related to the proliferation and apoptosis of tumor cells. Ki-67 is a marker of cell proliferation, is mainly expressed in the nucleus of proliferating cells, and is used to evaluate the proliferation state of tumor cells (6). Higher values of Ki-67 indicate increased malignancy and invasiveness of tumours (7). p53 is an important tumor suppressor gene that controls the initiation of the cell cycle, regulates cell division, inhibits cell growth, regulates transcription, and induces apoptosis (8).

DWI determines the cell density of tissues by detecting the diffusion of water molecules and quantifying it by using the ADC value (9). It has been shown (10) that the ADC mean value is related to the expression level of Ki-67 and p53 in esophageal squamous cell carcinoma, which can be used as a noninvasive biological indicator to predict the proliferation of esophageal squamous cell carcinoma cells and to determine the prognosis of patients. TA is a method to quantitatively measure the distribution and (or) relationship between histogram, pixel intensity or grey level of an image in the region of interest (11, 12). TA highlights subtle patterns of tissue distribution (texture features) that cannot be recognized by human eyes and extends the intrinsic value of images. Thus, in recent years, TA has been used with various cross-sectional imaging modalities and shows clinical applicability in the detection, diagnosis, prognosis, characterization and response evaluation of different cancers (13–15). In the present study, five models were developed to preoperatively predict the expression levels of Ki-67 and p53 in EC. The purpose of this study was to noninvasively evaluate the expression levels of Ki-67 and p53 in EC and to provide imaging markers for the clinical diagnosis and treatment of EC.

MATERIALS AND METHODS

Patients

The Institutional Review Board approved the present retrospective study, and informed consent was waived. Between January 2015 and December 2020, 172 patients who underwent conventional 1.5T MRI before surgery were enrolled by searching our pathology and radiology database in the study. The patients were screened through the medical record system of our hospital. The inclusion criteria were as follows: (a) histologic confirmation of primary EC according to the World Health Organization criteria; (b) no history of preoperative treatment; (c) preoperative available T_2WI, DWI and CE-T_1WI images; (d) available Ki-67 and p53 expression based on immunohistochemical detection; (e) lesion that could be measured and segmented on MRI. Patients were excluded for the following reasons: (a) incomplete medical records or did not receive treatment in our hospital (n=18); (b) other malignant tumors (n=2); (c) postoperative pathology of non-endometrial carcinoma (n=15); (d) inadequate histopathological reports (n=16); (e) without obvious lesions or maximal tumor diameter of less than 1 cm on MRI (n=11). Finally, 110 patients were included in the present study. The flowchart of the exclusion criteria is shown in **Figure 1**.

Patients were divided into a training cohort and a validation cohort at a ratio of 7:3. This division was based on the

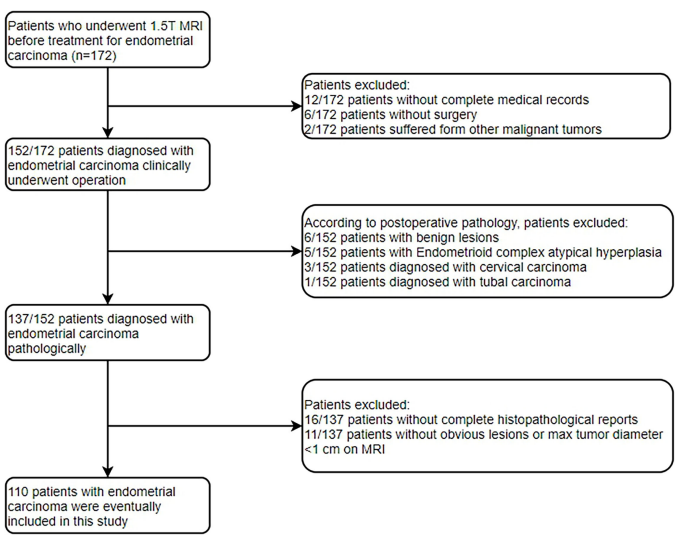

FIGURE 1 | Flowchart shows selection of studying population and exclusion criteria.

chronological order in which patients were examined to ensure the randomness of the pathological results in the training and validation cohorts. The prediction models of Ki-67 and p53 were built with a training cohort and evaluated with a validation cohort. In the p53 expression of EC, only 38 patients with negative p53 expression and 72 patients with positive p53 expression were enrolled. The ratio of negative p53 expression patients to positive p53 expression patients was about 1:1.89, revealing a sample imbalance. Therefore, the synthetic minority over-sampling technique (SMOTE) algorithm was used to balance the minority class, so that the two classes of EC patients were 1:1(72 negative p53 expression and 72 positive p53 expression).

MR Imaging

All MR imaging studies were performed with 1.5T MR imaging units (United Imaging Healthcare, uMR560, Shanghai) using a 6-channel body array coil. All patients were asked to fast for at least 4 hours, and intramuscular injection of scopolamine butyl bromide was given half an hour before the MRI examination to reduce bowel peristalsis. Detailed scanning parameters are listed as follows: (1) Axial fast spin echo (FSE) T_1-weighted images (T_1WI): repetition time (TR)/echo time (TE): 391 ms/9.3 ms, slice thickness: 6 mm, inter-slice gap: 2 mm, a field of view (FOV): 38 cm × 28 cm, and matrix size: 320 × 224. (2) Axial FSE T_2-weighted images (T_2WI): TR/TE: 4500 ms/93 ms, slice thickness: 6 mm, inter-slice gap: 2 mm, FOV: 28 cm × 25 cm, and matrix size: 320 × 224. (3) Axial DWI with b-values of 0 and 1000 s/mm^2: TR/TE: 3201 ms/75.4 ms, slice thickness: 6 mm, inter-slice gap: 2 mm, FOV: 38 cm× 28 cm, and matrix size: 128 × 128. (4) Three-dimensional volumetric interpolated quick gradient echo contrast-enhanced imaging on axial: TR/TE: 8 ms/3 ms, slice thickness: 5 mm, inter-slice gap: 0 mm, FOV: 38 cm×28 cm, and matrix size 256×192. The image was exported in DICOM format.

Image Analysis

For the measurement of ADC values, two subspecialty radiologists (reader 1 and reader 2) with 8 and 10 years of experience in imaging diagnosis independently examined the images to obtain ADC values. The original ADC data were directly analyzed in the postprocessing workstation (United Imaging Healthcare). Under the guidance of T_2WI, the region of interest (ROI) was delineated in the solid part of the largest tumor layer on the DWI image with b=1000 s/mm^2, avoiding hemorrhage and necrotic areas as much as possible. The averages were obtained after the repetition of the measurement three times. The ADC value extraction process is shown in **Figure 2**.

For the assessment of texture features, the conventional axial T_2WI image, DWI with a b value of 1000 s/mm^2, and axial CE-T_1WI image were segmented by reader 2. The conventional axial T_2WI image, DWI with a b value of 1000 s/mm^2, and axial CE-T_1WI image were imported into ITK-SNAP software (version 3.6.0, http://www.itksnap.org). The three-dimensional region of interest (3D ROI) of the whole tumor was manually delineated at each level of sequence, including areas of hemorrhage and necrosis site. To reduce registration errors, a DWI map with a b value of 1000 s/mm^2 was used to assist segmentation. The 3D ROI file was then imported into AK (Analysis Kit, Kinetics Version 2.1, GE Health-care) software to extract texture features. Finally, a total of 828 texture features of the whole tumor were automatically extracted from each of the

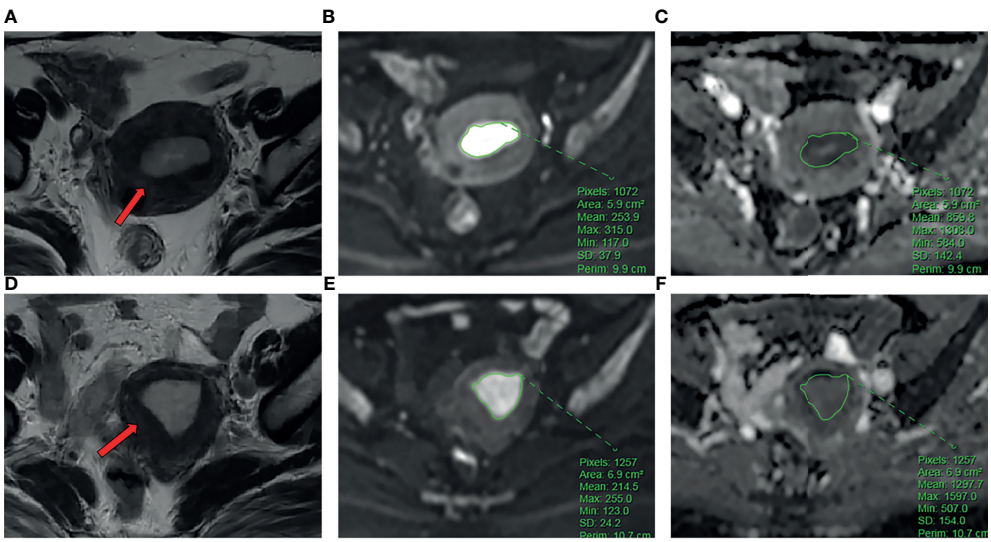

FIGURE 2 | **(A-C)** The patient is a 54-year-old female with EC. Ki-67 expression was 70%, and p53 expression was positive. **(A)** Axial T_2WI showed an irregular mass in the uterine cavity (arrow). **(B)** ROI of the largest lesion area on DWI. **(C)** The ADC values on ADC map. **(D–F)** The patient is a 58-year-old female with EC. Ki-67 expression was 60%, and p53 expression is negative. **(D)** Axial T_2WI showed an irregular mass in the uterine cavity (arrow). **(E)** ROI of the largest lesion area on DWI. **(F)** The ADC values on ADC map.

three MR scanning sequences. As an example, the texture feature extraction process on T_2WI is shown in **Figure 3**. After one week, 30 patients were randomly selected, and the images of 30 patients were re-segmented by reader 1 and reader 2. The intraclass correlation coefficients (ICCs) were used to evaluate the stability of texture features between inter- and intrareader segmentations. The texture features with ICC > 0.75 were preserved.

Pathological Examination

Postoperative Ki-67 and p53 testing were performed by two professional pathologists with more than 8 years of pathological diagnosis experience. The diagnostic criteria of immunohistochemical staining for p53 included non-staining (0), faint staining (1+), moderate staining (2+) and strong staining (3+). 0 was viewed as negative expression, while 1+ ~ 3+ was viewed as positive expression. The expression of Ki-67 was localized in the nucleus of tumor cells, and five fields were randomly selected under the high-power microscope. The tumor cells were determined to be positive if there were brown particles in the cytoplasm of the tumor cells, and the staining intensity was higher than the background nonspecific staining. According to Li et al. (16), Ki-67 < 50% is the low expression group, and Ki-67 ≥ 50% is the high expression group.

Statistical Analysis

The data were analyzed by SPSS 26.0 (IBM Corporation, Armonk NY, USA), IPMS (Version 2.4.0, GE Health-care) software, and MedCalc Statistical Software version 15.2.2 (MedCalc Software bvba, Ostend, Belgium). Data that had a normal distribution are expressed as the mean ± standard deviation, while abnormally distributed data are expressed as the median. Independent sample *t*-tests or Mann-Whitney *U*-tests were used to compare the ADC values and the texture features of each group. $P < 0.05$ was considered statistically significant. Univariate and multivariate logistic regression analyses and cross-validation were performed on the texture features with statistical significance between each subgroup to select the optimal texture features. The ADC model, TA model, and combined model were built in the training cohorts and validation cohorts to predict the expression levels of Ki-67 and p53. The ROC curves were plotted to assess the performance of the five models in both cohorts. The AUCs were compared using DeLong's test of equality. $P < 0.05$ was considered as an independent predictor. A calibration curve was plotted to evaluate the agreement between the prediction result and gold standard.

RESULTS

Clinical and Pathological Findings

Among the 110 EC patients, there were 50 cases of low Ki-67 expression and 60 cases of high Ki-67 expression as well as 38 cases of negative p53 expression and 72 cases of positive p53 expression. The age, FIGO stage, and histological type are presented in **Table 1**. Regarding Ki-67 expression, there was no significant difference between the two groups in age (P=0.319), but FIGO stage (P=0.020) and histological type (P<0.001) were significant differences. Regarding p53 expression, age (P=0.634) and FIGO stage (P=0.063) were not significantly different between the two groups, but histological type (P=0.030) was statistically significant.

ICC Analysis of ADC Values

ICC analysis of measurements of ADC values by the two attending physicians showed good agreement between the surveyors [ICC = 0.883, 95% CI (0.825-0.921), P<0.001]. Therefore, this study used only the results of the first radiologist for a full-text analysis. The ADC values of subgroups were compared by independent sample *t*-test, and the results are shown in **Table 2**. The ADC values in EC with high Ki-67 expression were lower than that of the low Ki-67 expression (P =0.007 and P<0.001) with AUCs of 0.698 and 0.853 in the training and validation cohorts, respectively. The ADC value in

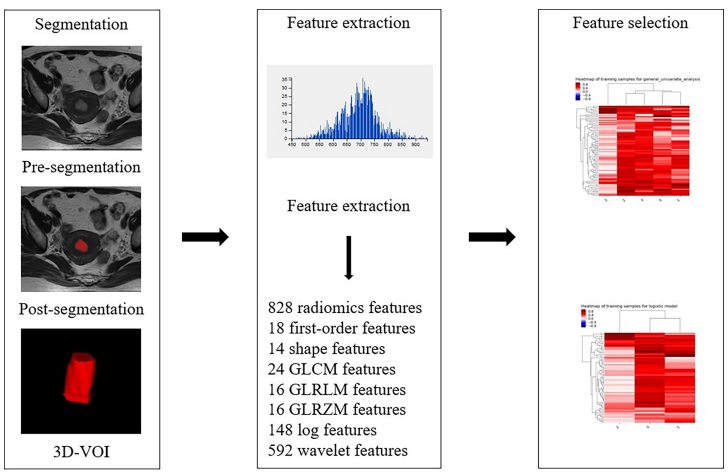

FIGURE 3 | Radiomic workflow.

TABLE 1 | Patients clinical and pathological characteristics.

	Ki-67 (n=110)				p53 (n=110)			
	Patients (n)	Low expression (<50%)	High expression (≥ 50%)	*P*-value	Patients (n)	Negative expression (0)	Positive expression (1+ ~ 3+)	*P*-value
Total	110	50 (45.5%)	60 (54.5%)		110	38 (34.5%)	72 (65.5%)	
Age		53.6 ± 8.3[a]	55.3 ± 9.1	0.319[b]		54.0 ± 8.6	54.8 ± 8.9	0.634
FIGO[c] stage								
I-II	97	48 (96.0%)	49 (81.7%)	0.020[d]	97	37 (97.4%)	60 (83.3%)	0.063
III-IV	13	2 (4.0%)	11 (18.3%)		13	1 (2.6%)	12 (16.7%)	
Histologic type								
[e]EMC	89	48 (96.0%)	41 (68.3%)	<0.001	89	35 (92.1%)	54 (75.0%)	0.030
[f]NEMC	21	2 (4.0%)	19 (31.7%)		21	3 (7.9%)	18 (25.0%)	

[a]*Data are mean ± standard deviation.*
[b]*T-statistical test.*
[c]*FIGO, International Federation of Gynecology and Obstetrics.*
[d]*Chi-square test.*
[e]*EMC, Endometrioid carcinoma.*
[f]*NEMC, Non-endometrioid carcinoma.*

EC with positive p53 expression was significantly lower than that in EC with negative p53 expression, and the difference was statistically significant (*P*=0.039 and *P*=0.048). The AUC of the ADC values in differentiating the level of p53 expression were 0.626 and 0.702 in the training and validation cohorts, respectively.

Texture Feature Difference and TA Prediction Model of the Expression Level of Ki-67 and p53 in EC

A total of 828 texture features were obtained from AK software based on T_2WI, DWI and CE-T_1WI. Sufficient dimension reduction was obtained with the use of univariate and multivariate logistic regression analysis and cross-validation in the training cohort. Three texture features based on T_2WI, DWI, and CE-T_1WI were extracted from Ki-67 expression, and the detailed information for these texture features is listed in **Table 3**. Four texture features based on T_2WI, DWI, and CE-T_1WI were extracted from p53 expression, and the detailed information for these texture features is listed in **Table 4**. The AUC, sensitivity, and specificity of the models that MR imaging-based TA used to predict the expression level of Ki-67 and p53 in the training and validation cohorts are shown in **Table 5**.

Efficacy of Five Models in Predicting the Expression Levels of Ki-67 and p53 in EC

ROC curves were used to evaluate the diagnostic efficacy of prediction models based on ADC values, T_2WI, DWI, CE-T_1WI, and ADC values combined with T_2WI + DWI + CE-T_1WI in predicting the expression levels of Ki-67 and p53 in EC. The AUC of ADC values in predicting Ki-67 and p53 expression levels in the training and validation cohorts were 0.698, 0.853 and 0.626, 0.702, respectively. The AUC of the TA model based on T_2WI, DWI, CE-T_1WI, and ADC value combined with T_2WI + DWI + CE-T_1WI in the training and validation cohorts for predicting the expression of Ki-67 were 0.741, 0.765, 0.733, 0.922 and 0.688, 0.691, 0.651, 0.938, respectively, and for predicting the expression of p53 were 0.763, 0.805, 0.781, 0.901 and 0.796, 0.713, 0.657, 0.922, respectively, with great performance. DeLong's test was used to analyze the improvement resulting from the combined model compared to the other single models in the training and validation cohorts (**Table 6**). The diagnostic efficiency of the combined model was superior to that of the single prediction models based on ADC values, T_2WI, DWI and CE-T_1WI in the training and validation cohorts. In general, there was no statistical significance among each single model, but the ADC values model was superior to DWI and CE-T_1WI in the training group for p53. The ROC curves for the training cohorts are shown in **Figure 4**. The calibration curves for each training group are shown in **Figure 5**, and the statistics of the Hosmer–Lemeshow test in each group were not significant (P > 0.05), indicating good calibration.4.

DISCUSSION

In recent years, research on tumor biomarkers has increased, aiming to improve the survival rate and quality of life of cancer patients.

TABLE 2 | The ADC value in relation to Ki-67 and p53 and its predictive performance.

	Training cohort				Validation cohort			
	n	ADC value×10^{-3}mm^2/s	*P*-value	AUC	*n*	ADC value×10^{-3}mm^2/s	*P*-value	AUC
low Ki-67 expression	34	0.933 ± 0.125	0.007	0.698	16	0.974 ± 0.131	<0.001	0.853
high Ki-67 expression	43	0.844 ± 0.150			17	0.772 ± 0.160		
negative p53 expression	28	0.929 ± 0.153	0.039	0.626	10	0.962 ± 0.183	0.048	0.702
positive p53 expression	49	0.858 ± 0.137			23	0.830 ± 0.163		

TABLE 3 | Statistical results of texture features of Ki-67 high and low expression groups in EC.

Texture features	low Ki-67 expression	high Ki-67 expression	Multivariate logistic regression analysis		AUC
			OR	*P*	
T_2WI- texture features					
T_2WI-wavelet-HLL_firstorder_Skewness	-0.805 ± 0.622	-0.399 ± 0.440	48.597	0.011	0.701
T_2WI-wavelet-LLL_firstorder_Minimum	1125.378 ± 359.711	1277.809 ± 309.657	24.502	0.024	0.648
T_2WI-wavelet-HHL_glszm_SZN	2.867(1.782,3.522)	2.833(1.800,5.870)	14.557	0.047	0.530
DWI- texture features					
DWI-glcm_Correlation	0.212 ± 0.225	0.312 ± 0.202	14.134	0.020	0.646
DWI-wavelet-HHL_glszm_HGLZE	1.757 ± 0.333	1.969 ± 0.362	40.908	0.008	0.662
DWI-wavelet-LHL_firstorder_IR	3.006 ± 1.488	3.690 ± 1.633	49.623	0.017	0.669
CE-T_1WI- texture features					
CE-T_1WI-wavelet-HLL_glszm_SAE	0.315 ± 0.091	0.339 ± 0.088	20.763	0.042	0.625
CE-T_1WI-wavelet-HLH_firstorder_Kurtosis	4.503 ± 1.212	3.924 ± 0.684	0.037	0.018	0.647
CE-T_1WI-wavelet-LLH_glcm_Correlation	0.251 ± 0.177	0.344 ± 0.169	24.602	0.018	0.644

OR, odds ratio; SZN, SizeZoneNonUniformity; HGLZE, HighGrayLevelZoneEmphasis; IR, InterquartileRange; SAE, SmallAreaEmphasis.

At the same time, as early detection of EC is critical for treatment, it is important to identify reliable histopathology markers to improve diagnostic accuracy and prognosis. Previous studies have found that Ki-67 and p53 may contribute to the accuracy of cytodiagnosis of different EC lesions (17). However, Ki-67 and p53 are commonly detected using immunohistochemistry, which was not only invasive, but may also be influenced by subjective factors. In the present study, a novel MRI analysis method was proposed to detect the expression levels of Ki-67 and p53 in immunohistochemistry. Not only is MRI noninvasive, but it adds texture features without increasing the patient's risk of side effects. Quantitative analysis of the texture of the image may also have an advantage over more targeted biopsies.

The ADC values reflect the diffusion of water molecules in the gap between tumor tissues (18), and they have been shown to be negatively correlated with the proliferation degree and cell density of tumors. The present study suggested that the ADC value in the high Ki-67 expression group was significantly lower than that in the low Ki-67 expression group in EC, which was similar to previous studies in EC (19). With the increase in the expression level of Ki-67, the proliferation activity of EC cells increases, tumors grow vigorously, cell density increases, the arrangement is closer, and the extracellular space decreases, resulting in lower ADC values.

p53 is located on chromosome 17p13-p3 and can be divided into two types, namely, wild type and mutant type, and the pathologically detectable form is mutant p53. When the expression of mutant p53 increases, it may give rise to higher cell proliferative activity, poorer differentiation, and more malignant degree in EC. The present study suggested that the ADC value in the positive p53 group was significantly lower than that in the negative p53 group in EC. Our results were expected and consistent with most previously reported data (10, 20). Although our study showed that the ADC value differed between different subgroups of Ki-67 and p53, the AUC of ADC value for Ki-67 and p53 were 0.698 and 0.626, respectively, which indicated poor performance. This may be because ADC values may not only be related to the movement of

TABLE 4 | Statistical results of texture features of p53 negative and positive expression groups in EC.

Texture features	Negative p53 expression	Positive p53 expression	Multivariate logistic regression analysis		AUC
			OR	*P*	
T_2WI- texture features					
T_2WI -wavelet-LLH_glszm_GLNN	0.021 ± 0.008	0.026 ± 0.009	57.716	0.002	0.696
T_2WI-wavelet-HHH_firstorder_Skewness	0.058 ± 0.257	-0.054 ± 0.251	0.015	0.004	0.601
T_2WI -wavelet-HHL_glszm_GLN	8.149 ± 3.764	7.402 ± 3.465	0.032	0.009	0.562
T_2WI-wavelet-HHL_glcm_ClusterShade	-0.004 ± 0.013	0.004 ± 0.022	56.545	0.023	0.645
DWI- texture features					
DWI -wavelet-HLH_glszm_GLNN	0.605 ± 0.070	0.558 ± 0.054	0.008	<0.001	0.703
DWI -wavelet-LHH_glszm_GLNN	0.520 (0.501,0.571)	0.556(0.520,0.625)	20.397	0.004	0.611
DWI -wavelet-LHL_glrlm_LRLGLE	14.721 ± 5.226	19.409 ± 10.092	63.688	0.006	0.645
DWI -wavelet-LHL_glszm_SZN	2.088 (1.617,3.159)	1.588(1.000,2.582)	0.035	0.014	0.637
CE-T_1WI- texture features					
CE-T_1WI-firstorder_Maximum	138.960 ± 30.666	116.564 ± 33.654	0.015	0.006	0.700
CE-T_1WI-firstorder_Kurtosis	3.265 ± 0.836	3.000 ± 0.679	0.012	0.003	0.612
CE-T_1WI-glszm_SAE	0.219 ± 0.085	0.241 ± 0.067	38.569	0.009	0.620
CE-T_1WI-glcm_InverseVariance	0.435 ± 0.068	0.396 ± 0.053	0.048	0.022	0.690

OR, odds ratio; GLNN, GrayLevelNon-UniformityNormalized; GLN, GrayLevelNon-Uniformity; LRLGLE, LongRunLowGrayLevelEmphasis; SZN, SizeZoneNonUniformity; SAE, SmallAreaEmphasis.

TABLE 5 | The predictive performance of the models in training and validation cohort.

	Model	Training cohort			Validation cohort		
		AUC[a] (95%CI[b])	SEN[c] (%)	SPE[d] (%)	AUC[a] (95%CI[b])	SEN[c] (%)	SPE[d] (%)
Ki-67	T_2WI model	0.741 (0.629-0.835)	53.5	85.3	0.688 (0.503-0.837)	94.1	37.5
	DWI model	0.765 (0.655-0.854)	90.7	55.9	0.691 (0.507-0.840)	52.9	87.5
	CE-T_1WI model	0.733 (0.619-0.827)	72.1	64.7	0.651 (0.466-0.808)	94.1	43.8
	Combined[e] model	0.922 (0.838-0.971)	90.7	82.4	0.938 (0.795-0.992)	76.5	100.0
p53	T_2WI model	0.763 (0.653-0.853)	57.1	85.7	0.796 (0.620-0.915)	65.2	100.0
	DWI model	0.805 (0.699-0.887)	71.4	85.7	0.713 (0.530-0.856)	87.0	60.0
	CE-T_1WI model	0.781 (0.673-0.868)	57.1	92.9	0.657 (0.471-0.812)	73.9	70.0
	Combined[e] model	0.901 (0.811-0.957)	83.7	85.7	0.922 (0.773-0.986)	100.0	80.0

[a]*AUC, area under the curve;*
[b]*CI, confidence interval;*
[c]*SEN: sensitivity;*
[d]*SPE, specificity;*
[e]*Combined, ADC value combined with T_2WI + DWI + CE-T_1WI.*

TABLE 6 | AUC of the five models was compared.

	Ki-67 (*P*-value)		p53 (*P*-value)	
	Training	Validation	Training	Validation
Combined *vs*. ADC	<0.001	0.069	<0.001	0.031
Combined *vs*. T_2WI	<0.001	0.009	0.010	0.114
Combined *vs*. DWI	0.003	0.007	0.013	0.040
Combined *vs*. CE-T_1WI	<0.001	0.006	0.007	0.054
ADC *vs*. T_2WI	0.609	0.140	0.077	0.450
ADC *vs*. DWI	0.399	0.063	0.033	0.944
ADC *vs*. CE-T_1WI	0.681	0.113	0.033	0.746
T_2WI *vs*. DWI	0.771	0.975	0.585	0.545
T_2WI *vs*. CE-T_1WI	0.900	0.802	0.799	0.383
DWI *vs*. CE-T_1WI	0.702	0.783	0.714	0.701

water molecules, but also affected by the microcirculation of the blood and tumor heterogeneity; therefore, they cannot truly reflect the movement of water molecules in tissues.

TA is a method that quantifies pixel intensity variations (heterogeneity). TA quantifies tumor heterogeneity by calculating the grey changes of pixels in the image (21). Some studies (22, 23) have found that magnetic resonance imaging–based texture features show the association among deep myometrial invasion, lymphovascular space invasion, and histological high-grade EC. However, only first-order statistical features were extracted and analyzed in these previous studies. In the present study, comprehensive texture features, including

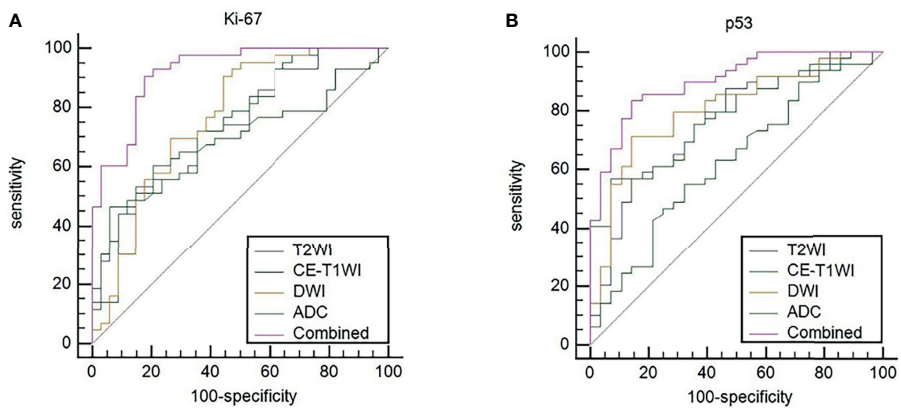

FIGURE 4 | **(A)** ROC curves to predict Ki-67 expression levels in EC. **(B)** ROC curves to predict p53 expression levels in EC. Equality of AUC was assessed by the DeLong's test.

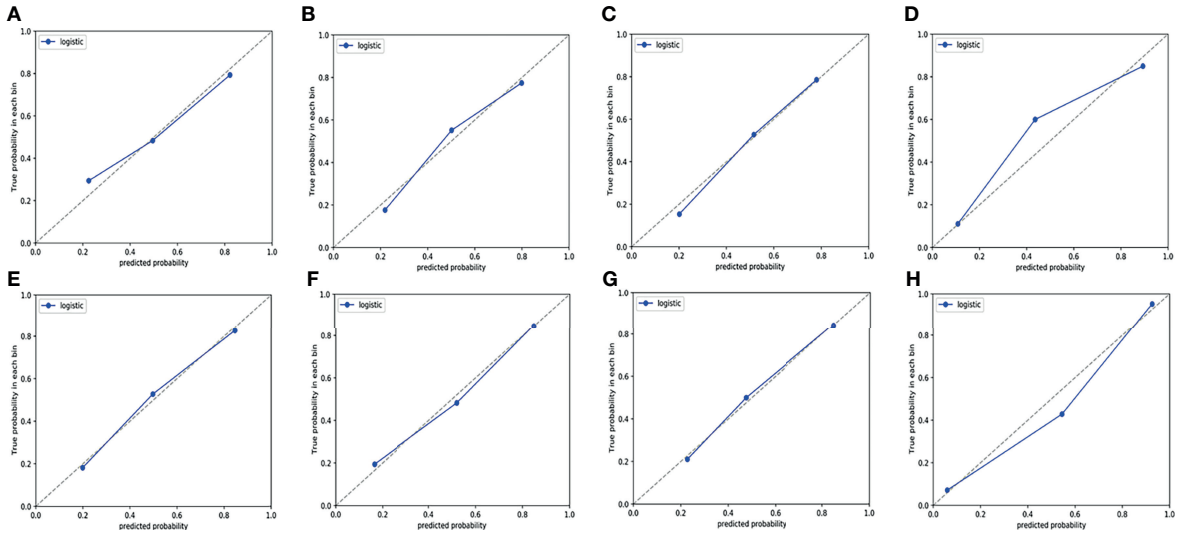

FIGURE 5 | Calibration curves of the prediction model in training cohort. **(A–D)** Calibration curves for a model that predicts the expression level of Ki-67. **(A)** T_2WI. **(B)** DWI. **(C)** CE-T_1WI. **(D)** ADC value combined with T_2WI + DWI + CE-T_1WI. **(E–H)** Calibration curves for a model that predicts the expression level of p53. **(E)** T_2WI. **(F)** DWI. **(G)** CE-T_1WI. **(H)** ADC value combined with T_2WI + DWI + CE-T_1WI. The 45° dotted line represents the ideal prediction, while the blue line represents the prediction performance of the prediction model. The closer the blue line is to the dotted line, the better the performance of the prediction model.

first-order statistics, shape-based, GLCM, GLRLM, and GLSZM were extracted based on T_2WI, DWI, and CE-T_1WI, and they were used to predict the expression levels of Ki-67 and p53 in patients with EC. The texture feature parameters are different in each sequence, and the area under the curve (AUC ≥ 0.7) of the "wavelet-HLL_firstorder_Skewness" of Ki-67 and the "firstorder_Maximum" and "wavelet-HLH_glszm_GLNN" of p53 are more significant. In our study, the Skewness value of the high Ki-67 expression group was higher than that of the low Ki-67 expression group, which indicated that the distribution of the tissue strength grade of the high Ki-67 expression group in EC was more disordered and heterogeneous. Skewness measures the asymmetry of the distribution of values about the mean value. A high skewness value indicates a more asymmetrical the strength grade distribution and greater heterogeneity. The maximum value represents the maximum grey level intensity within the ROI. In the present study, the maximum value of the p53-negative group was higher than that of the p53-positive group, indicating more tumor hemorrhage, secretion, and solid components in the p53-positive group of EC. GLNN measures the variability of grey-level intensity values in the image with a lower value indicating a greater similarity in intensity values. In the present study, the GLNN value of the p53-negative group was lower than that of the p53-positive group, which indicated that the ECs of the p53-positive group were more inhomogeneous and complex than those of the p53-negative group.

Different from previous studies, several studies (24, 25) on TA used one or two MRI sequences. We included T_2WI, DWI, and CE-T_1WI sequences of EC and established a series of models in which the ADC value and TA predicted the expression levels of Ki-67 and p53. When the ROC curve was used to evaluate the performance of the predictive model, the AUC of the TA model based on T_2WI, DWI, and CE-T_1WI in the training cohort for predicting the expression of Ki-67 were 0.741, 0.765, and 0.733, respectively, and for predicting the expression of p53 were 0.763, 0.805, and 0.781, respectively. The AUC performed well. The results showed that the TA of T_2WI, DWI, and CE-T_1WI was helpful to evaluate the expression levels of Ki-67 and p53 in EC. In three sequences of MRI, the AUC of the TA model based on DWI image texture features was higher, which was different from the results reported by Dong et al. (26) who distinguished solitary fibrous tumor/hemangiopericytoma and angiomatous meningioma base on texture feature. One explanation may be that DWI provides a better representation of the microscopic geometry of the EC tissue and the diffusion of water molecules inside and outside the cell and that the images contain more differential texture features with discriminating value. However, there was no significant difference in the TA diagnostic efficiency among the three sequences (T_2WI, DWI, and CE-T_1WI). It is noteworthy that the diagnostic efficiency of the combined models was better than that of the single model ($P < 0.05$). The combined model performed well in identifying the expression level of Ki-67 and p53 in EC with AUCs of 0.922 and 0.938 for Ki-67 expression and 0.901 and 0.922 for p53 expression in the training and validation cohorts, respectively. Thus, the present findings suggested that the constructed model of multiparameter MRI TA can capture higher-order interactions between data, reflect tumor heterogeneity from different aspects, and achieve better predictive efficiency. In addition, when using DeLong's test to evaluate improvements to the combined model, the diagnostic efficiency of the combined models was better than that of the single ADC model, T_2WI model, DWI model and CE-T_1WI model ($P < 0.05$). The ADC value improved the diagnostic efficiency of the model, which

was consistent with the results of previous studies (27) combining the ADC value with radiomics in EC.

However, there were several limitations in the present study. First, the sample size of this study was small, and it was a retrospective study, indicating potential bias in the selection of enrolled cases. Second, the ADC values were measured based on the maximum level of solid tumor components, which did not represent the overall tumor condition. Third, our model did not include EC FIGO stage, grading, or other clinical indicators. Therefore, future studies will be performed to further increase the sample size.

CONCLUSIONS

In conclusion, a combination of ADC values and TA based on three MRI sequences were developed to provide a noninvasive method for preoperatively predicting the expression levels of Ki-67 and p53 in EC. To some extent, this noninvasive imaging marker can compensate for the limitation of endometrium curettage biopsy and adverse impact of tumor heterogeneity, and it provide an objective imaging basis for clinical and accurate individualized treatment.

DATA AVAILABILITY STATEMENT

The original contributions presented in the study are included in the article/supplementary material. Further inquiries can be directed to the corresponding author.

ETHICS STATEMENT

The studies involving human participants were reviewed and approved by the Medical Ethics Committee of Anhui Provincial Cancer Hospital(2021-54). The patients/participants provided their written informed consent to participate in this study. Written informed consent was obtained from the individual(s) for the publication of any potentially identifiable images or data included in this article.

AUTHOR CONTRIBUTIONS

JD, XJ, HJ, CW, and CBW contributed to conception and design. XJ, HJ, and ZZ contributed to the collection and arrangement of data. XJ, HJ, CW, CBW, and JD contributed to data analysis and manuscript writing. All authors contributed to the article and approved the submitted version.

FUNDING

This work was supported by 2020 SKY Image Research Fund (No. Z-2014-07-2003-11) and National key research and development program (No. 2016YFB1000905).

ACKNOWLEDGMENTS

We are grateful to the technical assistance provided by United Imaging Healthcare.

REFERENCES

1. Sung H, Ferlay J, Siegel RL, Laversanne M, Soerjomataram I, Jemal A, et al. Global Cancer Statistics 2020: GLOBOCAN Estimates of Incidence and Mortality Worldwide for 36 Cancers in 185 Countries. *CA Cancer J Clin* (2021) 71(3):209–49. doi: 10.3322/caac.21660
2. Henley SJ, Ward EM, Scott S, Ma J, Anderson RN, Firth AU, et al. Annual Report to the Nation on the Status of Cancer, Part I: National Cancer Statistics. *Cancer* (2020) 126(10):2225–49. doi: 10.1002/cncr.32802
3. Jia M, Jiang P, Huang Z, Hu J, Deng Y, Hu Z. The Combined Ratio of Estrogen, Progesterone, Ki-67, and P53 to Predict the Recurrence of Endometrial Cancer. *J Surg Oncol* (2020) 122(8):1808–14. doi: 10.1002/jso.26212
4. Liu Y, Du FY, Chen W, Fu PF, Yao MY, Zheng SS. G15 Sensitizes Epithelial Breast Cancer Cells to Doxorubicin by Preventing Epithelial-Mesenchymal Transition Through Inhibition of GPR30. *Am J Transl Res* (2015) 7(5):967–75.
5. Koi C, Hachisuga T, Murakami M, Kurita T, Nguyen TT, Shimajiri S, et al. Overexpression of P53 in the Endometrial Gland in Postmenopausal Women. *Menopause* (2015) 22(1):104–7. doi: 10.1097/GME.0000000000000265
6. Li LT, Jiang G, Chen Q, Zheng JN. Ki67 is a Promising Molecular Target in the Diagnosis of Cancer (Review). *Mol Med Rep* (2015) 11(3):1566–72. doi: 10.3892/mmr.2014.2914
7. Xu Q, Chen C, Liu B, Lin Y, Zheng P, Zhou D, et al. Association of Irhom1 and Irhom2 Expression With Prognosis in Patients With Cervical Cancer and Possible Signaling Pathways. *Oncol Rep* (2020) 43(1):41–54. doi: 10.3892/or.2019.7389
8. Awais R, Spiller DG, White MR, Paraoan L. P63 is Required Beside P53 for PERP-Mediated Apoptosis in Uveal Melanoma. *Br J Cancer* (2016) 115 (8):983–92. doi: 10.1038/bjc.2016.269
9. Zhang Q, Yu X, Lin M, Xie L, Zhang M, Ouyang H, et al. Multi-B-Value Diffusion Weighted Imaging for Preoperative Evaluation of Risk Stratification in Early-Stage Endometrial Cancer. *Eur J Radiol* (2019) 119:108637. doi: 10.1016/j.ejrad.2019.08.006
10. Wang Y, Bai G, Zhang X, Shan W, Xu L, Chen W. Correlation Analysis of Apparent Diffusion Coefficient Value and P53 and Ki-67 Expression in Esophageal Squamous Cell Carcinoma. *Magn Reson Imaging* (2020) 68:183–9. doi: 10.1016/j.mri.2020.01.011
11. Varghese BA, Cen SY, Hwang DH, Duddalwar VA. Texture Analysis of Imaging: What Radiologists Need to Know. *AJR Am J Roentgenol* (2019) 212 (3):520–8. doi: 10.2214/AJR.18.20624
12. Lubner MG, Smith AD, Sandrasegaran K, Sahani DV, Pickhardt PJ. CT Texture Analysis: Definitions, Applications, Biologic Correlates, and Challenges. *Radiographics* (2017) 37(5):1483–503. doi: 10.1148/rg.2017170056
13. Ye R, Weng S, Li Y, Yan C, Chen J, Zhu Y, et al. Texture Analysis of Three-Dimensional MRI Images May Differentiate Borderline and Malignant Epithelial Ovarian Tumors. *Korean J Radiol* (2021) 22(1):106–17. doi: 10.3348/kjr.2020.0121
14. De Cecco CN, Ganeshan B, Ciolina M, Rengo M, Meinel FG, Musio D, et al. Texture Analysis as Imaging Biomarker of Tumoral Response to Neoadjuvant Chemoradiotherapy in Rectal Cancer Patients Studied With 3-T Magnetic Resonance. *Invest Radiol* (2015) 50(4):239–45. doi: 10.1097/RLI.0000000000000116
15. Choi MH, Lee YJ, Yoon SB, Choi JI, Jung SE, Rha SE, et al. MRI of Pancreatic Ductal Adenocarcinoma: Texture Analysis of T2-Weighted Images for Predicting Long-Term Outcome. *Abdom Radiol (NY)* (2019) 44(1):122–30. doi: 10.1007/s00261-018-1681-2
16. Li C, Zheng M, Zheng X, Fang X, Dong J, Wang C, et al. Predictive Ki-67 Proliferation Index of Cervical Squamous Cell Carcinoma Based on IVIM-

DWI Combined With Texture Features. *Contrast Media Mol Imaging* (2021) 2021:8873065. doi: 10.1155/2021/8873065
17. Apostolou G, Apostolou N, Nikolaidou C, Kavantzas N, Patsouris E, Athanassiadou P. Cytodiagnosis of Endometrial Carcinoma and Hyperplasia on Imprint Smears With Additional Immunocytochemistry Using Ki-67 and P53 Biomarkers. *Cytopathology* (2014) 25(2):86–94. doi: 10.1111/cyt.12095
18. Taouli B, Koh DM. Diffusion-Weighted MR Imaging of the Liver. *Radiology* (2010) 254(1):47–66. doi: 10.1148/radiol.09090021
19. Jiang JX, Zhao JL, Zhang Q, Qing JF, Zhang SQ, Zhang YM, et al. Endometrial Carcinoma: Diffusion-Weighted Imaging Diagnostic Accuracy and Correlation With Ki-67 Expression. *Clin Radiol* (2018) 73(4):413.e1–6. doi: 10.1016/j.crad.2017.11.011
20. Wang F, Wang Y, Zhou Y, Liu C, Liang D, Xie L, et al. Apparent Diffusion Coefficient Histogram Analysis for Assessing Tumor Staging and Detection of Lymph Node Metastasis in Epithelial Ovarian Cancer: Correlation With P53 and Ki-67 Expression. *Mol Imaging Biol* (2019) 21(4):731–9. doi: 10.1007/s11307-018-1295-7
21. Ganeshan B, Miles KA. Quantifying Tumour Heterogeneity With CT. *Cancer Imaging* (2013) 13(1):140–9. doi: 10.1102/1470-7330.2013.0015
22. Ueno Y, Forghani B, Forghani R, Dohan A, Zeng XZ, Chamming's F, et al. Endometrial Carcinoma: MR Imaging-Based Texture Model for Preoperative Risk Stratification-A Preliminary Analysis. *Radiology* (2017) 284(3):748–57. doi: 10.1148/radiol.2017161950
23. Bereby-Kahane M, Dautry R, Matzner-Lober E, Cornelis F, Sebbag-Sfez D, Place V, et al. Prediction of Tumor Grade and Lymphovascular Space Invasion in Endometrial Adenocarcinoma With MR Imaging-Based Radiomic Analysis. *Diagn Interv Imaging* (2020) 101(6):401–11. doi: 10.1016/j.diii.2020.01.003
24. Dang M, Lysack JT, Wu T, Matthews TW, Chandarana SP, Brockton NT, et al. MRI Texture Analysis Predicts P53 Status in Head and Neck Squamous Cell Carcinoma. *AJNR Am J Neuroradiol* (2015) 36(1):166–70. doi: 10.3174/ajnr.A4110
25. Sun X, Pang P, Lou L, Feng Q, Ding Z, Zhou J. Radiomic Prediction Models for the Level of Ki-67 and P53 in Glioma. *J Int Med Res* (2020) 48 (5):300060520914466. doi: 10.1177/0300060520914466
26. Dong J, Yu M, Miao Y, Shen H, Sui Y, Liu Y, et al. Differential Diagnosis of Solitary Fibrous Tumor/Hemangiopericytoma and Angiomatous Meningioma Using Three-Dimensional Magnetic Resonance Imaging Texture Feature Model. *BioMed Res Int* (2020) 2020:5042356. doi: 10.1155/2020/5042356
27. Zhang K, Zhang Y, Fang X, Fang M, Shi B, Dong J, et al. Nomograms of Combining Apparent Diffusion Coefficient Value and Radiomics for Preoperative Risk Evaluation in Endometrial Carcinoma. *Front Oncol* (2021) 11:705456. doi: 10.3389/fonc.2021.705456

Conflict of Interest: The authors declare that the research was conducted in the absence of any commercial or financial relationships that could be construed as a potential conflict of interest.

frontiers | Frontiers in Oncology

TYPE Original Research
PUBLISHED 05 October 2022
DOI 10.3389/fonc.2022.992906

OPEN ACCESS

EDITED BY
Chuanming Li,
Chongqing University Central Hospital, China

REVIEWED BY
Zixing Huang,
Sichuan University, China
Yubing Dai,
University of Houston, United States

*CORRESPONDENCE
Zhuoyue Tang
zhuoyue_tang@cqmu.edu.cn

SPECIALTY SECTION
This article was submitted to Cancer Imaging and Image-directed Interventions, a section of the journal Frontiers in Oncology

RECEIVED 13 July 2022
ACCEPTED 20 September 2022
PUBLISHED 05 October 2022

CITATION
Li Q, Song Z, Zhang D, Li X, Liu Q, Yu J, Li Z, Zhang J, Ren X, Wen Y and Tang Z (2022) Feasibility of a CT-based lymph node radiomics nomogram in detecting lymph node metastasis in PDAC patients. *Front. Oncol.* 12:992906. doi: 10.3389/fonc.2022.992906

Feasibility of a CT-based lymph node radiomics nomogram in detecting lymph node metastasis in PDAC patients

Qian Li[1,2,3,4], Zuhua Song[4], Dan Zhang[4], Xiaojiao Li[4], Qian Liu[4], Jiayi Yu[4], Zongwen Li[4], Jiayan Zhang[4], Xiaofang Ren[4], Youjia Wen[4] and Zhuoyue Tang[1,2,3,4]*

[1]Department of Radiology, Chongqing Medical University, Chongqing, China, [2]Chongqing Institute of Green and Intelligent Technology, Chinese Academy of Sciences, Chongqing, China, [3]Chongqing School, University of Chinese Academy of Sciences, Chongqing, China, [4]Department of Radiology, Chongqing General Hospital, Chongqing, China

Objectives: To investigate the potential value of a contrast enhanced computed tomography (CECT)-based radiological-radiomics nomogram combining a lymph node (LN) radiomics signature and LNs' radiological features for preoperative detection of LN metastasis in patients with pancreatic ductal adenocarcinoma (PDAC).

Materials and methods: In this retrospective study, 196 LNs in 61 PDAC patients were enrolled and divided into the training (137 LNs) and validation (59 LNs) cohorts. Radiomic features were extracted from portal venous phase images of LNs. The least absolute shrinkage and selection operator (LASSO) regression algorithm with 10-fold cross-validation was used to select optimal features to determine the radiomics score (Rad-score). The radiological-radiomics nomogram was developed by using significant predictors of LN metastasis by multivariate logistic regression (LR) analysis in the training cohort and validated in the validation cohort independently. Its diagnostic performance was assessed by receiver operating characteristic curve (ROC), decision curve (DCA) and calibration curve analyses.

Results: The radiological model, including LN size, and margin and enhancement pattern (three significant predictors), exhibited areas under the curves (AUCs) of 0.831 and 0.756 in the training and validation cohorts, respectively. Nine radiomic features were used to construct a radiomics model, which showed AUCs of 0.879 and 0.804 in the training and validation cohorts, respectively. The radiological-radiomics nomogram, which incorporated the LN Rad-score and the three LNs' radiological features, performed better than the Rad-score and radiological models individually, with AUCs of 0.937 and 0.851 in the training and validation cohorts, respectively. Calibration curve analysis and DCA revealed that the radiological-radiomics nomogram showed satisfactory consistency and the highest net benefit for preoperative diagnosis of LN metastasis.

Conclusions: The CT-based LN radiological-radiomics nomogram may serve as a valid and convenient computer-aided tool for personalized risk assessment of LN metastasis and help clinicians make appropriate clinical decisions for PADC patients.

KEYWORDS

pancreatic ductal adenocarcinoma, lymph node metastasis, radiomics, nomogram, computed tomography

Introduction

Pancreatic ductal adenocarcinoma (PDAC), an aggressive malignancy, is expected to become the second leading cause of cancer deaths worldwide by 2030, of which 5-year overall survival rate is still as low as 9% (1). Despite advances in therapeutic methods, radical resection with appropriate lymphadenectomy remains the only curative method. Lymph node (LN) metastasis, one of the strongest postoperative prognostic indicators, is closely associated with poor prognosis (2–5). In clinical practice, the extent of lymph node dissection in pancreatic cancer remains controversial, including extended and standard lymphadenectomies. Preoperative diagnosis of LN metastasis plays a crucial role in selecting a reasonable LN dissection method, which could not only avoid the omission of metastatic LNs but also decrease postoperative complications and prevent overtreatment. In addition, the National Comprehensive Cancer Network guidelines recommend preoperative neoadjuvant treatment in PDAC patients with LN metastasis, which is associated with a survival benefit (6–8). Therefore, accurate preoperative diagnosis of LN metastasis plays an important role in providing individualized treatment plans for PDAC patients.

Computed tomography (CT) is the primary examination method for PDAC tumor staging in some clinical practice guidelines (9, 10). Many studies (11, 12) proposed the short-axis diameter of LN above 10 mm as a criterion to diagnose metastatic LNs; however, its diagnostic accuracy is easily influenced by enlarged LNs secondary to inflammatory hyperplasia. Other CT image features (11, 13, 14), including LN shape, border contour and heterogeneity, are utilized to improve diagnostic performance for LN metastasis in PDAC. It is worth noting that detecting these features relies on subjective judgment and may be challenging for first-line radiologists with no substantial diagnosis experience. Both qualitative and semiquantitative analyses by visual evaluation on conventional radiological features cannot accurately detect metastatic LNs, so more studies are needed for exploring preoperative diagnostic tools to detect LN metastasis in PDAC patients.

In recent years, computer-aided imaging analysis could be applied in clinic because of the sustained and fast growth of computer science. Radiomics is an emerging discipline that can rapidly extract innumerable features from medical images such as CT, magnetic resonance and ultrasound images in an automated, high-throughput manner. These features could reflect tumor heterogeneity quantitatively and the underlying pathophysiology, which are imperceptible to naked eyes (15–17). This method has been used to evaluate the LN status preoperatively in head and neck, colon, papillary thyroid, cervical and prostate cancers, with ideal predictive accuracy (18–22). In PDAC, current studies are mainly based on original tumor radiomics to predict LN metastasis (23–25), and studies based on LN radiomics to discriminate metastatic from non-metastatic LNs are scarce. In this study, we hypothesized that LN radiomic features may contribute to evaluating the LN status preoperatively and attempted to develop a contrast-enhanced CT (CECT)-based LN radiological-radiomics nomogram for detecting LN metastasis in patients with PDAC.

Materials and methods

Patients and LNs

This retrospective study was approved by the ethics committee of Chongqing general Hospital, and the requirement for written informed consent was waived. From January 2019 to October 2021, PDAC patients administered surgical resection with lymph node dissection in Chongqing General Hospital were retrospectively reviewed.

Inclusion criteria were (1): pathologically confirmed PDAC and LN status; (2) thin-layer CECT examination within 2 weeks before surgery. Exclusion criteria were: (1) a history of systemic treatment before surgery; (2) other coexisting primary

malignancies; (3) missed clinical appointment; (4) image quality unsatisfactory for analysis.

The Japan Pancreas Society's nodal classification of regional lymph node stations of the pancreas was used throughout the study to describe radiological and pathological LN groups (26). The criteria for LN eligibility were: (1) when LNs in one group were all pathologically confirmed to be metastatic or non-metastatic, all the LNs of this group were included; (2) when LNs in one group contained both metastatic and non-metastatic LNs, all the LNs of this group were excluded; (3) LNs with a short-axis diameter below 5 mm were excluded. The flowchart for selecting the study population is shown in Figure 1.

A total of 196 LNs (113 non-metastatic and 83 metastatic) with histological confirmation in 61 patients (31 males and 30 females; mean age, 62.3 ± 9.2 years; age range, 39–80 years) were analyzed. The subjects were divided into the training (January 2020 to October 2021) and validation (January 2019 to December 2019) cohorts at a ratio of 7:3 according to the time of CT. The training cohort included 43 patients with 137 LNs, and validation cohort included 18 patients with 59 LNs.

The CECT protocol

The CT images of 39 participants were acquired on a spectral CT scanner (IQon Spectral CT, Philips Healthcare). Typical imaging parameters were: tube voltage, 120 kV; smart mAs; rotation time, 0.5 s; detector collimation, 64 × 0.625 mm; field of view, 350 × 350 mm; matrix, 512 × 512; layer thickness, 5 mm; reconstruction thickness, 1.25 mm. A nonionic contrast medium (Iohexol, 350 mgI/ml, Schering, Berlin, Germany) was injected with an automatic injector at a dose of 1.5 ml/kg at 3.5 ml/s, followed by 30 ml of saline flashing at the same rate. Arterial phase scans were started with a delay of 10s after passing the predetermined threshold of 150 HU within the abdominal aorta (activated bolus tracking). Portal vein phase scans were started 20 s after the arterial phase.

The CT images of 22 participants were acquired on a 64-slice CT scanner (Aquilion CX, Canon Medical Systems). The same acquisition protocol was used: tube voltage, 120 kV; smart mAs; rotation time, 0.5 s; detector collimation, 64 × 0.5 mm; field of view, 350 × 350 mm; matrix 512 × 512; layer thickness, 5 mm; reconstruction thickness, 1.25 mm. The nonionic contrast medium Iohexol (350 mgI/ml) was injected with an automatic injector at a dose of 1.5 ml/kg at 3.5 ml/s, followed by 30 ml of saline flashing at the same rate. Arterial phase images were obtained 28 s after contrast medium injection, while portal venous phase scans were obtained 22 s after arterial phase image acquisition.

All images were uploaded to the picture archiving and communication system (PACS) for further examination.

Clinical and radiological characteristics

Preoperative demographic characteristics, laboratory findings and CECT conventional features were obtained. The radiological features of LNs, including size, shape, margin, and degree and pattern of enhancement, were analyzed by two radiologists with 7 and 9 years of experience in abdominal imaging, respectively. They were blinded to pathological data and research design. Inter-reader agreement was investigated for evaluating the radiological features by intraclass correlation coefficient (ICC). The sizes of LNs were reflected by their maximal short-axis diameters. LN shapes were categorized as regular (oval) and irregular (round, spiculated or lobulated), and LN margin was blurred or clearly delineated. The enhancement patterns of LNs were categorized as homogenous or heterogeneous in the portal venous phase. The degree of enhancement was estimated with reference to the soft tissue (14, 27, 28).

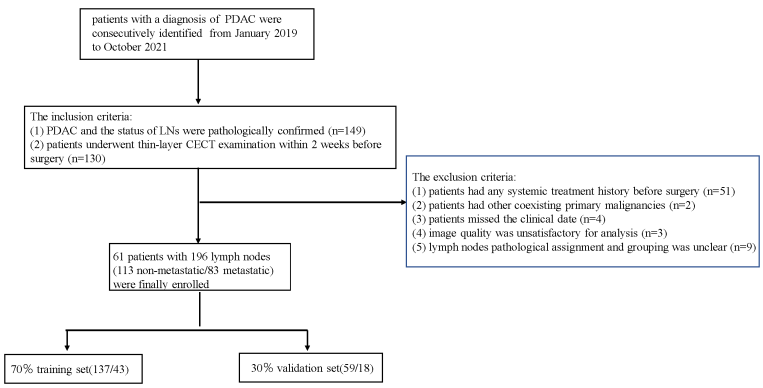

FIGURE 1
Flowchart of patients' selection.

Image processing, VOI delineation, and radiomic analysis

This study workflow is shown in Figure 2. The detailed steps for Volume of Interest (VOI) segmentation and feature extraction were as follows. ① The original portal venous phase images were downloaded from the PACS (Carestream) and saved as Digital Imaging and Communication in Medicine (DICOM) files. ② The concrete steps for image normalization were: (a) for image registration, every portal venous phase image slice from the raw data was resampled to a standardized pixel dimension size of 1.0 × 1.0 × 1.0 mm^3; (b) for gray-level discretization, the image intensity of every portal venous phase image was normalized *via* the gray-level discretization method with a fixed number of bins (256 bins); (c) portal venous phase images were viewed in a fixed head window (level = 60 Hounsfield unit (HU); width = 400 HU). ③ VOIs were acquired by sketching LN borders manually slice-by-slice on axial sections, automatically merged into a 3D region using an open source software (3D Slicer, version 4.13.0; Boston, MA, USA), and adjusted on sagittal and coronal sections by a radiologist with 7 years of abdominal diagnosis experience. ④ All VOIs were confirmed again by a senior radiologist with 20 years of abdominal diagnosis experience. ⑤ The radiomic features were automatically extracted from the VOIs with SlicerRadiomics (an extension for 3D-slicer).

Finally, a total amount of 1037 radiomic features in eight categories (first-order, shape-based histogram, gray-level cooccurrence matrix (GLCM), grey level size zone matrix (GLSZM), gray level run length matrix, gray level dependence matrix, neighboring grey-tone difference matrix and wavelet-based features) were extracted from each VOI automatically. A two-step program was designed to reduce high-dimensional data and avoid overfitting. First, features with ICC above 0.8 were considered to be reproducible and stable. Secondly, the least absolute shrinkage and selection operator (LASSO) algorithm was used to select optimal features with nonzero coefficients, with parameter tuning performed with 10-fold cross-validation to screen optimal radiomic features.

Model building

The differences in CT radiological features between metastatic and non-metastatic LNs were first compared by univariate analysis. Subsequently, significant ($P<0.05$) radiological features in the univariate analysis were entered into multivariate analysis to determine independent predictors of metastatic LNs and to develop a radiological model by multivariate logistic regression (LR) analysis in the training cohort. Odds ratio (OR) and 95% confidence interval (CI) for each independent factor were calculated.

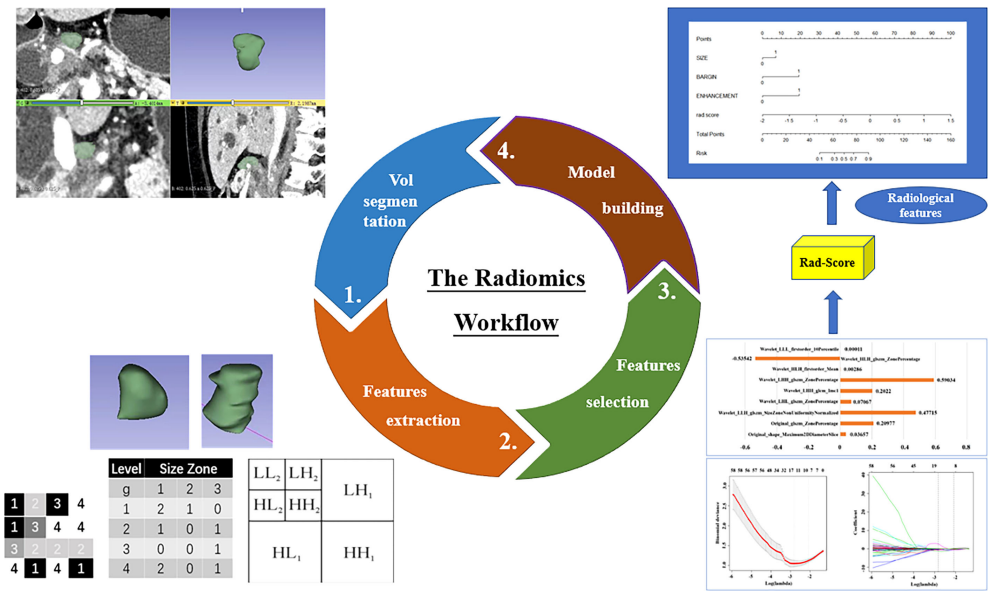

FIGURE 2
The workflow of the radiomics analysis of LNs in this study. Step 1: LNs were semi-automatically segmented slice by slice in portal venous phase images. Step 2: Radiomics features were extracted from the identified VOIs. Step 3: The LASSO logistic regression with penalty parameter tuning conducted by 10-fold cross-validation was used to select the optimal radiomics features. Step 4: The LN Rad-score and the nomogram incorporating radiological features with Rad-score were established.

A radiomics score (Rad-score) was calculated for each LN by determining the linear combination of the optimal radiomic features weighted by their respective LASSO coefficients in the training cohort. The Rad-score model for assessing the metastatic LNs of PDAC patients was first developed in the training cohort.

To provide a simple tool for clinicians to predict metastatic LNs in PDAC, a radiological-radiomics nomogram, which combined the LN Rad-score and independent LN's radiological features, was built by multivariate LR analysis in the training cohort.

Model evaluation

The diagnostic performances of the three models were assessed in the validation cohort by receiver operating characteristic (ROC) curve analysis. The area under the ROC curve (AUC), sensitivity and specificity were all determined, and the Delong test was performed to compare the AUCs of the three models. The calibration ability of the radiological-radiomics nomogram was assessed by calibration curve analysis in the whole cohort, which could compare consistency between the pathological findings of LNs and nomogram-evaluated outcomes. The clinical values of the Rad-score model and the radiological-radiomics nomogram were assessed using decision curve analysis (DCA) by calculating the net benefits in the training and validation cohorts for a range of threshold probabilities (29).

Statistical analysis

Statistical analysis was performed with the R software (http://www.R-project.org), MedCalc (version 18.2.1), SPSS (version 25.0) and empower (R) (www.empowerstats.com, X&Y Solutions, Inc., Boston, MA). Baseline clinical characteristics were expressed as mean ± standard deviation, or number and percentage, as appropriate. The two-sample t test was performed to compare continuous variables. The chi-squared test was carried out to compare categorical variables. A two-sided P value below 0.05 was considered statistically significant. Inter-reader agreement was calculated using ICC analysis.

Results

Patient characteristics and LNs' radiological features

The clinical characteristics of the training and validation cohorts are summarized in Table 1. There were no significant differences between the training and validation cohorts in clinical characteristics. The radiological features of metastatic and non-metastatic LNs in the training cohort are summarized in Table 2. Agreement for evaluating radiological features between two radiologists was good to excellent overall. ICC of LN margin, size, shape, density and pattern of enhancement were 0.871, 0.906, 0.892, 0.963 and 0.906, respectively. After univariate and multivariate analyses, LN size(odds ratio [OR], 5.025; 95% CI, 1.453 - 17.374; P = 0.011), LN margin(OR, 7.482; 95% CI, 2.705 - 20.696; P < 0.001)and enhancement pattern (OR, 7.039; 95% CI, 2.107 - 23.513; P = 0.002) showed statistically significant differences, and were included as independent predictors of LN metastasis to construct a radiological model. The diagnostic performance of the radiological model was moderate, with an AUC of 0.831(95% CI, 0.761 - 0.900), a sensitivity of 0.632 and a specificity of 0.900 in the training

TABLE 1 Patients characteristics.

Characteristic	Training Cohort (n = 43)	Validation Cohort (n = 18)	p
Gender, No. (%)			0.943
male	22 (51.2)	9 (50)	
female	21 (48.8)	9 (50)	
Age (Mean ± SD)	62.56 ± 8.797	62.11 ± 10.51	0.865
CA199 level, No. (%)			0.276
Abnormal	33 (76.7)	16 (88.9)	
Normal	10 (23.3)	2 (11.1)	
CA125 level, No. (%)			0.147
Abnormal	32 (74.4)	10 (55.6)	
Normal	11 (25.6)	8 (44.4)	
Location, No. (%)			0.924
Head and neck	12 (27.9)	5 (27.8)	
body	21 (48.8)	8 (44.4)	
tail	10 (23.3)	5 (27.8)	

TABLE 2 Univariate and multivariable analysis of CT radiological features for LN metastasis evaluation in the training cohort.

Factors	Univariate analysis			Multivariate analysis		
	Odds ratio	(95% CI)	*p*	Odds ratio	(95% CI)	*p*
Size	11.943	3.827-37.272	< 0.001	5.025	1.453-17.374	0.011
Shape	1.700	0.773-3.741	0.187			
Margin	10.000	4.080-24.512	< 0.001	7.482	2.705-20.696	< 0.001
Degree of enhancement						
Mild	ref.					
Moderate	2.273	0.930-5.554	0.072			
Strong	1.773	0.718-4.377	0.214			
Patterns of enhancement	11.401	3.768-34.500	< 0.001	7.039	2.107-23.513	0.002

cohort, and an AUC of 0.756(95% CI, 0.629 - 0.884), a sensitivity of 0.615 and a specificity of 0.848 in the validation cohort (Figure 4).

Rad-score and radiological-radiomics nomogram construction and performance evaluation

To identify PDAC patients with LN metastasis, a total of 9 most predictive radiomic features with nonzero coefficients in the LASSO algorithm were finally selected (Figure 3) and incorporated into the Rad-score model. The formula was as follows: Rad-score = 0.2098 × Original_glszm_ZonePercentage + 0.0366 × Original_shape_Maximum2DDiameterSlice + 0.0001Wavelet_LLL_firstorder_10Percentile + 0.029Wavelet_HLH_firstorder_Mean + 0.2022 × Wavelet_LHH_glcm_Imc 1 + (− 0.5354) × Wavelet_HLH_glszm_ZonePercentage + 0.0707 × Wavelet_LHL_glszm_ZonePercentage + 0.5903 × Wavelet_LHH_glszm_ZonePercentage + 0.4772 × Wavelet_LLH_glszm_SizeZoneNonUniformityNormalized. The Rad-score model showed a better performance than the radiological model the radiological model, with an AUC of 0.879(95%CI, 0.824 - 0.934), sensitivity of 0.684 specificity of 0.838 in the training cohort, and an AUC of 0.804(95%CI, 0. 685 - 0.924), sensitivity of 0.654, specificity of 0.818 in the validation cohort (Figure 4). The DeLong test displayed that there was no significant differences between the AUCs of the radiological model and Rad-score models in the training cohort (P = 0.258, DeLong test) and validation cohort (P = 0.543, DeLong test).

Three radiological features (LN size, LN margin and enhancement pattern) combined with the LN Rad-score were used to build a radiological-radiomics nomogram by multivariate LR analysis. The radiological-radiomics nomogram for identifying PDAC patients with LN metastasis risk in the training cohort is shown in Figure 5A. This nomogram showed an AUC of 0.937 (95%CI, 0. 900 - 0.974), a sensitivity of 0.772 and a specificity of 0.863 in the training cohort, and an AUC of 0.851(95%CI, 0.741 - 0.961), a sensitivity of 0.692 and a specificity of 0.909 in the validation cohort (Figure 4). The DeLong test revealed that the radiological-radiomics nomogram had enhanced predictive performance than the radiomics and radiological models in the training cohort(P = 0.010, DeLong test; P < 0.0001, DeLong test), with no significant differences in the validation cohort(P = 0.228, DeLong test; P = 0.084, DeLong test).

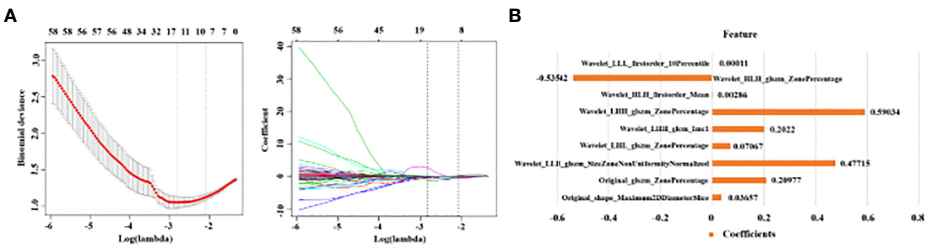

FIGURE 3
The framework for radiomics features selection. **(A)** The LASSO logistic regression was used to select LN radiomics. A tuning parameter was selected *via* 10-fold cross-validation and nine with nonzero coefficients were selected finally. **(B)** Histogram shows the role of nine selected radiomics features used to calculate the Rad-score. The y-axis represents individual radiomics features, with their coefficients in the LASSO regression analysis plotted on the x-axis.

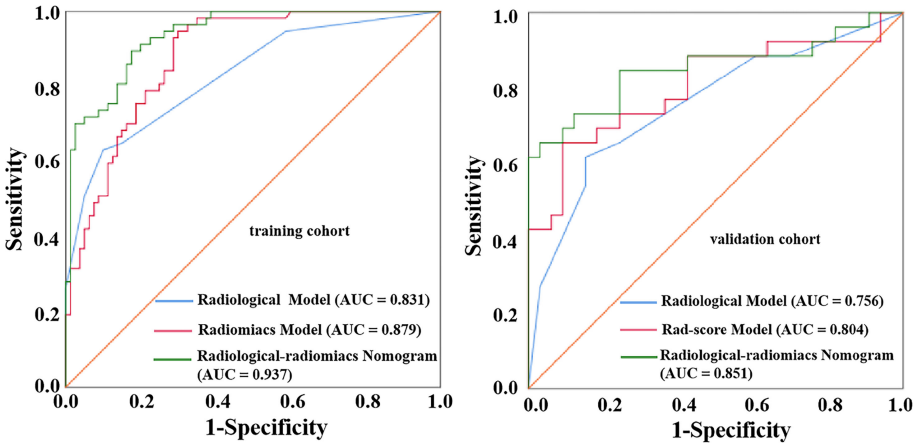

FIGURE 4
ROC curves of the radiological model, Rad-score model and radiological-radiomics nomogram for diagnosing metastatic LNs in the training cohort and validation cohort.

Calibration curve analysis of the nomogram demonstrated the prediction results were in good agreement with the actual observations both in the training and validation cohorts (Figure 5B).

DCA of the Rad-score model and radiological-radiomics nomogram in the training and validation cohorts are presented in Figure 6. The curves demonstrated that the Rad-score model and radiological-radiomics nomogram provided more benefit than the treat all or none principle in PDAC patients for all threshold probabilities in the training cohort and all most threshold probabilities in the validation cohort.

Discussion

In this retrospective study, we developed a radiological-radiomics nomogram that incorporated the LN radiomics signature with LNs' radiological features to evaluate the status of LNs in patients with PDAC. In addition, the radiological-radiomics nomogram performed better than the Rad-score and radiological models. These findings indicated that LN radiomics analysis could be effective for preoperative diagnosis of metastatic LNs in patients with PDAC.

In the current study, we found LN size, LN margin and enhancement pattern were the optimal radiological features to detect LN metastasis. Heterogeneous enhancement, which may reflect unevenly distributed tumor angiogenesis and internal necrosis, is considered a reliable feature of LN metastasis (27, 28). Blurred margin may be caused by tumor cell infiltration into peri-nodal adipose tissue. A short-axis diameter of LNs greater than 10 mm is widely used to diagnose nodal involvement in PDAC. In agreement, we also demonstrated that large LNs (>10 mm) are more prevalent in metastatic LNs compared with non-metastatic LNs. Roche et al. also indicated this criterion could lead to high diagnostic specificity in evaluating the LN status (30). Based on these three predictors we constructed a radiological model to identify metastatic LNs in patients with PDAC, which

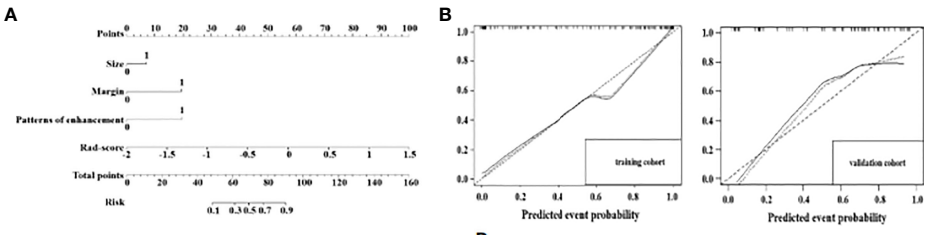

FIGURE 5
A radiological-radiomics nomogram was plotted combining independent radiological features with Rad-score in the training cohort **(A)**. Calibration curves for the radiological-radiomics nomogram in the training cohort and in the validation cohort **(B)**. The 45° straight line indicates the ideal performance of the radiological-radiomics nomogram. A closer distance between two curves indicates higher accuracy.

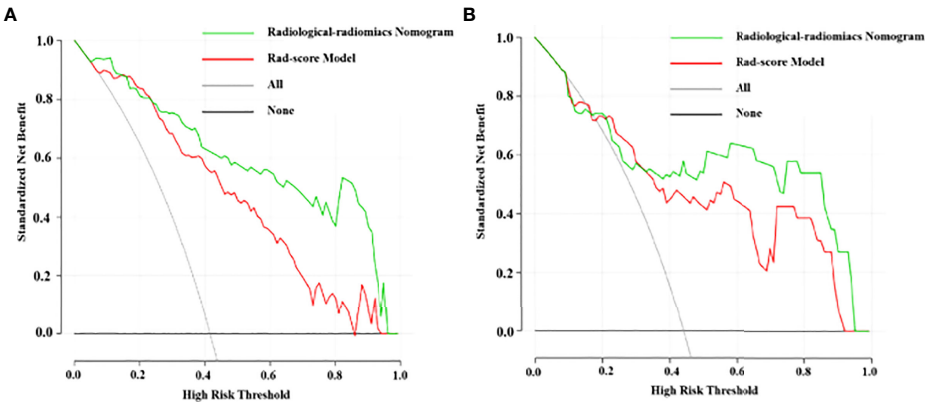

FIGURE 6
DCA for the Rad-score model and radiological-radiomics nomogram in the training cohort **(A)** and validation cohort **(B)**. The y-axis measures the net benefit and the x-axis represents the threshold probability. The grey line that all patients had LN metastasis and the black line indicate no patients had LN metastasis. The red line and the green line indicate the net benefit of the Rad-score model and the radiological-radiomics nomogram at different threshold probabilities, respectively. The radiomics nomogram had a higher overall net benefit in differentiating LN metastasis than Rad-score model.

had a good diagnostic performance with AUCs of 0.831 and 0.756 in the training and validation cohorts. These results revealed that the radiological model could be used for differential diagnosis between metastatic and non-metastatic LNs. However, texture heterogeneity as a fundamental feature of the LN itself through naked-eye observation has not been applied (31, 32).

Radiomics can extract high-dimensional objective and quantitative features from the segmented volumes and to assess the spatial distribution of voxels that could profile heterogeneity (17). The present study applied LN radiomics to evaluate the LN status and found 9 radiomic features quantified on portal-venous CT-image that could help diagnose metastatic LNs in PDAC. Among these features, most were determined on images preprocessed with wavelet filters (33), which indicated that higher order statistics features are more valuable for evaluating the LN status. Five GLSZM features could imply the extent of the spatial correlation or uniformity of gray-levels. GLCM Informational Measure of Correlation 1 was increased in metastatic LNs, which indirectly indicated that metastatic LNs have a higher degree of heterogeneity. First order features, including mean and 10^{th} percentile, significantly correlate with the LN status, which provide statistical information on the distribution and number of pixels with the same intensity in the VOI (34). Furthermore, this study found that Maximum2D Diameter Slice, which can express the largest pairwise Euclidean distance between LN surface voxels in the slice plane, was larger in the metastasis group. This was a reasonable evidence that metastatic LNs are preferably larger.

The Rad-score model composed of the above radiomic features showed better diagnostic performance compared with the radiological model, with AUCs of 0.879 and 0.804 in the training and validation cohorts, respectively.

By incorporating the radiological model and the Rad-score, we built a LN radiological-radiomics nomogram, which had the highest AUC (training cohort, 0.937; validation cohort, 0.851) and diagnostic sensitivity (training cohort, 0.772; validation cohort, 0.692). This nomogram showed significantly better diagnostic efficacy for metastatic LNs in patients with PDAC compared with the Rad-score and radiological models in the training cohort (all $P<0.05$, DeLong test). This finding revealed that combining the internal texture heterogeneity and radiological features of LNs could be a prospective approach to enhance precision medicine. Furthermore, this nomogram could conveniently and visually estimate the status of LNs in PDAC patients. With the help of the radiological-radiomics nomogram, individualized risk assessment in terms of detecting LN metastasis could be implemented for PDAC patients. Finally, the calibration curve of the nomogram showed good agreement between nomogram-evaluated and pathological results in the training and validation cohorts. In addition, we performed a decision curve analysis demonstrating a clinical net benefit for the radiological-radiomics nomogram. This curve showed the nomogram could confer enhanced net benefits than treating all or no patients for all threshold probabilities in the training cohort and almost all in the validation cohort.

There were several limitations in this study. Firstly, because this was a single-center retrospective study, further refinements with multicenter studies are needed to confirm these findings. Secondly, VOIs were segmented semi-automatically in this research and errors were inevitable due to segmentation

uncertainty even though good agreement in inter-observer and intra-observer reproducibility was achieved. Deep learning for automatic segmentation to increase efficiency and reproducibility still needs further exploration (35). Thirdly, tumor radiomics was not included in this study, so the diagnostic value of combining the radiomics and tumor radiomic features of LNs requires further investigation. Fourthly, we only performed LN radiomics analysis based on the portal venous phase images and didn't compare or combine with other phase images to definite which may have the potential to improve diagnostic efficiency. This owns the significance for further exploration.

Conclusion

This study developed and validated a radiological-radiomics nomogram that integrated the LN Rad-score and LNs' radiological features for preoperatively evaluating the LN status in PDAC patients. This nomogram could serve as an easy-to-use, noninvasive and effective tool to assist radiologists in diagnosing metastatic LNs and to guide the clinical decision-making process for PDAC patients.

Data availability statement

The original contributions presented in the study are included in the article/supplementary material. Further inquiries can be directed to the corresponding author.

Ethics statement

This study was approved by the ethics committee of Chongqing general Hospital, and the requirement for informed consent was waived.

Author contributions

TZY designed and supervised the study. Qian Li conducted the experiments and drafted the manuscript. ZD revised the manuscript. RXF, WYJ and ZJY collected the imaging data. Qian Liu, LXJ and YJY analyzed the data. SZH and LZW performed statistical analysis. All the authors listed have made substantial, direct and intellectual contributions to the work and approved the manuscript for publication.

Funding

This study was supported by the medical research Key Program of the combination of Chongqing National health commission and Chongqing science and technology bureau, China (no 2019ZDXM010) and the medical research Program of the combination of Chongqing National health commission and Chongqing science and technology bureau, China (no 2020FYYX151).

Conflict of interest

The authors declare that the research was conducted in the absence of any commercial or financial relationships that could be construed as a potential conflict of interest.

Publisher's note

References

1. Siegel RL, Miller KD, Jemal A. Cancer statistics, 2020. *CA Cancer J Clin* (2020) 70:7–30. doi: 10.3322/caac.21590

2. Conroy T, Bachet JB, Ayav A, Huguet F, Lambert A, Caramella C, et al. Current standards and new innovative approaches for treatment of pancreatic cancer. *Eur J Cancer* (2016) 57:10–22. doi: 10.1016/j.ejca.2015.12.026

3. NNakagohri T, Kinoshita T, Konishi M, Takahashi S, Gotohda N. Nodal involvement is strongest predictor of poor survival in patients with invasive adenocarcinoma of the head of the pancreas. *Hepatogastroenterology* (2006) 53 (69):447–51. doi: 10.1136/gut.2005.089136

4. Paiella S, Sandini M, Gianotti L, Butturini G, Salvia R, Bassi C. The prognostic impact of para-aortic lymph node metastasis in pancreatic cancer: A systematic review and meta-analysis. *Eur J Surg Oncol* (2016) 42(5):616–24. doi: 10.1016/j.ejso.2016.02.003

5. Konstantinidis IT, Deshpande V, Zheng H, Wargo JA, Fernandez-del Castillo C, Thayer SP, et al. Does the mechanism of lymph node invasion affect survival in patients with pancreatic ductal adenocarcinoma? *J Gastrointest Surg* (2010) 14 (2):261–7. doi: 10.1007/s11605-009-1096-z

6. Perlmutter BC, Hossain MS, Naples R, Tu C, Vilchez V, McMichael J, et al. Survival impact based on hepatic artery lymph node status in pancreatic adenocarcinoma: A study of patients receiving modern chemotherapy. *J Surg Oncol* (2021) 123(2):399–406. doi: 10.1002/jso.26281

7. Suraci C, Young K, Dove J, Shabahang M, Blansfield J. Predicting positive margins in pancreatic head adenocarcinoma after neoadjuvant therapy: Investigating disparities in quality care using the national cancer database. *Ann Surg Oncol* (2021) 28(3):1595–601. doi: 10.1245/s10434-020-08766-2

8. Tran Cao HS, Zhang Q, Sada YH, Silberfein EJ, Hsu C, Van Buren G2nd, et al. Value of lymph node positivity in treatment planning for early stage pancreatic cancer. *Surgery* (2017) 162(3):557–67. doi: 10.1016/j.surg.2017.05.003

9. Khorana AA, Mangu PB, Berlin J, Engebretson A, Hong TS, Maitra A, et al. Potentially curable pancreatic cancer: American society of clinical oncology clinical

practice guideline update. *J Clin Oncol* (2017) 35(20):2324–8. doi: 10.1200/JCO.2017.72.4948

10. Tempero MA, Malafa MP, Al-Hawary M, Behrman SW, Benson AB, Cardin DB, et al. CT and pathologic assessment of prospective nodal staging in patients with ductal adenocarcinoma of the head of the pancreas. *AJR Am J Roentgenol* (2021) 19(4):439–480. doi: 10.6004/jnccn.2021.0017

11. Roche CJ, Hughes ML, Garvey CJ, Campbell F, White DA, Jones L, et al. CT and pathologic assessment of prospective nodal staging in patients with ductal adenocarcinoma of the head of the pancreas. *AJR Am J Roentgenol* (2003) 180 (2):475–80. doi: 10.2214/ajr.180.2.1800475

12. Tseng DS, van Santvoort HC, Fegrachi S, Besselink MG, Zuithoff NP, Borel Rinkes IH, et al. Diagnostic accuracy of CT in assessing extra-regional lymphadenopathy in pancreatic and peri-ampullary cancer: a systematic review and meta-analysis. *Surg Oncol* (2014) 23(4):229–35. doi: 10.1016/j.suronc.2014.10.005

13. Imai H, Doi R, Kanazawa H, Kamo N, Koizumi M, Masui T, et al. Preoperative assessment of para-aortic lymph node metastasis in patients with pancreatic cancer. *Int J Clin Oncol* (2010) 15(3):294–300. doi: 10.1007/s10147-010-0066-5

14. Loch FN, Asbach P, Haas M, Seeliger H, Beyer K, Schineis C, et al. Accuracy of various criteria for lymph node staging in ductal adenocarcinoma of the pancreatic head by computed tomography and magnetic resonance imaging. *World J Surg Oncol* (2020) 18(1):213. doi: 10.1186/s12957-020-01951-3

15. Gillies RJ, Kinahan PE, Hricak H. Radiomics: Images are more than pictures, they are data. *Radiology* (2016) 278(2):563–77. doi: 10.1148/radiol.2015151169

16. Lambin P, Rios-Velazquez E, Leijenaar R, Carvalho S, van Stiphout RG, Granton P, et al. Radiomics: extracting more information from medical images using advanced feature analysis. *Eur J Cancer* (2012) 48(4):441–6. doi: 10.1016/j.ejca.2011.11.036

17. Lambin P, Leijenaar RTH, Deist TM, Peerlings J, de Jong EEC, van Timmeren J, et al. Radiomics: the bridge between medical imaging and personalized medicine. *Nat Rev Clin Oncol* (2017) 14(12):749–62. doi: 10.1038/nrclinonc.2017.141

18. Zhou Y, Su GY, Hu H, Ge YQ, Si Y, Shen MP, et al. Radiomics analysis of dual-energy CT-derived iodine maps for diagnosing metastatic cervical lymph nodes in patients with papillary thyroid cancer. *Eur Radiol* (2020) 30(11):6251–62. doi: 10.1007/s00330-020-06866-x

19. Li M, Zhang J, Dan Y, Yao Y, Dai W, Cai G, et al. A clinical-radiomics nomogram for the preoperative prediction of lymph node metastasis in colorectal cancer. *J Transl Med* (2020) 18(1):46. doi: 10.1186/s12967-020-02215-0

20. Ho TY, Chao CH, Chin SC, Ng SH, Kang CJ, Tsang NM. Classifying neck lymph nodes of head and neck squamous cell carcinoma in MRI images with radiomic features. *J Digit Imaging* (2020) 33(3):613–8. doi: 10.1007/s10278-019-00309-w

21. Peeken JC, Shouman MA, Kroenke M, Rauscher I, Maurer T, Gschwend JE, et al. A CT-based radiomics model to detect prostate cancer lymph node metastases in PSMA radioguided surgery patients. *Eur J Nucl Med Mol Imaging* (2020) 47 (13):2968–77. doi: 10.1007/s00259-020-04864-1

22. Song J, Hu Q, Ma Z, Zhao M, Chen T, Shi H. Feasibility of T2WI-MRI-based radiomics nomogram for predicting normal-sized pelvic lymph node metastasis in cervical cancer patients. *Eur Radiol* (2021) 31(9):6938–48. doi: 10.1007/s00330-021-07735-x

23. Gao J, Han F, Jin Y, Wang X, Zhang J. A radiomics nomogram for the preoperative prediction of lymph node metastasis in pancreatic ductal adenocarcinoma. *Front Oncol* (2020) 10:1654. doi: 10.3389/fonc.2020.01654

24. Liu P, Gu Q, Hu X, Tan X, Liu J, Xie A, et al. Applying a radiomics-based strategy to preoperatively predict lymph node metastasis in the resectable pancreatic ductal adenocarcinoma. *J Xray Sci Technol* (2020) 28(6):1113–21. doi: 10.3233/XST-200730

25. Bian Y, Guo S, Jiang H, Gao S, Shao C, Cao K, et al. Relationship between radiomics and risk of lymph node metastasis in pancreatic ductal adenocarcinoma. *Pancreas* (2019) 48(9):1195–203. doi: 10.1097/MPA.0000000000001404

26. Efremidis SC, Vougiouklis N, Zafiriadou E, Sofianou F, Sbarounis C, Fardellas Y, et al. Pathways of lymph node involvement in upper abdominal malignancies: evaluation with high-resolution CT. *Eur Radiol* (1999) 9(5):868–74. doi: 10.1007/s003300050757

27. Kim YC, Park MS, Cha SW, Chung YE, Lim JS, Kim KS, et al. Comparison of CT and MRI for presurgical characterization of paraaortic lymph nodes in patients with pancreatico-biliary carcinoma. *World J Gastroenterol* (2008) 14 (14):2208–12. doi: 10.3748/wjg.14.2208

28. Lee JH, Han SS, Hong EK, Cho HJ, Joo J, Park EY, et al. Predicting lymph node metastasis in pancreatobiliary cancer with magnetic resonance imaging: A prospective analysis. *Eur J Radiol* (2019) 116:1–7. doi: 10.1016/j.ejrad.2019.04.007

29. Kerr KF, Brown MD, Zhu K, Janes H. Assessing the clinical impact of risk prediction models with decision curves: Guidance for correct interpretation and appropriate use. *J Clin Oncol* (2016) 34(21):2534–40. doi: 10.1200/JCO.2015.65.5654

30. Roche CJ, Hughes ML, Garvey CJ, Campbell F, White DA, Jones L, et al. CT and pathologic assessment of prospective nodal staging in patients with ductal adenocarcinoma of the head of the pancreas. *AJR Am J Roentgenol* (2003) 180 (2):475–80. doi: 10.2214/ajr.180.2.1800475

31. Lunt SJ, Chaudary N, Hill RP. The tumor microenvironment and metastatic disease. *Clin Exp Metastasis* (2009) 26(1):19–34. doi: 10.1007/s10585-008-9182-2

32. Davnall F, Yip CS, Ljungqvist G, Selmi M, Ng F, Sanghera B, et al. Assessment of tumor heterogeneity: an emerging imaging tool for clinical practice? *Insights Imaging* (2012) 3(6):573–89. doi: 10.1007/s13244-012-0196-6

33. van Griethuysen JJM, Fedorov A, Parmar C, Hosny A, Aucoin N, Narayan V, et al. Computational radiomics system to decode the radiographic phenotype. *Cancer Res* (2017) 77(21):e104–7. doi: 10.1158/0008-5472

34. Just N. Improving tumour heterogeneity MRI assessment with histograms. *Br J Cancer* (2014) 111(12):2205–13. doi: 10.1038/bjc.2014.512

35. Tonozuka R, Itoi T, Nagata N, Kojima H, Sofuni A, Tsuchiya T, et al. Deep learning analysis for the detection of pancreatic cancer on endosonographic images: a pilot study. *J Hepatobiliary Pancreat Sci* (2021) 28(1):95–104. doi: 10.1002/jhbp.825

frontiers | Frontiers in Oncology

TYPE Original Research
PUBLISHED 20 October 2022
DOI 10.3389/fonc.2022.994285

OPEN ACCESS

EDITED BY
Chuanming Li,
Chongqing University Central Hospital, China

REVIEWED BY
Sheng Lin,
The Affiliated Hospital of Southwest Medical University, China
Yuchuan Hu,
Tangdu Hospital, China

*CORRESPONDENCE
Wu Zhou
zhouwu@gzucm.edu.cn
Yi-Kai Xu
yikai.xu@163.com

†These authors have contributed equally to this work

SPECIALTY SECTION
This article was submitted to Cancer Imaging and Image-directed Interventions, a section of the journal Frontiers in Oncology

RECEIVED 14 July 2022
ACCEPTED 26 September 2022
PUBLISHED 20 October 2022

CITATION
Hao P, Deng B-Y, Huang C-T, Xu J, Zhou F, Liu Z-X, Zhou W and Xu Y-K (2022) Predicting anaplastic lymphoma kinase rearrangement status in patients with non-small cell lung cancer using a machine learning algorithm that combines clinical features and CT images. *Front. Oncol.* 12:994285. doi: 10.3389/fonc.2022.994285

Predicting anaplastic lymphoma kinase rearrangement status in patients with non-small cell lung cancer using a machine learning algorithm that combines clinical features and CT images

Peng Hao[1†], Bo-Yu Deng[2†], Chan-Tao Huang[1], Jun Xu[1], Fang Zhou[1], Zhe-Xing Liu[3], Wu Zhou[2*] and Yi-Kai Xu[1*]

[1]Nanfang Hospital, Southern Medical University, Guangzhou, China, [2]School of Medical Information Engineering, Guangzhou University of Chinese Medicine, Guangzhou, China, [3]School of Biomedical Engineering, Southern Medical Uinversity, Guangzhou, China

Purpose: To develop an appropriate machine learning model for predicting anaplastic lymphoma kinase (ALK) rearrangement status in non-small cell lung cancer (NSCLC) patients using computed tomography (CT) images and clinical features.

Method and materials: This study included 193 patients with NSCLC (154 in the training cohort, 39 in the validation cohort), 68 of whom tested positive for ALK rearrangements and 125 of whom tested negative. From the nonenhanced CT scans, 157 radiomic characteristics were extracted, and 8 clinical features were collected. Five machine learning (ML) models were assessed to find the best classification model for predicting ALK rearrangement status. A radiomic signature was developed using the least absolute shrinkage and selection operator (LASSO) algorithm. The predictive performance of the models based on radiomic features, clinical features, and their combination was assessed by receiver operating characteristic (ROC) curves.

Results: The support vector machine (SVM) model had the highest AUC of 0.914 for classification. The clinical features model had an AUC=0.805 (95% CI 0.731–0.877) and an AUC=0.735 (95% CI 0.566–0.863) in the training and validation cohorts, respectively. The CT image-based ML model had an AUC=0.953 (95% CI 0.913–1.0) in the training cohort and an AUC=0.890 (95% CI 0.778–0.971) in the validation cohort. For predicting ALK rearrangement status, the ML model based on CT images and clinical features performed better than the model based on only clinical information

or CT images, with an AUC of 0.965 (95% CI 0.826–0.882) in the primary cohort and an AUC of 0.914 (95% CI 0.804–0.893) in the validation cohort.

Conclusion: Our findings revealed that ALK rearrangement status could be accurately predicted using an ML-based classification model based on CT images and clinical data.

KEYWORDS

tomography, X-ray computed, anaplastic lymphoma kinase, gene mutation, non-small cell lung cancer, machine learning, texture

Introduction

Lung cancer is the leading cause of cancer-related death worldwide. In 2013, in women aged 40 to 59 years, lung cancer surpassed breast cancer as the main cause of cancer death (1). Non-small cell lung cancer (NSCLC) is the most common histological subtype, accounting for 85%-90% of lung cancers (2). In the past decade, the emergence of novel drugs that target signalling pathways activated by genetic changes, for example, EGFR mutations and ALK rearrangement status, has revolutionized the treatment of NSCLC patients (3). The presence of an ALK rearrangement protein has been discovered in a small percentage of NSCLC patients, mostly in those with lung adenocarcinoma (3). Approximately 5% of lung adenocarcinomas have ALK rearrangement status, which is mutually exclusive with EGFR mutations. Crizotinib is a promising ALK fusion status inhibitor (4). Thus, identifying ALK rearrangements in NSCLC patients is crucial for therapy planning.

Because histologic and genetic information from invasive biopsies is often taken from only a section of a generally heterogeneous tumour, this characterization information does not provide a thorough depiction of functional and physiological aspects of lesions (5). The most common method for diagnosing and assessing treatment response of lung malignancies is computed tomography (CT). Thus, previous research has examined the link between some gene mutations in lung cancer and clinical features and radiological characteristics of lung cancer (6). Some CT imaging features, such as central tumour location, pleural effusion, lobulated margin, large mass and distant metastases, have been linked to ALK gene rearrangements in these studies (7–13). However, the evaluation of these radiological characteristics of lung cancer, is time-consuming and greatly dependent on the radiologist's knowledge. Machine learning (ML) is a computer-based method for diagnosing lung cancer, predicting survival, and forecasting gene mutations. It can help radiologists discover more about the phenotype of a tumour including that is not obvious on CT scans (14–19). To avoid overfitting and develop robust predictive or prognostic models, a successful radiomic prediction study requires several phases, including accurate statistical analysis, feature selection, and classification. To select a subset of features that can be merged into a multiparametric model, a variety of ML algorithms can be utilized. Although radiomic analysis has used a variety of ML approaches for categorization, there is no "one size fits all" solution because the effectiveness of different ML processes has been proven to vary depending on the kind of data or applicant (20).

As a result, the goal of this research was to investigate effective radiomics-based ML algorithms that predict ALK rearrangements in patients with NSCLC.

Materials and methods

Patients inclusion

From May 2012 to February 2020, we retrospectively reviewed all CT scans of NSCLC patients from PACS system at Nanfang hospital. This retrospective study examined 1002 patients with pathologically proven lung cancer who underwent surgery or received a biopsy. The clinical features of the patients were retrieved from the hospital information system. This study included patients over the age of 18 who met the following criteria: (1) had tumour specimens with confirmed ALK gene rearrangements and pathological testing; (2) had pretreatment CT images; and (3) had complete clinical data. The exclusion criteria were as follows: (1) patients receiving treatment before CT scan (2) the time between CT examination and treatment was longer than one month; (3) multiple tumour nodules were found in the lung; (4) tumour lesions were near the hilar and could not be separated from neighbouring hilar architecture. According to these criteria, 716 patients were included, 648 of whom were ALK negative and 68 of whom were positive for ALK rearrangements. Twenty percent of the ALK negative patients were randomly chosen to

participate in our study. Finally, this study included 193 patients, 125 ALK negative patients and 68 ALK positive patients. The flowchart of patients selection for non-small cell lung cancer (NSCLC) was show in Figure 1. The TNM system was utilized for staging based on the American Joint Committee on Cancer (AJCC) manual (21). The patients were divided into two groups: a primary cohort (n=154 patients) and an independent validation cohort (n=39 patients), were randomly chosen in a ratio of 8:2 from patients with and without ALK rearrangements. This study was approved by the Ethical Committee of the Nanfang Hospital.

The patients were examined with 256-slice iCT (Philips Health care, Best, Netherlands) or Siemens Medical Solutions' Sensation 64, Definition AS (Forchheim, Germany) equipment. The scanning parameters of the two scanners were as follows: tube rotation time 0.5 s vs. 0.5 s, pitch 0.87 vs. 1.2, detector collimation 128 0.625 vs. 64, tube voltage 120 kV, tube current 100-300 mA, field view 350 mm, matrix 512×512, slice thickness 1-5 mm, reconstruction interval 1 mm, and voxel spacing (X and Y directions) 0.52-1.36 mm. Two different scanners from different manufacturers were adopted. Standardization and normalization were applied to all matrices before analysis (22).

Analysis of ALK rearrangement status

For genetic status determination, tissue samples acquired from biopsy or surgical excision were employed. The tissue specimens were prepared using formalin fixation and paraffin embedding. Immunohistochemistry with the D5F3 antibody, which has already been widely utilized for this purpose, was employed to detect ALK rearrangement gene expression. Two senior pathologists validated the findings. Wild-type ALK was defined as a specimen that did not have the ALK fusion gene present.

Radiomic analysis

The radiomic analysis included five steps, which was illustrated in Figure 2.

Segmentation of tumours

For each patient, horizontal, coronal and sagittal views were used for tumour segmentation by using ITK-SNAP software (http://www.itksnap.org/). A chest radiologist with 8 years of experience manually segregated the regions of interest (ROIs) and a senior with ten years of expertise reviewed all the ROIs. To ensure segmentation reproducibility, 30 patients were chosen at random to validate the inter-observer agreement between two observers' delineations of ROIs using the dice similarity coefficient (DSC) by using Matlab 2018b, average value:0.8349 (from 0.6680 to 0.9186).To illustrate,the level of volume agreement the categorization scale below was used: DSC≥0.85 (High Agreement), 0.85>DSC≥0.70(Medium Agreement), 0.7>DSC≥0.5 (Low Agreement), DSC<0.5(Very Low Agreement) (23) Some inappropriate segmentations for ROI bounds were modified where necessary. An automatic active contour segmentation method was used to refine the manually segmented findings.

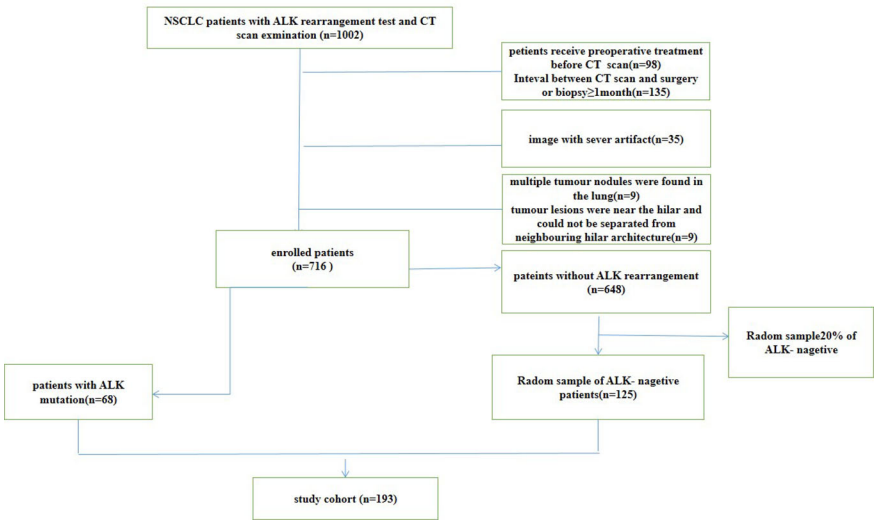

FIGURE 1
The flowchart of patients selection for non-small cell lung cancer (NSCLC).

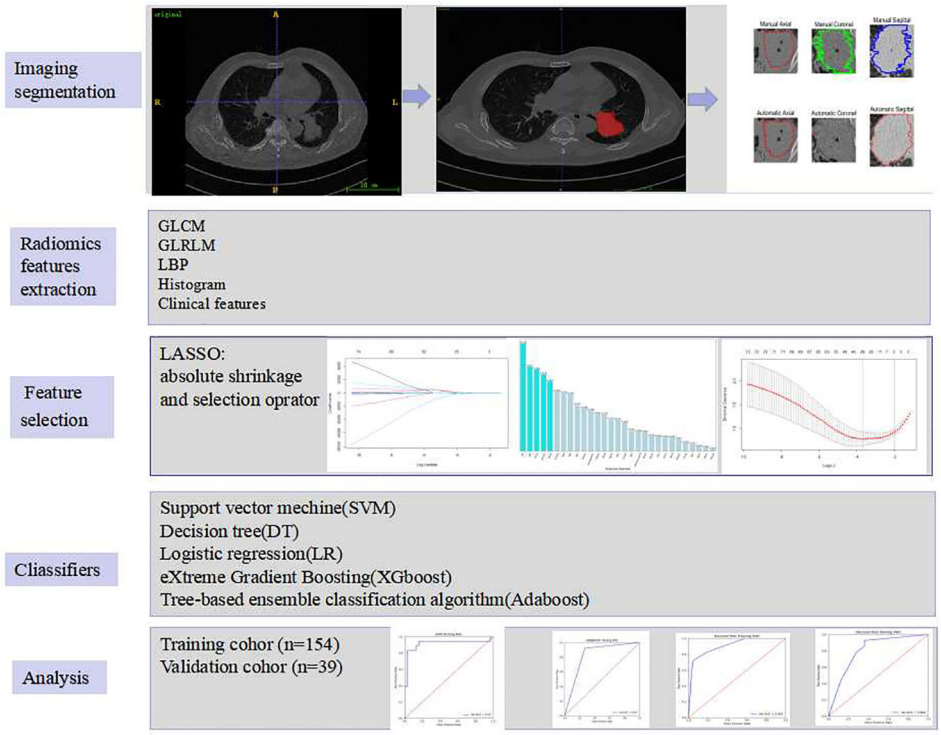

FIGURE 2
The radiogenomics framework of this study.

Radiomic features extraction

Radiomic characteristics were extracted from two-dimensional region of interest (2D-ROI). Pyradiomics (http://pyradiomics.readthedocs.io/en/latest/index.html) was utilized. To be potentially clinically beneficial, we constructed classifiers based on radiomic features acquired from each ROI. Grey level co-occurrence matrix (GLCM), grey level run length matrix (GLRLM), local binary pattern (LBP), histogram, and clinical parameters were acquired from each ROI. The texture and clinical features were then normalized.

Feature selection and classification algorithms

The LASSO technique and 10-fold cross-validation were used to obtain the best subset of radiomic characteristics. A variety of classifiers, including support vector machine (SVM), eXtreme gradient boosting (XGboost), tree-based ensemble classification algorithm (Adaboost), decision tree (DT) and logistic regression (LR), were assessed. The model's performance was evaluated using receiver operating characteristic (ROC) curves and the area under the ROC curve (AUC) by 100 repeated tests. Accuracy, sensitivity, F1, recall and mean absolute error were all calculated as well.

Statistics analysis

Data was analysed with IBM SPSS 25.0 (http://www.ibm.com). For continuous variables, the two independent samples t-test or the Mann–Whitney U test were used, and the significant differences in the ML model between the ALK^+ and ALK^- groups were investigated using the same statistical methodologies. For categorical variables, such as gender, history of smoking, smoking index, clinical stage, distant metastasis, and tumour's degree of pathological invasiveness and EGFR mutation of tumour, the chi-square test or Fisher's exact test was used. The difference in AUCs between the two models was calculated statistically using DeLong's test. The ML model was implemented using the Keras toolkit and Python (version 3.6.8, https://www.python.org/).

Results

Patient Cohort

The clinical characteristics of the patients were described in Table 1. The ALK rearrangement-positive patients were significantly younger than the ALK rearrangement-negative individuals ($P < 0.001$). In addition, more patients with stage III-IV cancer were found in the ALK mutation group ($P < 0.001$).

Performance of the radiomic machine learning algorithm

The best subset of radiomic characteristics was selected using the LASSO technique and 10-fold cross-validation. The radiomic features were retrieved from the 193 patients in the training set to create the radiomic signature. (Figures 3–5). The chosen radiomic properties were as follows: 37hist, 94hist, 99hist, 116hist, 117hist, 123hist, calcutes, homogeneity, Lbp1, Lbp2, Lbp5, PR, SRE, SALGLE (Table 2). Age and phase are proved significant clinical features.

Supervised learning classification

After applying SVM, XGboost, Adaboost, LBP, DT, and LR to determine the optimal features, we identified the most appropriate approach for generating the final classification model based on their performances. We also used grid-search cross-validation to find the best parameters for all of the ML techniques discussed above. In terms of detecting ALK mutations, SVM exceeded the other traditional ML methods as shown in Tables 3, 4 and Figure 6.

Predictive performance of the machine learning model

The SVM classifier had the highest AUC for classification (Table 5). In the primary cohort, the ML model trained on both CT scans and clinical features performed well AUC=0.965 (95% CI 0.8257–0.8823), which was verified in the validation cohort AUC=0.914 (95% CI 0.804–0.891; $P<0.001$). For the CT image-based model, the AUC was 0.953 (95% CI 0.913–1.0) and 0.890 (95% CI 0.778–0.971) for the primary and validation cohorts, respectively. The performance of the ML models trained on both

TABLE 1 Clinical characteristics of the ALK (+) and ALK (-) patients.

Characteristics	ALK (+) (n = 68)	ALK (-) (n = 125)	P-value[b]
Age (years[a])	50.94 ± 12	57.57 ± 10.3	<0.001*
Gender			0.748
Males	31 (46)	60 (48)	
Females	37 (54)	65 (52)	
Smoking status			0.704
Never	52 (76)	92 (74)	
Former	10 (15)	24 (19)	
Current	6 (9)	9 (7)	
SI (pack-years)			0.248
SI ≤ 10	52 (76)	85 (68)	
10 < SI < 20	6 (9)	22 (18)	
SI ≥ 20	10 (15)	18 (14)	
EGFR mutation			<0.001*
Positive	0 (0)	74 (59)	
Negative	68 (100)	51 (41)	
Pathology features			0.169
AIS	1 (1)	9 (7)	
IVC	67 (99)	116 (93)	
TNM stage			<0.001*
I-II	7 (10)	57 (46)	
III-IV	61 (90)	68 (54)	
DM			<0.001*
Positive	55 (81)	62 (49.6)	
Negative	13 (19)	63 (50.4)	

[a]Mean ± standard deviation (range).
[b]ALK– group vs. ALK+ group.
*P < 0.05.
ALK, anaplastic lymphoma kinase; AIS, adenocarcinoma *in situ*; IAC, invasive adenocarcinoma; SI, smoking index; DM, distant metastasis.

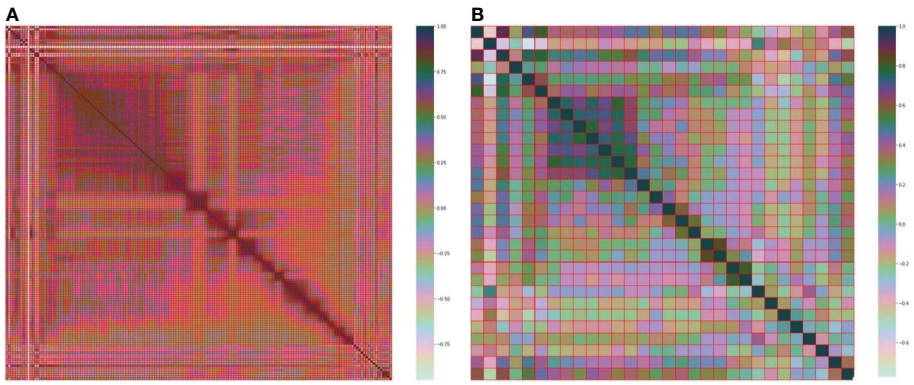

FIGURE 3
(A) Heatmap of the 157 radiomic features. **(B)** Heatmap of the 30 most important radiomic characteristics.

CT images and clinical characteristics was significantly higher than that of the clinical model. The result for the primary cohort trained on the clinical model was an AUC=0.805 (95% CI 0.731–0.877; P<0.0001), and that for the validation cohort was an AUC=0.735 (95% CI 0.566–0.863; P<0.005). The decision curves are shown in Figure 7. The results indicated that ML models trained on both CT images and clinical data performed better than ML models trained by only CT images or the clinical characteristics.

Discussion

Our findings demonstrated that using the SVM classifier to predict ALK gene rearrangements based on both CT scans and clinical characteristics was the most effective strategy. In our study, the integrated model exhibited the highest AUC, which exceeds the clinical models based on previously identified CT characteristics (also known as morphological or semantic CT features) (12, 24) and combined with clinical features, semantic CT features, and radiomic features (25).

Among clinical features, we found ALK^+ patients are often younger than ALK^- patients, which is consistent with prior studies (7). Female sex and smoking history, on the other hand, do not differ much between the two groups of patients. The bulk of the patients in our ALK^+ study was in advanced stages of cancer (III-IV). ALK gene rearrangements were more common in lung cancer at advanced stages, in accordance with a prior study (10). Clinical information is useful in improving the integrated model for ALK rearrangement status detection, as it

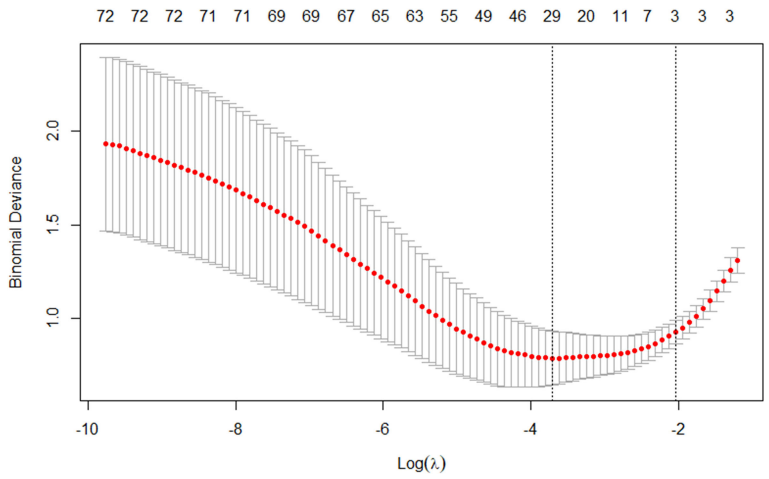

FIGURE 4
The tuning parameter in the LASSO model was chosen using a 10-fold cross-validation method based on minimum criterion. The LASSO regression cross-validation model's binomial deviances as a function of logs(λ) were plotted.

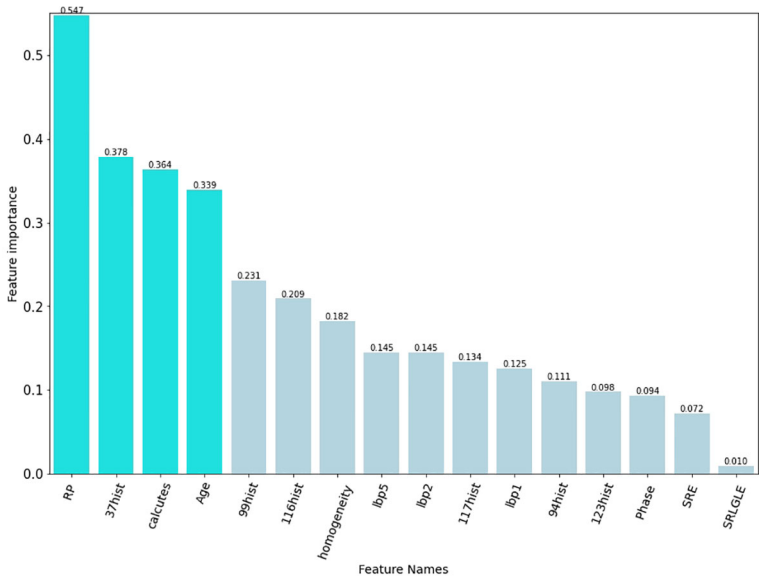

FIGURE 5
The final elements that were chosen to be maintained. The preserved characteristics were on the y axis, and the matching LASSO regression coefficients were on the x axis. The log(λ) coefficients of the features that have been fitted.

increases the integrated model's performance by incorporating clinical characteristics for lesions in the primary and validation cohorts. A previous study had proposed a predictive model for detecting ALK rearrangements, using age as the only clinical component selected and many semantic CT features (AUC=0.846) (9).

Our findings imply that radiomics can be used to predict ALK rearrangement status on CT images in patients with NSCLC. The histogram and texture categories served as the foundation for the radiomic model, which implies that the intensity change of tumours was a potent predictor of the ALK genetic mutation. In this study, we found that Rp, 37hist, and calutes, that linked with ALK mutations. The AUC for postcontrast CT radiomic characteristics detecting ALK rearrangements was 0.829, according to Ma et al. (26). However, their research was based on enhanced CT scans. The radiomic model in our study demonstrates that radiomic features extracted from nonenhanced CT images are sufficient for developing a reliable ALK rearrangements prediction model in NSCLC patients.

Radiomics is an emerging discipline attempting to bridge the gap between medical imaging and personalized medicine (27,

TABLE 2 Selected features with descriptions.

Feature Name	Description
Gray-level co-occurrence matrix (**GLCM**) Homogeneitycalutes	Localization of regions with significant intensity changes; gradients detect edges and quantify region boundaries
Gray-level run length matrix (**GLRLM**) Short-run emphasis (SRE)Short-Run Low Gray-Level Emphasis (SRLGLE) Run percentage (RP)	Measure of the gray scale texture repeatability
Local binary pattern (**LBP**) Lbp1 Lbp2 Lbp5	The lbp (local binary pattern) is an operator used to describe the local texture features of an image.Reflects the content of each pixel to the surrounding pixels.
Histogram 37hist 99hist 94hist 116hist 117hist 123hist	Refect the distribution of voxel gray intensity

10.3389/fonc.2022.994285

TABLE 3 Assessment of different classifier feature selection-based machine learning models for predicting ALK fusion type in the validation cohort.

	Accuracy	Precision	AUC	F1	Mean absolute error	Recall
LR	0.869	0.871	0.887	0.803	0.131	0.762
Adaboost	0.808	0.714	0.806	0.722	0.192	0.747
Decision Tree	0.812	0.790	0.806	0.708	0.188	0.665
XGBoost	0.842	0.822	0.875	0.759	0.158	0.720
SVM	0.849	0.932	0.890	0.747	0.151	0.63

TABLE 4 Assessment of different classifier feature selection-based machine learning models for predicting ALK fusion type in the training cohort.

	Accuracy	Precision	AUC	F1	Mean absolute error	Recall
LR	0.928	0.955	0.958	0.889	0.072	0.835
Adaboost	1	1	1	1	0	1
Decision Tree	0.894	0.913	0.906	0.836	0.106	0.778
XGBoost	0.989	0.990	0.996	0.983	0.011	0.977
SVM	0.943	0.985	0.953	0.911	0.057	0.851

28) by investigating the value of medical images in the diagnosis, grading, and prognostication of diseases using medical image analysis technologies and ML algorithms. However, the best way to use certain medical images or objectives is unclear due to the various feature selection approaches and ML algorithms (29).

In recent years, researchers have investigated the efficacy of various feature selection and ML algorithms in medical image classification to determine whether they are appropriate for the given medical image data. For example, Shiri I et al. (20) examined radiomic characteristics from low-dose CT,

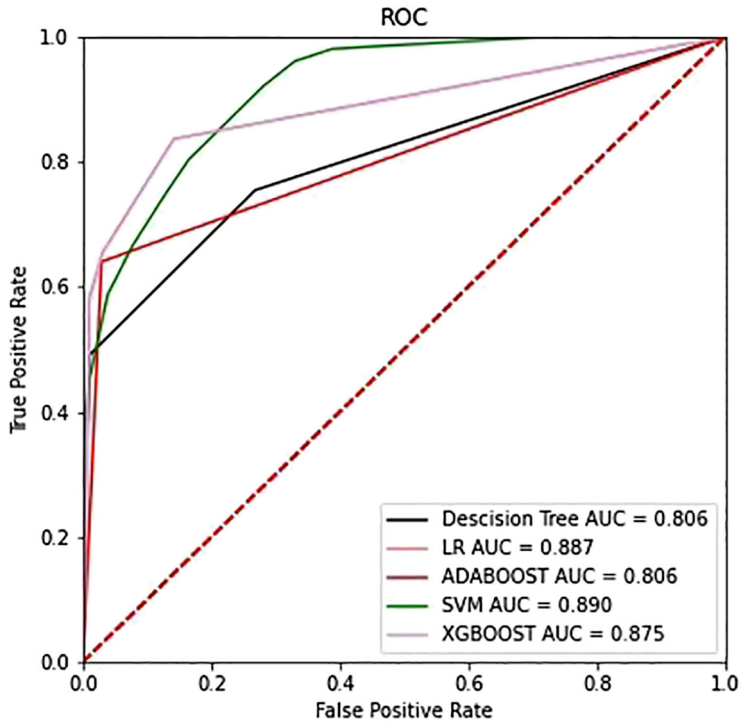

FIGURE 6
The ROC curves of the top four models selected from the training phase on the testing dataset.

10.3389/fonc.2022.994285

TABLE 5 Predictive performance of SVM in the primary and validation cohorts.

Model	Cohorts	Accuracy	Precision	AUC	F1	Mean absolute error	Recall
Clinacal features	Primary	0.758	0.826	0.805	0.612	0.242	0.569
	Validation	0.689	0.5	0.735	0.483	0.311	0.455
CT image	Primary	0.923	0.946	0.953	0.877	0.077	0.792
	Validation	0.858	0.938	0.890	0.769	0.142	0.675
CT image and clinigal features	Primary	0.943	0.985	0.965	0.911	0.057	0.851
	Validation	0.849	0.932	0.914	0.747	0.151	0.63

diagnostic quality CT, and PET-CT as well as ML techniques in NSCLC patients. Their results predicted mutation status of EGFR and KRAS. Then, six feature selection procedures and 12 classifiers were used, and multivariate ML-based AUC performances for EGFR and KRAS were improved to 0.82 and 0.83, respectively. Lan Song et al. compared the performance of three feature selection approaches and two classification methods for predicting ALK fusion in lung cancer patients using clinical characteristics combined with conventional CT and radiomic data (25). They extracted 1218 radiomic characteristics from CT scans and discovered that the LR and DT classifiers had the best prediction performance (AUC=0.890). The optimal ML classifier and feature selection method varied between studies, which could be related to a variety of factors, such as visual modalities, feature extraction algorithms, the number of features chosen, the goal task, and cohort size. According to Han's study, radiomics-based ML was used to determine the best model for NSCLC histologic subtypes (29), and SVM paired with LASSO produced the highest prediction efficacy, similar to our study.

Even though our model's performance was quite promising, there are a few limitations in this study that need to be addressed. First, although the results were favourable, the model's ability to handle imbalanced data must be improved to generalize the prediction outcome to more datasets. Second, we may need to employ a cutting-edge deep learning method to perform the

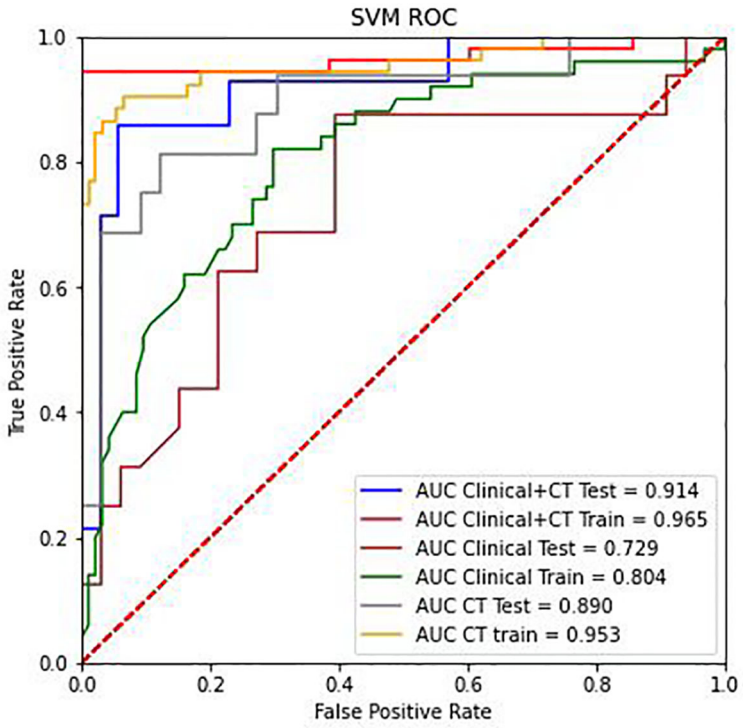

FIGURE 7
The ROC curve analysis of the CT radiomics models, clinical features, and combinations of CT radiomics and clinical features in the training group and testing group.

classification task is warranted. Several studies have successfully constructed models to address this issue with positive results (30). These findings have encouraged us to use neural networks to construct the baseline model in future studies.

In conclusion, the ML model that combined CT scans and clinical features are able to accurately identify the status of the ALK gene. This study provides a noninvasive solution, which is a quick and simple way to guide clinical genetic diagnosis.

Data availability statement

The original contributions presented in the study are included in the article/supplementary material. Further inquiries can be directed to the corresponding author.

Ethics statement

The studies involving human participants were reviewed and approved by The Nanfang Hospital's Ethical Committee. The patients/participants provided their written informed consent to participate in this study. Written informed consent was obtained from the individual(s) for the publication of any potentially identifiable images or data included in this article.

Author contributions

Guarantor of integrity of the entire study: PH, B-YD, WZ and Y-KX. Study concepts and design: PH, Z-XL and Y-KX. Literature research: PH, B-YD. Clinical studies: JX, C-TH, FZ. Experimental studies/data analysis: B-YD, WZ. Statistical analysis: FZ. Manuscript preparation: PH, Z-XL and Y-KX. Manuscript editing: PH, B-YD. PH and B-YD contribute equally to this work. All authors contributed to the article and approved the submitted version.

Funding

Natural Science Foundation of Guangdong Province (NO. 2017A030310102).

Acknowledgments

We thank the SPRINGER NATURE Author Services for its linguistic assistance during the preparation of this manuscript.

Conflict of interest

The authors declare that the research was conducted in the absence of any commercial or financial relationships that could be construed as a potential conflict of interest.

Publisher's note

References

1. Siegel RL, Miller KD, Jemal A. Cancer statistics 2017. *CA: A Cancer J Clin* (2017) 67(1):7–30. doi: 10.3322/caac.21387

2. Ganeshan B, Panayiotou E, Burnand K, Dizdarevic S, Miles K. Tumour heterogeneity in non-small cell lung carcinoma assessed by CT texture analysis: A potential marker of survival. *Eur Radiol* (2012) 22(4):796–802. doi: 10.1007/s00330-011-2319-8

3. Mok TS, Wu Y, Ahn M, Garassino MC, Kim HR, Ramalingam SS, et al. Osimertinib or platinum–pemetrexed in EGFR T790M–positive lung cancer. *New Engl J Med* (2017) 376(7):629–40. doi: 10.1056/NEJMoa1612674

4. Shaw AT, Kim D, Nakagawa K, Seto T, Crinó L, Ahn M, et al. Crizotinib versus chemotherapy in AdvancedALK-positive lung cancer. *New Engl J Med* (2013) 368(25):2385–94. doi: 10.1056/NEJMoa1214886

5. Cai W, Lin D, Wu C, Li X, Zhao C, Zheng L, et al. Intratumoral heterogeneity of ALK-rearranged and ALK/EGFR coaltered lung adenocarcinoma. *J Clin Oncol* (2015) 33(32):3701–9. doi: 10.1200/JCO.2014.58.8293

6. Miao Y, Zhu S, Li H, Zou J, Zhu Q, Lv T, et al. Comparison of clinical and radiological characteristics between anaplastic lymphoma kinase rearrangement and epidermal growth factor receptor mutation in treatment naïve advanced lung adenocarcinoma. *J Thorac Dis* (2017) 9(10):3927–37. doi: 10.21037/jtd.2017.08.134

7. Rizzo S, Petrella F, Buscarino V, De Maria F, Raimondi S, Barberis M, et al. CT radiogenomic characterization of EGFR, K-RAS, and ALK mutations in non-small cell lung cancer. *Eur Radiol* (2016) 26(1):32–42. doi: 10.1007/s00330-015-3814-0

8. Zhou JY, Zheng J, Yu ZF, Xiao WB, Zhao J, Sun K, et al. Comparative analysis of clinicoradiologic characteristics of lung adenocarcinomas with ALK rearrangements or EGFR mutations. *Eur Radiol* (2015) 25(5):1257–66. doi: 10.1007/s00330-014-3516-z

9. Yamamoto S, Korn RL, Oklu R. ALK molecular phenotype in non – small cell lung cancer: CT radiogenomic characterization. *Radiology* (2014) 272(2):568–76. doi: 10.1148/radiol.14140789

10. Choi C. Advanced adenocarcinoma of the lung: Comparison of CT characteristics of patients with anaplastic lymphoma kinase gene rearrangement and those with epidermal growth factor receptor mutation. *Radiology* (2015) 275 (1):272–9. doi: 10.1148/radiol.14140848

11. Mendoza DP. Computed tomography imaging characteristics of NoneSmall-cell lung cancer with anaplastic lymphoma kinase rearrangements: A systematic review and meta-analysis. *Clin Lung Cancer* (2019) 132:28–35. doi: 10.1016/j.cllc.2019.05.006

12. Jeong CJ, Lee HY, Han J, Jeong JY, Lee KS, Choi YL, et al. Role of imaging biomarkers in predicting anaplastic lymphoma kinase-positive lung adenocarcinoma. *Clin Nucl Med* (2015) 40(1):e34–9. doi: 10.1097/RLU.0000000000000581

13. Yildiz VO, Ozkan E, West A. CT Gray-level texture analysis as a quantitative imaging biomarker of epidermal growth factor receptor mutation status in adenocarcinoma of the lung. *AJR Am J Roentgenol* (2015) 205:1016–25. doi: 10.2214/AJR.14.14147

14. Tu W, Sun G, Fan L, Wang Y, Xia Y, Guan Y, et al. Radiomics signature: A potential and incremental predictor for EGFR mutation status in NSCLC patients, comparison with CT morphology. *Lung Cancer* (2019) 132:28–35. doi: 10.1016/j.lungcan.2019.03.025

15. Yang X, He J, Wang J, Li W, Liu C, Gao D, et al. CT-based radiomics signature for differentiating solitary granulomatous nodules from solid lung adenocarcinoma. *Lung Cancer* (2018) 125:109–14. doi: 10.1016/j.lungcan.2018.09.013

16. Evelyn EC, de Jong E, Van Elmpt W, Rizzo S, Colarieti A, Spitaleri G, Leijenaar R, et al. Applicability of a prognostic CT-based radiomic signature model trained on stage I-III non-small cell lung cancer in stage IV non-small cell lung cancer. *Lung Cancer* (2018) 124:6–11. doi: 10.1016/j.lungcan.2018.07.023

17. Lu J, Ji X, L. W, Y. J. Machine learning-based radiomics for prediction of epidermal growth factor receptor mutations in lung adenocarcinoma. *Dis Markers* (2022) 2022:2056837. doi: 10.1155/2022/2056837

18. Le NQK, Kha QH, Nguyen VH. Machine learning-based radiomics signatures for EGFR and KRAS mutations prediction in non-Small-Cell lung cancer. *Int J Mol Sci* (2021) 22(17):9254. doi: 10.3390/ijms22179254

19. Lan S, Zhenchen Z, Huanwen W, Han W, Cheng X, Li J, et al. Individualized nomogram for predicting ALK rearrangement status in lung adenocarcinoma patients. *Eur Radiol* (2021) 31(4):2034–47.

20. Shiri I, Maleki H, Hajianfar G, Abdollahi H, Ashrafinia S, Hatt M, et al. Next-generation radiogenomics sequencing for prediction of EGFR and KRAS mutation status in NSCLC patients using multimodal imaging and machine learning algorithms. *Mol Imaging Biol* (2020) 22(4):1132–48. doi: 10.1007/s11307-020-01487-8

21. Edge SB, Compton CC. The American joint committee on cancer: The 7th edition of the AJCC cancer staging manual and the future of TNM. *Ann Surg Oncol* (2010) 17(6):1471–4. doi: 10.1245/s10434-010-0985-4

22. Park S, Lee SM, Do K, Lee J, Bae W, Park H, et al. Deep learning algorithm for reducing CT slice thickness: Effect on reproducibility of radiomic features in lung cancer. *Korean J Radiol* (2019) 20(10):1431. doi: 10.3348/kjr.2019.0212

23. Crispin-Ortuzar M, Apte AP, Iyer A. Technical note: Extension of CERR for computational radiomics: a comprehensive MATLAB platform for reproducible radiomics research. *Med Phys* (2018) 45(8):3713–20. doi: 10.1002/mp.13046

24. Halpenny DF, Riely GJ, Hayes S, Yu H, Zheng J, Moskowitz CS, et al. Are there imaging characteristics associated with lung adenocarcinomas harboring ALK rearrangements? *Lung Cancer* (2014) 86(2):190–4. doi: 10.1016/j.lungcan.2014.09.007

25. Song L, Zhu Z, Mao L, Li X, Han W, Du H, et al. Clinical, conventional CT and radiomic feature-based machine learning models for predicting ALK rearrangement status in lung adenocarcinoma patients. *Front Oncol* (2020) 10:369. doi: 10.3389/fonc.2020.00369

26. Ma D, Gao X, Dan Y, Zhang A, Wang W, Yang G, et al. Evaluating solid lung adenocarcinoma anaplastic lymphoma kinase gene rearrangement using noninvasive radiomics biomarkers. (2020) 13:6927–6935. doi: 10.2147/OTT.S257798

27. Lambin P, Leijenaar RTH, Deist TM, Peerlings J, De Jong EEC, Van Timmeren J, et al. Radiomics: The bridge between medical imaging and personalized medicine. *Nat Rev Clin Oncol* (2017) 14(12):749–62. doi: 10.1038/nrclinonc.2017.141

28. Gillies RJ, Kinahan PE, Hricak H. Radiomics: Images are more than pictures, they are data. *Radiology* (2016) 278(2):563–77. doi: 10.1148/radiol.2015151169

29. Han Y, Ma Y, Wu Z, Zhang F, Zheng D, Liu X, et al. Histologic subtype classification of non-small cell lung cancer using PET/CT images. *Eur J Nucl Med Mol Imaging* (2021) 48(2):350–60. doi: 10.1007/s00259-020-04771-5

30. Song Z, Liu T, Shi L, et al. The deep learning model combining CT image and clinicopathological information for predicting ALK fusion status and response to ALK-TKI therapy in non-small cell lung cancer patients. *Eur J Nucl Med Mol Imaging* (2021) 48(2):361–71. doi: 10.1007/s00259-020-04986-6

frontiers | Frontiers in Oncology

TYPE Original Research
PUBLISHED 28 October 2022
DOI 10.3389/fonc.2022.1034817

OPEN ACCESS

EDITED BY
Chuanming Li,
Chongqing University Central Hospital, China

REVIEWED BY
Yuwei Xia,
Huiying Medical Technology Co.,Ltd., China
Tian-wu Chen,
Affiliated Hospital of North Sichuan Medical College, China

*CORRESPONDENCE
Zhichao Li
Lizc47@gmail.com
Caiyong Li
31956829@qq.com

†These authors have contributed equally to this work and share first authorship

SPECIALTY SECTION
This article was submitted to Cancer Imaging and Image-directed Interventions, a section of the journal Frontiers in Oncology

RECEIVED 02 September 2022
ACCEPTED 05 October 2022
PUBLISHED 28 October 2022

CITATION
Yang R, Hui D, Li X, Wang K, Li C and Li Z (2022) Prediction of single pulmonary nodule growth by CT radiomics and clinical features — a one-year follow-up study. *Front. Oncol.* 12:1034817. doi: 10.3389/fonc.2022.1034817

Prediction of single pulmonary nodule growth by CT radiomics and clinical features — a one-year follow-up study

Ran Yang[1†], Dongming Hui[1†], Xing Li[2], Kun Wang[2], Caiyong Li[2*] and Zhichao Li[1*]

[1]Department of Radiology, Second People's Hospital of JiuLongPo District, Chongqing, China, [2]Department of Radiology, Chongqing Western Hospital, Chongqing, China

Background: With the development of imaging technology, an increasing number of pulmonary nodules have been found. Some pulmonary nodules may gradually grow and develop into lung cancer, while others may remain stable for many years. Accurately predicting the growth of pulmonary nodules in advance is of great clinical significance for early treatment. The purpose of this study was to establish a predictive model using radiomics and to study its value in predicting the growth of pulmonary nodules.

Materials and methods: According to the inclusion and exclusion criteria, 228 pulmonary nodules in 228 subjects were included in the study. During the one-year follow-up, 69 nodules grew larger, and 159 nodules remained stable. All the nodules were randomly divided into the training group and validation group in a proportion of 7:3. For the training data set, the t test, Chi-square test and Fisher exact test were used to analyze the sex, age and nodule location of the growth group and stable group. Two radiologists independently delineated the ROIs of the nodules to extract the radiomics characteristics using Pyradiomics. After dimension reduction by the LASSO algorithm, logistic regression analysis was performed on age and ten selected radiological features, and a prediction model was established and tested in the validation group. SVM, RF, MLP and AdaBoost models were also established, and the prediction effect was evaluated by ROC analysis.

Results: There was a significant difference in age between the growth group and the stable group ($P < 0.05$), but there was no significant difference in sex or nodule location ($P > 0.05$). The interclass correlation coefficients between the two observers were > 0.75. After dimension reduction by the LASSO algorithm, ten radiomic features were selected, including two shape-based features, one gray-level-cooccurence-matrix (GLCM), one first-order feature, one gray-level-run-length-matrix (GLRLM), three gray-level-dependence-matrix (GLDM) and two gray-level-size-zone-matrix (GLSZM). The logistic regression model combining age and radiomics features achieved an AUC of 0.87 and an accuracy of 0.82 in the training group and an AUC of 0.82 and an accuracy of 0.84 in the verification group for the prediction of nodule growth. For nonlinear models, in the training group, the AUCs of the SVM, RF, MLP and boost models were 0.95, 1.0, 1.0 and 1.0,

respectively. In the validation group, the AUCs of the SVM, RF, MLP and boost models were 0.81, 0.77, 0.81, and 0.71, respectively.

Conclusions: In this study, we established several machine learning models that can successfully predict the growth of pulmonary nodules within one year. The logistic regression model combining age and imaging parameters has the best accuracy and generalization. This model is very helpful for the early treatment of pulmonary nodules and has important clinical significance.

KEYWORDS

pulmonary nodule, computed tomography, prediction, growth, radiomics, LASSO, logistics regression

Introduction

According to the glossary of terms proposed by the Fleischner Society, a pulmonary nodule is defined as an approximately rounded opacity with a diameter of less than 3 cm (1). Recently, an increasing number of pulmonary nodules have been found during screening. Studies have shown that approximately 12.0% of the US population has incidental pulmonary nodules (2). Pulmonary nodules may develop into lung cancer. A total of 2.27% of incidental pulmonary nodules developed into lung cancer during a 2-year follow-up (2). According to data from the World Health Organization (3), lung cancer was the leading cause of cancer death, with 1.8 million deaths in 2020. Early diagnosis can greatly help with treatment (4) and improve the prognosis of millions of patients.

However, for single pulmonary nodules, there are many difficulties in the selection of treatment methods and operation time. Several societies, such as The American College of Chest Physicians (5), The British Thoracic Society (6), and The Fleischner Society of the United States (7–9), have developed guidelines for the management of pulmonary nodules. The American College of Radiology has also developed a structured report template (Lung-RADS) based on the needs of diagnostic radiology practice (10). These guidelines provide recommendations for the management of pulmonary nodules according to the classification of risk factors and nodule morphology. For different types of nodules, it is recommended to carry out a second CT test at different intervals, and further treatment is determined according to the dynamic changes of nodules. The practice intervals recommended by these guidelines currently depend solely on the size of the nodules. For example, the Fleischner Society's 2017 guideline (9) recommends review after 12 months for solid nodules smaller than 6 mm and within 3-6 months for partially solid and ground-glass nodules larger than 6 mm. If the growth of nodules can be predicted in advance, the review interval can be adjusted according to the predicted results and biopsy/surgical pathology can be conducted earlier and improve the prognosis of patients.

Conventional HRCT can reflect the size and general morphology of nodules but cannot provide depth information based on the visual information. Radiomics was proposed by Philippe Lambin in 2011. It refers to an automated and repeatable analysis that uses a high-throughput method to extract a large number of image features from radiographs (11). Since the concept of radiomics emerged, it has been widely used in the identification, grading, efficacy evaluation and prognostics of various tumors (12–15). For example, radiomics has been successfully used to distinguish benign and malignant pulmonary nodules (16, 17). Yu et al. also developed a transfer learning radiomics (TLR) model for the prediction of lymph node metastasis of papillary thyroid carcinoma and achieved high accuracy (18). However, until now, there has been no study to predict the growth of pulmonary nodules in one year using radiomics.

In this study, we intended to collect more than 200 patients with incidental pulmonary nodules and to follow up with them for one year to observe the dynamic changes in the nodules. After that, the correlation between the high-throughput features extracted by radiomics and the growth of pulmonary nodules was then analyzed. On this basis, a model was proposed to predict whether nodules are likely to grow within one year. This model can help doctors operate on dangerous nodules in time and reduce the number of re-examinations for stable nodules.

Materials and methods

Patients

From Jan 2020 to Dec 2021, a total of 314 patients from the Second People's Hospital of JiuLongPo District and Chongqing Western Hospital were involved, and all of them were followed up for one year. This study was approved by the ethics

committees of the two hospitals. As a retrospective analysis, the informed consent requirement was waived.

The inclusion criteria were as follows: (a) patients with high-resolution chest CT images at baseline and at the one-year follow-up. (c) The nodule was solitary, and the baseline diameter of pulmonary nodules was ≥3 mm and ≤20 mm. The exclusion criteria were as follows: (a) the patient's information was incomplete. (b) The image quality was low, (c) the nodules disappeared during follow-up, and (d) multiple pulmonary nodules were found in the baseline images. An overview of the workflow of this study is shown in Figure 1.

The follow-up protocol were as follows: (a) the size of the nodule was 6-8mm, and HRCT of lung scan was performed at 6-12 months. (b) The nodules were 8-20mm in size and HRCT of lung scans were performed every 3 months.

Through the exclusion criteria, 228 of 314 patients for follow-up were finally included. All patients were randomly divided into a training group and a validation group at a ratio of 7:3. The pulmonary nodules were labeled growth or stable according to whether they grew within the one-year follow-up. According to the literature (19), growing nodules were defined as nodules that increased in diameter by more than 1.8 mm in one year. Stable nodules were defined as a change in size of less than 1.8 mm over a year.

CT scanning

The CT images were obtained on a dual source scanner (Siemens SOMATOM Drive, Siemens Healthineers, Germany), a 64-slice detector scanner (Canon Aquilion PRIME TSX-303A, Canon Medical, Japan) and a 16-slice detector scanner (Philips Brilliance 16, Philips Medical, Netherlands). The scanning parameters were as follows:

a. SOMATOM Drive: tube voltage: 120 kV; tube current: automatic; detector collimation = 0.6 mm * 128; pitch: 1.2; rotation time = 0.5 s; reconstruction layer thickness: 1 mm; reconstruction matrix: 512 * 512.
b. Aquilion PRIME: tube voltage: 120 kV; tube current: automatic; detector collimation = 0.5 mm * 64; pitch: 0.824; rotation time = 0.75 s; reconstruction layer thickness: 1 mm; reconstruction matrix: 512*512;
c. Brilliance 16: tube voltage: 120 kV; tube current: 200-300 mAs; detector collimation = 0.75 mm * 16; pitch: 0.938; rotation time = 0.75 s; reconstruction layer thickness: 1 mm; reconstruction matrix: 512*512.

The scan area was from the thoracic entrance to the lung base, covering the whole lung. The scanning was started when the patient held their breath at the end of inhalation.

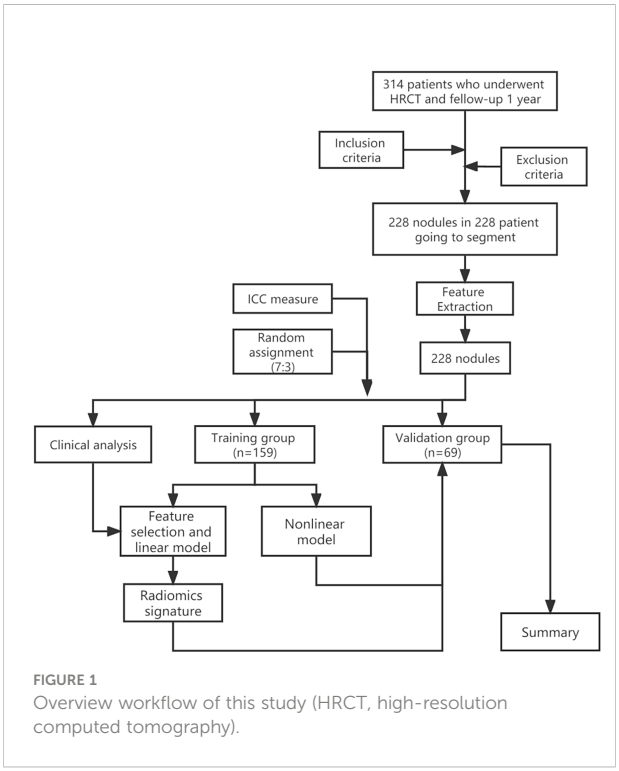

FIGURE 1
Overview workflow of this study (HRCT, high-resolution computed tomography).

Region-of-interest segmentation

All images were exported as Dicom files from the scanners. The DICOM images were converted to Nifft format by MRICroGL software (version: 2.1.60). The Nifft format images were imported into 3D-Slicer (an open-source software application for visualization and analysis of medical image computing data sets) (20). The regions of interest (ROIs) were independently segmented by two radiologists with more than 6 years of clinical experience. Two-dimensional ROIs were limned around the boundary of the lesions on each layer of axial CT images. Three-dimensional ROIs (volume of interest) were conducted by the accumulation of all two-dimensional region ROIs.

Radiomics features extraction

Radiomics features were extracted by an open-source python package of Pyradiomics (21). The implementation of all radiomics features followed the Imaging Biomarkers Standardization Initiative recommendations (22). This process worked on the original images, wavelet images and Laplacian of Gaussian images. A total of 1316 features were extracted. The extracted features are listed in Supplementary Table 1. The definitions of the texture parameters are shown on the site of Pyradimics (https://pyradiomics.readthedocs.io/en/latest/features.html). The workflow of this process is shown in Figure 2.

Prediction model building

The radiomics signature was constructed in 4 steps. In step one, all radiomic feature values were normalized. In step two, the

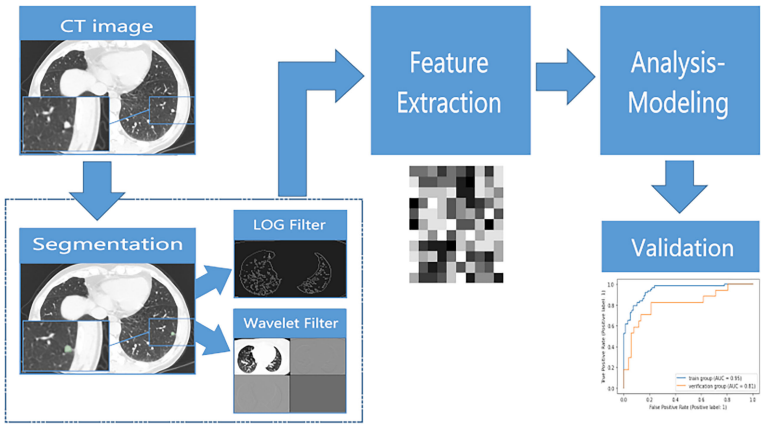

FIGURE 2
The flow chart of radiomic feature extraction and model building.

algorithm of the least absolute shrinkage and selection operator (LASSO) method was used to select the features with a nonzero coefficient. In step three, the coefficients of the features from step two were computed using multivariate logistic regression analysis. In step four, the radscore was constructed by linearly combining the coefficients of the features from the third step.

The support vector machine (SVM), random forest (RF), adaptive boosting (Adaboost), and multilayer perceptron (MLP) machine learning algorithms were used to train the model. The algorithm deployment procedure was assessed by stratified 10-fold cross-validation in the training group, which tested each model ten times to maximize the use of data and promote the accuracy of the models (23). The grid search was used to optimize the parameters of the models. The ROC areas under the receiver operating characteristic curve (AUC) and accuracy were calculated to assess the differential ability of the models. The ML algorithms were all programmed using the Python (version 3.8) machine-learning library known as scikit-learn (version 1.1) (24).

A simple threshold screening model was constructed and was compared with the method using nodule size as a basis for the follow-up in the guidelines. The length of the nodule along the X, Y and Z axes was used to calculate the average nodule length, and the average length was used as a screening index. ROC curves were calculated under SPSS using average length. The 1-specificity and sensitivity of different lengths were calculated, and then the Jorden index was calculated to find diagnostic thresholds. The average length of 6 mm from the literature (9) was also used as the threshold for predicting nodular growth. Statistical Analysis

Statistical analyses were performed using IBM SPSS Statistics 25.0. A two-sided p value < 0.05 was considered to indicate a statistically significant difference. The approximate t test was used for the intergroup comparison of continuous variables after the homogeneity test of variance. The chi-square test was used for the intergroup comparison of categorical variables. To meet the requirements of the chi-square test (R*C), the number of nodules in the left inferior lobe anterior basal segment was merged with the posterior basal segment, and the number of nodules in the right inferior lobe anterior basal segment, medial basal segment and posterior basal segment were merged. The radiomics features between the two observers were assessed for reproducibility with intraclass correlation coefficients.

Results

Clinical characteristics of the patients

A total of 228 nodules were finally included in the study. Eighty nodules grew in one year (growth group), and 148 nodules remained stable (stable group). The clinical characteristics of the patients in the two groups are listed in Table 1. The age of the stable group was 52.56 ± 12.14 and that of the growth group was 58.41 ± 14.02. An approximate t test was performed on age, as the square difference between the two groups was even (Levene's Test F value =2.337 at p value = 0.128). There was a significant difference in age between the two groups (t value =-2.26, p value =0.025, 95% confidence interval (CI): -9.172~-2.522), and the age of the growth group was older than that of the stable group (Supplementary Figure 1). The sex ratios were 83:98 and 41:56 (male:female) for the stable and growth groups, respectively. There was no statistically significant difference between the two groups ($\chi 2$ = 0.329 at p value = 0.566, Supplementary Figure 2). The diameters of the nodules in the stable group and the growing group were 5.56 ± 1.19 mm and 7.82 ± 2.58 mm, respectively, showing a significant difference in the T test (t = -9.042 at p value < 0.001, 95% CI -2.75 ~ -1.77, Supplementary Figures 3–5). The chi-

10.3389/fonc.2022.1034817

TABLE 1 Clinical characteristics of the patients in the training and validation cohort.

Characteristics	Growth (n = 80)	Stable (n = 148)	F value (t/χ^2)	P value
Sexy			0.055	0.815[a]
Male	36	69		
Female	44	79		
Age	56.75 (13.832)	52.73 (12.241)	-2.26	0.025
Diameter(mm)				< 0.001
Mean ± SD	7.82 ± 2.58	5.56 ± 1.19		
Median	7.23	5.51		
Range	3.87-17.11	3.25-9.08		
Nodule Position			16.157	0.502[a]
LS1+2	11	15		
LS3	4	1		
LS4	0	5		
LS5	1	5		
LS6	7	7		
LS7+8	3	10		
LS9	5	11		
LS10	3	2		
RS1	10	27		
RS2	10	10		
RS3	5	10		
RS4	4	7		
RS5	2	4		
RS6	6	12		
RS7	0	1		
RS8	2	9		
RS9	5	9		
RS10	2	4		
Nodule Type				Not analysis
Solid	24	47		
PS	10	4		
PGG	46	97		
Morphology				Not analysis
Smooth	53	109		
Lobulated	15	29		
Spiculated	12	10		

Quantitative variables are expressed as the mean ± standard deviation. Qualitative variables are expressed as proportion. [a]Chi-square test was used for gender and nodule position analysis. LS1+2, Left superior lobe Apical posterior segment; LS3, Left superior lobe Anterior segment; LS4, Left superior lobe Superior lingula segment; LS 5, Left superior lobe Inferior lingula segment; LS6, Left inferior lobe Superior segment; LS7+8, Left inferior lobe Anterior basal segment; LS9, Left inferior lobe Lateral basal segment; LS10, Left inferior lobe Posterior basal segment;RS1, Right superior lobe Apical segment; RS2, Right superior lobe posterior segment; RS3, Right superior lobe Anterior segment; RS4, Right middle lobe Lateral segment; RS5, Right middle lobe Medial segment; RS6, Right inferior lobe Superior segment; RS7, Right inferior lobe Medial segment; RS8, Right inferior lobe Anterior segment; RS9, Right inferior lobe Lateral segment; RS 10,Right inferior lobe Posterior segment; PS, Partly solid; PGG, Purely ground glass.

square test showed no significant difference in nodule location between the two groups ($\chi 2 = 13.294$ at p value = 0.425).

Characteristics of the radiomics parameters

A total of 1316 features were extracted from each nodule. A total of 107 features were extracted from the original image, 465 features were extracted from the LOG filtered image, and 744 features were extracted from the wavelet filtered image. With the least absolute shrinkage and selection operator (LASSO), ten features were selected to form a radiomics signature for predicting the growth of nodules. The ten selected features with their contribution coefficients are shown in Figure 3. They included two shape-based features, one gray-level-cooccurrence-matrix (GLCM), one first-order feature, one gray-level-run-length-matrix (GLRLM), three gray-level-dependence-matrix (GLDM) and two gray-level-size-zone-matrix (GLSZM).

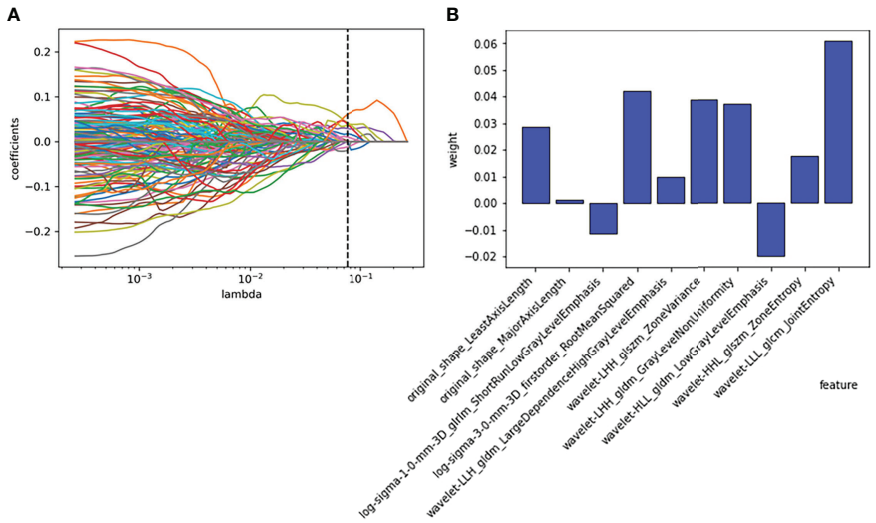

FIGURE 3
Employing the least absolute shrinkage and selection operator (LASSO) algorithm to reduce the redundancy feature. **(A)** Regression coefficient diagram of LASSO. **(B)** Features selected and their weight.

Linear prediction model

The ten radiomics features selected by LASSO and the clinical signature (age) were combined to establish a classification model by logistic regression. The AUC and accuracy attained by the combined model on the training group and validation group were 0.87 (95% CI: 0.74–0.98), 0.82, 0.82 (95% CI: 0.68–0.95) and 0.84, respectively (Figure 4B). The relationship between the predicted value and the true value is shown in the line chart in the Supplementary Materials (Supplementary Figure 6). The established logistics classification formulation is stated in the Supplementary Material, and the nomogram is described in Figure 5.

While using the nodule diameter line length as the screening threshold, in the training group, the diagnostic threshold for mean length was 6.3 mm (sensitivity: 0.778, specificity: 0.771, AUC: 0.81). With 6.3 mm as the threshold, the accuracy and AUC in the validation group were 0.754 and 0.777, respectively, but when 6 mm was used as the threshold to predict growth in all 278 patients, the accuracy and AUC were 0.705 and 0.728, respectively (Figure 4A).

Nonlinear prediction models

In this study, four nonlinear methods were trained to predict the growth of the nodules, including support vector machine (SVM), random forest (RF), adaptive boosting (Adaboost), and multilayer perceptron (MLP). The ROC curves of the four nonlinear models in the training group and validation group are shown in Figure 4, and the classification reports of these models are listed in Table 2.

In the training group, the AUC of the SVM model was 0.95 (95% CI: 0.82-0.99, Figure 6A), the accuracy rate was 0.86, the AUC of the RF model was 1.00 (95% CI: 0.76-1.0, Figure 6B), the accuracy rate was 0.99, the AUC of the MLP model was 1.00 (95% CI: 1.00: 0.79-1.0, Figure 6C), and the accuracy was 1.00. The AUC of the Adaboost model was 1.00 (95% CI: 0.84-1.0, Figure 6D), and the accuracy was 1.00. In the validation group, the AUC of the SVM model was 0.81 (95% CI: 0.64-0.89, Figure 6A), the accuracy rate was 0.81, the AUC of the RF model was 0.77 (95% CI: 0.660-0.83, Figure 6B), the accuracy rate was 0.74, and the AUC of the MLP model was 0.81 (95% CI: 0.69-0.92, Figure 6C). The AUC of the Adaboost model was 0.71 (95% CI: 0.62-0.76, Figure 6D), and the accuracy was 0.78.

Discussion

Pulmonary nodules are very common, and it is difficult to accurately predict their growth. Tumor growth kinetics (TGK) have usually been used for the prediction of tumor growth in the past. It is generally considered to have three well-defined phases: the first (lagged phase) is associated with tumor establishment in the host; the second stage (log or exponential) is associated with rapid tumor growth; and the third stage (stationary phase) shows slow growth of the tumor and gradual convergence to the final volume (25). To describe tumor growth, the exponential growth model (26), linear growth model and Gompertzian growth model (27) have been proposed. These models require pathological data of tumors, such as cell lines, cell surface

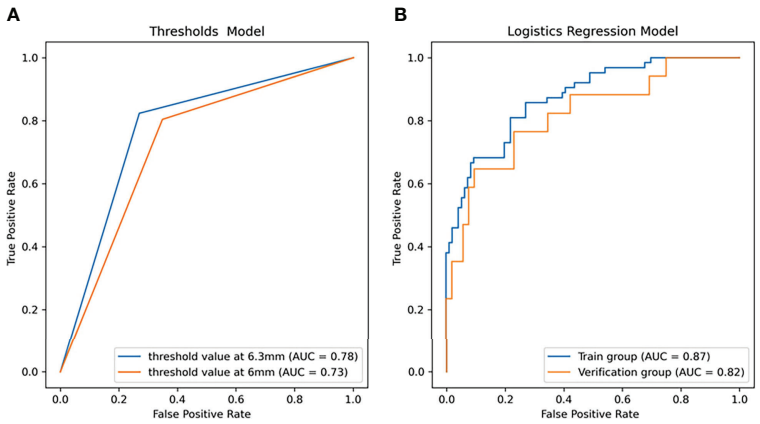

FIGURE 4
The receiver operator characteristic (ROC) curves of the linear models for predicting the growth of the nodules within one year. **(A)** ROC curve of the threshold prediction model (area under the ROC curve (AUC) = 0.73 as threshold at 6 mm, AUC = 0.77 as threshold at 6.3 mm). **(B)** ROC curve of logistic regression (LR) (AUC = 0.87 in the training group, AUC =0.82 in the validation group).

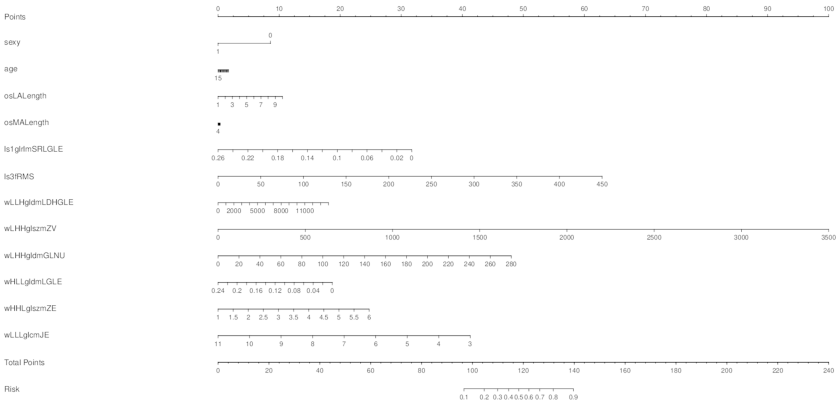

FIGURE 5
A nomogram was made to predict the one-year growth of single pulmonary nodules.

diffusion, and cell proliferation, which cannot be obtained before surgery.

In clinical practice, CT follow-up is of great clinical significance to help manage pulmonary nodules without pathological information. The Fleischner Society of the United States, the American College of Chest Physicians, the British Thoracic Society, and the American College of Radiology have published their guidelines for the management of nodules based on CT findings to help physicians develop an effective follow-up protocol. However, even among the most widely applied Fleischner guidelines, there was considerable heterogeneity in the choice of nodule treatment in clinical practice (8). Additionally, the CT findings adopted by these guidelines were gross morphology, which was limited in information. Previous studies have shown that radiomics features can be used to analyze the biological and pathophysiological information of lung cancer and provide rapid and accurate noninvasive biomarkers for its diagnosis, prognosis and treatment response monitoring (28). This study was the first to use radiomics tools to predict single pulmonary nodule growth within one year. The results showed that our model performs well in both the training group and the validation group. This model could help to develop a follow-up plan for uncertain pulmonary nodules and reduce the over treatment of nodules in clinical practice.

In this study, five different machine learning methods were used to develop prediction models of whether pulmonary nodules would increase within one year. In general, the growth of nodules was related to gender, adhesion, location, size, and characteristics of nodules (29). The size and characteristics (such as solid, subsolid, ground glass, and spiculated) in the guidelines were gross changes,

TABLE 2 The classification report of the different models on the validation group.

Model	Precision	Recall	F1-score	Accuracy
Logistic Regression				0.84
Stable	0.89	0.90	0.90	
Growth	0.69	0.65	0.67	
SVM				0.81
Stable	0.88	0.87	0.87	
Growth	0.61	0.65	0.63	
MLP				0.68
Stable	0.88	0.67	0.76	
Growth	0.41	0.71	0.52	
RF				0.74
Stable	0.84	0.81	0.82	
Growth	0.47	0.53	0.50	
Adaboost				0.78
Stable	0.88	0.83	0.85	
Growth	0.55	0.65	0.59	

The precision, recall, F1-score of the logistic regression, SVM, MLP and Adaboost model in the validation group. SVM, Support vector machine; RF, Random Forest; MLP, Multilayer perceptron.

and high-throughput radiomics features could decompose these features into more detailed texture features to determine more nuanced information. These features included size and shape-based features, first-order features of the image gray histogram, second-order features of image voxel relations, such as gray-level cooccurrence matrix (GLCM), run length matrix (RLM), size zone matrix (SZM) and neighborhood gray tone difference matrix (NGTDM), texture features extracted by wavelet and Gaussian Laplacian filter, etc. (22). These high-dimensional data contained information reflecting the underlying pathophysiology (30), which can be revealed by quantitative image analysis (31, 32). In this study, the 1316 radiomics features extracted from the CT images were reduced to ten features with the LASSO algorithm. The ten features and their weights are shown in Figure 3B. Among them, the morphological features LeastAxisLength and MajorAxisLength reflected the nodule size, which corresponded to the nodule diameter adopted in the guidelines (5–7, 9). In a previous study of portal phase expansive versus infiltrative tumor growth front, wavelet_LHH_glrlm_ShortRun-LowGrayLevelEmphasis was considered to be the best predictor of tumor growth (33, 34). The pathological association of textural features derived from gray-level cooccurrence matrices (GLCMs) has been proven and applied to the diagnosis of breast cancer (35). The GLSZM and GLDM features could reflect tumor heterogeneity and homogeneity (36).

Generally, age, sex and nodule location are related to whether a nodule is benign or malignant (7, 9, 37), but whether these factors could predict the growth of a nodule within one year is unclear. In this study, the average age of the patients with enlarged nodules was older than that of the patients with stable nodules at the 1-year follow-up, and the difference was statistically significant. These results indicated that age was an independent predictor of nodule growth (38). There was no significant difference in sex or nodule location between the two groups. This finding was inconsistent with literature reports that women and nodules in the upper lobe of the right lung were risk factors for lung cancer (39). A possible reason was that this study focused on nodular growth rather than benign or malignant nodules, and the growth curves of benign and malignant nodules partially overlapped (40).

In this study, the logistic regression model has the best AUC and accuracy compared to the SVM, RF, MLP and AdaBoost models. It can help doctors predict whether the nodules will grow after one year and has important clinical significance. In previous studies, logistic regression models have been used to predict the malignant degree of solitary pulmonary nodules (41), showing good predictive performance. The nonlinear ML algorithm can deal with multidimensional features and identify some underlying patterns from data that are not linear or polynomial. Previously, Jiang Yuming et al. found that an SVM model can predict the survival rate of gastric cancer patients (42). Mitra Montazeri found that the random forest model is a useful tool for survival prediction and medical decision-making of breast cancer (43). QZ et al. successfully used the AdaBoost model to predict local prostate cancer recurrence (44). MLP models have also been used to predict mortality in elderly patients with hip fractures (45). In this study, the LR model obtained the best AUC and F1 scores in the validation group among the five models, so it was selected to construct the prediction formula and nomogram. The SVM, RF, MLP and AdaBoost models had high AUC and accuracy in the training group but showed low performance in the validation group. Therefore, overfitting may exist and could affect the generalization of the model. According to previous studies, the more complex the model is, the overfit is more likely, the more

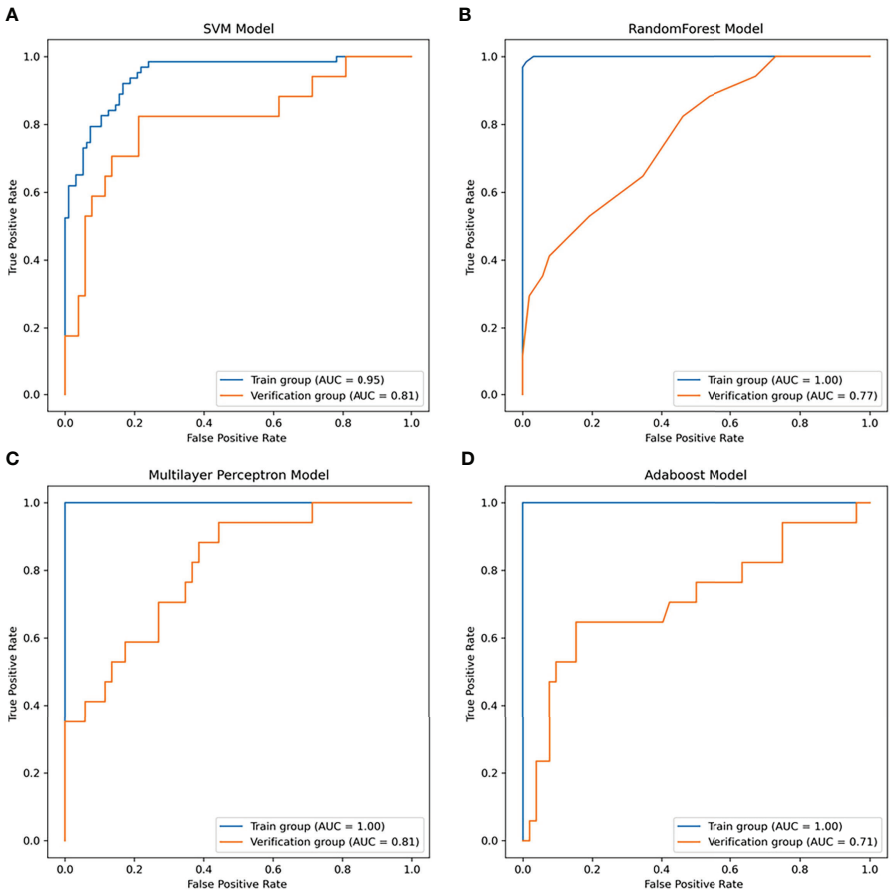

FIGURE 6
The receiver operator characteristic (ROC) curves of the nonlinear models for predicting the growth of the nodules within one year. **(A)** ROC curve of the SVM model (area under the ROC curve (AUC) = 0.95 in the training group, AUC =0.81 in the validation group). **(B)** ROC curve of the random forest (RF) model (AUC = 1.0 in the training group, AUC =0.77 in the validation group). **(C)** ROC curve of the multilayer perceptron (MLP) model (AUC = 1.0 in the training group, AUC =0.81 in the validation group). **(D)** ROC curve of the Adaboost model (AUC = 1.0 in the training group, AUC =0.71 in the validation group).

parameters need to be adjusted, and more samples are needed to learn (46). Therefore, in this study, these models performed worse than the LR models.

In conclusion, in this study, we found that the logistical regression model combining high-resolution CT-derived radiomics and age could accurately predict whether a lung nodule will increase after one year. It has great potential clinical value in helping clinicians develop diagnostic and treatment strategies.

The study has several limitations. First, the sample size was relatively small due to the strict inclusion/exclusion criteria, nearly one-third of the patients were lost to follow-up, and there may have been a potential selection bias. Second, patients with multiple nodules were not included in the analysis. Third, in the model construction, only the imaging features of high-resolution CT plain scans were used, and other imaging data were not considered. In the future, more patients need to be followed up to verify the validity of the model, and different imaging technologies, such as CT enhancement and MRI, should be combined to further improve the prediction efficiency of the model.

Data availability statement

The original contributions presented in the study are included in the article/Supplementary Material. Further inquiries can be directed to the corresponding authors.

Ethics statement

The studies involving human participants were reviewed and approved by the ethic committee of the second people's hospital of JiuLongPo district and the Chongqing western hospital.

Written informed consent to participate in this study was provided by the participants' legal guardian/next of kin.

Author contributions

RY, DH, XL and KW collected the relevant data, and RY and ZL analyzed the data. DH, and ZL wrote this manuscript. ZL put forward the study topic and revised the manuscript. All authors read and approved this manuscript.

Funding

This study was supported by grants from the Science and Health Joint Medicine research project of Chongqing (including traditional Chinese medicine) (grant number 2022MSXM140).

Acknowledgments

The authors thank Siemens Healthcare, Philips Healthcare, and Canon Medical for their kind support.

Conflict of interest

The authors declare that the research was conducted in the absence of any commercial or financial relationships that could be construed as a potential conflict of interest.

Publisher's note

Supplementary material

The Supplementary Material for this article can be found online at: https://www.frontiersin.org/articles/10.3389/fonc.2022.1034817/full#supplementary-material

References

1. Hansell DM, Bankier AA, MacMahon H, McLoud TC, Muller NL, Remy J. Fleischner society: glossary of terms for thoracic imaging. *Radiology* (2008) 246 (3):697–722. doi: 10.1148/radiol.2462070712

2. Osarogiagbon RU, Miller EA, Faris N, Pinsky PF. Incidental pulmonary nodules, lung cancer screening, and lung cancer in the Medicare population. *J Clin Oncol* (2022) 40(16_suppl):6536–. doi: 10.1200/JCO.2022.40.16_suppl.6536

3. Organization WH. *Cancer 2022* . Available at: https://www.who.int/news-room/fact-sheets/detail/cancer.

4. Henschke C, McCauley D, Yankelevitz DP, Naidich D, McGuinness G, Miettinen OS, et al. Early lung cancer action project: Overall design and findings from baseline screening. *Lancet* (1999) 354(9173):99–105. doi: 10.1016/S0140-6736(99)06093-6

5. Gould MK, Donington J, Lynch WR, Mazzone PJ, Midthun DE, Naidich DP, et al. Evaluation of individuals with pulmonary nodules: When is it lung cancer? diagnosis and management of lung cancer, 3rd ed: American college of chest physicians evidence-based clinical practice guidelines. *Chest* (2013) 143(5 Suppl): e93S–e120S. doi: 10.1378/chest.12-2351

6. Callister ME, Baldwin DR, Akram AR, Barnard S, Cane P, Draffan J, et al. British Thoracic society guidelines for the investigation and management of pulmonary nodules. *Thorax* (2015) 70(8):794–8. doi: 10.1136/thoraxjnl-2015-207168

7. Macmahon H. Guidelines for management of small pulmonary nodules detected on CT scans : a statement from the fleischner society. *Radiology* (2005) 237(2):395–400. doi: 10.1148/radiol.2372041887

8. Mets OM, de Jong PA, Chung K, Lammers JJ, van Ginneken B, Schaefer-Prokop CM, et al. Fleischner recommendations for the management of subsolid pulmonary nodules: High awareness but limited conformance - a survey study. *Eur Radiol* (2016) 26(11):3840–9. doi: 10.1007/s00330-016-4249-y

9. Macmahon H, Naidich DP, Goo JM, Lee KS, Leung A, Mayo JR, et al. Guidelines for management of incidental pulmonary nodules detected on CT images: From the fleischner society 2017. *Radiology* (2017) 284(1):228–43. doi: 10.1148/radiol.2017161659

10. McKee BJ, Regis SM, McKee AB, Flacke S, Wald C. Performance of ACR lung-RADS in a clinical CT lung screening program. *J Am Coll Radiol Jacr* (2015) 12(3):273–6. doi: 10.1016/j.jacr.2014.08.004

11. Lambin P, Rios-Velazquez E, Leijenaar R, Carvalho S, van Stiphout RG, Granton P, et al. Radiomics: Extracting more information from medical images using advanced feature analysis. *Eur J Cancer* (2012) 48(4):441–6. doi: 10.1016/j.ejca.2011.11.036

12. Wong AJ, Kanwar A, Mohamed AS, Fuller CD. Radiomics in head and neck cancer: From exploration to application. *Trans Cancer Res* (2016) 5(4):371–82. doi: 10.21037/tcr.2016.07.18

13. Cameron A, Khalvati F, Haider M, Wong A. MAPS: A quantitative radiomics approach for prostate cancer detection. *IEEE Trans Biomed Eng* (2015) 63(6):1–. doi: 10.1109/TBME.2015.2485779

14. Li H, Zhu Y, Burnside ES, Huang E, Drukker K, Hoadley KA, et al. Quantitative MRI radiomics in the prediction of molecular classifications of breast cancer subtypes in the TCGA/TCIA data set. *NPJ Breast Cancer.* (2016) 2:16012. doi: 10.1038/npjbcancer.2016.12

15. Nie K, Shi L, Chen Q, Hu X, Jabbour SK, Yue N, et al. Rectal cancer: Assessment of neoadjuvant chemoradiation outcome based on radiomics of multiparametric MRI. *Clin Cancer Res* (2016) 22(21):5256–64. doi: 10.1158/1078-0432.CCR-15-2997

16. Tu W-T, Fan L, Liu S-Y. Progress on research of radiomics in lung cancer. *Chin J Cancer Prev Treat* (2018) 25(8):604–8.Available at: https://www.researchgate.net/publication/330886520_Progress_on_research_of_radiomics_in_lung_cancer.

17. Kalpathy-Cramer J, Mamomov A, Zhao B, Lu L, Cherezov D, Napel S, et al. Radiomics of lung nodules: A multi-institutional study of robustness and agreement of quantitative imaging features. *Tomography J Imaging Res* (2016). doi: 10.18383/j.tom.2016.00235

18. Yu J, Deng Y, Liu T, Zhou J, Jia X, Xiao T, et al. Lymph node metastasis prediction of papillary thyroid carcinoma based on transfer learning radiomics. *Nat Commun* (2020) 11(1):4807. doi: 10.1038/s41467-020-18497-3

19. Bankier AA, Macmahon H, Goo JM, Rubin GD, Schaefer-Prokop CM, Naidich DP. Recommendations for measuring pulmonary nodules at CT: A statement from the fleischner society. *Radiology* (2017) 285(2):584–600. doi: 10.1148/radiol.2017162894

20. Fedorov A, Beichel R, Kalpathy-Cramer J, Finet J, Fillion-Robin JC, Pujol S, et al. 3D slicer as an image computing platform for the quantitative imaging network. *Magn Reson Imaging.* (2012) 30(9):1323–41. doi: 10.1016/j.mri.2012.05.001

21. van Griethuysen JJM, Fedorov A, Parmar C, Hosny A, Aucoin N, Narayan V, et al. Computational radiomics system to decode the radiographic phenotype. *Cancer Res* (2017) 77(21):e104–e7. doi: 10.1158/0008-5472.CAN-17-0339

22. Zwanenburg A, Vallieres M, Abdalah MA, Aerts H, Andrearczyk V, Apte A, et al. The image biomarker standardization initiative: Standardized quantitative radiomics for high-throughput image-based phenotyping. *Radiology* (2020) 295 (2):328–38. doi: 10.1148/radiol.2020191145

23. Molinaro A, Simon R, Pfeiffer R. Prediction error estimation: A comparison of resampling methods. *Bioinformatics* (2005) 21(15):3301–7. doi: 10.1093/bioinformatics/bti499

24. Pedregosa F, Varoquaux G, Gramfort A, Michel V, Thirion B, Grisel O, et al. Scikit-learn: Machine learning in Python. *J Mach Learn Res* (2011) 12(85):2825–30. Available at: http://jmlr.org/papers/v12/pedregosa11a.html.

25. González M, Joa J, Cabrales L, Pupo A, González GVS. Is cancer a pure growth curve or does it follow a kinetics of dynamical structural transformation? *BMC Cancer* (2017) 17(1):174. doi: 10.1186/s12885-017-3159-y

26. Shackney SE. Tumor growth, cell cycle kinetics, and cancer treatment. *Med Oncol* (1993), 43–60.

27. Brú A, Albertos S, Luis Subiza J, García-Asenjo JL, Brú I. The universal dynamics of tumor growth. *Biophys J* (2003) 85(5):2948–61. doi: 10.1016/S0006-3495(03)74715-8

28. Tunali I, Gillies RJ, Schabath MB. Application of radiomics and artificial intelligence for lung cancer precision medicine. *Cold Spring Harb Perspect Med* (2021) 11(8):a039537. doi: 10.1101/cshperspect.a039537

29. Mazzone PJ, Lam L. Evaluating the patient with a pulmonary nodule: A review. *Jama* (2022) 327(3):264–73. doi: 10.1001/jama.2021.24287

30. Kotrotsou A, Zinn PO, Colen RR. Radiomics in brain tumors: An emerging technique for characterization of tumor environment. *Magn Reson Imaging Clin N Am* (2016) 24(4):719–29. doi: 10.1016/j.mric.2016.06.006

31. Yang L, Gu D, Wei J, Yang C, Rao S, Wang W, et al. A radiomics nomogram for preoperative prediction of microvascular invasion in hepatocellular carcinoma. *Liver Cancer*. (2019) 8(5):373–86. doi: 10.1159/000494099

32. Schniering J, Maciukiewicz M, Gabrys HS, Brunner M, Blüthgen C, Meier C, et al. Computed tomography-based radiomics decodes prognostic and molecular differences in interstitial lung disease related to systemic sclerosis. *Eur Respir J* (2022) 59(5):2004503. doi: 10.1183/13993003.04503-2020

33. Granata V, Fusco R, De Muzio F, Cutolo C, Setola SV, Dell' Aversana F, et al. Contrast MR-based radiomics and machine learning analysis to assess clinical outcomes following liver resection in colorectal liver metastases: A preliminary study. *Cancers (Basel)* (2022) 14(5):1110. doi: 10.3390/cancers14051110

34. Granata V, Fusco R, De Muzio F, Cutolo C, Mattace Raso M, Gabelloni M, et al. Radiomics and machine learning analysis based on magnetic resonance imaging in the assessment of colorectal liver metastases growth pattern. *Diagnostics (Basel)* (2022) 12(5):1115. doi: 10.3390/diagnostics12051115

35. Li X, Guindani M, Ng CS, Hobbs BP. Spatial Bayesian modeling of GLCM with application to malignant lesion characterization. *J Appl Stat* (2018) 46(2):230–46. doi: 10.1080/02664763.2018.1473348

36. Mayerhoefer ME, Materka A, Langs G, Häggström I, Szczypiński P, Gibbs P, et al. Introduction to radiomics. *J Nucl Med* (2020) 61(4):488–95. doi: 10.2967/jnumed.118.222893

37. Naidich DP, Bankier AA, Macmahon H, Schaefer-Prokop CM, Pistolesi M, Goo JM, et al. Recommendations for the management of subsolid pulmonary nodules detected at CT: A statement from the fleischner society. *Radiology* (2013) 266(1):304–17. doi: 10.1148/radiol.12120628

38. Xia T, Cai M, Zhuang Y, Ji X, Fu G. Risk factors for the growth of residual nodule in surgical patients with adenocarcinoma presenting as multifocal ground-glass nodules. *Eur J Radiology*. (2020) 133(5):109332. doi: 10.1016/j.ejrad.2020.109332

39. Cruickshank A, Stieler G, Ameer F. Evaluation of the solitary pulmonary nodule. *Internal Med J* (2019) 49(3):306–15. doi: 10.1111/imj.14219

40. Wang X, Han R, Guo F, Li X, Zheng W, Wang Q, et al. Analysis of growth curve type in pulmonary nodules with Different characteristics. *Zhongguo Fei Ai Za Zhi.* (2017) 20(5):334–40. doi: 10.3779/j.issn.1009-3419.2017.05.06

41. Valero MS, Pastor-Valero M, Librero J. Solitary pulmonary nodule malignancy predictive models applicable to routine clinical practice: A systematic review. *Systematic Rev* (2021) 10(1):308. doi: 10.1186/s13643-021-01856-6

42. Jiang Y, Xie J, Huang W, Chen H, Xi S, Han Z, et al. Tumor immune microenvironment and chemosensitivity signature for predicting response to chemotherapy in gastric cancer. *Cancer Immunol Res* (2019) 7(12):2065–73. doi: 10.1158/2326-6066.CIR-19-0311

43. Montazeri M, Montazeri M, Montazeri M, Beigzadeh A. Machine learning models in breast cancer survival prediction. *Technol Health Care* (2016) 24(1):31–42. doi: 10.3233/THC-151071

44. Zhong QZ, Long LH, Liu A, Li CM, Xiu X, Hou XY, et al. Radiomics of multiparametric MRI to predict biochemical recurrence of localized prostate cancer after radiation therapy. *Front Oncol* (2020) 10:731. doi: 10.3389/fonc.2020.00731

45. Cary MPJr., Zhuang F, Draelos RL, Pan W, Amarasekara S, Douthit BJ, et al. Machine learning algorithms to predict mortality and allocate palliative care for older patients with hip fracture. *J Am Med Dir Assoc* (2021) 22(2):291–6. doi: 10.1016/j.jamda.2020.09.025

46. Ying X. An overview of overfitting and its solutions. *J physics: Conf Ser* (2019) 1168(2):022. doi: 10.1088/1742-6596/1168/2/022022

frontiers | Frontiers in Oncology

TYPE Original Research
PUBLISHED 01 November 2022
DOI 10.3389/fonc.2022.1034519

OPEN ACCESS

EDITED BY
Chuanming Li,
Chongqing University Central Hospital, China

REVIEWED BY
Zhichao Li,
Chongqing Western Hospital, China
Chao Li,
Eastern Hepatobiliary Surgery Hospital, China

*CORRESPONDENCE
Gang Wang
wanggang@qdu.edu.cn

SPECIALTY SECTION
This article was submitted to Cancer Imaging and Image-directed Interventions, a section of the journal Frontiers in Oncology

RECEIVED 01 September 2022
ACCEPTED 17 October 2022
PUBLISHED 01 November 2022

CITATION
Zhang S, Duan C, Zhou X, Liu F, Wang X, Shao Q, Gao Y, Duan F, Zhao R and Wang G (2022) Radiomics nomogram for prediction of microvascular invasion in hepatocellular carcinoma based on MR imaging with Gd-EOB-DTPA. *Front. Oncol.* 12:1034519. doi: 10.3389/fonc.2022.1034519

Radiomics nomogram for prediction of microvascular invasion in hepatocellular carcinoma based on MR imaging with Gd-EOB-DTPA

Shuai Zhang[1], Chongfeng Duan[1], Xiaoming Zhou[1], Fang Liu[1], Xin Wang[1], Qiulin Shao[1], Yuanxiang Gao[1], Feng Duan[1], Ruirui Zhao[2] and Gang Wang[1]*

[1]Department of Radiology, The Affiliated Hospital of Qingdao University, Qingdao, China, [2]Operating Room, The Affiliated Hospital of Qingdao University, Qingdao, China

Objective: To develop a radiomics nomogram for predicting microvascular invasion (MVI) before surgery in hepatocellular carcinoma (HCC) patients.

Materials and Methods: The data from a total of 189 HCC patients (training cohort: n = 141; validation cohort: n = 48) were collected, involving the clinical data and imaging characteristics. Radiomics features of all patients were extracted from hepatobiliary phase (HBP) in 15 min. Least absolute shrinkage selection operator (LASSO) regression and logistic regression were utilized to reduce data dimensions, feature selection, and to construct a radiomics signature. Clinicoradiological factors were identified according to the univariate and multivariate analyses, which were incorporated into the final predicted nomogram. A nomogram was developed to predict MVI of HCC by combining radiomics signatures and clinicoradiological factors. Radiomics nomograms were evaluated for their discrimination capability, calibration, and clinical usefulness.

Results: In the clinicoradiological factors, gender, alpha-fetoprotein (AFP) level, tumor shape and halo sign served as the independent risk factors of MVI, with which the area under the curve (AUC) is 0.802. Radiomics signatures covering 14 features at HBP 15 min can effectively predict MVI in HCC, to construct radiomics signature model, with the AUC of 0.732. In the final nomogram model the clinicoradiological factors and radiomics signatures were integrated, outperforming the clinicoradiological model (AUC 0.884 vs. 0.802; p <0.001) and radiomics signatures model (AUC 0.884 vs. 0.732; p < 0.001) according to

Delong test results. A robust calibration and discrimination were demonstrated in the nomogram model. The results of decision curve analysis (DCA) showed more significantly clinical efficiency of the nomogram model in comparison to the clinicoradiological model and the radiomic signature model.

Conclusions: Depending on the clinicoradiological factors and radiological features on HBP 15 min images, nomograms can effectively predict MVI status in HCC patients.

KEYWORDS

hepatocellular carcinoma, microvascular invasion, radiomics, gadoxetic acid-enhanced mri, nomogram

Introduction

Hepatocellular carcinoma (HCC) is the most prevalent cancer in China, with a high fatality rate (1, 2). Despite the surgical resection adopted as an effective treatment for HCC, recurrences remain common (3), which are experienced by approximately 70% of liver resection patients within five years, and approximately 25% of liver transplant patients (4). The microvascular invasion (MVI) refers to the tumor invasion in small intrahepatic vessels, covering portal veins, hepatic vessels, and lymphatic vessels (5). MVI in HCC is considered a feature of histologically generated case changes, implying the early postoperative recurrence with correspondingly lower survival (6). It is critical to accurately identify MVI in patients with HCC for developing appropriate treatment options. Surgery with wide margins is considered the best option for patients at high risk for MVI (7). However, in contrast to macrovascular invasion that can be detected by diagnostic imaging, MVI can only be diagnosed by pathologic evaluation currently. Thus, a quantitative method urgently required for preoperative prediction of MVI.

It has been demonstrated that by converting medical images into higher quality, quantifiable and mineable data, the radiomic features can serve as the diagnostic and prognostic markers for cancer phenotypes and tumor microenvironments (8, 9). Our previous study (10) has indicated that MVI could be predicted by radioactivity in the hepatobiliary phase (HBP) on Gd-EOB-DTPA magnetic resonance imaging. However, further integration with clinical data and radiological features is required for physicians to accept its full and robust role in patient management. As a direct extension of our previous work, the objective of this study is to predict the state of MVI in HCC patients by creating a nomogram that incorporated the clinicoradiological factors and radiomics signatures.

Materials and methods

Patients

This retrospective study was approved by an institutional review board, with the patient's own informed consent waived. 189 consecutive HCC patients from the period January 2015 to April 2022 were enrolled. The cohort was divided into a training set from January 2015 to May 2020, with 82 MVI+ patients (76 men and 6 women; range, 37-79 years) and 59 MVI- patients (40 men and 19 women; range, 35-77 years) and a validation set from May 2020 to April 2022, with 29 MVI+ patients (25 men and 4 women; range, 38-76 years) and 19 MVI- patients (14 men and 5 women; range, 39-75 years). The inclusion criteria were: (1) Gd-EOB-DTPA-enhanced MRI performed within one month before surgical resection; (2) The postoperative pathological features met the clinical criteria for HCC. The criteria for exclusion were: (1) patients receiving liver cancer-related treatment before surgery; (2) patients with macrovascular invasion on MRI; and (3) insufficient images for radiomic analysis.

MR Techniques

MR imaging was performed on all participants with a 3.0 T scanner (GEHCGEHC, GE medical systems, Waukesha, WI). All patients received the GdEOB-DTPA (Primovist, Bayer HealthCare, Berlin, Germany) with 0.1 mL/kg (0.025 mmol/kg). After 5 minutes, 10 minutes, and 15 minutes (i.e., HBP are the three different time periods mentioned above, respectively) injected with the comparator agent, data on the inhibition of liver production by 3D fat-suppressed Liver Acquisition with Volumetric Acceleration (LAVA, GE Healthcare) sequence in

the axial plane were collected. Contrasts for LAVA sequences include TR/TE, 2.5/1.1; slice spacing, 2.5 mm; thickness, 5 mm; reverse time, 5.0 ms; field of view, 380-450mm; Get the number of characters, 0.70; and the bandwidth, 976.6 kHz.

Clinicoradiological risk factors

The clinical characteristics of the patients were recorded by our hospital's HIS system, including patient age, gender, alpha-fetoprotein (AFP) level, presence of liver cirrhosis, and hepatitis B and C surface antigen (HBsAg) status (positive or negative). The MVI statue was obtained from the pathology report. The imaging, including diameter, halo sign, shape, border, radiocapsule, necrosis, and tumor/liver signal ratio, was carried out based on MRI findings by two radiologists independently through the collection of pictures and communication systems (PACS).

Tumor diameter was defined as the largest diameter imaged by transverse at HBP 15 minutes; Halo sign was defined as a hypointense ring in the center of the lesion on HBP images; Tumor shape was classified as round or non-round, with the ratio of long diameter to short diameter less than 1.2 means round, otherwise, it means not round; Radiological capsule appearance was defined as hyperenhancing structures surrounding the tumor in the portal vein or at extension; tumor/liver signal ratio was expressed as the signal of the tumor/surrounding liver parenchyma on HBP images; necrosis was defined as high T2 and no enhancement in the tumor. To identify the single factor for MVI discrimination, univariate analysis was performed, and significant univariate factors ($P<0.1$) were entered into a multivariate logistic regression mode in the training cohort. $P<0.05$ was regarded as significant in the multivariate analysis.

MR Radiomics analysis

Radiomics analysis mainly refers to tumor segmentation, feature extraction, feature selection, and model building and evaluation. The regions of interest (ROIs) were delineated on HBP 15 min images by IBEX software (http://bit.ly/IBEX). Tumor ROIs were manually segmented covering the whole tumor by two abdominal radiologists blinded to the pathology results (Figure 1). A total of 1768 MR image features of HBP 15 min from the tumor were analyzed using IBEX software. Radiomic parameters were determined depending on IBEX software, obtaining a total of 8 groups of parameters, each with different radiomics. To analyze and examine the reproducibility of the features extracted by repeated sequences, 30 tumor samples were randomly selected for the calculation of the intra-group correlation coefficient (ICC), with the features with ICC<0.80 excluded. The classification of images and the main filtering process were detailed in a previous study (10). The least shrinkage regression analysis and selection operator (LASSO) were adopted to select the most critical parameters obtained within 15 minutes of HBP. The combination of radiological features calculated by the LASSO coefficient weighting method was considered the radiomics score for each patient.

Construction and evaluation of MVI prediction models

After univariate and multivariate logistic regression, the significant variables were selected to establish the clinicoradiological model. Radiomics signature model was built based on selected radiomics features. The nomogram model was constructed combining the clinicoradiological risk factors and

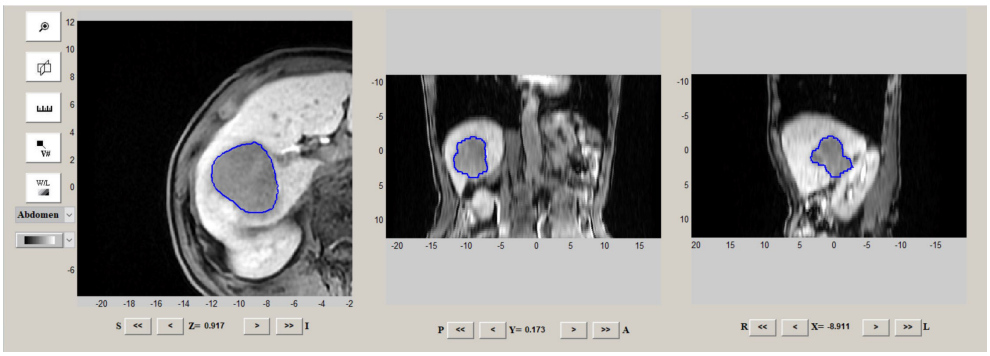

FIGURE 1
Example of ROIs delineation on HBP 15 min images by IBEX software.

radiomics signature. The potential predictive value of the three models was first assessed in the training cohort and then validated in the validation cohort by converted into quantifiable data using the area under the curve (AUC) in the receiver operating characteristic (ROC) curve, with the curves expanded for multiple contrasts by performing the Delong test on Bonferroni-adjusted p-values. AUC with 95% CI, precision, sensitivity and specificity was calculated.

Construction and validation of the radiomics nomogram

The nomogram is calibrated by drawing a calibration curve in the training cohort. The Hosmer-Lemeshow test was carried out to analyze and determine the agreement between the MVI predicted by the nomogram and the actual MVI derived from the calibration curve. Decision curves were plotted to assess the clinical validity of nomogram in the combined training and validation cohorts.

Statistical Analysis

SPSS (version 20, Chicago, IL, USA) and R (https://www.r-project.org/) were utilized as the statistical analysis tool. Only two-tailed in the case of $p<0.05$ was considered statistically significant.

Results

Construction of clinical radiological characteristics and clinical radiological models of patients

The clinicoradiological characteristics of the patients are detailed in Table 1. After univariate and multivariate analysis, it was determined that gender (odds ratio (OR) 6.06; 95% confidence interval (CI) 1.93–18.99), AFP level (OR 3.44; 95% CI 1.33–8.92), halo sign (OR 0.14; 95% CI 0.02–0.92), and shape (OR 0.12; 95% CI 0.05-0.31) can be chosen to construct clinical models.

Radiomics signature calculation

A total of 1768 features were obtained from MR image features on HBP within 15 minutes. 356 radiomic features with most significant difference were then selected from the MVI+ and MVI- groups and introduced into a LASSO logistic regression model to screen out the most contributing features. Finally, 14 features with significant relation to MVI status were chosen for construction of the radiomics signature. Radiomics scores were calculated with the following formulas:

Radiomics score = -0.0144246× MedianAbsoluteDeviation-0.149397×5Percentile+0.00529663×Mass-6.210769×SphericalDisproportion-0.0005163601×4.7AutoCorrelation+0.02526177×1.7Contrast-0.008745637×9.4Contrast-

TABLE 1 Comparisons of clinicoradiological characteristics in MVI (+) and MVI (-) patients.

Clinicoradiological characteristics	MVI (+) (N=82)	MVI (-) (N=59)	Univariate analysis		Multivariate analysis	
			Odd ratios (95%CI)	p	Odd ratios 95%CI)	p
Clinical characteristics						
Age, (Median [range]), year	57[37-79]]	55[35-77]	1 (0.96-1.03)	0.841	–	–
Gender (male/female)	76/6	40/19	6.02 (2.23-16.25)	<0.001	6.06 (1.93-18.99)	0.002
Cirrhosis (present/absent)	81/1	55/4	5.89 (0.64-54.17)	0.117	–	–
HBsAg (positive/negative)	75/7	54/5	0.99 (0.3-3.29)	0.99	–	–
HCsAg (positive/ngative)	4/78	1/58	2.97 (0.32-27.3)	0.335	–	–
AFP (> 400 ng/mL≤ 400 ng/mL)	32/50	10/49	2.98 (1.32-6.72)	0.009	3.44 (1.33-8.92)	0.011
MR imaging features						
Diameter (Median [range]), milimetre	20.95[6-167]	23[3.36-106.7]	1.01 (1-1.02)	0.136	–	–
Halo sign (present/absent)	2/80	6/53	0.22 (0.04-1.13)	0.071	0.14 (0.02-0.92)	0.04
Shape (round/not round)	11/71	31/28	0.14 (0.06-0.32)	<0.001	0.12 (0.05-0.31)	<0.001
Boundary (clear/unclear)	74/8	55/4	0.67 (0.19-2.35)	0.534	–	–
Radiologic capsule (present/absent)	13/69	7/52	1.4 (0.52-3.75)	0.504	–	–
Necrosis (present/absent)	28/54	17/42	1.28 (0.62-2.65)	0.503	–	–
Tumor/liver signal ratio (mean ± SD)	0.5585±0.1659	0.52±0.1581	1.87 (0.23-15.06)	0.555	–	–

P values were obtained from univariate and multivariate regression analyses between the MVI (+) and MVI (-) patients.
AFP alpha-fetoprotein, HBsAg hepatitis B surface antigen status, HCsAg hepatitis C surface antigen status, MVI, microvascular invasion.

1.448129×6.1DifferenceEntropy-0.1107169×4.7Dissimilarity-15.27011×8.4InverseDiffNorm+3.353539×1.1InverseVariance+4.034202×11.4InverseVariance-5.335912×12.4InverseVariance-0.607462×8.4MaxProbability.

Performance of the models

As shown in Table 2 and Figure 2, In the training cohort, the AUC of the clinicoradiological model was 0.802 (95% CI: 0.730-0.875), radiomics signature model was 0.732 (95% CI: 0.650-0.813), and the nomogram model was 0.884 (95% CI: 0.790-0.924), with the Delong test results of the three models listed in Table 2. In the training cohort, the nomogram model was significantly better than the clinicoradiological model and radiomics signature model (P<0.001). In the validation cohort, the radiomics signature model and the nomogram model showed comparable discriminative power (AUC, 0.770 vs. 0.878, P = 0.0990), while the final nomogram model was significantly better than clinicoradiological model (AUC, 0.878 vs. 0.749, P = 0.0428).

Nomogram construction

The nomogram model integrating clinicoradiological factors and radiomic signatures displayed robust predictive performance, so the calculated nomogram was adopted as the prediction graph (Figure 3). Acceptable calibrations of the nomogram are shown in Figure 4. The Hosmer-Lemeshow test suggested no significant difference between the predicted calibration curve and the MVI ideal curve in the training and validation cohorts (P = 0.450, P=0.761, respectively). In Figure 5 the DCA results of the above three models in the training and validation cohorts are depicted. The nomogram model exhibited a larger net benefit in comparison to clinicoradiological model and radiomics signature model.

Discussion

Previous studies indicated that MVI was the most robust independent predictor of recurrence and poor outcome for HCC (11, 12). Surgeons would be able to make better management decisions and improve prognostication if they were aware of MVI status before surgery. If the risk of predicted MVI indicates high, other alternative treatment options, such as the adjuvant therapy performed before surgery, should be considered or liver transplantation may not suitable for the patient (13). But for now, the predictive accuracy of MVI remains difficult, so we attempted to address this problem with radiomics.

Radiomics analysis is currently considered as a potential bridge connecting medical imaging and personalized medicine (14). The quantitative image processing can contribute to effectively evaluating the spatial relationship of pixel intensities (15) with a large role in medical practice and application value (16). As a relatively novel field, radiomics help to deeply mine medical imaging data by applying advanced computational methods, and the collected data can be further converted into quantitative data that can be applied to diagnosing the parameters of cancer, stage, prognosis, predicting treatment response, monitoring disease, etc. (8).

Some recent studies have demonstrated that the combined radiomics features can also play a predictive role in preoperative MVI in HCC patients (17–20). Consistently, we also found the good discrimination shown by radiomics features, as the AUC was 0.732. It is challenging to analyze and interpret the relationship between radiomic features and MVI status, considering more information maximized from radiographic analysis in comparison to visual inspection.

We found that gender can serve as an independent risk factor for MVI, which is obviously distinguished from previous studies (18, 21). The value of gender in predicting MVI in HCC has not been demonstrated, and further research is required. HCC is often associated with a higher level of AFP, which significantly increased in MVI patients. Our final study demonstrated AFP level as an independent risk factor for MVI, which is also consistent with previous conclusions (18,

TABLE 2 Predictive performance of the three models.

	Training cohort				Validation cohort			
	AUC (95%CI)	SEN	SPE	P	AUC (95%CI)	SEN	SPE	P
(1) Clinicoradiological model	0.802(0.730-0.875)	0.627	0.878		0.749(0.601-0.896)	0.409	1.000	
(2) Radiomics signature model	0.732(0.650-0.813)	0.797	0.573		0.770(0.613-0.928)	0.909	0.579	
(3) Radiomics nomogram model	0.884(0.790-0.924)	0.829	0.938		0.878(0.773-0.983)	0.909	0.573	
1 vs. 2				0.1868				0.8624
1 vs. 3				0.0002				0.0428
2 vs. 3				0.0003				0.0990

1 indicates clinicoradiological model; 2 indicates radiomics score model; 3 indicates radiomics nomogram model.
SEN sensitivity, SPE specificity, AUC area under the curve, CI confidence interval.
*P < 0.05 indicates a significant difference.

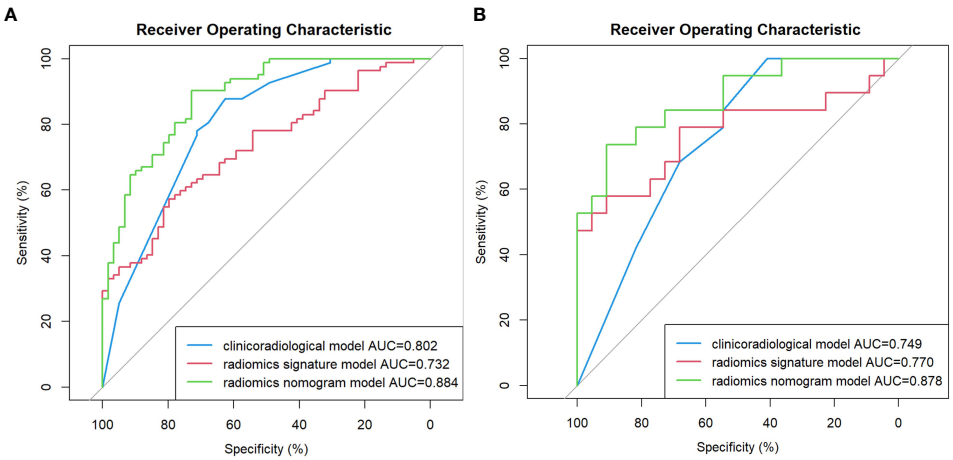

FIGURE 2
Comparison of receiver operating characteristic (ROC) curves for the prediction of microvascular invasion. ROC curves of the clinicoradiological model, the radiomics signature model and the radiomics nomogram model in the training and validation cohort **(A, B)**, respectively.

22). Previous studies have also concluded that larger tumors significantly increased the risk probability of MVI in HCC (23, 24). However, this association was not indicated in our study, probably due to the selection bias. In addition, we found that the absence of halo signs and non-circular MR imaging features are the key predictor of MVI, which is consistent with previous studies (25–27). The results of observation on the pathological data indicated that among the current cases of MVI+ HCC, the most common is the single-nodular type and the multi-nodular type with additional nodular growth or fusion (28), which means the non-round tumor shape is the MR image feature of MVI+ HCC. In our previous study (10), HBP 15 minutes has better radiomic characteristics in comparison to HBP 5 minutes and HBP 10 minutes. In addition, the case collection and analysis were conducted at the same medical center with the same research methods. Therefore, all feature scoring in our study was based exclusively on HBP 15 min images in previous study. Despite the good performance exhibited by radiomic signatures, it remains a gap compared to clinical radiology models (AUC 0.732 vs. 0.802). We further incorporated radiomics signatures into clinicoradiological model to enhance the predictive power. The subsequence radiomic nomograms displayed modified diagnostic performance, suggesting the higher usefulness of combined approach in MVI prediction in comparison to clinical radiology models. This was consistent with previous study (22, 29), also showing that combined radiomics signatures

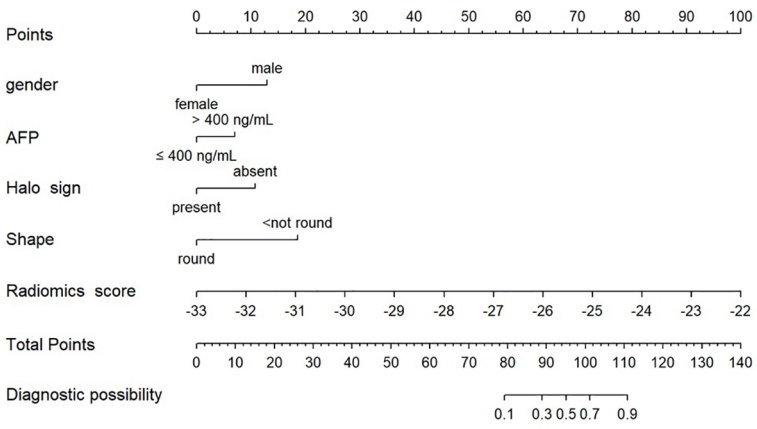

FIGURE 3
Radiomics nomogram combining the radiomics signature derived from HBP 15min MR images and clinicoradiological factors including gender, AFP, halo sign and shape for predicting MVI in the training cohort.

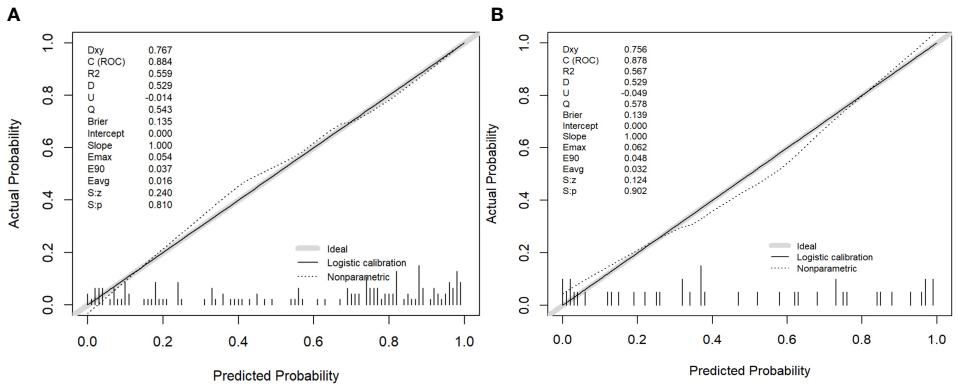

FIGURE 4
The performance of the nomogram was assessed by calibration curves in the training and validation cohort **(A, B)**, respectively. The y-axis represents the actual microvascular invasion (MVI) rate, the x-axis represents the predicted MVI possibility, and the diagonal dashed line indicates the ideal prediction by a perfect model.

and clinicoradiological factors should clearly be preferred over clinical risk factors alone in predicting MVI in HCC. For further comparison of the three models, we applied decision curve analysis, which is used for constructing models capable of assessing clinical outcomes and calculating the loss of gain from the assessment model for each individual, largely compensating for the shortcomings of traditional statistical measures (30). In terms of decision curve analysis, the radiomics nomogram proposed in our study is potentially serving to estimate postoperative outcomes in clinic.

In conclusion, the radiomics nomogram successfully presented in our study possesses significant utility in predicting MVI in HCC. It will contribute to providing an important reference for clinicians to protocol the best treatment plan, thereby improving clinical outcomes.

Limitations

There also exist some limitations in this study. First, this study is a retrospective single-center study, which requires in-depth prospective multicenter validation with a larger cohort. Second, the complex relationship between radiomic signatures and biological behavior fails to be effectively explained.

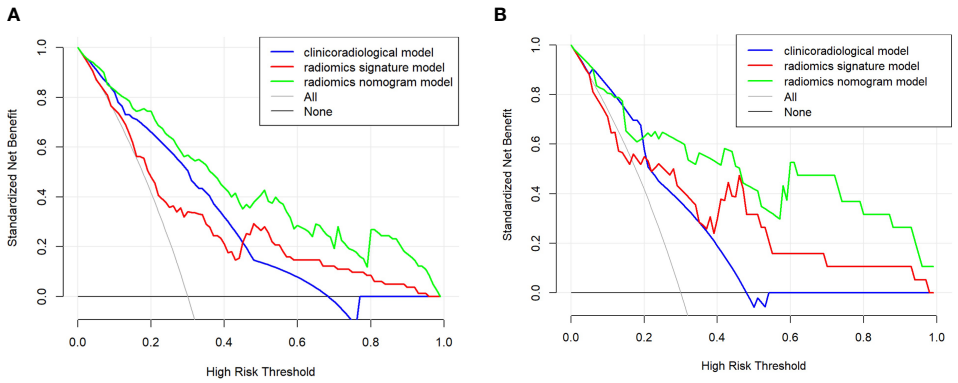

FIGURE 5
The clinical utility of the nomogram was evaluated by decision curves in the training and validation cohort **(A, B)**, respectively. In the decision curves, the black line indicates the net benefit of assuming that there are no patients with microvascular invasion (MVI), and the grey line indicates the net benefit of assuming all patients with MVI. The radiomics nomogram model (green line) provided a greater net benefit than the clinicoradiological model (blue line) and radiomics signature model (red line).

Data availability statement

The original contributions presented in the study are included in the article/supplementary material Further inquiries can be directed to the corresponding author.

Ethics statement

Ethical review and approval was not required for the study on human participants in accordance with the local legislation and institutional requirements. Written informed consent for participation was not required for this study in accordance with the national legislation and the institutional requirements.

Author contributions

SZ and GW completed the initial manuscript and designed the whole study. CD and RZ collected patients and recorded the needed information. FL and XW collected CT texture features. QS and CD helped collected cases and reviewed the manuscript. XZ and YG provide. All authors contributed to the article and approved the submitted version

Funding

This study was funded by the clinical medicine +X scientific research project of the Affiliated Hospital of Qingdao University (QDFY+X202101021).

Conflict of interest

The authors declare that the research was conducted in the absence of any commercial or financial relationships that could be construed as a potential conflict of interest.

Publisher's note

References

1. Ding J, Wang H. Multiple interactive factors in hepatocarcinogenesis. *Cancer Lett* (2014) 346(1):17–23. doi: 10.1016/j.canlet.2013.12.024

2. Chen W, Zheng R, Baade PD, Zhang S, Zeng H, Bray F, et al. Cancer statistics in China, 2015. *CA Cancer J Clin* (2016) 66(2):115–32. doi: 10.3322/caac.21338

3. Poon RT, Fan ST, Lo CM, Liu CL, Wong J. Long-term survival and pattern of recurrence after resection of small hepatocellular carcinoma in patients with preserved liver function: implications for a strategy of salvage transplantation. *Ann Surg* (2002) 235(3):373–82. doi: 10.1097/00000658-200203000-00009

4. Bruix J, Gores GJ, Mazzaferro V. Hepatocellular carcinoma: clinical frontiers and perspectives. *Gut* (2014) 63(5):844–55. doi: 10.1136/gutjnl-2013-306627

5. Gouw AS, Balabaud C, Kusano H, Todo S, Ichida T, Kojiro M. Markers for microvascular invasion in hepatocellular carcinoma: where do we stand? *Liver Transpl* (2011) 17 Suppl 2:S72–80. doi: 10.1002/lt.22368

6. Huang C, Zhu XD, Ji Y, Ding GY, Shi GM, Shen YH, et al. Microvascular invasion has limited clinical values in hepatocellular carcinoma patients at Barcelona clinic liver cancer (BCLC) stages 0 or b. *BMC Cancer* (2017) 17(1):58. doi: 10.1186/s12885-017-3050-x

7. Hirokawa F, Hayashi M, Miyamoto Y, Asakuma M, Shimizu T, Komeda K, et al. Outcomes and predictors of microvascular invasion of solitary hepatocellular carcinoma. *Hepatol Res* (2014) 44(8):846–53. doi: 10.1111/hepr.12196

8. Limkin EJ, Sun R, Dercle L, Zacharaki EI, Robert C, Reuzé S, et al. Promises and challenges for the implementation of computational medical imaging (radiomics) in oncology. *Ann Oncol* (2017) 28(6):1191–206. doi: 10.1093/annonc/mdx034

9. Braman NM, Etesami M, Prasanna P, Dubchuk C, Gilmore H, Tiwari P, et al. Intratumoral and peritumoral radiomics for the pretreatment prediction of pathological complete response to neoadjuvant chemotherapy based on breast DCE-MRI [published correction appears in breast cancer res. *Breast Cancer Res* (2017) 19(1):57. doi: 10.1186/s13058-017-0846-1

10. Zhang S, Xu G, Duan C, Zhou X, Wang X, Yu H, et al. Radiomics analysis of MR imaging with gd-EOB-DTPA for preoperative prediction of microvascular invasion in hepatocellular carcinoma: Investigation and comparison of different hepatobiliary phase delay times. *BioMed Res Int* (2021) 2021:6685723. doi: 10.1155/2021/6685723

11. Roayaie S, Blume IN, Thung SN, Guido M, Fiel MI, Hiotis S, et al. A system of classifying microvascular invasion to predict outcome after resection in patients with hepatocellular carcinoma. *Gastroenterology* (2009) 137(3):850–5. doi: 10.1053/j.gastro.2009.06.003

12. Renzulli M, Buonfiglioli F, Conti F, Brocchi S, Serio I, Foschi FG, et al. Imaging features of microvascular invasion in hepatocellular carcinoma developed after direct-acting antiviral therapy in HCV-related cirrhosis. *Eur Radiol* (2018) 28 (2):506–13. doi: 10.1007/s00330-017-5033-3

13. Omata M, Cheng AL, Kokudo N, Kudo M, Lee JM, Jia J, et al. Asia-Pacific clinical practice guidelines on the management of hepatocellular carcinoma: a 2017 update. *Hepatol Int* (2017) 11(4):317–70. doi: 10.1007/s12072-017-9799-9

14. Gillies RJ, Kinahan PE, Hricak H. Radiomics: Images are more than pictures, they are data. *Radiology* (2016) 278(2):563–77. doi: 10.1148/radiol.2015151169

15. Summers RM. Texture analysis in radiology: Does the emperor have no clothes? *Abdom Radiol (NY)* (2017) 42(2):342–5. doi: 10.1007/s00261-016-0950-1

16. Rao SX, Lambregts DM, Schnerr RS, Beckers RC, Maas M, Albarello F, et al. CT texture analysis in colorectal liver metastases: A better way than size and volume measurements to assess response to chemotherapy? *United Eur Gastroenterol J* (2016) 4(2):257–63. doi: 10.1177/2050640615601603

17. Wang Q, Li C, Zhang J, Hu X, Fan Y, Ma K, et al. Radiomics models for predicting microvascular invasion in hepatocellular carcinoma: A systematic review and radiomics quality score assessment. *Cancers (Basel)* (2021) 13 (22):5864. doi: 10.3390/cancers13225864

18. Peng J, Zhang J, Zhang Q, Xu Y, Zhou J, Liu L. A radiomics nomogram for preoperative prediction of microvascular invasion risk in hepatitis b virus-related hepatocellular carcinoma. *Diagn Interv Radiol* (2018) 24(3):121–7. doi: 10.5152/dir.2018.17467

19. Ma X, Wei J, Gu D, Zhu Y, Feng B, Liang M, et al. Preoperative radiomics nomogram for microvascular invasion prediction in hepatocellular carcinoma using contrast-enhanced CT. *Eur Radiol* (2019) 29(7):3595–605. doi: 10.1007/s00330-018-5985-y

20. Zhang R, Xu L, Wen X, Zhang J, Yang P, Zhang L, et al. A nomogram based on bi-regional radiomics features from multimodal magnetic resonance imaging

for preoperative prediction of microvascular invasion in hepatocellular carcinoma. *Quant Imaging Med Surg* (2019) 9(9):1503–15. doi: 10.21037/qims.2019.09.07

21. Erstad DJ, Tanabe KK. Prognostic and therapeutic implications of microvascular invasion in hepatocellular carcinoma. *Ann Surg Oncol* (2019) 26 (5):1474–93. doi: 10.1245/s10434-019-07227-9

22. Lei Z, Li J, Wu D, Xia Y, Wang Q, Si A, et al. Nomogram for preoperative estimation of microvascular invasion risk in hepatitis b virus-related hepatocellular carcinoma within the Milan criteria. *JAMA Surg* (2016) 151(4):356–63. doi: 10.1001/jamasurg.2015.4257

23. Fakhry C, Zhang Q, Nguyen-Tân PF, Rosenthal DI, Weber RS, Lambert L, et al. Development and validation of nomograms predictive of overall and progression-free survival in patients with oropharyngeal cancer. *J Clin Oncol* (2017) 35(36):4057–65. doi: 10.1200/JCO.2016.72.0748

24. Schlichtemeier SM, Pang TC, Williams NE, Gill AJ, Smith RC, Samra JS, et al. A pre-operative clinical model to predict microvascular invasion and long-term outcome after resection of hepatocellular cancer: The Australian experience. *Eur J Surg Oncol* (2016) 42(10):1576–83. doi: 10.1016/j.ejso.2016.05.032

25. Hu H, Zheng Q, Huang Y, Huang XW, Lai ZC, Liu J, et al. A non-smooth tumor margin on preoperative imaging assesses microvascular invasion of hepatocellular carcinoma: A systematic review and meta-analysis. *Sci Rep* (2017) 7(1):15375. doi: 10.1038/s41598-017-15491-6

26. Wu TH, Hatano E, Yamanaka K, Seo S, Taura K, Yasuchika K, et al. A non-smooth tumor margin on preoperative imaging predicts microvascular invasion of hepatocellular carcinoma. *Surg Today* (2016) 46(11):1275–81. doi: 10.1007/s00595-016-1320-x

27. Zhou M, Shan D, Zhang C, Nie J, Wang G, Zhang Y, et al. Value of gadoxetic acid-enhanced MRI for microvascular invasion of small hepatocellular carcinoma: a retrospective study. *BMC Med Imaging* (2021) 21(1):40. doi: 10.1186/s12880-021-00572-w

28. Sumie S, Kuromatsu R, Okuda K, Ando E, Takata A, Fukushima N, et al. Microvascular invasion in patients with hepatocellular carcinoma and its predictable clinicopathological factors. *Ann Surg Oncol* (2008) 15(5):1375–82. doi: 10.1245/s10434-008-9846-9

29. Yang L, Gu D, Wei J, Yang C, Rao S, Wang W, et al. A radiomics nomogram for preoperative prediction of microvascular invasion in hepatocellular carcinoma. *Liver Cancer* (2019) 8(5):373–86. doi: 10.1159/000494099

30. Rousson V, Zumbrunn T. Decision curve analysis revisited: overall net benefit, relationships to ROC curve analysis, and application to case-control studies. *BMC Med Inform Decis Mak* (2011) 11:45. doi: 10.1186/1472-6947-11-45

frontiers | Frontiers in Oncology

TYPE Original Research
PUBLISHED 15 December 2022
DOI 10.3389/fonc.2022.1035307

OPEN ACCESS

EDITED BY
Chuanming Li,
Chongqing University Central Hospital, China

REVIEWED BY
Yanwei Miao,
Dalian Medical University, China
Zhiyong Li,
Dalian Medical University, China

*CORRESPONDENCE
Jianlin Wu
cjr.wujianlin@vip.163.com
Xiaohui Zhang
xiaohui99@hotmail.co.uk

†These authors have contributed equally to this work and share first authorship

SPECIALTY SECTION
This article was submitted to Cancer Imaging and Image-directed Interventions, a section of the journal Frontiers in Oncology

RECEIVED 02 September 2022
ACCEPTED 25 November 2022
PUBLISHED 15 December 2022

CITATION
Shen J, Du H, Wang Y, Du L, Yang D, Wang L, Zhu R, Zhang X and Wu J (2022) A novel nomogram model combining CT texture features and urine energy metabolism to differentiate single benign from malignant pulmonary nodule. *Front. Oncol.* 12:1035307. doi: 10.3389/fonc.2022.1035307

A novel nomogram model combining CT texture features and urine energy metabolism to differentiate single benign from malignant pulmonary nodule

Jing Shen[1,2†], Hai Du[1,3†], Yadong Wang[4,5], Lina Du[2,6], Dong Yang[2,7], Lingwei Wang[8], Ruiping Zhu[9], Xiaohui Zhang[10*] and Jianlin Wu[2*]

[1]Graduate School, Tianjin Medical University, Tianjin, China, [2]Department of Radiology, Affiliated Zhongshan Hospital of Dalian University, Dalian, China, [3]Department of Radiology, Ordos Central Hospital, Ordos Inner Mongolia, China, [4]School of Medicine, Dalian University, Dalian, China, [5]Department of Research, Dalian Detecsen Biomedical Co., LTD, Dalian, China, [6]Graduate School, Dalian Medical University, Dalian, China, [7]Graduate School, Dalian University, Dalian, China, [8]Department of Cardio-Thoracic Surgery, Affiliated Zhongshan Hospital of Dalian University, Dalian, China, [9]Department of Pathology, Affiliated Zhongshan Hospital of Dalian University, Dalian, China, [10]College of Environment and Chemical Engineering, Dalian University, Dalian, China

Objective: To investigate a novel diagnostic model for benign and malignant pulmonary nodule diagnosis based on radiomic and clinical features, including urine energy metabolism index.

Methods: A total of 107 pulmonary nodules were prospectively recruited and pathologically confirmed as malignant in 86 cases and benign in 21 cases. A chest CT scan and urine energy metabolism test were performed in all cases. A nomogram model was established in combination with radiomic and clinical features, including urine energy metabolism levels. The nomogram model was compared with the radiomic model and the clinical feature model alone to test its diagnostic validity, and receiver operating characteristic (ROC) curves were plotted to assess diagnostic validity.

Results: The nomogram was established using a logistic regression algorithm to combine radiomic features and clinical characteristics including urine energy metabolism results. The predictive performance of the nomogram was evaluated using the area under the ROC and calibration curve, which showed the best performance, area under the curve (AUC) = 0.982, 95% CI = 0.940–1.000, compared to clinical and radiomic models in the testing cohort. The clinical benefit of the model was assessed using the decision curve analysis (DCA) and using the nomogram for benign and malignant pulmonary nodules, and preoperative prediction of benign and malignant pulmonary nodules using nomograms showed better clinical benefit.

Conclusion: This study shows that a coupled model combining CT imaging features and clinical features (including urine energy metabolism) in combination with the nomogram model has higher diagnostic performance than the radiomic and clinical models alone, suggesting that the combination of both methods is more advantageous in identifying benign and malignant pulmonary nodules.

KEYWORDS

pulmonary nodules, nomogram, texture analysis, urine energy metabolism, benign, malignant

Introduction

Lung cancer is one of the malignant tumors with high morbidity and mortality, the incidence and mortality rates of which have been on the rise in recent years. The incidence and mortality of lung cancer in China ranked first among all malignant tumors in 2015 with those in the world at about 11.4% and 18%, respectively (1). The 5-year survival rate can approach 50% if early diagnosis and therapy are successful, and early detection and treatment of lung cancer are the keys to improving patient survival rates (2). With the wide application of high-resolution CT, pulmonary nodules are ubiquitous in CT screening. Benign and malignant pulmonary nodules have different treatments and prognoses. Semantic characteristics of pulmonary nodules such as size, attenuation, and margins are often insufficient for characterization. Follow-up CT increases the cost and radiation burden on the patient, in addition to the patient's concern about waiting too long to learn the results (3–5). Therefore, the accurate diagnosis of lung nodules is particularly important. Although conventional CT features are helpful in identifying benign and malignant nodules, there is still some controversy as to which morphological features are valuable for the differential diagnosis of pulmonary nodules (6).

CT texture analysis can objectively and effectively evaluate the CT value of each pixel in the lesion and can detect the subtle density changes in the lesion that cannot be observed by the naked eye, reflecting to some extent the heterogeneity of the tumor (7). CT texture analysis has now been shown to distinguish between tumor grade and genetic mutations (8–10). Digumarthy et al. (11) performed CT texture analysis in 175 patients with pulmonary nodules prior to operation and showed that CT texture analysis could reliably predict well-differentiated and poorly differentiated pulmonary malignant tumors. Awe et al. (12) analyzed the application of CT texture analysis in pancreatic lesions, showing the clinical potential of CT texture analysis in the diagnosis and risk classification of pancreatic lesions. Despite the usefulness of CT texture analysis in tumor diagnosis and grading, results have been obtained in the decision-making and efficacy assessment of treatment options, but the lack of uniform standards for image texture feature parameters has led to inconsistent conclusions (7).

The hallmarks of cancer were reported by Robert Weinberg and Douglas Hanahan in 2000 (13, 14), which can intervene in tumor stages. The main reason for this is abnormal cellular energy metabolism. Cell energy metabolism technology has played an important role in research recently, which quantitatively and automatically reflects the status of the living cells, such as mitochondrial oxygen consumption rate and glycolytic acid production rate. Some earlier proteomic studies in lung cancer diagnosis based on urine or serum specimens have been investigated. Prospective biomarker studies have shown elevated DNA methylation markers CDO1 and SOX17 in the urine of patients with non-small-cell lung cancer (NSCLC) (15). Another prospective study showed that an untargeted urinary metabolome was associated with a lower lung cancer risk in never-smoking women and suggested that an abnormal urine metabolome may be associated with a higher risk of lung cancer (16). However, few studies have focused on the role of the urocyte energy metabolome in the discrimination between benign and malignant nodules.

In this study, morphological assessment, CT texture analysis, and urine cell energy metabolism test were used to investigate their values in the diagnosis of benign and malignant pulmonary nodules and to compare the diagnostic effectiveness of each feature alone and in combination.

Materials and methods

Ethical approval of the study protocol

The protocol of this prospective study was approved by the ethics committee of Zhongshan Hospital Affiliated to Dalian University (No. 2021029, Dalian, China). Informed consent was obtained from each patient.

Patients and study design

This was a single-institution prospective study with 107 patients eventually enrolled consecutively and urine collected from September 2021 to August 2022 at the inpatient Thoracic Surgery Department. All of the patients underwent a chest CT scan within 7 days prior to surgery and were registered as patients with a single pulmonary nodule. All patients received pulmonary surgery (video-assisted thoracoscopic surgery), and pathology results were obtained. Urine energy metabolism index was performed on all patients (Dalian DeTecsen Biomedical Co., Ltd., Dalian, China). Inclusion criteria: 1) All patients received plain CT scans and urine energy level tests in our hospital before surgery; 2) Postoperative pathological results were determined. Exclusion criteria: 1) Patients with multiple nodules including pathologically confirmed benign and malignant lesions; 2) Poor image quality due to respiratory and motion artifacts during scanning; 3) Lesions with other lesions that do not properly depict the region of interest (ROI). A flowchart of the study subjects is shown in Figure 1.

CT scanning techniques

The patient was scanned in the supine position after deep inspiration in a breath-hold position. The scanning area was from the apex of the lung to the level of the bilateral costophrenic angle (including the whole lung). Siemens Somatom FLASH scanner was used for CT scanning, with a tube voltage of 120 kV, tube current automatic mAs technology, the pitch of 1.0, matrix of 512 × 512, a layer thickness of 1.0 mm, and the bone reconstruction algorithm.

Urine cell energy metabolism test

The urine cell energy metabolism index was tested on all of the patients (Dalian DeTecsen Biomedical Co., Ltd., Dalian, China). Morning urine was collected within 3 days before surgery, and all of the patients were asked not to eat or drink for more than 8 h. By using enzymes and cofactors, the cellular energy metabolites and their derivatives in the urine cell energy metabolism can reflect a stable color reaction with the probe. The qualitative results can be obtained by colorimetric measurement at 450 nm wavelength. According to the color reaction, urine energy metabolism results were classified into four degrees: negative (0), weak positive (1), positive (2), and strong positive (3).

Data preprocessing and analysis

In this work, 107 patients were enrolled; 80 cases were randomly selected as the training cohort and 27 patients as the

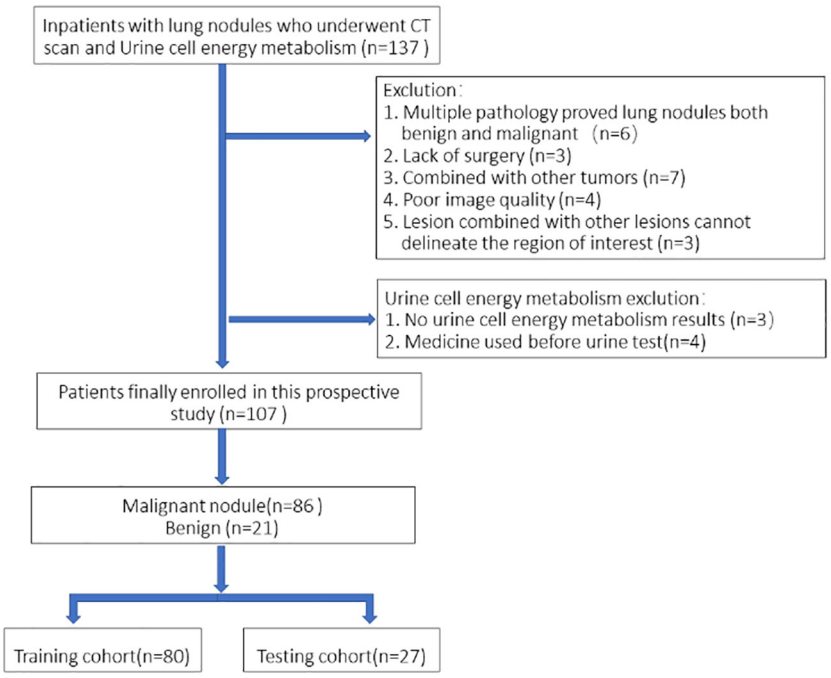

FIGURE 1
Flowchart of the study subjects based on exclusion criteria.

testing cohort. Clinical features including urine energy metabolism results, age, gender, CT values, nodule diameter, and edge and nodule position were collected. Images of all nodules were independently segmented by two radiologists and measured using a double-blind method. Calculation of intraclass correlation coefficient (ICC) ≥0.75 was considered robust. All of the features were divided into three groups: (I) geometry, (II) intensity, and (III) texture. Geometric features characterize the three-dimensional shape of the tumor. The intensity features describe the voxel intensities within the tumor. The texture features describe the patterns and higher-order spatial distributions of the intensities.

Feature extraction, selection, and model building

All radiomic features were extracted using Pyradiomic's in-house feature analysis program (http://pyradiomics.readthedocs.io). Several different texture feature extraction methods were used, including the gray-level run length matrix (GLRLM), gray-level size zone matrix (GLSZM), gray-level co-occurrence matrix (GLCM), and neighborhood gray-tone difference matrix (NGTDM) methods. The least absolute shrinkage and selection operator (LASSO) regression model was used for signature construction of the discovery dataset. After LASSO feature screening, the final retained features are put into machine learning models, including logistic regression (LR), support vector machine (SVM), random forest, and XGBoost, for risk model construction.

Radiomic features were constructed from correlation filters, and the most robust non-redundant and predictive features were selected by LASSO. Finally, a combined nomogram model was built with clinical signatures and radiomic signatures for final interpretation and analysis. Figure 2 shows the workflow of radiomic analysis in this study. To reduce the side effects of outliers, all pixel values were sorted for each image and truncation with an intensity range of 0.5–99.5 percentiles. Spatial normalization was employed to reduce the voxel spacing variation effect. A fixed resolution resampling method was used in our experiment to handle the aforementioned problems.

The radiomic nomogram was established in combination with radiomic signature and clinical signatures. The diagnostic efficacy of the radiomic nomogram was tested in the test cohort, and receiver operating characteristic (ROC) curves were drawn to evaluate the diagnostic efficacy of the nomogram. The

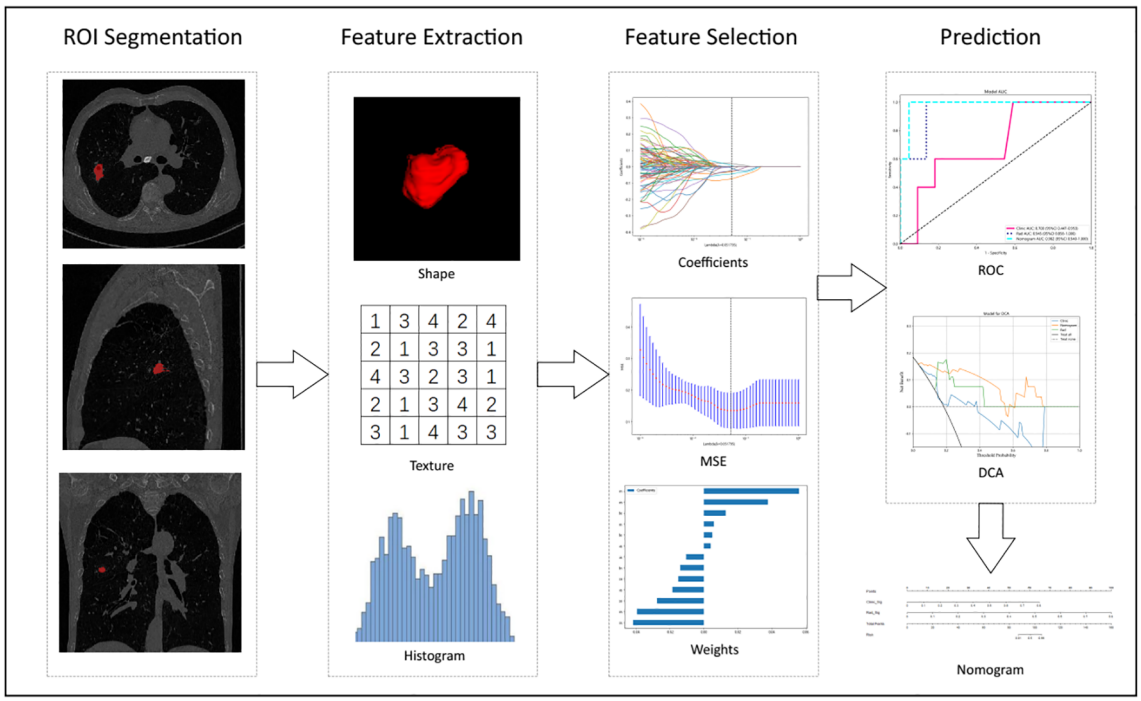

FIGURE 2
Workflow of radiomic analysis in this study. Nodules were segmented by radiologists, and features were extracted and selected by LASSO based on which the prediction model, DCA, Decision curve analysis, and nomogram were built.

calibration efficiency of the nomogram was evaluated by plotting calibration curves, and Hosmer–Lemeshow analytical fit was used to evaluate the calibration ability of the nomogram. Mapping decision curve analysis (DCA) was adopted to evaluate the clinical utility of the predictive models.

Statistics

Clinical features, including urine energy metabolism results, age, gender, CT values, nodule diameter, and edge and nodule position, were analyzed by t-test, Mann–Whitney U test, or χ^2 test. *P* values<0.05 were significantly considered and ultimately used. For the repeatability of the features, Spearman's rank correlation coefficient was also used to calculate the correlation between features and to retain one of the features with a correlation coefficient >0.9 between any two features. To maximize the ability to retain the depicted features, we used a greedy recursive deletion strategy for feature filtering, that is, the feature with the greatest redundancy in the current set is removed each time. The LASSO regression model was used for the signature-constructed discovery dataset. Subsequently, we obtained a radiomic score for each patient by retaining a linear combination of features, weighted by their model coefficients. The Python scikit-learn package was used for LASSO regression modeling.

Results

Comparison of patient clinical characteristics

A total of 107 cases of pulmonary nodules were analyzed and separated into malignant and benign groups according to the pathology results (80 *vs*. 27 cases). The mean age of the malignant and benign groups was 63.84 ± 9.69 years *vs*. 56.57 ± 13.16 years, respectively (P = 0.005). There was no significant difference in terms of gender between the two groups (P = 0.389). Table 1 shows the baseline clinical characteristics of patients in our cohort. Age, long diameter, short diameter, diameter, and energy level showed significant differences (P< 0.05) in our cohort for clinical feature construction, but the differences between CT value, position, and edge were not significant (P > 0.05).

Feature selection and Rad score establishment

All radiomic features were extracted, and prediction models were constructed using the selected features. A total of 13 features with non-zero coefficients were selected to establish the Rad score with a LASSO LR model. Figure 3 shows the coefficients and mean standard error (MSE) for the 10-fold

TABLE 1 Baseline clinical characteristics of patients in our cohort.

Features	All (n=107)	Malignant (n=86)	Benign (n=21)	*P* value
Age (years)	62.41±10.79	63.84±9.69	56.57±13.16	0.005
Long diameter(mm)	23.24±17.73	25.06±18.14	15.78±13.97	0.031
Short diameter(mm)	16.08±11.77	17.45±12.37	10.45±6.49	0.014
Diameter(mm)	19.66±14.54	21.26±15.07	13.11±9.95	0.021
CT value (HU)	-172.83±326.18	-154.69±333.26	-247.08±290.95	0.246
Gender				0.389
0	60 (0.561)	50 (0.581)	10 (0.476)	
1	47 (0.439)	36 (0.419)	11 (0.524)	
Position				0.222
0	27 (0.252)	24 (0.279)	3 (0.143)	
1	24 (0.224)	18 (0.209)	6 (0.286)	
2	5 (0.047)	4 (0.047)	1 (0.048)	
3	32 (0.299)	28 (0.326)	4 (0.191)	
4	19 (0.178)	12 (0.139)	7 (0.333)	
Edge				0.744
0	39 (0.365)	32 (0.372)	7 (0.333)	
1	68 (0.636)	54 (0.628)	14 (0.667)	
Urine energy metabolism				0.048
Negative(0)	27 (0.252)	17 (0.198)	10 (0.476)	
Weak positive(1)	22 (0.206)	19 (0.221)	3 (0.143)	
Positive(2)	50 (0.467)	44 (0.512)	6 (0.286)	
Strong positive(3)	8 (0.075)	6 (0.069)	2 (0.095)	

validation. Figure 3C shows the coefficient values for the final selection of non-zero features.

Rad score is shown as follows:

$$\begin{aligned} Rad\_score = {} & 0.21873191752687882 + 0.003986 \star \\ & \exp onential\_glszm\_SmallAreaEmphasis \\ & -0.027538 \star lbp\_3D\_k\_gldm\_DependenceVariance + \\ & 0.037759 \star lbp\_3D\_k\_glszm\_LowGrayLevelZoneEmphasis - \\ & 0.039335 \star lbp\_3D\_k\_glszm\_SmallAreaHighLevelEmphasis - \\ & 0.015027 \star lbp\_3D\_m2\_glszm\_GrayLevelVariance - \\ & 0.041688 \star lbp\_3D\_m2\_glszm\_SmallAreaLowGrayLevel \\ & Emphasis + 0.056017 \star original\_firstorder\_Minimum - \\ & 0.018478 \star wavelet\_HHL\_firstorder\_Kurtosis - \\ & 0.010406 \star wavelet\_HLH\_firstorder\_Kurtosis + \\ & 0.004868 \star wavelet\_HLH\_glcm\_ClusterShade - \\ & 0.013882 \star wavelet\_HLH\_glcm\_Idn + \\ & 0.012870 \star wavelet\_LLH\_glcm\_ClusterShade \\ & +0.005921 \star wavelet\_LLL\_firstorder\_Minimum \end{aligned}$$

Several models were built and compared to find the best performing model. Supplementary Table S1 shows all of the models we used to predict benign and malignant pulmonary nodules, and the XGBoost model had the best performance compared to the other models. XGBoost achieved the best value of area under the curve (AUC) in the training and testing cohorts, with AUCs of 0.999 and 0.945 for predicting benign and malignant lung nodules, respectively. Therefore, when building clinical features, XGBoost was chosen as the base model. The optimal model was obtained by comparing the radiomic features with LR, SVM, k-nearest neighbor (KNN), decision tree, random forest, extra trees, XGBoost, and lightGBM classifier. Figure 4 showed the ROC analysis of different models on radiomic signatures.

Comparison of clinical, radiomic, and nomogram models

For the AUC, the clinical features [0.997, 95% confidence interval (CI) = 0.990–1.000) and the radiomic features (0.999, 95% CI = 0.996–1.000) were perfectly fitted for the training cohort. In the testing cohort, the clinical characteristics appeared to be overfitted (0.700, 95% CI = 0.473–0.953), but the radiomic signature remained well fitted (0.945, 95% CI = 0.858–1.000). The nomogram using the LR algorithm, combining clinical features and radiomic features, showed the best performance (0.982, 95% CI = 0.940–1.000). In order to compare the clinical signature and radiomic signature and nomogram, DeLong test was used. The results indicated that the AUC comparison between the nomogram and the clinical signature achieved 0.019 and that the nomogram model outperformed the clinical model in the discrimination between malignant and benign nodules. The AUC comparison between the nomogram and radiomic achieved 0.457, which means that both models performed well in differentiating malignant and benign nodules. Figure 5 showed the AUC in both the training and testing cohorts.

Nomogram calibration curves showed good agreement between predicted and observed benign and malignant pulmonary nodules in the training and testing cohorts. The *P* values for the Hosmer–Lemeshow test were 0.109, 0.832, and 0.123 in respect of clinical signature, radiomic signature, and nomogram, suggesting that the nomogram fitted perfectly in both the training and testing cohorts. Figure 6 showed the calibration curves in the training and testing cohorts.

In this study, we also evaluated each model through the DCA. The DCA for the clinical features, radiomic features, and radiomic nomogram is presented in Figure 7. Compared to the scenario without the prediction model (i.e., all treatment or no treatment regimen), the radiomic nomogram significantly improved the patient's intervention outcome with a prediction probability of 0.05–0.78 compared to 0.05–0.38 for the clinical features and 0.12–0.43 for the radiomic signature. Nomograms were higher than other signatures. The preoperative use of radiological nomograms to predict benign and malignant pulmonary nodules showed better clinical benefit. Figure 8 shows the nomogram for clinical use, with the total score reflecting the probability of malignancy in pulmonary nodules.

Discussion

This study showed that for the diagnosis of pulmonary nodules, the combined model based on radiomic features and clinical features including urine energy level had higher diagnostic performance than the radiomic features and clinical features alone. The prediction probability was higher than that of a single method, suggesting that the combination of the two methods is more advantageous in identifying benign and malignant pulmonary nodules.

Radiomics aims to develop new imaging biomarkers to better understand the microbiology of cancer (17) and to provide additional data on the biological composition of lung nodules, which is frequently used for lung cancer screening and diagnosis. Multiple studies have demonstrated the effectiveness of radiomics in discriminating between malignant and benign nodules. Our study showed that the radiomic features performed better than clinical features in both the training cohort and testing cohort. Several radiomic features contribute to the identification of malignant nodules, such as kurtosis and entropy, which have a sensitivity of 83% and specificity of 69% for assessing lung nodule identification. These findings were also reported in previous studies by Sacconi et al. (9), and these CT texture parameters (e.g., skewness and entropy) are also good predictors of epidermal growth factor receptor (EGFR) mutations and lung adenocarcinoma patient survival. Several studies have demonstrated that radiomics was an effective tool in differentiating between malignant and benign tumors, with an

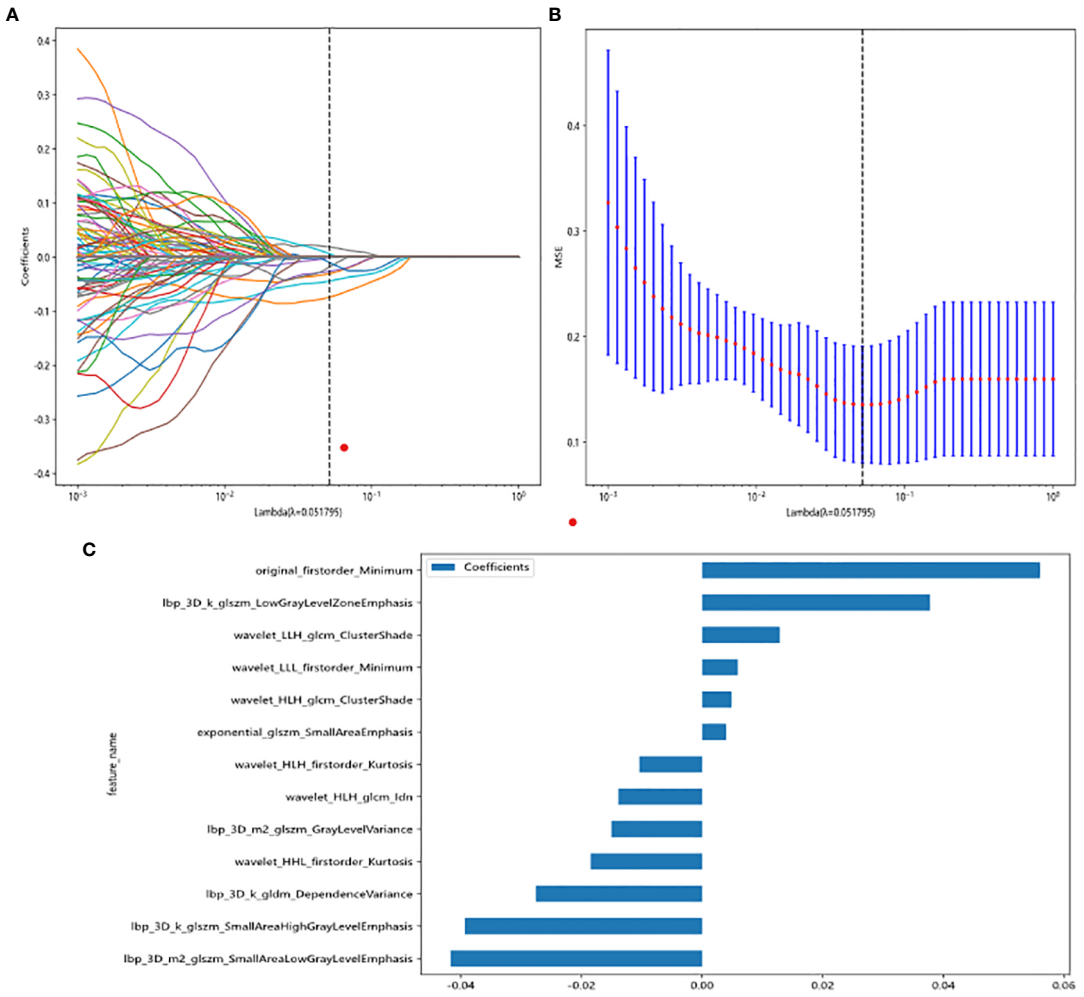

FIGURE 3
Radiomic feature selection based on LASSO algorithm and Rad score establishment. **(A, B)** Ten-fold cross-validated coefficients and 10-fold cross-validated MSE. **(C)** The histogram of the Rad score based on the selected features.

accuracy of 79.06%–81%, a sensitivity of 76.2%–78.00%, and a specificity of 76.11%–91.7% (18, 19). Another study (20) showed that radiomic signatures achieve an AUC of 72% for the classification of malignant and benign nodules but with limited accuracy (11). Radiomic texture analysis and CT features are more effective in distinguishing persistent pulmonary nodules from transient pulmonary tuberculosis than clinical and CT features alone (21). In addition, it is difficult to distinguish the invasion degree of lung adenocarcinoma only by traditional CT features alone (22, 23). This was consistent with the study by Kumar et al. (18), which showed that the accuracy of differentiation between malignant and benign nodules reached 79.06%, with a sensitivity of 78.00% and specificity of 76.11%. In the study by Wu et al. (20), radiomic signature allowed the classification of malignant and benign nodules with an AUC equal to 72%.

In order to more accurately identify the macroscopic and microscopic changes of lung nodules and comprehensively demonstrate the changes of tumor heterogeneity in lung nodules, the combined prediction method can not only absorb the morphological changes of lung nodules but also reflect the characteristics of the microstructure of lung nodules in combination with radiomic features (24). In our investigation, the clinical signature (0.997, 95% CI = 0.990–1.000) and radiomic signature (0.999, 95% CI = 0.996–1.000) both achieve the ideal fitting in the training cohort. Clinical signatures in the testing cohort appear to be overfitting those who attained 0.700, 95% CI = 0.473–0.953, although radiomic signatures continued to match well (0.982, 95% CI = 0.940–1.000). Several studies have tried to compare the added value of clinical features with these radiomic features. In fact, they could improve the performance of machine learning methods to differentiate

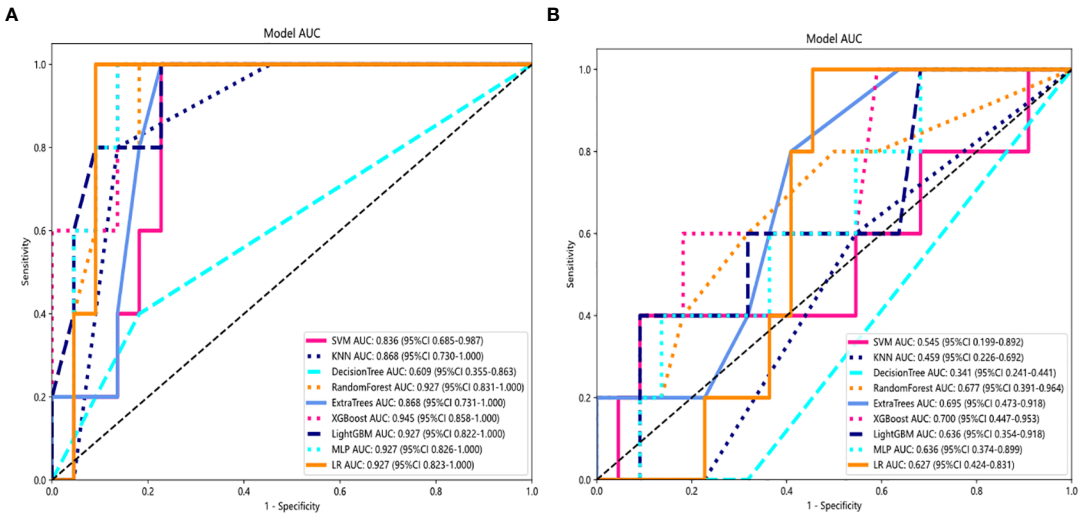

FIGURE 4
Comparison of radiometric feature model predictions for the training **(A)** and testing cohorts **(B)**. XGBoost achieved the best performance in both the training and testing cohorts.

between focal pneumonia and adenocarcinoma (25) or NSCLC (26). The addition of clinical features could not also produce an improvement in the model performance (27), highlighting the importance of the radiomic features. In nearly all cases, the diagnostic accuracy is improved by combining the radiomic model with clinical data, such as serum markers, demographics, histopathology, and genomics (28). These results were consistent with our results that the combined nomogram model based on radiomic and clinical features performed best in the differentiation of malignant and benign nodules.

Urinary tests had been used as noninvasive cost-effective tools for cancer detection (29), the components of which can reflect the circulome of the tumor. Studies have shown that urine can indicate lung cancer by proteomic biomarker panels (30). Urine cellular energy metabolism as a body fluid for lung nodule diagnosis has several advantages. First, it can be easily obtained. Second, urinary metabolism index was reliably detected by mass spectrometry (MS) (31–33). Studies (34–37) have shown significant differences between patients with lung cancer and healthy subjects based on urine metabolomic profiles. A cross-

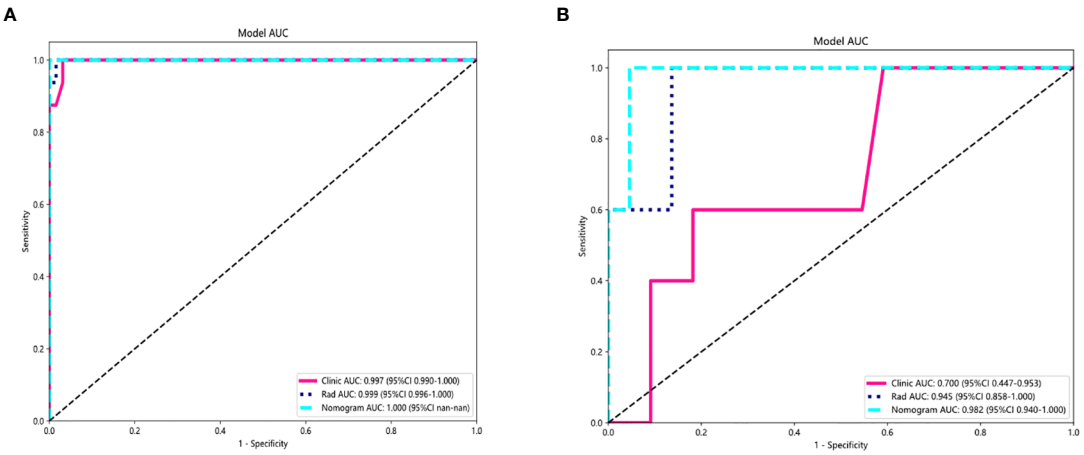

FIGURE 5
AUC Comparison of clinical, radiological, and nomogram models in the training **(A)** and testing **(B)** cohorts. The combined nomogram performed optimally in both the training and testing cohorts.

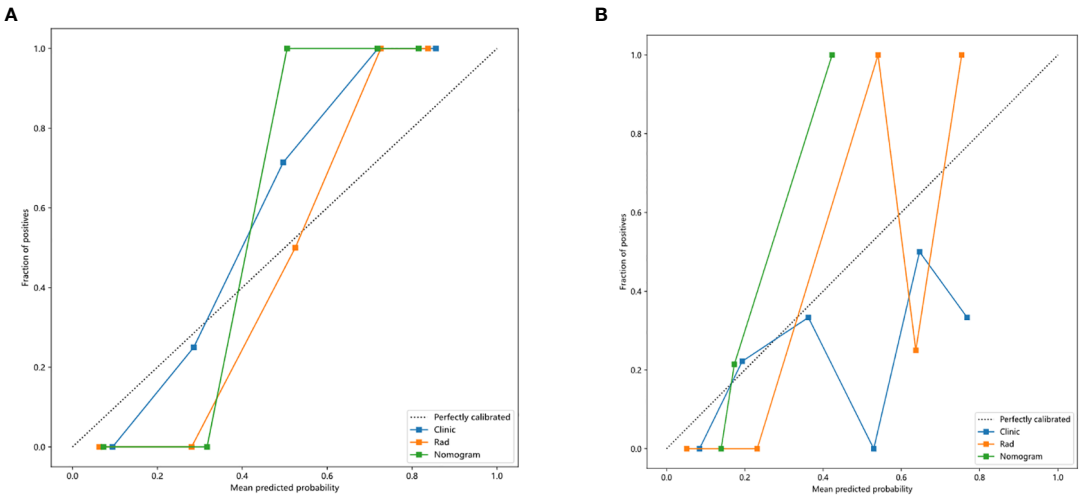

FIGURE 6
Calibration curves in the training and testing cohorts showing that the nomogram fits perfectly well in both the training **(A)** and testing cohorts **(B)**.

validated model based on nuclear magnetic resonance (NMR) spectroscopy differentiated lung cancer (n = 71) from healthy controls (n = 54) with a sensitivity and specificity of 93% and 94%, respectively (35). Our result showed that the combined model including clinical features and urine energy metabolism index showed the best predicting performance. This is consistent with the opinion of Zhang et al. (38) that urinary biomarkers help discriminate lung cancer from control groups, which may be an auxiliary diagnostic tool for lung cancer detection along with radiology features. Considering the complexity of the pathways and metabolites in the disease processes, many biological explanations are hypothetical and unsupported by evidence. Metabolites may increase during the initial stages of the disease process but decrease rapidly as the disease progresses (29). The urinary metabolomic test has promising clinical utility; these studies still need additional distinct validation as the next step toward clinical implementation.

This study has the following limitations: 1) the sample size is small, and there may be selection bias; 2) The boundary of lesions was manually delineated, and some small blood vessels or bronchi may not be completely avoided, and human error is unavoidable. In conclusion, radiomic analysis of pulmonary

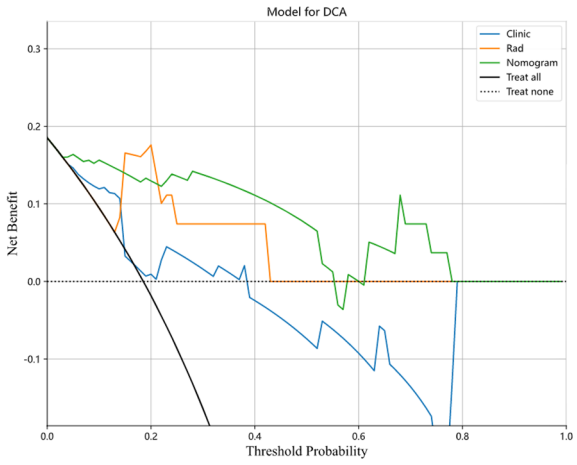

FIGURE 7
Decision curves of the clinical, radiomic, and nomogram models in the testing cohort. Nomogram model shows the best clinical benefit in predicting benign and malignant lung nodules compared to the clinical and radiological models.

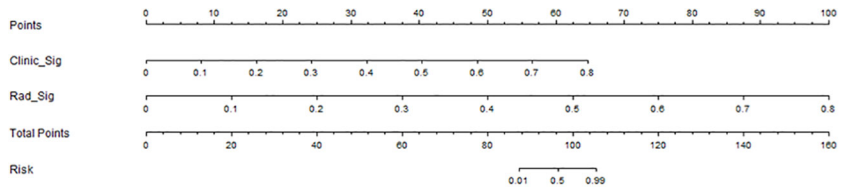

FIGURE 8
Clinical application of the nomogram in the differentiation of benign and malignant pulmonary nodules.

nodules and clinical features including urine energy levels are valuable for the differential diagnosis of benign and malignant pulmonary nodules, and their combined model has a high diagnostic efficiency.

Conclusions

The combined nomogram model based on radiomic and clinical signature-urine including cellular energy features is helpful for the prediction of benign and malignant pulmonary nodules. The model has higher predictive performance compared with models based on radiomic and clinical features only and is expected to provide more information for future decisions on pulmonary nodules.

Data availability statement

The raw data supporting the conclusions of this article will be made available by the authors, without undue reservation.

Ethics statement

The studies involving human participants were reviewed and approved by Affiliated Zhongshan Hospital of Dalian University. The patients/participants provided their written informed consent to participate in this study. Written informed consent was obtained from the individual(s) for the publication of any potentially identifiable images or data included in this article.

Author contributions

JS, JW and XZ conceived the study. JS, LW, LD and DY collected the data. JS, YW, RZ and HD analyzed the data. JS wrote the manuscript. JW and XZ provided study supervision. All authors contributed to the article and approved the submitted version.

Acknowledgments

The authors thank all the staff from the Departments of Radiology and Thoracic surgery, Affiliated Zhongshan Hospital of Dalian University, for their help in collecting the clinical data.

Conflict of interest

Author YW was employed by Dalian Detecsen Biomedical Co., LTD.

The remaining authors declare that the research was conducted in the absence of any commercial or financial relationships that could be construed as a potential conflict of interest.

The reviewers YM and ZL declared a shared parent affiliation with the author LD to the handling editor at the time of review.

Publisher's note

Supplementary material

The Supplementary Material for this article can be found online at: https://www.frontiersin.org/articles/10.3389/fonc.2022.1035307/full#supplementary-material

References

1. Oncology Society of Chinese Medical Association and Chinese Medical Association Publishing House. Oncology Society of Chinese Medical Association guideline for clinical diagnosis and treatment of lung cancer (2021 edition). *Zhonghua Zhong Liu Za Zhi* (2021) 43(6):591–621. doi: 10.3760/cma.j.cn112152-20210207-00118

2. Rivera MP, Katki HA, Tanner NT, Triplette M, Sakoda LC, Wiener RS, et al. Addressing disparities in lung cancer screening eligibility and healthcare access. an official American thoracic society statement. *Am J Respir Crit Care Med* (2020) 202 (7):e95–112. doi: 10.1164/rccm.202008-3053ST

3. Ozeki N, Iwano S, Taniguchi T, Kawaguchi K, Fukui T, Ishiguro F, et al. Therapeutic surgery without a definitive diagnosis can be an option in selected patients with suspected lung cancer. *Interact Cardiovasc Thorac Surg* (2014) 19 (5):830–7. doi: 10.1093/icvts/ivu233

4. Merritt RE, Shrager JB. Indications for surgery in patients with localized pulmonary infection. *Thorac Surg Clin* (2012) 22(3):325–32. doi: 10.1016/j.thorsurg.2012.05.005

5. Scott WJ. Surgical treatment of other bronchial tumors. *Chest Surg Clin N Am* (2003) 13(1):111–28. doi: 10.1016/s1052-3359(02)00038-8

6. Fu BJ, Lv FJ, Li WJ, Lin RY, Zheng YN, Chu ZG. Significance of intra-nodular vessel sign in differentiating benign and malignant pulmonary ground-glass nodules. *Insights Imaging* (2021) 12(1):65. doi: 10.1186/s13244-021-01012-7

7. Lubner MG, Smith AD, Sandrasegaran K, Sahani DV, Pickhardt PJ. CT texture analysis: Definitions, applications, biologic correlates, and challenges. *Radiographics* (2017) 37(5):1483–503. doi: 10.1148/rg.2017170056

8. Yip SSF, Liu Y, Parmar C, Li Q, Liu S, Qu F, et al. Associations between radiologist-defined semantic and automatically computed radiomic features in non-small cell lung cancer. *Sci Rep* (2017) 7(1):3519. doi: 10.1038/s41598-017-02425-5

9. Sacconi B, Anzidei M, Leonardi A, Boni F, Saba L, Scipione R, et al. Analysis of CT features and quantitative texture analysis in patients with lung adenocarcinoma: A correlation with EGFR mutations and survival rates. *Clin Radiol* (2017) 72(6):443–50. doi: 10.1016/j.crad.2017.01.015

10. Bayanati H, Thornhill R E, Souza CA, Sethi-Virmani V, Gupta A, Maziak D, et al. Quantitative CT texture and shape analysis: can it differentiate benign and malignant mediastinal lymph nodes in patients with primary lung cancer? *Eur Radiol* (2015) 25(2):480–7. doi: 10.1007/s00330-014-3420-6

11. Digumarthy SR, Padole AM, Lo Gullo R, Singh R, Shepard JO, Kalra MK. CT texture analysis of histologically proven benign and malignant lung lesions. *Med (Baltimore)* (2018) 97(26):e11172. doi: 10.1097/MD.0000000000011172

12. Awe AM, Rendell VR, Lubner MG, Winslow ER. Texture analysis: An emerging clinical tool for pancreatic lesions. *Pancreas* (2020) 49(3):301–12. doi: 10.1097/MPA.0000000000001495

13. Hanahan D, Weinberg RA. The hallmarks of cancer. *Cell* (2000) 100(1):57–70. doi: 10.1016/S0092-8674(00)81683-9

14. Hanahan D, Weinberg RA. Hallmarks of cancer: the next generation. *Cell* (2011) 144(5):646–74. doi: 10.1016/j.cell.2011.02.013

15. Wever BMM, Bach S, Tibbesma M, Ter Braak TJ, Wajon D, Dickhoff C, et al. Detection of non-metastatic non-small-cell lung cancer in urine by methylation-specific PCR analysis: A feasibility study. *Lung Cancer* (2022) 170:156–64. doi: 10.1016/j.lungcan.2022.06.013

16. Seow WJ, Shu XO, Nicholson JK, Holmes E, Walker DI, Hu W, et al. Association of untargeted urinary metabolomics and lung cancer risk among never-smoking women in China. *JAMA Netw Open* (2019) 2(9):e1911970. doi: 10.1001/jamanetworkopen.2019.11970

17. O'Connor JP, Rose CJ, Waterton JC, Carano RA, Parker GJ, Jackson A. Imaging intratumor heterogeneity: Role in therapy response, resistance, and clinical outcome. *Clin Cancer Res* (2015) 21(2):249–57. doi: 10.1158/1078-0432.CCR-14-0990

18. Kumar D, Chung AG, Shaifee MJ, Khalvati F, Haider MA, Wong A, et al. "Discovery radiomics for pathologically-proven computed tomography lung cancer prediction" In *Image Analysis and Recognition. ICIAR 2017* Karray F., Campilho A., Cheriet F. (Lecture Notes in Computer Science Springer, Cham) (2017), 10317. doi: 10.1007/978-3-319-59876-5_7

19. Liu Y, Balagurunathan Y, Atwater T, Antic S, Li Q, Walker RC, et al. Radiological image traits predictive of cancer status in pulmonary nodules. *Clin Cancer Res* (2017) 23(6):1442–9. doi: 10.1158/1078-0432.CCR-15-3102

20. Wu W, Parmar C, Grossmann P, Quackenbush J, Lambin P, Bussink J, et al. Exploratory study to identify radiomics classifiers for lung cancer histology. *Front Oncol* (2016) 6:71. doi: 10.3389/fonc.2016.00071

21. Lee SH, Lee SM, Goo JM, Kim KG, Kim YJ, Park CM. Usefulness of texture analysis in differentiating transient from persistent part-solid nodules(PSNs): A retrospective study. *PloS One* (2014) 9(1):e85167. doi: 10.1371/journal.pone.0085167

22. Zhou QJ, Zheng ZC, Zhu YQ, Lu PJ, Huang J, Ye JD, et al. Tumor invasiveness defined by IASLC/ATS/ERS classification of ground-glass nodules can be predicted by quantitative CT parameters. *J Thorac Dis* (2017) 9(5):1190–200. doi: 10.21037/jtd.2017.03.170

23. Hu D, Zhen T, Ruan M, Wu L. The value of percentile base on computed tomography histogram in differentiating the invasiveness of adenocarcinoma appearing as pure ground-glass nodules. *Med (Baltimore)* (2020) 99(45):e23114. doi: 10.1097/MD.0000000000023114

24. Lambin P, Rios-Velazquez E, Leijenaar R, Carvalho S, van Stiphout RG, Granton P, et al. Radiomics: Extracting more information from medical images using advanced feature analysis. *Eur J Cancer* (2012) 48(4):441–6. doi: 10.1016/j.ejca.2011.11.036

25. Zhang T, Yuan M, Zhong Y, Zhang YD, Li H, Wu JF, et al. Differentiation of focal organising pneumonia and peripheral adenocarcinoma in solid lung lesions using thin-section CT-based radiomics. *Clin Radiol* (2019) 74(1):78.e23–30. doi: 10.1016/j.crad.2018.08.014

26. Wu W, Pierce LA, Zhang Y, Pipavath SNJ, Randolph TW, Lastwika KJ, et al. Comparison of prediction models with radiological semantic features and radiomics in lung cancer diagnosis of the pulmonary nodules: A case-control study. *Eur Radiol* (2019) 29(11):6100–8. doi: 10.1007/s00330-019-06213-9

27. Balagurunathan Y, Schabath MB, Wang H, Liu Y, Gillies RJ. Quantitative imaging features improve discrimination of malignancy in pulmonary nodules. *Sci Rep* (2019) 9(1):8528. doi: 10.1038/s41598-019-44562-z

28. Gillies RJ, Schabath MB. Radiomics improves cancer screening and early detection. *Cancer Epidemiol Biomarkers Prev* (2020) 29(12):2556–67. doi: 10.1158/1055-9965.EPI-20-0075

29. Dinges SS, Hohm A, Vandergrift LA, Nowak J, Habbel P, Kaltashov IA, et al. Cancer metabolomic markers in urine: Evidence, techniques and recommendations. *Nat Rev Urol* (2019) 16(6):339–62. doi: 10.1038/s41585-019-0185-3

30. Weeks ME, Hariharan D, Petronijevic L, Radon TP, Whiteman HJ, Kocher HM, et al. Analysis of the urine proteome in patients with pancreatic ductal adenocarcinoma. *Proteomics Clin Appl* (2008) 2(7-8):1047–57. doi: 10.1002/prca.200780164

31. Jakobsen KR, Paulsen BS, Bæk R, Varming K, Sorensen BS, Jørgensen MM. Exosomal proteins as potential diagnostic markers in advanced non-small cell lung carcinoma. *J Extracell Vesicles* (2015) 4:26659. doi: 10.3402/jev.v4.26659

32. Hoorn EJ, Pisitkun T, Zietse R, Gross P, Frokiaer J, Wang NS, et al. Prospects for urinary proteomics: Exosomes as a source of urinary biomarkers. *Nephrol (Carlton)* (2005) 10(3):283–90. doi: 10.1111/j.1440-1797.2005.00387.x

33. Barratt J, Topham P. Urine proteomics: The present and future of measuring urinary protein components in disease. *CMAJ* (2007) 177(4):361–8. doi: 10.1503/cmaj.061590

34. Xu H, Liu R, He B, Bi CW, Bi K, Li Q. Polyamine metabolites profiling for characterization of lung and liver cancer using an LC-tandem MS method with multiple statistical data mining strategies: Discovering potential cancer biomarkers in human plasma and urine. *Molecules* (2016) 21(8):1040. doi: 10.3390/molecules21081040

35. Carrola J, Rocha CM, Barros AS, Gil AM, Goodfellow BJ, Carreira IM, et al. Metabolic signatures of lung cancer in biofluids: NMR-based metabonomics of urine. *J Proteome Res* (2011) 10(1):221–30. doi: 10.1021/pr100899x

36. An Z, Chen Y, Zhang R, Song Y, Sun J, He J, et al. Integrated ionization approach for RRLC-MS/MS-based metabonomics: Finding potential biomarkers for lung cancer. *J Proteome Res* (2010) 9(8):4071–81. doi: 10.1021/pr100265g

37. Yang Q, Shi X, Wang Y, Wang W, He H, Lu X, et al. Urinary metabonomic study of lung cancer by a fully automatic hyphenated hydrophilic interaction/RPLC-MS system. *J Sep Sci* (2010) 33(10):1495–503. doi: 10.1002/jssc.200900798

38. Zhang C, Leng W, Sun C, Lu T, Chen Z, Men X, et al. Urine proteome profiling predicts lung cancer from control cases and other tumors. *EBioMedicine* (2018) 30:120–8. doi: 10.1016/j.ebiom.2018.03.009

frontiers | Frontiers in Oncology

TYPE Original Research
PUBLISHED 01 February 2023
DOI 10.3389/fonc.2023.1074060

OPEN ACCESS

EDITED BY
Chuanming Li,
Chongqing University Central Hospital, China

REVIEWED BY
Hongna Tan,
People's Hospital of Zhengzhou University, China
Maira Santana,
Universidade de Pernambuco, Brazil

*CORRESPONDENCE
Xin Zhao
zhaoxinxct@vip.163.com
Yanwu Zhang
yanwuzhang@zzu.edu.cn

SPECIALTY SECTION
This article was submitted to Cancer Imaging and Image-directed Interventions, a section of the journal Frontiers in Oncology

RECEIVED 19 October 2022
ACCEPTED 16 January 2023
PUBLISHED 01 February 2023

CITATION
Lyu Y, Chen Y, Meng L, Guo J, Zhan X, Chen Z, Yan W, Zhang Y, Zhao X and Zhang Y (2023) Combination of ultrafast dynamic contrast-enhanced MRI-based radiomics and artificial neural network in assessing BI-RADS 4 breast lesions: Potential to avoid unnecessary biopsies. *Front. Oncol.* 13:1074060. doi: 10.3389/fonc.2023.1074060

Combination of ultrafast dynamic contrast-enhanced MRI-based radiomics and artificial neural network in assessing BI-RADS 4 breast lesions: Potential to avoid unnecessary biopsies

Yidong Lyu[1], Yan Chen[2], Lingsong Meng[2], Jinxia Guo[3], Xiangyu Zhan[1], Zhuo Chen[1], Wenjun Yan[1], Yuyan Zhang[1], Xin Zhao[2*] and Yanwu Zhang[1*]

[1]Department I of Breast, Third Affiliated Hospital of Zhengzhou University, Zhengzhou, China, [2]Department of Radiology, Third Affiliated Hospital of Zhengzhou University, Zhengzhou, Henan, China, [3]General Electric (GE) Healthcare, MR Research China, Beijing, China

Objectives: To investigate whether combining radiomics extracted from ultrafast dynamic contrast-enhanced MRI (DCE-MRI) with an artificial neural network enables differentiation of MR BI-RADS 4 breast lesions and thereby avoids false-positive biopsies.

Methods: This retrospective study consecutively included patients with MR BI-RADS 4 lesions. The ultrafast imaging was performed using Differential subsampling with cartesian ordering (DISCO) technique and the tenth and fifteenth postcontrast DISCO images (DISCO-10 and DISCO-15) were selected for further analysis. An experienced radiologist used freely available software (FAE) to perform radiomics extraction. After principal component analysis (PCA), a multilayer perceptron artificial neural network (ANN) to distinguish between malignant and benign lesions was developed and tested using a random allocation approach. ROC analysis was performed to evaluate the diagnostic performance.

Results: 173 patients (mean age 43.1 years, range 18–69 years) with 182 lesions (95 benign, 87 malignant) were included. Three types of independent principal components were obtained from the radiomics based on DISCO-10, DISCO-15, and their combination, respectively. In the testing dataset, ANN models showed excellent diagnostic performance with AUC values of 0.915-0.956. Applying the high-sensitivity cutoffs identified in the training dataset demonstrated the potential to reduce the number of unnecessary biopsies by 63.33%-83.33% at the price of one false-negative diagnosis within the testing dataset.

Conclusions: The ultrafast DCE-MRI radiomics-based machine learning model could classify MR BI-RADS category 4 lesions into benign or malignant, highlighting its potential for future application as a new tool for clinical diagnosis.

KEYWORDS

ultrafast dynamic contrast-enhanced MRI, radiomics, neural network, breast imaging reporting and data system, breast cancer

Introduction

Breast cancer is the most common malignant tumor in women and the second leading cause of cancer-related death in women (1). Early cancer detection is beneficial to improve the prognosis of patients with breast cancer (2). Breast magnetic resonance imaging (MRI) plays an important role in the diagnosis (3), treatment (4), and prognostic assessment (5) of breast cancer. American College of Radiology (ACR) Breast Imaging Reporting and Data System (BI-RADS) is helpful for clinical decision-making (6, 7). BI-RADS category 4 lesions with a varying range of probability of malignancy (2%-95%) (6, 8), however, are regarded as suspicious lesions and usually recommended for biopsy (7), which may lead to a large number of negative biopsies (9) as well as the psychological and financial burden for patients. Therefore, it is necessary to find a sensitive tool to improve the assessment of BI-RADS 4 lesions. In order to avoid false positive BI-RADS 4 category assignments, previous studies utilized either advanced MRI techniques (10–13) or specific clinical decision rule incorporated morphological and kinetic BI-RADS descriptors (14, 15). Although these approaches showed encouraging results, additional measurements increase the scan time and the decision rule require human image features interpretation that may lead to inter-reader variation (16).

Radiomics is an emerging field that can non-invasively provide rich information on lesions by quantitatively analyzing numerous features extracted from traditional medical images (17). Different from the conventional visual interpretations of radiologists, this technique can objectively quantify the heterogeneity of diseases. Consequently, radiomics has been successfully explored as a means to aid decision-making for the diagnosis and risk stratification of several kinds of cancers, for example, glioblastoma (18), lung cancer (19), cervical carcinoma (20), and hepatocellular carcinoma (21). Radiomics also shows encouraging results for improving the accuracy of breast cancer diagnosis, prognosis, and prediction of recurrence (22–25).

Ultrafast dynamic contrast-enhanced magnetic resonance imaging (DCE-MRI) is a newly proposed imaging protocol that can provide improved temporal resolution while maintaining reasonable spatial resolution (26, 27). Several fast acquisition techniques have played an important role in ultrafast imaging, consisting of view sharing, sophisticated parallel imaging, and compressed sensing (27–29). Differential sub-sampling with cartesian ordering (DISCO), which utilizes pseudorandom segmentation of the k-space and two-point Dixon fat-water separation, is a type of view-sharing technique (30). All the methods with 3-10 s of temporal resolution can capture kinetic information of a lesion in the very early post-contrast phase. Many studies have demonstrated that the early image features of ultrafast imaging are beneficial for breast cancer diagnosis and characterization (27, 29, 31).

The radiomics models have been developed by some studies to improve the assessment of BI-RADS 4 lesions (32–34). However, they examined the features from conventional sequences including ADC maps, T1W images, T2W images, or T1 contrast-enhanced images. Few studies have reported the diagnostic efficiency of radiomics features based on ultrafast imaging in distinguishing breast suspicious lesions. Therefore, the purpose of this study was (a) to investigate if combining radiomics features extracted from ultrafast imaging (using the DISCO technique) with an artificial neural network (ANN) can differentially diagnose the MR BI-RADS 4 breast lesions, (b) to determine whether and how many false-positive biopsies could be potentially avoided by comparing the results with prospectively prescribed biopsy indications by experienced breast radiologists.

Materials and methods

Patients

This retrospective study was approved by the Institutional Review Board of our institution and written informed consent was waived. We consecutively reviewed 365 patients who presented suspicious lesions by mammography or breast ultrasonography and underwent breast MRI for diagnosis or preoperative staging from April 2020 to May 2021. Samples of all lesions were obtained by biopsy or surgery and analyzed subsequently by an experienced pathologist. The pathological results of all lesions were regarded as the reference standard. 192 patients were excluded due to the following reasons (1): poor image quality fails to satisfy the diagnostic requirement (n = 10) (2); no pathological results available (n = 39) (3); prior biopsy or chemotherapy before MRI examination (n = 60) (4) BI-RADS category 3 or 5 lesions (n = 83). Finally, 173 patients with 182 MR BI-RADS category 4 lesions were included. Nine patients had breast lesions in both breasts. The flowchart of patient selection is shown in Figure 1.

MRI acquisition protocol

All patients underwent breast MRI in a prone position using a 3.0-T scanner (SIGNA Pioneer, GE Healthcare, Waukesha, WI, USA) with an 8-channel breast coil. The MRI protocol included axial T1-weighted imaging, axial T2-weighted imaging with fat suppression, diffusion-weighted imaging, and dynamic contrast-enhanced (DCE) imaging. DCE-MRI consisted of a pre-contrast image of conventional DCE-MRI, followed by 15 phases of ultrafast DCE-MRI, and then five conventional DCE-MRI. Ultrafast imaging that utilized the DISCO technique was performed with the start of gadolinium-based contrast medium injection. Utilizing an MR power injector, gadolinium diamine (GE Healthcare, Shanghai, China) was administered at a dose of 0.1 mmol/kg of body weight and a rate of 2.5 ml/s, followed immediately by a 20-ml saline flush with the same rate. Only the DISCO images were used for radiomics analysis. The acquisition parameters are shown in Supplementary Material 1 Table S1.

Image segmentation and feature extraction

The tenth and fifteenth postcontrast DISCO images (hereafter DISCO-10 and DISCO-15, respectively), which were acquired

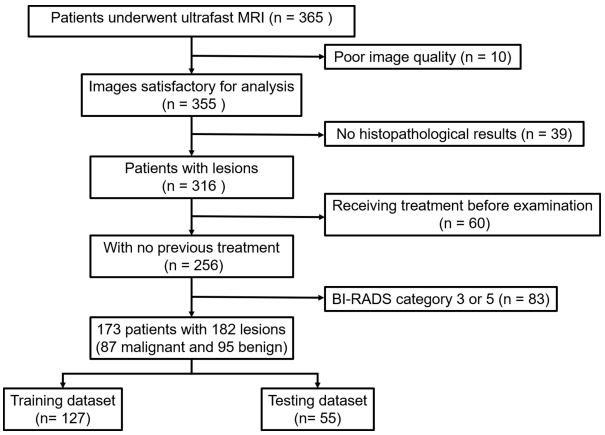

FIGURE 1
Flowchart of patient selection in this study.

respectively at ~70 and ~105 seconds after contrast was injected, were selected for analysis since the peak contrast time between the lesion and the background peaked was approximately 60-120 seconds (35).

For lesion segmentation, three steps were performed: first, two experienced radiologists (reader 1 with 5 years and reader 2 with 10 years of experience in reading breast images, respectively) reviewed the images in consensus identifying the location of the targeted lesion before sketching the region of interest (ROI). Both readers were blinded to initial radiological reports and the pathologic outcomes. Second, reader 1 manually sketched the ROI by using ITK-SNAP software (version 3.6.0, www.itksnap.org). The ROI traced the borders of each lesion and included the entire enhancing area. This step yielded a 3-dimensional (3D) ROI. Third, all segmentations were reviewed by a senior radiologist (reader 3 with more than 15 years of experience) and revised as necessary by adding or replacing seed points.

To evaluate the intra- and interobserver consistency of image segmentation and feature, 50 cases were randomly selected. Reader 1 repeatedly draw the ROIs four weeks later. Reader 3 (with more than experience of 15 years) who was blinded to pathological information independently outlined the ROIs according to the same procedure. The intraclass correlation coefficient (ICC) was used to evaluate intra- and interobserver agreement and ICC > 0.75 was regarded as a satisfactory result (20, 36).

In this study, radiomics extraction was performed by using a freely available software named FeAture Explorer version 5.0 (FAE 5.0) (37). A total of 107 features were automatically extracted from each lesion ROI, consisting of 18 histogram features, 14 shape features, and 75 texture features. The texture features included gray level co-occurrence matrix (GLCM) (24 features), gray-level dependence matrix (GLDM) (14 features), gray level run length matrix (GLRLM) (16 features), gray level size zone matrix (GLSZM) (16 features), neighboring gray-tone difference matrix (NGTDM) (5 features). The details of the features are summarized in Supplementary Material 1 Table S2.

Feature selection and model development

For feature selection, we performed the principal component analysis (PCA) with varimax rotation using SPSS software (version 26.0, IBM) and utilized Kaiser's criterion (eigenvalue > 1) to select the components for further analysis. Three different kinds of principal components were obtained from the features of DISCO-10, DISCO-15, and their combination, respectively (Figure 2).

A multilayer perceptron (MLP) artificial neural network (ANN) was performed to develop the predictive models using the selected components as input. The output layer of the model was the likelihood of malignancy using histological results as the gold standard. The ANN architecture was determined using an automatic selection method based on optimal diagnostic efficiency. The number of units in the hidden layer was set between 1 and 50. To improve inter-reader comparability, we set a seed of 20220928 as a random number generator. The training was performed in batch mode utilizing the scaled conjugate gradient as an optimization algorithm. The initial lambda was set to 0.0000005, sigma to 0.00005, interval center to 0, and interval offset to 0.5. For stopping rules, the maximum steps without a decrease in an error of 1, the minimum relative change in training error of 0.0001, and the minimum relative change in training error ratio of 0.001 were adopted. The data of computing prediction error and the number of training epochs were automatically chosen. The dataset was randomly split into a training set and a testing set in a ratio of approximately 7:3. All radiomics models were trained based on the training set, and then tested based on the testing set. All analyses were performed using SPSS software (version 26.0, IBM).

Statistical analysis

The receiver operating characteristic (ROC) curve analysis was performed to assess the diagnostic performance using histopathology as the reference standard. The area under the curve (AUC),

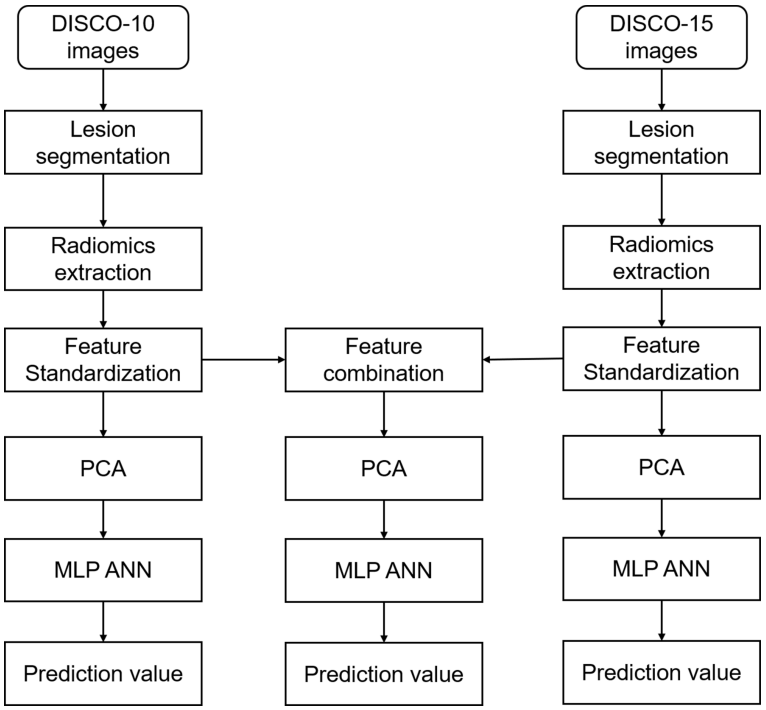

FIGURE 2
Flowchart of radiomics analysis in this study. *DISCO*, Differential sub-sampling with cartesian ordering; *PCA*, principal component analysis; *MLP ANN*, multilayer perceptron artificial neural network.

sensitivity, specificity, positive predictive value (PPV), and negative predictive value (NPV) were calculated. The exploratory cutoff value was selected within the training dataset with a sensitivity of approximately 90% or above and validated using the testing dataset. When the AUC in the training dataset is significantly higher than in the testing dataset, the model is assumed to be overfitted. The differences in AUCs and specificity for different models were compared using the Delong test and McNemar test, respectively. All statistical analyses were performed using the statistical software SPSS version 26.0 (IBM) and MedCalc version 19.8 (MedCalc). $P < 0.05$ was considered statistically significant.

Results

Population and lesion descriptors

A total of 173 patients (mean age, 43.1 ± 11.7 years; range 18-69 years); with 182 lesions were included in the study. Histopathology identified 95 (52.2%) benign and 87 (47.8%) malignant lesions, including invasive ductal carcinoma 68 (78.2%), ductal carcinoma *in situ* 14 (16.1%), mucinous carcinoma 4 (4.6%), invasive lobular carcinoma 1 (1.1%). The mean lesion size was 2.3 ± 1.6 cm. After the random split, approximately 70% (127/182) of cases were regarded as the training dataset and 30% (55/182) as the testing dataset. The detailed results are summarized in Table 1.

PCA of radiomic features

We obtained excellent intra- and inter-observer consistency in 214 (107 × 2) features and no feature was removed. The mean ICCs were 0.96 ($P < 0.001$) and 0.92 ($P < 0.001$) for intra- and inter-observer, respectively.

PCA was performed and yielded three categories of principal components (PC), consisting of eleven PC for DISCO-10, eleven PC for DISCO-15, and sixteen PC for their combination, respectively. The PC was utilized as input layers for the multilayer perceptron ANN. The detailed results of the PCA are summarized in Supplementary Materials 2–4.

Diagnostic performance of ANN

Figure 3 illustrates the ROC curves of different models within the training and testing dataset. The AUC of DISCO-10, DISCO-15, and their combination was 0.817 (95%CI, 0.739-0.880), 0.889 (95%CI, 0.821-0.938), and 0.902 (95%CI, 0.836-0.948) in training dataset and 0.937 (95%CI, 0.838-0.985), 0.915 (95%CI, 0.808-0.973), and 0.956 (95%CI, 0.864-0.993) in the testing dataset, respectively (Table 2). Compared with the training dataset, the AUC values in the testing dataset were higher for DISCO-10 ($P = 0.012$), DISCO-15 ($P = 0.625$), and the combined method ($P = 0.127$), which indicated that classification models were not overfitted. On the testing dataset, the

TABLE 1 Histopathology results in this study.

Histology	Training (n = 127)	Testing (n= 55)
Malignant	62 (48.8%)	25 (45.5%)
Invasive ductal carcinoma	47 (75.8%)	21 (84%)
Ductal carcinoma in situ	10 (16.1%)	4 (16%)
Mucinous carcinoma	4 (6.5%)	
Invasive lobular carcinoma	1 (1.6%)	
Benign	65 (51.2%)	30 (54.5%)
Fibroadenomas	34 (52.3%)	19 (63.4%)
Adenosis	15 (23.1%)	8 (26.7)
Papilloma	9 (13.9%)	1 (3.3)
Inflammation	6 (9.2%)	1 (3.3)
Phyllodes tumor	1 (1.5%)	1 (3.3)

combined scheme yielded the highest AUC value compared with the single sequence radiomics model based on DISCO-10 ($P = 0.294$), and DISCO-15 ($P = 0.122$). DISCO-10 achieved a slightly higher AUC in comparison with DISCO-15 ($P = 0.411$). The details of the ANN architecture are provided in Supplementary Materials 5.

Potential of the ANN to avoid unnecessary biopsies

In this study, three exploratory cut-off values (> 0.144, > 0.171, > 0.459) predicted probability of malignancy were identified in the training dataset, yielding the sensitivity of 95.16%, 93.55%, 90.32%, and the specificity of 20.69%, 38.46%, and 70.77%, respectively (Table 3, Figure 4).

In the testing dataset, evaluating the diagnostic performance of the DISCO-10 using the predefined cut-off value (> 0.144) showed a sensitivity of 96% and a specificity of 63.33%. For the diagnostic performance of DISCO-15, applying the cut-off value (> 0.171) resulted in a sensitivity of 96% and a specificity of 70%. When using the exploratory cut-off value of 0.459 of the combined method, the sensitivity and specificity were 96% and 83.33%, respectively (Table 3, Figure 4). By means of three ANN models, nineteen of 30, twenty-one of 30, and twenty-five of 30 benign breast lesions were correctly diagnosed, while leading to one false-negative diagnosis respectively (Table 3). The combined scheme showed slightly higher specificity compared with DISCO-10 ($P = 0.109$) and DISCO-15 ($P = 0.289$), but not significantly. The false-negative and false-positive diagnoses using different ANN models within the testing set at a sensitivity of 96% are summarized in Table 4. Representative clinical cases are illustrated in Figure 5.

Discussion

We demonstrated that the investigated ultrafast DCE-MRI-based radiomics combined with ANN could be used to differentially diagnose the MR BI-RADS 4 lesions. The constructed classifiers showed good discriminative performance with the AUC values ranging from 0.915 to 0.956. Rather than assigning a category that was only associated with a variable range of malignant tumor rates, the MLP classifier provided individually predicted likelihood of

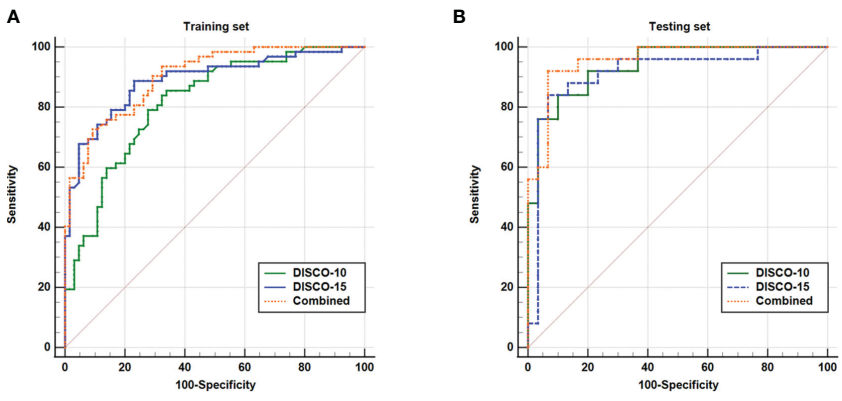

FIGURE 3
ROC curves of the ANN for the training **(A)** and testing **(B)** datasets.

TABLE 2 Comparison for AUCs of different models within the training and testing set.

	AUC	SE	95%CI
Training (n = 127)			
DISCO-10	0.817	0.037	0.739 - 0.880
DISCO-15	0.889	0.030	0.821 - 0.938
Combined	0.902	0.025	0.836 - 0.948
Testing (n = 55)			
DISCO-10	0.937	0.030	0.838 - 0.985
DISCO-15	0.915	0.044	0.808 - 0.973
Combined	0.956	0.025	0.864 - 0.993

Pairwise comparison of ROC curves within the testing set: Combined vs. DISCO-10 (P = 0.294); Combined vs. DISCO-15 (P = 0.122); DISCO-10 vs. DISCO-15 (P = 0.411).
AUC, area under the curve; SE, standard error; CI, confidence interval.

malignancy. Applying the high-sensitivity cutoffs for breast cancer might have avoided 63.33%-83.33% of all unnecessary biopsies at the price of one false-negative diagnosis.

Although MR BI-RADS category 4 lesions show varying malignancy rates, biopsies are usually recommended in clinical practice, resulting in a substantial number of false positive lesions and a waste of medical resources. Therefore, methods for improving pre-interventional lesion assessment are warranted. Radiomics is increasingly considered an important diagnostic tool, providing quantitative multi-dimensional features extracted from imaging data that may reflect the potential phenotype of tumor disease (17). Many studies have shown that radiomics is useful in evaluating MR BI-RADS 4 lesions. Hu et al. (32) developed a radiomics nomogram based on an apparent diffusion coefficient map to differentially diagnose BI-RADS 4 findings and found a moderate diagnostic performance with an AUC of 0.79, which was lower compared to our results. The possible reason may be that the ultrafast DCE series could provide more information in differentiating breast lesions compared with ADC (38). Zhang et al. (34) and Cui et al. (33) applied MRI-based radiomics models to predict the benignity and malignancy of BI-RADS 4 lesions and yielded a good diagnostic efficiency with the AUC of 0.939 and 0.94, respectively, which were comparable to our results. While in this study, the radiomics were extracted from ultrafast DCE-MRI, which appeared to reduce greatly magnet time.

Avoiding unnecessary biopsies remains a hot topic in the clinical management of breast lesions. Currently, a clinical decision rule named the Kaiser score has been proposed to assess breast lesions, with improved diagnostic accuracy and the potential to avoid unnecessary biopsies (14, 39–43). Although this method may simplify the image interpretation compared with BI-RADS assignment, differences resulting from experience at different levels (44) and inter-observer variation (16) remain. Interestingly, our results showed that there was no significant difference in the diagnostic performance between the radiomics models and the Kaiser score (Supplementary Materials 6). This indicated that the

TABLE 3 Diagnostic performance of the ANN models.

	Criterion	Sensitivity (%) (TP/TP + FN)	95% CI	Specificity (%) (TN/TN + FP)	95% CI	PPV	NPV
Training (n = 127)							
DISCO-10	>0.144	95.16 (59/62)	86.5-99.0	27.69 (18/65)	17.3-40.2	55.7	85.7
DISCO-15	>0.171	93.55 (58/62)	84.3-98.2	38.46 (25/65)	26.7-51.4	59.2	86.2
Combined	>0.459	90.32 (56/62)	80.1-96.4	70.77 (46/65)	58.2-81.4	74.7	88.5
Testing (n = 55)							
DISCO-10	>0.144	96.00 (24/25)	79.6-99.9	63.33 (19/30)	43.9-80.1	68.6	95.0
DISCO-15	>0.171	96.00 (24/25)	79.6-99.9	70.00 (21/30)	50.6-85.3	72.7	95.5
Combined	>0.459	96.00 (24/25)	79.6-99.9	83.33 (25/30)	65.3-94.4	82.8	96.2

Comparison of specificity for different models within the testing set: Combined vs. DISCO-10 (P = 0.109); Combined vs. DISCO-15 (P = 0.289); DISCO-10 vs. DISCO-15 (P = 0.727).
TP, true positive; FN, false negative; TN, true negative; FP, false positive; CI, confidence interval; PPV, positive predictive value; NPV, negative predictive value; DISCO, Differential sub-sampling with cartesian ordering.

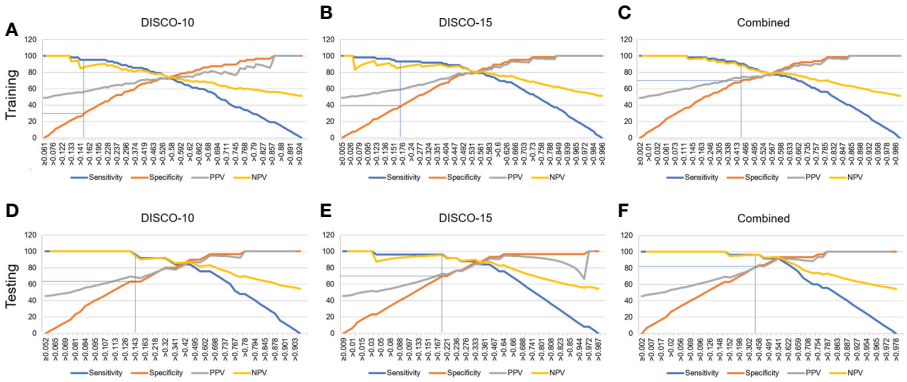

FIGURE 4
Estimated proportion of sensitivity, specificity, PPV, and NPV (y-axis) at different predicted probability thresholds (x-axis) for training dataset (A-C) and testing dataset (D-F). (A-C) The vertical blue lines indicate the cutoff values of 0.144, 0.171, and 0.459 at high sensitivity (>90%) for DISCO-10, DISCO-15, and combined methods within the training dataset, respectively. (D-F) The vertical blue lines indicate the diagnostic performance within the testing dataset using the predefined cutoff values. PPV, positive predictive value; NPV, negative predictive value.

radiomics-based machine learning model might provide comparable results compared with the Kaiser score method while not required to perform image feature interpretation.

The exploratory cutoff at high sensitivity may be used to evaluate the number of avoidable false-positive biopsies (15, 16, 45). Utilizing the radiomics derived from ultrafast DCE-MRI combined with the MLP ANN classifier, we identified that about 63.33%-83.33% of unnecessary biopsies might have been avoided in the testing dataset while maintaining a high sensitivity (96%, 24/25). This was an encouraging result, which had the potential to provide more valuable information to support clinical decision-making.

Currently, abbreviated breast MRI, which can substantially shorten examination and reading times, has been proposed for increasing access to screening for women at average risk of breast cancer. Many studies have demonstrated that abbreviated MRI can improve cancer detection in women with dense breasts (46, 47). However, this protocol may result in unnecessary biopsies because of the lack of kinetics information provided by DCE-MRI. Ultrafast imaging can fill this gap. The features including maximum slope and time to enhancement derived from ultrafast sequences have shown important value in improving tumor characterization, identifying prognostic factors, and assessing treatment (29, 31, 48, 49). But the calculation of these parameters requires commercial software that may not be universally available. In the present study, we explored a more intuitive and easy-to-apply method in a representative patient population and analyzed its clinical utility. To make the proposed approach available to every physician, open-source software was used to perform radiomics extraction from the initial DICOM images. Exporting the learned weights of a well-trained ANN classifier into excel would allow our findings to be quickly integrated into clinical workflows and make it easy to obtain personal predictions of the malignant rates in patients with MR BI-RADS category 4 lesions. However, it should be noted that this is only a preliminary study in the investigated setting and larger patient cohorts are required to validate the results.

While DISCO-15 might have avoided more unnecessary biopsies compared with DISCO-10, not significantly. And the former showed a higher AUC value. In addition, combining DISCO-15 features with DISCO-10 did not yield significantly improved AUC and specificity. This might suggest that the late postcontrast phase of ultrafast DCE-MRI could provide little information for significantly improving diagnostic performance.

TABLE 4 False-negative and false-positive diagnoses using different models within the testing set at high level of sensitivity (96%).

	False negatives	n	False positives	n
DISCO-10		1		11
	Invasive ductal carcinoma	1	Fibroadenoma	7
			Adenosis	3
			Inflammation	1
DISCO-15		1		9
	Invasive ductal carcinoma	1	Fibroadenoma	8
			Adenosis	1
Combined		1		5
	Invasive ductal carcinoma	1	Fibroadenoma	4
			Adenosis	1

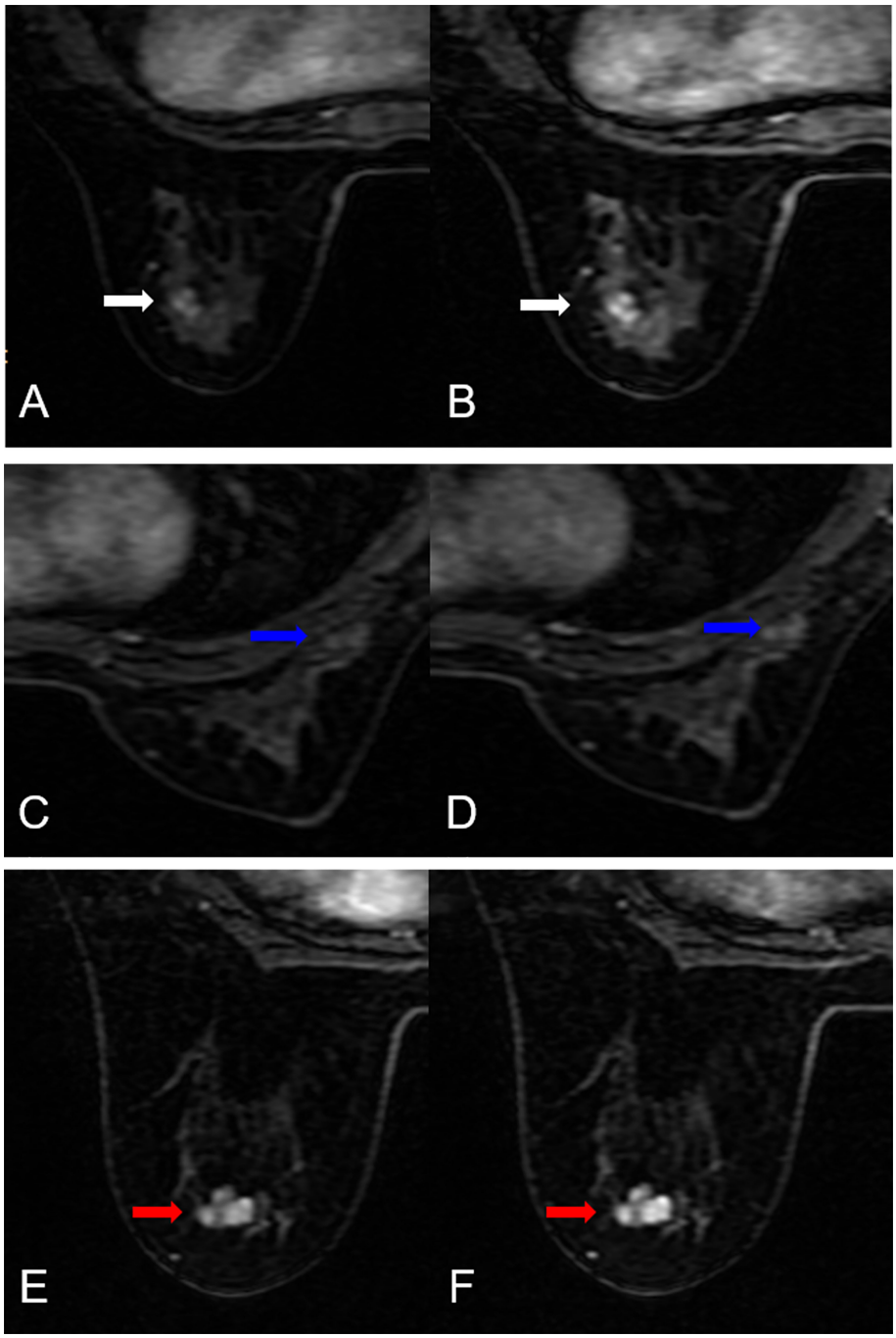

FIGURE 5
False-negative and false-positive results. **(A, B)** False-negative case: A 51-year-old female patient: MRI showed an irregular lesion in the left breast (white arrow. The lesion demonstrated heterogeneous internal enhancement **(A, B)**. **(A)** DISCO-10, **(B)** DISCO-15. The ANN classifiers predicted a low likelihood of malignancy (14.3% for DISCO-10, 4.2% for DISCO-15, and 15.2% for combined, respectively). Histology revealed an invasive ductal carcinoma. **(C–F)** False-positive cases. **(C, D)** A 34-year-old female patient: MRI showed an irregular lesion in the right breast (blue arrow). The lesion demonstrated heterogeneous internal enhancement **(C, D)**. **(C)** DISCO-10, **(D)** DISCO-15. The ANN classifiers predicted a high likelihood of malignancy (65.6% for DISCO-10, 64.0% for DISCO-15, and 75.4% for combined, respectively). Histology revealed an adenosis. **(E, F)** A 35-year-old female patient: MRI showed an irregular lesion in the left breast (red arrow). The lesion demonstrated heterogeneous internal enhancement **(E, F)**. **(E)** DISCO-10, **(F)** DISCO-15. The ANN classifiers predicted a high likelihood of malignancy (78.0% for DISCO-10, 97.2% for DISCO-15, and 78.7% for combined, respectively). Histology revealed a fibroadenoma.

There are several limitations in this study. First, the number of cases was relatively small, and it was a retrospective study merely performed in our institution. In order to validate the robustness of the classifier, larger datasets from multicenter are needed in further research. Second, only ultrafast imaging was used to perform radiomics analysis, other sequences, such as DWI, T2WI, and high-spatial-resolution DCE sequences were not included and required further investigation. Third, we analyzed the features of BI-RADS 4 lesions, and other category lesions consisting of category 3 or 5 were not included. We believe that the proposed ANN classifier might also

be beneficial in evaluating these lesions and we are currently examining this assumption (4). In this study, the risk factors such as patient age, personal disease history, and gene mutation that are highly associated with breast cancer were not included. The fusion of these features with principal component analysis might yield more stable and trustable diagnostic performance.

In conclusion, our preliminary results indicated that radiomics extracted from ultrafast DCE-MRI imaging combined with the multilayer perceptron artificial neural network could differentially diagnose MR BI-RADS category 4 breast lesions with excellent diagnostic performance, and have the potential to avoid more than 63.33% of unnecessary biopsies. Further investigation with larger patient cohorts is warranted to validate our results in the future.

Data availability statement

The datasets presented in this article are not readily available because of institutional restrictions. Requests to access the datasets should be directed to Xin Zhao, zhaoxinxct@vip.163.com.

Ethics statement

The studies involving human participants were reviewed and approved by the Third Affiliated Hospital of Zhengzhou University. Written informed consent for participation was not required for this study in accordance with the national legislation and the institutional requirements. Written informed consent was not obtained from the individual(s) for the publication of any potentially identifiable images or data included in this article.

Author contributions

Conception and design, YL. Administrative support, XZ and YWZ. Provision of study materials or patients, YC, XYZ, and ZC. Collection and assembly of data, WY, YYZ, and YC. Data analysis and interpretation, YL, LM, and JG. Writing - review and editing, YL, LM, and JG. Final approval of manuscript, all authors. All authors contributed to the article and approved the submitted version.

Funding

This research was funded by Henan Province Medical Science and Technology Research Plan Joint Construction Project (Grant No. LHGJ20210477).

Acknowledgments

We are grateful to our colleagues in the Radiology Department for their help in data collection.

Conflict of interest

JG was employed by General Electric GE Healthcare.

The remaining authors declare that the research was conducted in the absence of any commercial or financial relationships that could be construed as a potential conflict of interest.

The reviewer HT declared a shared parent affiliation with the authors YL, YC, LM, JG, XYZ, ZC, WY, YYZ, XZ, and YWZ to the handling editor at the time of review.

Publisher's note

Supplementary material

The Supplementary Material for this article can be found online at: https://www.frontiersin.org/articles/10.3389/fonc.2023.1074060/full#supplementary-material

References

1. Siegel RL, Miller KD, Fuchs HE, Jemal A. Cancer statistics, 2021. *CA: A Cancer J Clin* (2021) 71(1):7–33. doi: 10.3322/caac.21654

2. Byers T, Wender RC, Jemal A, Baskies AM, Ward EE, Brawley OW. The American cancer society challenge goal to reduce US cancer mortality by 50% between 1990 and 2015: Results and reflections. *CA Cancer J Clin* (2016) 66(5):359–69. doi: 10.3322/caac.21348

3. Bakker MF, de Lange SV, Pijnappel RM, Mann RM, Peeters PHM, Monninkhof EM, et al. Supplemental MRI screening for women with extremely dense breast tissue. *N Engl J Med* (2019) 381(22):2091–102. doi: 10.1056/NEJMoa1903986

4. Sumkin JH, Berg WA, Carter GJ, Bandos AI, Chough DM, Ganott MA, et al. Diagnostic performance of MRI, molecular breast imaging, and contrast-enhanced mammography in women with newly diagnosed breast cancer. *Radiology* (2019) 293 (3):531–40. doi: 10.1148/radiol.2019190887

5. Reig B, Lewin AA, Du L, Heacock L, Toth HK, Heller SL, et al. Breast MRI for evaluation of response to neoadjuvant therapy. *Radiographics* (2021) 41(3):665–79. doi: 10.1148/rg.2021200134

6. Strigel RM, Burnside ES, Elezaby M, Fowler AM, Kelcz F, Salkowski LR, et al. Utility of BI-RADS assessment category 4 subdivisions for screening breast MRI. *AJR Am J Roentgenol* (2017) 208(6):1392–9. doi: 10.2214/AJR.16.16730

7. D'Orsi C, Morris E, Mendelson E. ACR BI-RADS®atlas, breast imaging reporting and data system. (2013) (5th ed. Reston, VA: American College of Radiology).

8. Leithner D, Wengert G, Helbich T, Morris E, Pinker K. MRI In the assessment of BI-RADS(R) 4 lesions. *Top Magn Reson Imaging* (2017) 26(5):191–9. doi: 10.1097/RMR.0000000000000138

9. Elezaby M, Li G, Bhargavan-Chatfield M, Burnside ES, DeMartini WB. ACR BI-RADS assessment category 4 subdivisions in diagnostic mammography: Utilization and

outcomes in the national mammography database. *Radiology* (2018) 287(2):416–22. doi: 10.1148/radiol.2017170770

10. Dijkstra H, Dorrius MD, Wielema M, Pijnappel RM, Oudkerk M, Sijens PE. Quantitative DWI implemented after DCE-MRI yields increased specificity for BI-RADS 3 and 4 breast lesions. *J Magn Reson Imaging* (2016) 44(6):1642–9. doi: 10.1002/jmri.25331

11. Matsuda M, Tsuda T, Ebihara R, Toshimori W, Takeda S, Okada K, et al. Enhanced masses on contrast-enhanced breast: Differentiation using a combination of dynamic contrast-enhanced MRI and quantitative evaluation with synthetic MRI. *J Magn Reson Imaging* (2021) 53(2):381–91. doi: 10.1002/jmri.27362

12. Sun SY, Ding Y, Li Z, Nie L, Liao C, Liu Y, et al. Multiparameter MRI model with DCE-MRI, DWI, and synthetic MRI improves the diagnostic performance of BI-RADS 4 lesions. *Front Oncol* (2021) 11:699127. doi: 10.3389/fonc.2021.699127

13. Clauser P, Marcon M, Dietzel M, Baltzer PAT. A new method to reduce false positive results in breast MRI by evaluation of multiple spectral regions in proton MR-spectroscopy. *Eur J Radiol* (2017) 92:51–7. doi: 10.1016/j.ejrad.2017.04.014

14. Milos RI, Pipan F, Kalovidouri A, Clauser P, Kapetas P, Bernathova M, et al. The kaiser score reliably excludes malignancy in benign contrast-enhancing lesions classified as BI-RADS 4 on breast MRI high-risk screening exams. *Eur Radiol* (2020) 30(11):6052–61. doi: 10.1007/s00330-020-06945-z

15. Woitek R, Spick C, Schernthaner M, Rudas M, Kapetas P, Bernathova M, et al. A simple classification system (the tree flowchart) for breast MRI can reduce the number of unnecessary biopsies in MRI-only lesions. *Eur Radiol* (2017) 27(9):3799–809. doi: 10.1007/s00330-017-4755-6

16. Wengert GJ, Pipan F, Almohanna J, Bickel H, Polanec S, Kapetas P, et al. Impact of the kaiser score on clinical decision-making in BI-RADS 4 mammographic calcifications examined with breast MRI. *Eur Radiol* (2020) 30(3):1451–9. doi: 10.1007/s00330-019-06444-w

17. Gillies RJ, Kinahan PE, Hricak H. Radiomics: Images are more than pictures, they are data. *Radiology* (2016) 278(2):563–77. doi: 10.1148/radiol.2015151169

18. Park JE, Ham S, Kim HS, Park SY, Yun J, Lee H, et al. Diffusion and perfusion MRI radiomics obtained from deep learning segmentation provides reproducible and comparable diagnostic model to human in post-treatment glioblastoma. *Eur Radiol* (2020) 31(5):3127–3137. doi: 10.1007/s00330-020-07414-3

19. Wu G, Jochems A, Refaee T, Ibrahim A, Yan C, Sanduleanu S, et al. Structural and functional radiomics for lung cancer. *Eur J Nucl Med Mol Imaging* (2021) 48(12):3961–74. doi: 10.1007/s00259-021-05242-1

20. Xiao M, Ma F, Li Y, Li Y, Li M, Zhang G, et al. Multiparametric MRI-based radiomics nomogram for predicting lymph node metastasis in early-stage cervical cancer. *J Magn Reson Imaging* (2020) 52(3):885–96. doi: 10.1002/jmri.27101

21. Wu H, Han X, Wang Z, Mo L, Liu W, Guo Y, et al. Prediction of the ki-67 marker index in hepatocellular carcinoma based on CT radiomics features. *Phys Med Biol* (2020) 65(23):235048. doi: 10.1088/1361-6560/abac9c

22. Truhn D, Schrading S, Haarburger C, Schneider H, Merhof D, Kuhl C. Radiomic versus convolutional neural networks analysis for classification of contrast-enhancing lesions at multiparametric breast MRI. *Radiology* (2019) 290(2):290–7. doi: 10.1148/radiol.2018181352

23. Tao W, Lu M, Zhou X, Montemezzi S, Bai G, Yue Y, et al. Machine learning based on multi-parametric MRI to predict risk of breast cancer. *Front Oncol* (2021) 11:570747. doi: 10.3389/fonc.2021.570747

24. Wang X, Xie T, Luo J, Zhou Z, Yu X, Guo X. Radiomics predicts the prognosis of patients with locally advanced breast cancer by reflecting the heterogeneity of tumor cells and the tumor microenvironment. *Breast Cancer Res* (2022) 24(1):20. doi: 10.1186/s13058-022-01516-0

25. Conti A, Duggento A, Indovina I, Guerrisi M, Toschi N. Radiomics in breast cancer classification and prediction. *Semin Cancer Biol* (2021) 72:238–50. doi: 10.1016/j.semcancer.2020.04.002

26. Mann RM, Cho N, Moy L. Breast MRI: State of the art. *Radiology* (2019) 292(3):520–36. doi: 10.1148/radiol.2019182947

27. Morrison CK, Henze Bancroft LC, DeMartini WB, Holmes JH, Wang K, Bosca RJ, et al. Novel high spatiotemporal resolution versus standard-of-Care dynamic contrast-enhanced breast MRI. *Invest Radiol* (2017) 52(4):198–205. doi: 10.1097/rli.0000000000000329

28. Kim SY, Cho N, Choi Y, Shin SU, Kim ES, Lee SH, et al. Ultrafast dynamic contrast-enhanced breast MRI: Lesion conspicuity and size assessment according to background parenchymal enhancement. *Korean J Radiol* (2020) 21(5):561–71. doi: 10.3348/kjr.2019.0567

29. Kim JJ, Kim JY, Hwangbo L, Suh HB, Son Y, Nickel MD, et al. Ultrafast dynamic contrast-enhanced MRI using compressed sensing: Associations of early kinetic parameters with prognostic factors of breast cancer. *AJR Am J Roentgenol* (2021) 217(1):56–63. doi: 10.2214/AJR.20.23457

30. Saranathan M, Rettmann DW, Hargreaves BA, Lipson JA, Daniel BL. Variable spatiotemporal resolution three-dimensional Dixon sequence for rapid dynamic contrast-enhanced breast MRI. *J Magn Reson Imaging* (2014) 40(6):1392–9. doi: 10.1002/jmri.24490

31. Lee SJ, Ko KH, Jung HK, Koh JE, Park AY. The additional utility of ultrafast MRI on conventional DCE-MRI in evaluating preoperative MRI of breast cancer patients. *Eur J Radiol* (2020) 124:108841. doi: 10.1016/j.ejrad.2020.108841

32. Hu B, Xu K, Zhang Z, Chai R, Li S, Zhang L. A radiomic nomogram based on an apparent diffusion coefficient map for differential diagnosis of suspicious breast findings. *Chin J Cancer Res* (2018) 30(4):432–8. doi: 10.21147/j.issn.1000-9604.2018.04.06

33. Cui Q, Sun L, Zhang Y, Zhao Z, Li S, Liu Y, et al. Value of breast MRI omics features and clinical characteristics in breast imaging reporting and data system (BI-RADS) category 4 breast lesions: an analysis of radiomics-based diagnosis. *Ann Transl Med* (2021) 9(22):1677. doi: 10.21037/atm-21-5441

34. Zhang R, Wei W, Li R, Li J, Zhou Z, Ma M, et al. An MRI-based radiomics model for predicting the benignity and malignancy of BI-RADS 4 breast lesions. *Front Oncol* (2021) 11:733260. doi: 10.3389/fonc.2021.733260

35. Chatterji M, Mercado CL, Moy L. Optimizing 1.5-Tesla and 3-Tesla dynamic contrast-enhanced magnetic resonance imaging of the breasts. *Magn Reson Imaging Clin N Am* (2010) 18(2):207–24, viii. doi: 10.1016/j.mric.2010.02.011

36. Yang C, Huang M, Li S, Chen J, Yang Y, Qin N, et al. Radiomics model of magnetic resonance imaging for predicting pathological grading and lymph node metastases of extrahepatic cholangiocarcinoma. *Cancer Lett* (2020) 470:1–7. doi: 10.1016/j.canlet.2019.11.036

37. Song Y, Zhang J, Zhang YD, Hou Y, Yan X, Wang Y, et al. FeAture explorer (FAE): A tool for developing and comparing radiomics models. *PloS One* (2020) 15(8):e0237587. doi: 10.1371/journal.pone.0237587

38. Dalmis MU, Gubern-Merida A, Vreemann S, Bult P, Karssemeijer N, Mann R, et al. Artificial intelligence-based classification of breast lesions imaged with a multiparametric breast MRI protocol with ultrafast DCE-MRI, T2, and DWI. *Invest Radiol* (2019) 54(6):325–32. doi: 10.1097/RLI.0000000000000544

39. Jajodia A, Sindhwani G, Pasricha S, Prosch H, Puri S, Dewan A, et al. Application of the kaiser score to increase diagnostic accuracy in equivocal lesions on diagnostic mammograms referred for MR mammography. *Eur J Radiol* (2021) 134:109413. doi: 10.1016/j.ejrad.2020.109413

40. Baltzer PA, Dietzel M, Kaiser WA. A simple and robust classification tree for differentiation between benign and malignant lesions in MR-mammography. *Eur Radiol* (2013) 23(8):2051–60. doi: 10.1007/s00330-013-2804-3

41. Dietzel M, Krug B, Clauser P, Burke C, Hellmich M, Maintz D, et al. A multicentric comparison of apparent diffusion coefficient mapping and the kaiser score in the assessment of breast lesions. *Invest Radiol* (2021) 56(5):274–82. doi: 10.1097/RLI.0000000000000739

42. Meng L, Zhao X, Lu L, Xing Q, Wang K, Guo Y, et al. A comparative assessment of MR BI-RADS 4 breast lesions with kaiser score and apparent diffusion coefficient value. *Front Oncol* (2021) 11:779642. doi: 10.3389/fonc.2021.779642

43. Meng L, Zhao X, Guo J, Lu L, Cheng M, Xing Q, et al. Evaluation of the differentiation of benign and malignant breast lesions using synthetic relaxometry and the kaiser score. *Front Oncol* (2022) 12:964078. doi: 10.3389/fonc.2022.964078

44. Dietzel M, Ellmann S, Schulz-Wendtland R, Clauser P, Wenkel E, Uder M, et al. Breast MRI in the era of diffusion weighted imaging: do we still need signal-intensity time curves? *Eur Radiol* (2020) 30(1):47–56. doi: 10.1007/s00330-019-06346-x

45. Chen ZW, Zhao YF, Liu HR, Zhou JJ, Miao HW, Ye SX, et al. Assessment of breast lesions by the kaiser score for differential diagnosis on MRI: the added value of ADC and machine learning modeling. *Eur Radiol* (2022) 32(10):6608–6618. doi: 10.1007/s00330-022-08899-w

46. Comstock CE, Gatsonis C, Newstead GM, Snyder BS, Gareen IF, Bergin JT, et al. Comparison of abbreviated breast MRI vs digital breast tomosynthesis for breast cancer detection among women with dense breasts undergoing screening. *Jama* (2020) 323(8):746–56. doi: 10.1001/jama.2020.0572

47. Kuhl CK. Abbreviated breast MRI for screening women with dense breast: the EA1141 trial. *Br J Radiol* (2018) 91(1090):20170441. doi: 10.1259/bjr.20170441

48. Pelissier M, Ambarki K, Salleron J, Henrot P. Maximum slope using ultrafast breast DCE-MRI at 1.5 Tesla: a potential tool for predicting breast lesion aggressiveness. *Eur Radiol* (2021) 31(12):9556–66. doi: 10.1007/s00330-021-08089-0

49. Ramtohul T, Tescher C, Vaflard P, Cyrta J, Girard N, Malhaire C, et al. Prospective evaluation of ultrafast breast MRI for predicting pathologic response after neoadjuvant therapies. *Radiology* (2022), 305(3):220389. doi: 10.1148/radiol.220389

frontiers | Frontiers in Oncology

TYPE Original Research
PUBLISHED 16 February 2023
DOI 10.3389/fonc.2023.990306

OPEN ACCESS

EDITED BY
Stefania Rizzo,
University of Italian Switzerland, Switzerland

REVIEWED BY
Osvaldo Gervasi,
University of Perugia, Italy
Xiao-Wan Bo,
Tongji University, China
Jing Gao,
Shanghai Jiao Tong University, China

*CORRESPONDENCE
Li Liu
lily_liu@tmmu.edu.cn
Xiaofei Hu
harryzonetmmu@163.com
Yi Wu
wuy1979@tmmu.edu.cn

SPECIALTY SECTION
This article was submitted to Cancer Imaging and Image-directed Interventions, a section of the journal Frontiers in Oncology

RECEIVED 09 July 2022
ACCEPTED 03 February 2023
PUBLISHED 16 February 2023

CITATION
Xiong M, Xu Y, Zhao Y, He S, Zhu Q, Wu Y, Hu X and Liu L (2023) Quantitative analysis of artificial intelligence on liver cancer: A bibliometric analysis.
Front. Oncol. 13:990306.
doi: 10.3389/fonc.2023.990306

Quantitative analysis of artificial intelligence on liver cancer: A bibliometric analysis

Ming Xiong[1], Yaona Xu[1], Yang Zhao[1], Si He[1], Qihan Zhu[1], Yi Wu[1]*, Xiaofei Hu[2]* and Li Liu[1,3]*

[1]Department of Digital Medicine, School of Biomedical Engineering and Medical Imaging, Third Military Medical University (Army Medical University), Chongqing, China, [2]Department of Nuclear Medicine, Southwest Hospital, Third Military Medical University (Army Medical University), Chongqing, China, [3]Department of Ultrasound, Southwest Hospital, Third Military Medical University (Army Medical University), Chongqing, China

Objective: To provide the current research progress, hotspots, and emerging trends for AI in liver cancer, we have compiled a relative comprehensive and quantitative report on the research of liver disease using artificial intelligence by employing bibliometrics in this study.

Methods: In this study, the Web of Science Core Collection (WoSCC) database was used to perform systematic searches using keywords and a manual screening strategy, VOSviewer was used to analyze the degree of cooperation between countries/regions and institutions, as well as the co-occurrence of cooperation between authors and cited authors. Citespace was applied to generate a dual map to analyze the relationship of citing journals and citied journals and conduct a strong citation bursts ranking analysis of references. Online SRplot was used for in-depth keyword analysis and Microsoft Excel 2019 was used to collect the targeted variables from retrieved articles.

Results: 1724 papers were collected in this study, including 1547 original articles and 177 reviews. The study of AI in liver cancer mostly began from 2003 and has developed rapidly from 2017. China has the largest number of publications, and the United States has the highest H-index and total citation counts. The top three most productive institutions are the League of European Research Universities, Sun Yat Sen University, and Zhejiang University. Jasjit S. Suri and *Frontiers in Oncology* are the most published author and journal, respectively. Keyword analysis showed that in addition to the research on liver cancer, research on liver cirrhosis, fatty liver disease, and liver fibrosis were also common. Computed tomography was the most used diagnostic tool, followed by ultrasound and magnetic resonance imaging. The diagnosis and differential diagnosis of liver cancer are currently the most widely adopted research goals, and comprehensive analyses of multi-type data and postoperative analysis of patients with advanced liver cancer are rare. The use of convolutional neural networks is the main technical method used in studies of AI on liver cancer.

Conclusion: AI has undergone rapid development and has a wide application in the diagnosis and treatment of liver diseases, especially in China. Imaging is an indispensable tool in this filed. Mmulti-type data fusion analysis and

development of multimodal treatment plans for liver cancer could become the major trend of future research in AI in liver cancer.

KEYWORDS

bibliometrics, VOSviewer, Citespace, artificial intelligence, liver cancer

Introduction

Liver cancer is an extremely aggressive malignant tumor, ranking 7th in incidence and 4th in mortality worldwide. Studies have revealed that liver cancer has a high recurrence rate and low recovery rate, especially after the middle and late stages, and the 5-year survival rate of liver cancer is only 5-30% (1, 2). Therefore, it has become a global health problem. Despite advances in diagnosis and treatment of liver cancer, including improved diagnostic imaging accuracy and improved survival after neoadjuvant or conversion therapy, but it is limited. Accurate screening of early-stage liver cancer patients and high-risk patients, and rational treatment decisions for patients with advanced stage liver cancer are of great significance for improving the quality of life of patients.

With the development of medical big data and computer technology, artificial intelligence (AI) based on machine learning and deep learning has been widely used in current medical research (3–6). Through self-learning, summary, and induction of data, it can produce an intelligent reasoning system and choose the optimal solution to guide clinical decision-making (7). Original AI was based on traditional machine-learning methods, including support vector machine and random forest models, which all relied on human experience for learning and simple summary. As early as 2003, Hussain constructed a predictive system consisting of 12 genes, with Fisher's linear classifier, for predicting early recurrence in patients with hepatocellular carcinoma (HCC) (8). During this period, most studies have focused on simple analyses of data, such as genes and molecules (9–11). With the standardization of imaging diagnosis and its important role in the clinical diagnosis of liver cancer, AI research based on imaging has emerged by extracting high-throughput features that cannot be detected and defined by human eyes from large-scale image data to establish an intelligent decision -making model to assist clinical decision-making (12, 13). In particular, deep learning based on convolutional neural networks (CNNs) has promoted progress in liver cancer research (14–19).

As more and more researchers are interested in the use of AI in liver cancer, a large number of related studies have started being published. For example, reviews describing an overview of deep learning, convolutional neural networks and other AI technologies applications in liver cancer (20–22), reviews on the applications of AI on assisted imaging in diagnosis, prognosis and detection of liver cancer (23–25), and explained the latest research, on limitations and future development trends of AI have all been recently published. However, current reviews may be unable to explore grasp the latest research trends and hotspots in this field because of lack of a large number of publications. Meanwhile, there is a lack of quantitative analysis of all literature in this field. Additionally, a summary and quantitative analyses of the global development trend and research hotspots of AI in liver cancer is of great importance for future research. Bibliometrics is a method of information visualization which can achieve quantitative analysis of literature in a specific research field in a worldwide context through statistical methods and visualizing the results with the help of software (26–29). Bibliometrics plays an important role in sorting out development trends and research hotspots of a given field and has been widely used in many fields (26–29).

Therefore, we aimed to quantitatively analyze existing studies involving AI in liver cancer using bibliometrics to provide the current research progress, hotspots, and emerging trends for AI in liver cancer which may help researchers better understand grasp future research interest. Information was collated regarding countries/regions, institutions, authors, and journals with the highest citations and publications and keywords.

Methods

Data sources and search strategies

The Web of Science Core Collection (WoSCC), which is a standardized and comprehensive dataset, was used to compile the publication dataset in this study. AI is a branch of computer science and a technology that uses machines to simulate human intelligence. AI in this paper mainly includes traditional machine learning and the most popular deep learning algorithms. Therefore, the searching query string was described as follows: TS = (((liver OR hepatic) NEAR/1 (cancer* OR tumor* OR tumor* OR disease OR lesion* OR carcinoma*)) OR "hepatocellular carcinoma" OR "HCC") AND TS = (((automated OR intelligent) NEAR/1 (classification OR diagnosis OR segment* OR detect*)) OR "artificial intelligence" OR "deep learning" OR "convolutional neural network*" OR "machine learning" OR "CNNs" OR "artificial neural network*" OR "computer-aided" OR "Bayes* network*" OR "supervised learning" OR "unsupervised clustering" OR "computer-assisted" OR (deep NEAR/1 network*) OR "ensemble learning"). The retrieval was carried out on January 18, 2022. Figure 1 shows the workflow of the retrieval strategy in this research.

Strategy of manual screening

According to our research area, which focuses on the applications of AI in liver cancer, we designed the following search items: the papers for analysis were restricted to those that (1) were written in

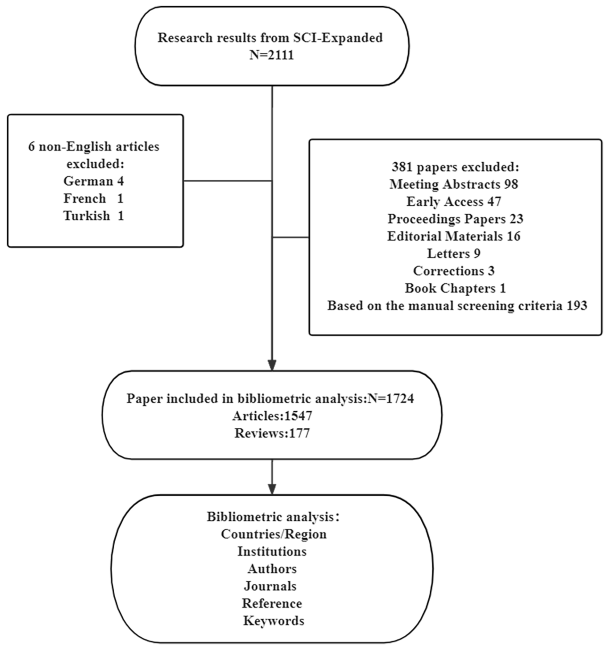

FIGURE 1
Flowchart of the search process in the study.

English, (2) focused on the field of liver cancer, (3) involved AI technologies. After the preliminary search, 2111 papers were included, and then we conducted further manual screening. In the manual screening process, all papers are divided into relevant, uncertain and excluded categories. Papers marked as unsure were screened by three of the authors (XH, LL, and MX) and discussed to determine whether they should be included. Unlike a systematic review, bibliometric analysis only requires screening of abstracts and full texts are only screened when necessary. According to the screening criteria, 193 papers were excluded because did not focus on the relevant field. Finally, 1724 papers were included in our study.

Bibliometric analysis and visualization

The analysis of the global trend of publications and citations and productive countries/regions is mainly to comprehensively understand the development trends of AI on liver cancer from beginning to end. The analysis of institutions, authors, and co-cited authors can quantitatively describe the strength of the cooperation between authors and institutions (30–32). Additionally, the analysis of top journals can analyze the level of cooperation and relationships in the concentrated fields of journals, which is beneficial to cross field cooperation in research (32). In particular, cluster co-occurrence analysis of keywords from different perspectives such as disease, data type, clinical goals, and clinical methods can help us understand the main topics and research trends in the current field of AI in liver cancer field.

We used VOSviewer (version 1.6.18) (33) and Citespace (version 6.1.R1) (34, 35) to perform bibliometric visual analysis on the data. VOSviewer was used to analyze the degree of cooperation between countries/regions and institutions, as well as the co-occurrence of cooperation between authors and cited authors. We used Citespace to generate a dual map, which showed the relationship between the main distribution fields of citing journals and citied journals. At the same time, we used Citespace to conduct a strong citation bursts ranking analysis of references. Meanwhile, an online SRplot was used for in-depth keyword analysis. In addition, we used Microsoft Excel 2019 (Microsoft, Redmond, WA) to analyze the targeted files. The top ten of top-cited or productive authors, countries/regions, publications, journals, and institutions were analyzed and tabulated.

In this study, five researchers (M.X., Y.X., Y.Z., S.H., and Q.Z.) were invited to search, download and analyze the publications to assure accuracy of data and repeatability of research.

Results

Global trend of publications and citations

A total of 1724 papers were collected from WoSCC database inception according to our data searching strategy, including 1547 original articles and 177 reviews (Figure 1). Research on AI in liver cancer started in 2003 and has increased every year (Figure 2). Research has advanced especially rapidly from 2017, accounting for almost 70% of all publications. As of the search date, all papers have been cited 27049 times, and the H-index and average citations per item are 67 and 15.69, respectively. The H-index (36) is a mixed index which could be used as a significant indicator of appraising both the number and level of academic output of a scientific researcher, country, journal, or institution.

Analysis of productive countries/regions

A total of 75 countries/regions had published related articles in this field, of which the top 10 in terms of publication count are China (608), the USA (470), India (129), Germany (122), Japan (118), Italy (105), England (75), South Korea (75), Canada (74), and France (73), accounting for 35.33%, 27.31%, 7.49%, 7.09%, 6.86%, 6.10%, 4.36%, 4.36%, 4.30%, and 4.24% of total publications, respectively (Table 1). The USA ranked first in H-index and total citations, with 49 and 10228 citations, respectively, which were both much higher than that of China in second place (38, 7298 citations, respectively). Moreover, the USA was first in terms of average citations per paper, followed by France and Italy. Figure 3 shows the degree of cooperation between countries when the minimum number of publications was set to at least 5. The lines between nodes indicate co-authorships between countries, where a thicker line indicates stronger cooperation (total link strength [TLS]). The top 5 TLSs were associated with the USA, China, India, Italy, and Canada.

Analysis of productive institutions

More than 2000 institutions have participated in research on AI in liver cancer, and the top 10 institutions with the highest contribution are shown in Table 2. The top three institutions were the League Of European Research Universities, Sun Yat Sen University, and Zhejiang University with a total of 109, 62, and 58 articles. Figure 4

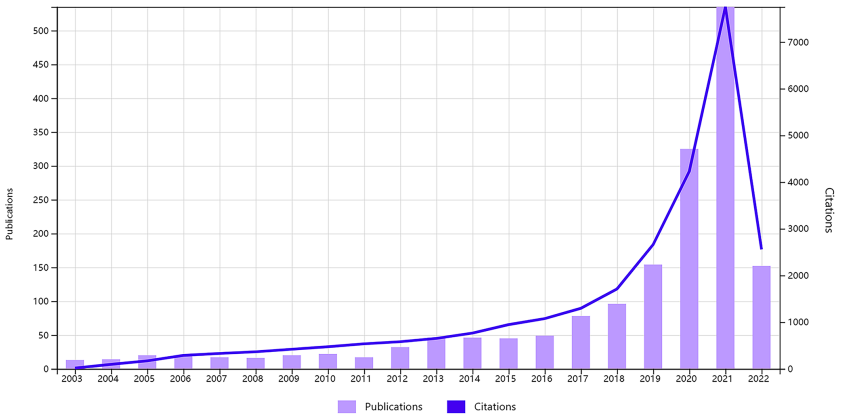

FIGURE 2
Global trend of publications and citations on artificial intelligence research in liver cancer from 2003 to 2022.

shows the TLS between institutions, and the top 3 TLSs were associated with Sun Yat Sen University (TLS = 187), Zhejiang University (TLS = 173), and the Mayo Clinic (TLS = 124).

Analysis of authors and co-cited authors

A total of 9916 authors and 37290 co-cited authors were included in the study. Table 3 shows the top 10 most productive authors, including 4 Chinese, 3 American, 2 Singaporean, and 1 Italian author. Jasjit S. Suri, Luca Saba, and Udyavara Rajendra Acharya were the top 3 authors, with 18, 17, and 15 articles, respectively. VOSviewer was also used to visualize the map of co-authorship of authors and co-citations (Figure 5). There were 78 authors with more than 45 citations, among which the top 3 TLSs were associated with U.R. Acharya (TLS = 2274), L. Saba (TLS = 1299), and O. Ronneberger (TLS = 1102).

Analysis of top journals

All related studies have been published in 585 journals. Table 4 shows the top 10 most productive journals, including their paper count, impact factor (IF), Journal Citation Ranking (JCR), H-index, and total count. The top 3 journals were *Frontiers in Oncology* (50, 2.90%), *European Radiology* (45, 2.61%), and *Scientific Reports* (41, 2.38%). Of the top 10 journals, there are 4 comprehensive medical journals (*Frontiers in Oncology*, *Scientific Reports*, *PLoS One*, *International Journal of Computer Assisted Radiology and Surgery*), 1 hepatobiliary professional journal (*World Journal of Gastroenterology*), 1 medical imaging journal (*European Radiology*), and 2 engineering journals (*Medical Physics*, *IEEE Access*). Forty percent of journals had a JCR of Q1. Figure 6 shows the dual map of journals and the relationship between citing journals and cited journals. There were mainly four citation paths, and the citing papers were mainly concentrated in three fields: (1) molecular, biology, and immunology; (2) medicine, medical, clinical; and (3) neurology, sports, ophthalmology. The cited papers were mainly located in 3 fields: (1) molecular, biology, genetics; (2) health, nursing, medicine; and (3) dermatology, dentistry, surgery.

Analysis of top cited references and co-citation references

Figure 7 shows the top 25 references with the strongest citation bursts. The explosion of citations in this field began in 2003, and a

TABLE 1 Top 10 productive countries/regions producing studies related to artificial intelligence in liver cancer.

Rank	Country	Counts	Percentage	H-index	Total citations	Average citation per paper
1	China	608	35.33	38	7298	12
2	USA	470	27.31	49	10228	21.76
3	India	129	7.49	21	1587	12.3
4	Germany	122	7.09	26	2169	17.78
5	Japan	118	6.86	25	2316	19.63
6	Italy	105	6.10	25	2171	20.68
7	England	75	4.36	20	1442	19.23
8	South Korea	75	4.36	15	655	8.73
9	Canada	74	4.30	18	1181	15.96
10	France	73	4.24	24	1541	21.11

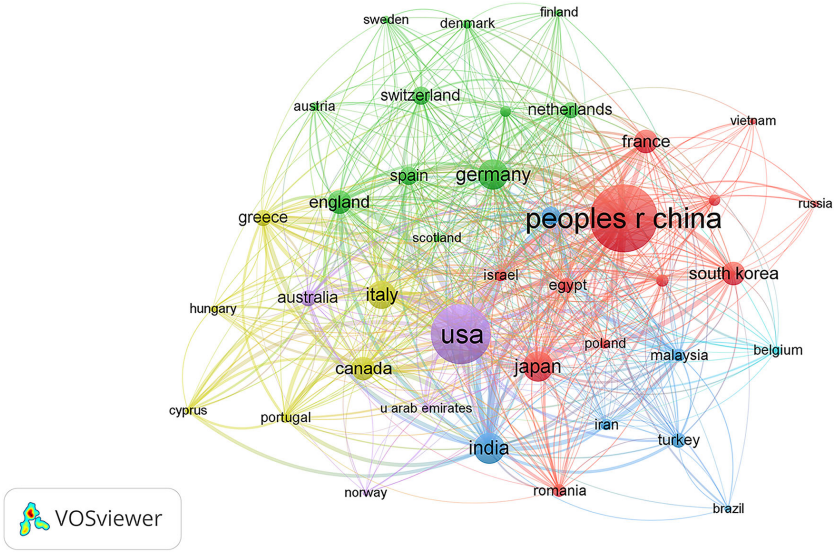

FIGURE 3
Citation network visualization map of countries/regions. The thickness of the lines reflects the citation strength.

large number of co-citation references were focused on the period from 2015 to 2019, indicating that research in this field was a hotspot in these years.

Analysis of keywords

An in-depth analysis of keywords from the diseases, data types, clinical goals, and methods (Figure 8) were conducted. Most articles focused on liver cancer, and HCC was widely studied as a single type of disease, followed by cirrhosis, fatty liver disease, liver fibrosis, liver transplantation, and hepatectomy, accounting for 30.76%, 33.52%, 11.10%, 9.45%, 8.39%, 4.41%, and 2.37%, respectively (Figure 8A). In terms of the data type, computed tomography (CT, 46.79%) was the most used, followed by ultrasound (23.58%), magnetic resonance imaging (MRI, 22.83%), and biopsy (6.79%) (Figure 8B). Figure 8E shows that in the study of liver cancer, including HCC, CT was the most used, followed by ultrasound and MRI. In addition, CT was mainly used for the research of liver fibrosis, ultrasound was mainly used for the research of fatty liver disease, and biopsy was mainly used for liver fibrosis research (Figure 8E). The differential diagnosis of HCC, are the key points, followed by the diagnosis of liver cirrhosis, liver fibrosis and fatty liver disease, are key points among the specific diagnosis, classification, and treatment of liver diseases. In terms of the prognosis of liver disease, the prognosis of HCC is a key focus, and the surgical methods for its treatment mainly include radiofrequency ablation and transarterial chemoembolization (Figure 8F). Three quarters of these papers were about diagnosis, classification, segmentation, or prediction, with relatively less attention to prognosis. Moreover, most liver cancer studies used CNNs, with a minority exclusively using more traditional techniques like support vector machine and decision trees (Figure 8D).

TABLE 2 Top 10 institutes with publications researching the use of artificial intelligence in liver cancer.

Rank	Institutions	Countries/regions	NP	H-index	NC	Average per item
1	League Of European Research Universities	Belgium	109	25	2746	25.49
2	Sun Yat Sen University	China	62	11	704	11.61
3	Zhejiang University	China	58	10	349	6.19
4	University Of Texas System	USA	57	17	1000	17.93
5	Chinese Academy Of Sciences	China	55	15	799	14.65
6	Fudan University	China	49	10	997	20.45
7	Udice French Research Universities	France	45	20	1103	24.62
8	Harvard University	USA	42	14	766	18.31
9	Stanford University	USA	40	19	791	20.25
10	University Of California System	USA	36	14	795	22.25

NP, number of publications; NC, number of citations.

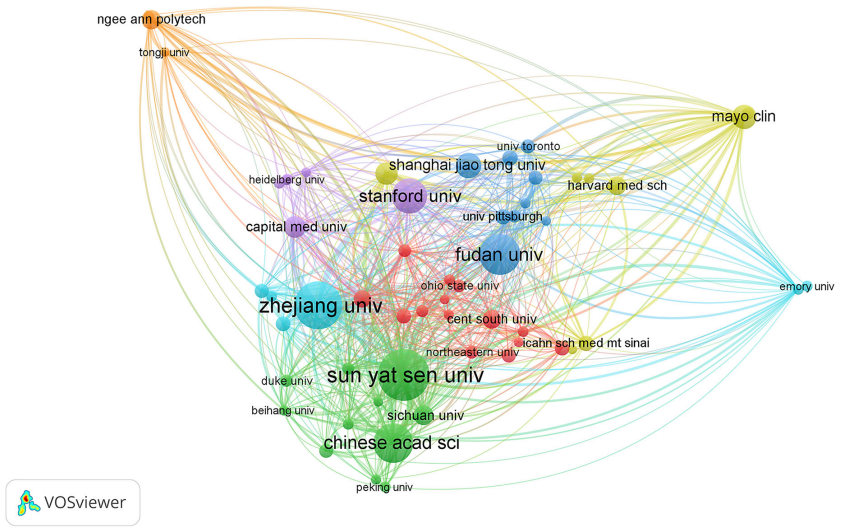

FIGURE 4
Citation network visualization map of institutions. The thickness of the lines reflects the citation strength.

TABLE 3 The 10 most productive authors of publications researching the use of artificial intelligence in liver cancer.

Rank	Author	Country	Count	Total citations	H-index	Average per item
1	Suri, Jasjit S.	USA	18	456	11	25.33
2	Saba, Luca	Italy	17	371	10	21.82
3	Acharya, Udyavara Rajendra	ingapore	15	519	11	34.6
4	Kuang, Ming	China	14	214	6	15.29
5	Chapiro, Julius	USA	12	237	6	19.75
6	Xing, Lei	USA	11	318	7	28.91
7	Hagiwara, Yuki	Singapore	11	207	6	18.82
8	Tian, Jie	China	11	191	7	17.36
9	Wang, Wei	China	11	177	5	16.09
10	Fan, Jiahao	China	9	56	5	6.22

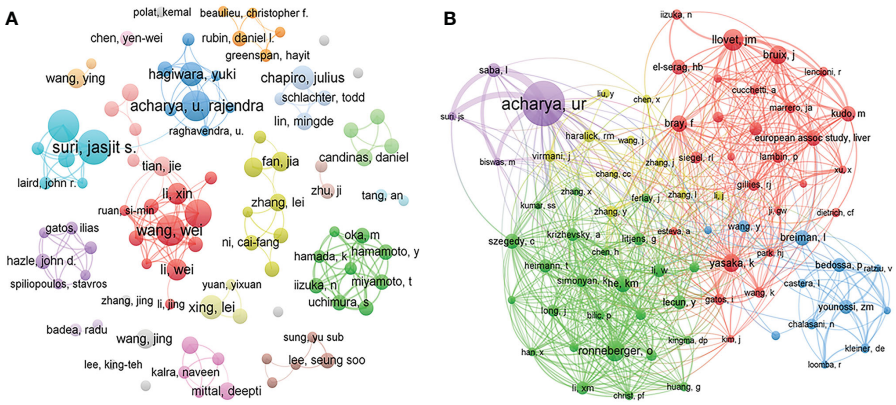

FIGURE 5
Visualization map of co-authorship **(A)** and co-citation **(B)** analyses of authors. The thickness of the lines reflects the citation strength.

TABLE 4 Top 10 journals related to research on artificial intelligence in liver cancer.

Rank	Journal	Count	IF (2020)	JCR (2020)	H-index	Total citations
1	*Frontiers in Oncology*	50	6.244	Q2	8	236
2	*European Radiology*	45	5.315	Q1	16	840
3	*Scientific Reports*	41	4.38	Q1	12	539
4	*Medical Physics*	35	4.071	Q1	13	549
5	*PLoS One*	35	3.24	Q2	15	675
6	*World Journal of Gastroenterology*	31	5.742	Q2	10	286
7	*International Journal of Computer Assisted Radiology and Surgery*	26	2.924	Q2/Q3	11	312
8	*Cancers*	23	6.639	Q1	5	74
9	*Computers in Biology and Medicine*	23	4.589	Q1/Q2	11	370
10	*IEEE Access*	22	3.367	Q2	7	139

IF, impact factor; JCR, Journal Citation Ranking.

Discussion

In this quantitative study, in order to systematically and quantitatively analyze the research status of AI in liver cancer, and explore the future research trends and hotspots in this field, we used a bibliometrics method to analyze the current research status of AI in liver cancer in terms of publication and citation trends, countries/regions and institutions, authors and co-cited authors, journals, cited references and co-citation references, and keywords. Ultimately, 1724 articles focusing on AI in liver cancer were collected from the WoSCC database and analyzed.

Research on AI in liver cancer mainly started in 2003 and entered a stage of rapid development in 2017. China is the most productive country with 35.33% of total publications; however, the USA ranked first according to the H-index, citations, and average citations per paper. It is notable that China, as a country with a high incidence of liver cancer, has a high number of studies on AI in liver cancer. However, most studies in China have limited impact, which may need further improvement from topic selection and research implementation. The League Of European Research Universities is the most productive institution, followed by Sun Yat Sen University and Zhejiang University. This is consistent with the conclusion of the most productive country above. We also found that cooperation between medical and industrial universities contributes to better research. For example, Sun Yat Sen University and the Chinese Academy Of Sciences (the second and fifth most productive institutions, respectively) have a strong TLS. Fu Dan University and Shanghai Jiaotong University also have a strong TLS. This indicated that the combination of medicine with engineering is helpful for the development of AI in medicine. It also suggested that studies should pay attention to the reasonable allocation of research teams.

The top three most productive journals had JCR scores of at least Q2. This shows that the field of AI in liver cancer is relatively mature and has a high level of concern and recognition. Moreover, most of the top 10 journals in this field are medical journals and include a small number of engineering journals, showing that the medical field pays more attention to AI in liver cancer. This suggests that we can consider and design studies from both medical and engineering aspects when conducting research, especially in medicine.

In the in-depth analysis of keywords, we found that most studies focused on liver cancer, especially HCC, showing that this is a research priority of liver disease. The second most common area of research was chronic hepatitis diseases such as liver cirrhosis, liver fibrosis, and fatty liver disease, which are more important for the prevention of liver cancer.

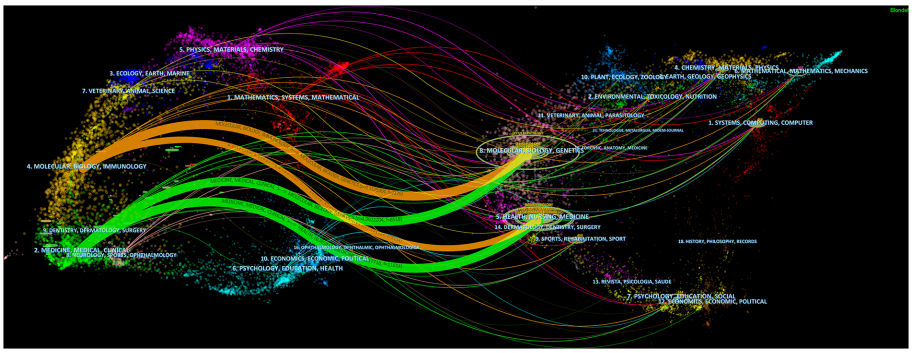

FIGURE 6
A dual-map overlap of journals with studies researching artificial intelligence in liver cancer.

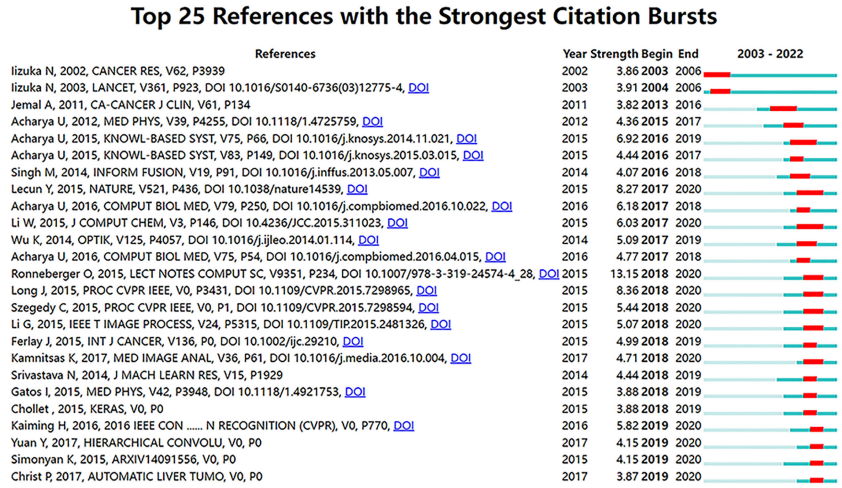

FIGURE 7
Visualization map of top 25 references with the strongest citation bursts from 2003 to 2022.

Regarding data type, studies of AI in liver cancer started from the simple data modeling of genetic or molecular data (9–11). With the development of medical imaging, research on medical imaging has been gradually increasing. CT, ultrasound, and MRI are the top three most used data types. First, this may because CT and MRI can be used as the basis for clinical treatment strategies for patients with liver cancer based on guidelines for liver cancer diagnosis. Moreover, ultrasound, as a screening method for patients at high risk of liver cancer, needs to be checked every six months. Therefore, the data volume of these three imaging methods has greatly increased, which has promoted the development of AI in liver cancer (37–39). Second, compared with MRI, CT has the advantages of fast inspection speed and cost-effectiveness, and is an indispensable and important imaging method in the diagnosis and treatment of liver cancer. Finally, although ultrasound is widely used in clinical practice, its image acquisition is seriously affected by the doctor's operation technique and machine model, the resolution is low, and the processing is difficult. Therefore, it is used less often than CT. However, it is worth noting that contrast-enhanced ultrasound has now been included as a recommended imaging modality for the diagnosis of liver cancer (40, 41) and is also widely used in the development and prognostic evaluation of ultrasound-guided radiofrequency ablation. This suggests that we could pay attention to the important role of ultrasound in liver cancer clinics in future research. At the same time, few studies used pathological, genetic, and other clinical data (42–44). The main reason may be that the medical cost of genetic examination is high and the realization of AI in multiomics research is difficult.

In the cross-analysis of data types and diseases, we found that biopsy was used as an important data type in studies of AI in liver fibrosis. This is mainly because the histopathological examination of liver biopsy is still the gold standard for the diagnosis of liver fibrosis (45). Conventional CT/MRI examinations can observe morphological changes of the liver; however, quantitative assessment of early-stage liver fibrosis is still difficult and is therefore less used. Although ultrasound elastography and magnetic resonance elastography (MRE) are highly effective non-invasive assessment methods in the diagnosis of liver fibrosis, a unified MRE liver elasticity value for liver fibrosis with different etiologies has not been established (46–48). This also indicates that the use of AI to quantitatively analyze liver fibrosis by imaging is a problem worthy of further study. In studies of AI in fatty liver disease, ultrasound is the first choice, mainly because of its high sensitivity in the diagnosis of diffuse fatty liver, convenience, cost-effectiveness, and safety, and plays an important role in judging the status of liver parenchyma.

In terms of clinical goals, the diagnosis and differential diagnosis of liver cancer on medical imaging are still major research priorities (19, 49–53). However, the clinical diagnosis of liver cancer is a comprehensive process, especially because of the variety and atypical characteristics of focal liver lesions. For example, dysplastic nodules in the state of liver cirrhosis have strong malignant potential, especially high-grade dysplastic nodules, and they are difficult to distinguish from early liver cancer in imaging. A comprehensive evaluation of the clinical indicators of the patient is usually required, including alpha-fetoprotein and abnormal prothrombin (54–58). However, there are still few studies that combine multiple types of data such as genetic data, molecular data, imaging data, and clinical indicators, and lack the support of large data and multi-center studies.

Studies on the treatment and prognosis of liver cancer mainly focused on the survival of a specific surgical method (59–66), such as radiofrequency ablation, transarterial chemoembolization and etc. Reports have proven that the modern therapies integrate a variety of neoadjuvant and adjuvant strategies have achieved dramatic improvements in survival, especially for patients with advanced HCC (66, 67). But the division of the patient population, the choice of potentially disclosing novel biomarkers still are controversies and the decision-making of precision treatment methods adapted to the specific patients, AI can play a role in this, but related research has not yet been seen.

In terms of methods used, some studies used traditional algorithms (51–53), such as support vector machine and random forests models, which were mainly concentrated in the early research stage. Since 2012, deep learning with CNNs has been widely used in the field, involving common tasks in the field of machine learning

10.3389/fonc.2023.990306

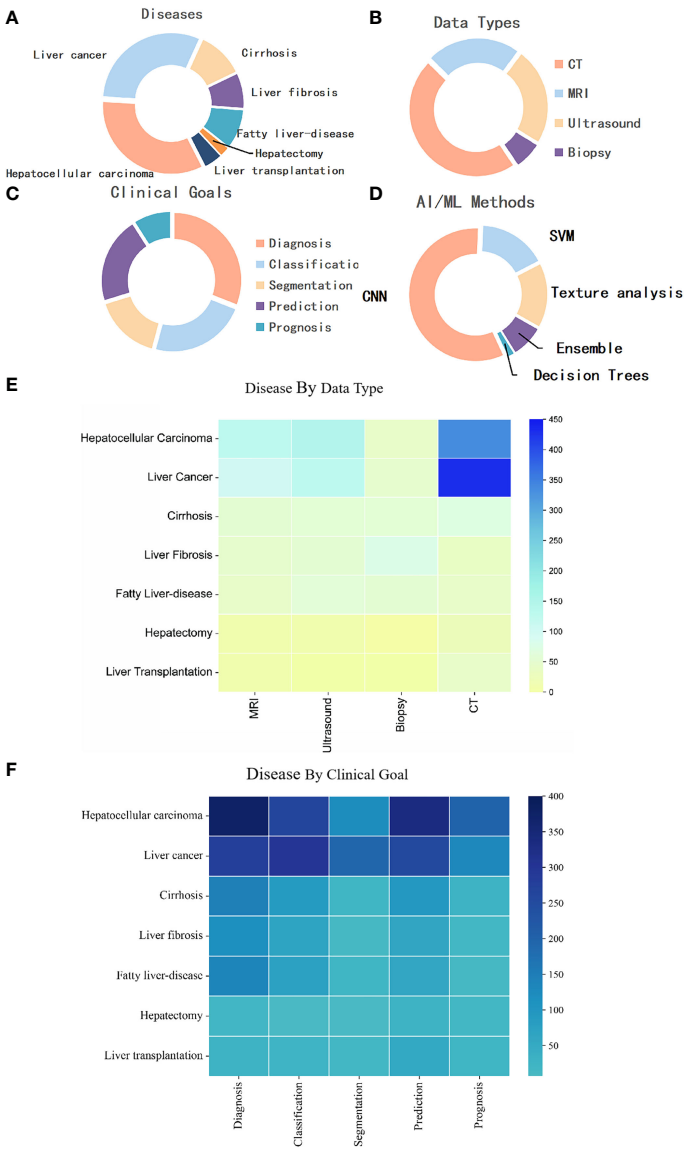

FIGURE 8
(A) Distribution of publications by disease category. **(B)** Distribution of publications by data modality. **(C)** Distribution of publications by goal. **(D)** Distribution of publications by AI/ML method. **(E)** Distribution of publications by disease by data type. **(F)** Distribution of publications by disease by clinical goal. MRI, magnetic resonance imaging; CNN, Convolutional Neural Network; SVM, support vector machine; CT, computed tomography.

such as diagnosis, prediction, and segmentation, and achieved good results (9, 49, 50, 68–70). Most tumor segmentation tasks use a U-Net method with a good effect, showing that U-Net has a good effect in the segmentation task in the medical field, especially for tasks with small amount of medical data (71, 72). It is estimated that the main research methods in later stages of research are still concentrated in the field of deep learning, which also indicates that future research aims to achieve better results and has higher technical requirements, especially for fusion modeling of multimodal data.

Previous meta-analyses and literature reviews focused on the applications of specific technologies in liver cancer or the development status of specific liver disease (22–29), such as reviewing studies on AI on assisted imaging in the diagnosis, prognosis and detection of liver cancer, or explaining the latest research, limitations, and future development trends of AI in a certain direction. However, they lack a quantitative analysis based on the available literatures. Therefore, a bibliometrics analysis was conducted in our study to summary the research status of AI in liver cancer. Bibliometrics analysis uses mathematical and statistical methods to study the literature system and bibliometric characteristics in a given field to mine the distribution structure, quantitative relationships, and changes of literature in this field. Visual display with the help of special software plays an important role in understanding the current development status and development trend of the field. However, our research also has limitations. First, we only included English articles in the WoSCC database and did not include articles in other databases or languages, which could lead to the omission of many studies. Second, keyword screening may not be perfect and could lead to omission of literature.

Conclusion

This study used bibliometrics to conduct an in-depth analysis of the published literature on AI in liver cancer. The results showed that AI has undergone rapid development and has a wide application in the diagnosis and treatment of liver diseases, especially in China, which has one of the highest incidences of liver cancer compared to other countries the world. In addition, intelligent analysis of imaging data is the hotspot and focus of current research in this field. However, combined with the current clinical difficulties such as accurate screening of early-stage liver cancer patients and high-risk patients, and selection of reasonable treatment decisions for advanced liver cancer patients, the use of AI for the fusion analysis of multiple types data in the process of diagnosis and treatment of liver cancer and multi-modal treatment decision-making for liver cancer are still relatively rare, and may become a future research trend.

Data availability statement

The raw data supporting the conclusions of this article will be made available by the authors, without undue reservation.

Author contributions

LL, XH, and YW conceived the study. MX, YX, YZ, SH, and QZ collected and analyzed the data. MX, YX, XH, and LL wrote the manuscript. LL, XH, and YW revised and reviewed the manuscript. All authors contributed to the article and approved the submitted version.

Funding

This work was supported by the National Natural Science Foundation of Chongqing (Grant No. cstc2021jcyj-msxmX0965), Joint Medical Research Project of Chongqing Science and Technology Commission and Health Commission (2021MSXM262), the National Natural Science Project (31771324 and 31671251), and Chongqing science and technology talent project (No.CQYC201905037).

Conflict of interest

The authors declare that the research was conducted in the absence of any commercial or financial relationships that could be construed as a potential conflict of interest.

Publisher's note

All claims expressed in this article are solely those of the authors and do not necessarily represent those of their affiliated organizations, or those of the publisher, the editors and the reviewers. Any product that may be evaluated in this article, or claim that may be made by its manufacturer, is not guaranteed or endorsed by the publisher.

References

1. International Agency for Research on Cancer and World Health Organization. *Cancer today* (2022). Available at: https://gco.iarc.fr/today/home (Accessed June 10, 2022).

2. Allemani C, Matsuda T, Di Carlo V, Harewood R, Matz M, Nikšić M, et al. Global surveillance of trends in cancer survival 2000-14 (CONCORD-3): analysis of individual records for 37 513 025 patients diagnosed with one of 18 cancers from 322 population-based registries in 71 countries. *Lancet* (2018) 391(10125):1023–75. doi: 10.1016/S0140-6736(17)33326-3

3. Zhang BH, Yang BH, Tang ZY. Randomized controlled trial of screening for hepatocellular carcinoma. *J Cancer Res Clin Oncol* (2004) 130(7):417–22. doi: 10.1007/s00432-004-0552-0

4. Shin HC, Roth HR, Gao M, Lu L, Xu Z, Nogues I, et al. Deep convolutional neural networks for computer-aided detection: CNN architectures, dataset characteristics and transfer learning. *IEEE Trans Med Imaging* (2016) 35(5):1285–98. doi: 10.1109/TMI.2016.2528162

5. Tran KA, Kondrashova O, Bradley A, Williams ED, Pearson JV, Waddell N. Deep learning in cancer diagnosis, prognosis and treatment selection. *Genome Med* (2021) 13 (1):152. doi: 10.1186/s13073-021-00968-x

6. Hosny A, Parmar C, Quackenbush J, Schwartz LH, Aerts HJWL. Artificial intelligence in radiology. *Nat Rev Cancer* (2018) 18(8):500–10. doi: 10.1038/s41568-018-0016-5

7. Schmidt-Erfurth U, Sadeghipour A, Gerendas BS, Waldstein SM, Bogunović H. Artificial intelligence in retina. *Prog Retin Eye Res* (2018) 67:1–29. doi: 10.1016/j.preteyeres.2018.07.004

8. Hussain HK, Londy FJ, Francis IR, Nghiem HV, Weadock WJ, Gebremariam A, et al. Hepatic arterial phase MR imaging with automated bolus-detection three-dimensional fast gradient-recalled-echo sequence: comparison with test-bolus method. *Radiology* (2003) 226(2):558–66. doi: 10.1148/radiol.2262011593

9. Iizuka N, Oka M, Yamada-Okabe H, Nishida M, Maeda Y, Mori N, et al. Oligonucleotide microarray for prediction of early intrahepatic recurrence of hepatocellular carcinoma after curative resection. *Lancet* (2003) 361(9361):923–9. doi: 10.1016/S0140-6736(03)12775-4

10. Ye QH, Qin LX, Forgues M, He P, Kim JW, Peng AC, et al. Predicting hepatitis b virus-positive metastatic hepatocellular carcinomas using gene expression profiling and supervised machine learning. *Nat Med* (2003) 9(4):416–23. doi: 10.1038/nm843

11. Lee JS, Chu IS, Heo J, Calvisi DF, Sun Z, Roskams T, et al. Classification and prediction of survival in hepatocellular carcinoma by gene expression profiling. *Hepatology* (2004) 40(3):667–76. doi: 10.1002/hep.20375

12. Kermany DS, Goldbaum M, Cai W, Valentim CCS, Liang H, Baxter SL, et al. Identifying medical diagnoses and treatable diseases by image-based deep learning. *Cell* (2018) 172(5):1122–1131.e9. doi: 10.1016/j.cell.2018.02.010

13. Campanella G, Hanna MG, Geneslaw L, Miraflor A, Werneck Krauss Silva V, Busam KJ, et al. Clinical-grade computational pathology using weakly supervised deep learning on whole slide images. *Nat Med* (2019) 25(8):1301–9. doi: 10.1038/s41591-019-0508-1

14. Saillard C, Schmauch B, Laifa O, Moarii M, Toldo S, Zaslavskiy M, et al. Predicting survival after hepatocellular carcinoma resection using deep learning on histological slides. *Hepatology* (2020) 72(6):2000–13. doi: 10.1002/hep.31207

15. Shi JY, Wang X, Ding GY, Dong Z, Han J, Guan Z, et al. Exploring prognostic indicators in the pathological images of hepatocellular carcinoma based on deep learning. *Gut* (2021) 70(5):951–61. doi: 10.1136/gutjnl-2020-320930

16. Cucchetti A, Piscaglia F, Grigioni AD, Ravaioli M, Cescon M, Zanello M, et al. Preoperative prediction of hepatocellular carcinoma tumour grade and micro-vascular invasion by means of artificial neural network: a pilot study. *J Hepatol* (2010) 52(6):880–8. doi: 10.1016/j.jhep.2009.12.037

17. Chaudhary K, Poirion OB, Lu L, Garmire LX. Deep learning-based multi-omics integration robustly predicts survival in liver cancer. *Clin Cancer Res* (2018) 24(6):1248–59. doi: 10.1158/1078-0432.CCR-17-0853

18. Vo VT, Yang HJ, Lee GS, Kang SR, Kim SH. Effects of multiple filters on liver tumor segmentation from CT images. *Front Oncol* (2021) 11:697178. doi: 10.3389/

fonc.2021.697178

19. Giordano S, Takeda S, Donadon M, Saiki H, Brunelli L, Pastorelli R, et al. Rapid automated diagnosis of primary hepatic tumour by mass spectrometry and artificial intelligence. *Liver Int* (2020) 40(12):3117–24. doi: 10.1111/liv.14604

20. Xiang K, Jiang B, Shang D. The overview of the deep learning integrated into the medical imaging of liver: a review. *Hepatol Int* (2021) 15(4):868–80. doi: 10.1007/s12072-021-10229-z

21. Nishida N, Yamakawa M, Shiina T, Kudo M. Current status and perspectives for computer-aided ultrasonic diagnosis of liver lesions using deep learning technology. *Hepatol Int* (2019) 13(4):416–21. doi: 10.1007/s12072-019-09937-4

22. Saba L, Biswas M, Kuppili V, Cuadrado Godia E, Suri HS, Edla DR, et al. The present and future of deep learning in radiology. *Eur J Radiol* (2019) 114:14–24. doi: 10.1016/j.ejrad.2019.02.038

23. Khan RA, Luo Y, Wu F-X. Machine learning based liver disease diagnosis: A systematic review. *Neurocomputing* (2022) 468(2022):492–509. doi: 10.1016/j.neucom.2021.08.138

24. Bharti P, Mittal D, Ananthasivan R. Computer-aided characterization and diagnosis of diffuse liver diseases based on ultrasound imaging: A review. *Ultrason Imaging* (2017) 39(1):33–61. doi: 10.1177/0161734616639875

25. Xu J, Jing M, Wang S, Yang C, Chen X. A review of medical image detection for cancers in digestive system based on artificial intelligence. *Expert Rev Med Devices* (2019) 16(10):877–89. doi: 10.1080/17434440.2019.1669447

26. Chen C, Dubin R, Kim MC. Emerging trends and new developments in regenerative medicine: a scientometric update (2000 - 2014). *Expert Opin Biol Ther* (2014) 14(9):1295–317. doi: 10.1517/14712598.2014.920813

27. Brandt JS, Hadaya O, Schuster M, Rosen T, Sauer MV, Ananth CV. A bibliometric analysis of top-cited journal articles in obstetrics and gynecology. *JAMA Netw Open* (2019) 2(12):e1918007. doi: 10.1001/jamanetworkopen.2019.18007

28. Ahmad P, Slots J. A bibliometric analysis of periodontology. *Periodontol* (2021) 85 (1):237–40. doi: 10.1111/prd.12376

29. Wilson M, Sampson M, Barrowman N, Doja A. Bibliometric analysis of neurology articles published in general medicine journals. *JAMA Netw Open* (2021) 4(4):e215840. doi: 10.1001/jamanetworkopen.2021.5840

30. Hassan W, Zafar M, Duarte AE, Kamdem JP, Teixeira da Rocha JB. Pharmacological research: A bibliometric analysis from 1989 to 2019. *Pharmacol Res* (2021) 169:105645. doi: 10.1016/j.phrs.2021.105645

31. Higaki A, Uetani T, Ikeda S, Yamaguchi O. Co-Authorship network analysis in cardiovascular research utilizing machine learning (2009-2019). *Int J Med Inform* (2020) 143:104274. doi: 10.1016/j.ijmedinf.2020.104274

32. Trujillo CM, Long TM. Document co-citation analysis to enhance transdisciplinary research. *Sci Adv* (2018) 4(1):e1701130. doi: 10.1126/sciadv.1701130

33. van Eck NJ, Waltman L. Software survey: VOSviewer, a computer program for bibliometric mapping. *Scientometrics* (2010) 84(2):523–38. doi: 10.1007/s11192-009-0146-3

34. Synnestvedt MB, Chen C, Holmes JH. CiteSpace II: visualization and knowledge discovery in bibliographic databases. *AMIA Annu Symp Proc* (2005) 2005:724–8.

35. Chen C. Searching for intellectual turning points: Progressive knowledge domain visualization. *Proc Natl Acad Sci USA* (2004) 101 Suppl 1(Suppl 1):5303–10. doi: 10.1073/pnas.0307513100

36. Ioannidis JPA, Baas J, Klavans R, Boyack KW. A standardized citation metrics author database annotated for scientific field. *PloS Biol* (2019) 17(8):e3000384. doi: 10.1371/journal.pbio.3000384

37. Heimbach JK, Kulik LM, Finn RS, Sirlin CB, Abecassis MM, Roberts LR, et al. AASLD guidelines for the treatment of hepatocellular carcinoma. *Hepatology* (2018) 67 (1):358–80. doi: 10.1002/hep.29086

38. European Association for the Study of the Liver. EASL clinical practice guidelines: Management of hepatocellular carcinoma. *J Hepatol* (2018) 69(1):182–236. doi: 10.1016/j.jhep.2018.03.019

39. Kokudo N, Hasegawa K, Akahane M, Igaki H, Izumi N, Ichida T, et al. Evidence-based clinical practice guidelines for hepatocellular carcinoma: The Japan society of hepatology 2013 update (3rd JSH-HCC guidelines). *Hepatol Res* (2015) 45(2):123–7. doi: 10.1111/hepr.12464

40. European Association for the Study of the Liver. EASL clinical practice guidelines: Management of hepatocellular carcinoma. *J Hepatol* (2019) 70(4):817. doi: 10.1016/j.jhep.2018.03.019

41. National Health Commission of the People's Republic of China. Guidelines for the diagnosis and treatment of primary liver cancer(V2019). *J Clin Hepatob Dis* (2022) 38 (2):288–303. doi: 10.3969/j.issn.1001-5256.2022.02.009

42. Zhang S, Liu Y, Chen J, Shu H, Shen S, Li Y, et al. Autoantibody signature in hepatocellular carcinoma using seromics. *J Hematol Oncol* (2020) 13(1):85. doi: 10.1186/s13045-020-00918-x

43. Ma L, Wang L, Khatib SA, Chang CW, Heinrich S, Dominguez DA, et al. Single-cell atlas of tumor cell evolution in response to therapy in hepatocellular carcinoma and intrahepatic cholangiocarcinoma. *J Hepatol* (2021) 75(6):1397–408. doi: 10.1016/j.jhep.2021.06.028

44. Zongyi Y, Xiaowu L. Immunotherapy for hepatocellular carcinoma. *Cancer Lett* (2020) 470:8–17. doi: 10.1016/j.canlet.2019.12.002

45. Di Tommaso L, Spadaccini M, Donadon M, Personeni N, Elamin A, Aghemo A, et al. Role of liver biopsy in hepatocellular carcinoma. *World J Gastroenterol* (2019) 25 (40):6041–52. doi: 10.3748/wjg.v25.i40.6041

46. Qayyum A, Hwang KP, Stafford J, Verma A, Maru DM, Sandesh S, et al. Immunotherapy response evaluation with magnetic resonance elastography (MRE) in advanced HCC. *J Immunother Cancer* (2019) 7(1):329. doi: 10.1186/s40425-019-0766-y

47. Pepin KM, Ehman RL, McGee KP. Magnetic resonance elastography (MRE) in cancer: Technique, analysis, and applications. *Prog Nucl Magn Reson Spectrosc* (2015) 90-91:32–48. doi: 10.1016/j.pnmrs.2015.06.001

48. Zhang T, Zhang G, Deng X, Zeng J, Jin J, Zeping H, et al. APS (Age, platelets, 2D shear-wave elastography) score predicts hepatocellular carcinoma in chronic hepatitis b. *Radiology* (2021) 301(2):350–9. doi: 10.1148/radiol.2021204700

49. Gao R, Zhao S, Aishanjiang K, Cai H, Wei T, Zhang Y, et al. Deep learning for differential diagnosis of malignant hepatic tumors based on multi-phase contrast-enhanced CT and clinical data. *J Hematol Oncol* (2021) 14(1):154. doi: 10.1186/s13045-021-01167-2

50. Cheng N, Chen D, Lou B, Fu J, Wang H. A biosensing method for the direct serological detection of liver diseases by integrating a SERS-based sensor and a CNN classifier. *Biosens Bioelectron* (2021) 186:113246. doi: 10.1016/j.bios.2021.113246

51. Shi J, Liu J, Tu X, Li B, Tong Z, Wang T, et al. Single-cell immune signature for detecting early-stage HCC and early assessing anti-PD-1 immunotherapy efficacy. *J Immunother Cancer* (2022) 10(1):e003133. doi: 10.1136/jitc-2021-003133

52. Ta CN, Kono Y, Eghtedari M, Oh YT, Robbin ML, Barr RG, et al. Focal liver lesions: Computer-aided diagnosis by using contrast-enhanced US cine recordings. *Radiology* (2018) 286(3):1062–71. doi: 10.1148/radiol.2017170365

53. Yang C, Huang X, Li Y, Chen J, Lv Y, Dai S. Prognosis and personalized treatment prediction in TP53-mutant hepatocellular carcinoma: an in silico strategy towards precision oncology. *Brief Bioinform* (2021) 22(3):bbaa164. doi: 10.1093/bib/bbaa164

54. Oestmann PM, Wang CJ, Savic LJ, Hamm CA, Stark S, Schobert I, et al. Deep learning-assisted differentiation of pathologically proven atypical and typical hepatocellular carcinoma (HCC) versus non-HCC on contrast-enhanced MRI of the liver. *Eur Radiol* (2021) 31(7):4981–90. doi: 10.1007/s00330-020-07559-1

55. Tzartzeva K, Obi J, Rich NE, Parikh ND, Marrero JA, Yopp A, et al. Surveillance imaging and alpha fetoprotein for early detection of hepatocellular carcinoma in patients with cirrhosis: A meta-analysis. *Gastroenterology* (2018) 154(6):1706–1718.e1. doi: 10.1053/j.gastro.2018.01.064

56. Wong RJ, Ahmed A, Gish RG. Elevated alpha-fetoprotein: differential diagnosis - hepatocellular carcinoma and other disorders. *Clin Liver Dis* (2015) 19(2):309–23. doi: 10.1016/j.cld.2015.01.005

57. Okuda H, Obata H, Nakanishi T, Furukawa R, Hashimoto E. Production of abnormal prothrombin (des-gamma-carboxy prothrombin) by hepatocellular carcinoma. a clinical and experimental study. *J Hepatol* (1987) 4(3):357–63. doi: 10.1016/s0168-8278(87)80546-9

58. Fujiyama S, Izuno K, Gohshi K, Shibata J, Sato T. Clinical usefulness of des-gamma-carboxy prothrombin assay in early diagnosis of hepatocellular carcinoma. *Dig Dis Sci* (1991) 36(12):1787–92. doi: 10.1007/BF01296626

59. Wu JP, Ding WZ, Wang YL, Liu S, Zhang XQ, Yang Q, et al. Radiomics analysis of ultrasound to predict recurrence of hepatocellular carcinoma after microwave ablation. *Int J Hyperthermia* (2022) 39(1):595–604. doi: 10.1080/02656736.2022.2062463

60. Yang Y, Zhou Y, Zhou C, Ma X. Deep learning radiomics based on contrast enhanced computed tomography predicts microvascular invasion and survival outcome in early stage hepatocellular carcinoma. *Eur J Surg Oncol* (2022) 48(5):1068–77. doi: 10.1016/j.ejso.2021.11.120

61. Zhang L, Jiang Y, Jin Z, Jiang W, Zhang B, Wang C, et al. Real-time automatic prediction of treatment response to transcatheter arterial chemoembolization in patients with hepatocellular carcinoma using deep learning based on digital subtraction angiography videos. *Cancer Imaging* (2022) 22(1):23. doi: 10.1186/s40644-022-00457-3

62. Li Q, Luo G, Li J. Evaluation of therapeutic effects of computed tomography imaging classification algorithm-based transcatheter arterial chemoembolization on primary hepatocellular carcinoma. *Comput Intell Neurosci* (2022) 2022:5639820. doi: 10.1155/2022/5639820

63. Müller L, Kloeckner R, Mähringer-Kunz A, Stoehr F, Düber C, Arnhold G, et al. Fully automated AI-based splenic segmentation for predicting survival and estimating the risk of hepatic decompensation in TACE patients with HCC. *Eur Radiol* (2022) 32 (9):6302–13. doi: 10.1007/s00330-022-08737-z

64. Liu Z, Liu Y, Zhang W, Hong Y, Meng J, Wang J, et al. Deep learning for prediction of hepatocellular carcinoma recurrence after resection or liver transplantation: a discovery and validation study. *Hepatol Int* (2022) 16(3):577–89. doi: 10.1007/s12072-022-10321-y

65. Liu F, Liu D, Wang K, Xie X, Su L, Kuang M, et al. Deep learning radiomics based on contrast-enhanced ultrasound might optimize curative treatments for very-early or early-stage hepatocellular carcinoma patients. *Liver Cancer* (2020) 9(4):397–413. doi: 10.1159/000505694

66. Petrowsky H, Fritsch R, Guckenberger M, De Oliveira ML, Dutkowski P, Clavien PA. Modern therapeutic approaches for the treatment of malignant liver tumours. *Nat Rev Gastroenterol Hepatol* (2020) 17(12):755–72. doi: 10.1038/s41575-020-0314-8

67. Gao Q, Wang ZC, Duan M, Lin YH, Zhou XY, Worthley DL, et al. Cell culture system for analysis of genetic heterogeneity within hepatocellular carcinomas and response to pharmacologic agents. *Gastroenterology* (2017) 152(1):232–242.e4. doi: 10.1053/j.gastro.2016.09.008

68. Phan DV, Chan CL, Li AA, Chien TY, Nguyen VC. Liver cancer prediction in a viral hepatitis cohort: A deep learning approach. *Int J Cancer* (2020) 147(10):2871–8. doi: 10.1002/ijc.33245

69. Chaichana A, Frey EC, Teyateeti A, Rhoongsittichai K, Tocharoenchai C, Pusuwan P, et al. Automated segmentation of lung, liver, and liver tumors from Tc-99m MAA SPECT/CT images for y-90 radioembolization using convolutional neural networks. *Med Phys* (2021) 48(12):7877–90. doi: 10.1002/mp.15303

70. Tsujimura K, Asamoto M, Suzuki S, Hokaiwado N, Ogawa K, Shirai T. Prediction of carcinogenic potential by a toxicogenomic approach using rat hepatoma cells. *Cancer Sci* (2006) 97(10):1002–10. doi: 10.1111/j.1349-7006.2006.00280.x

71. Seo H, Huang C, Bassenne M, Xiao R, Xing L. Modified U-net (mU-net) with incorporation of object-dependent high level features for improved liver and liver-tumor segmentation in CT images. *IEEE Trans Med Imaging* (2020) 39(5):1316–25. doi: 10.1109/TMI.2019.2948320

72. Wang J, Lv P, Wang H, Shi C. SAR-U-Net: Squeeze-and-excitation block and atrous spatial pyramid pooling based residual U-net for automatic liver segmentation in computed tomography. *Comput Methods Programs BioMed* (2021) 208:106268. doi: 10.1016/j.cmpb.2021.106268

frontiers | Frontiers in Oncology

TYPE Original Research
PUBLISHED 27 April 2023
DOI 10.3389/fonc.2023.1060687

OPEN ACCESS

EDITED BY
Sharon R. Pine,
University of Colorado Anschutz Medical Campus, United States

REVIEWED BY
Yankun Gao,
First Affiliated Hospital of Anhui Medical University, China
Varut Vardhanabhuti,
The University of Hong Kong,Hong Kong SAR, China

*CORRESPONDENCE
Shara W. Y. Lee
shara.lee@polyu.edu.hk
W. S. Leung
wsv.leung@polyu.edu.hk

RECEIVED 03 October 2022
ACCEPTED 10 April 2023
PUBLISHED 27 April 2023

CITATION
Ching JCF, Lam S, Lam CCH, Lui AOY, Kwong JCK, Lo AYH, Chan JWH, Cai J, Leung WS and Lee SWY (2023) Integrating CT-based radiomic model with clinical features improves long-term prognostication in high-risk prostate cancer. *Front. Oncol.* 13:1060687. doi: 10.3389/fonc.2023.1060687

Integrating CT-based radiomic model with clinical features improves long-term prognostication in high-risk prostate cancer

Jerry C. F. Ching[1], Saikit Lam[2,3], Cody C. H. Lam[1], Angie O. Y. Lui[1], Joanne C. K. Kwong[1], Anson Y. H. Lo[1], Jason W. H. Chan[1], Jing Cai[1], W. S. Leung[1]* and Shara W. Y. Lee[1]*

[1]Department of Health Technology and Informatics, The Hong Kong Polytechnic University, Hong Kong, Hong Kong SAR, China, [2]Department of Biomedical Engineering, The Hong Kong Polytechnic University, Hong Kong, Hong Kong SAR, China, [3]Research Institute for Smart Aging, The Hong Kong Polytechnic University, Hong Kong, Hong Kong SAR, China

Objective: High-risk prostate cancer (PCa) is often treated by prostate-only radiotherapy (PORT) owing to its favourable toxicity profile compared to whole-pelvic radiotherapy. Unfortunately, more than 50% patients still developed disease progression following PORT. Conventional clinical factors may be unable to identify at-risk subgroups in the era of precision medicine. In this study, we aimed to investigate the prognostic value of pre-treatment planning computed tomography (pCT)-based radiomic features and clinical attributes to predict 5-year progression-free survival (PFS) in high-risk PCa patients following PORT.

Materials and methods: A total of 176 biopsy-confirmed PCa patients who were treated at the Hong Kong Princess Margaret Hospital were retrospectively screened for eligibility. Clinical data and pCT of one hundred eligible high-risk PCa patients were analysed. Radiomic features were extracted from the gross-tumour-volume (GTV) with and without applying Laplacian-of-Gaussian (LoG) filter. The entire patient cohort was temporally stratified into a training and an independent validation cohort in a ratio of 3:1. Radiomics (R), clinical (C) and radiomic-clinical (RC) combined models were developed by Ridge regression through 5-fold cross-validation with 100 iterations on the training cohort. A model score was calculated for each model based on the included features. Model classification performance on 5-year PFS was evaluated in the independent validation cohort by average area-under-curve (AUC) of receiver-operating-characteristics (ROC) curve and precision-recall curve (PRC). Delong's test was used for model comparison.

Results: The RC combined model which contains 6 predictive features (tumour flatness, root-mean-square on fine LoG-filtered image, prostate-specific antigen serum concentration, Gleason score, Roach score and GTV volume) was the best-performing model (AUC = 0.797, 95%CI = 0.768-0.826), which significantly outperformed the R-model (AUC = 0.795, 95%CI = 0.774-0.816) and C-model (AUC = 0.625, 95%CI = 0.585-0.665) in the independent validation cohort. Besides, only the RC model score significantly classified patients in both cohorts into progression and progression-free groups regarding their 5-year PFS ($p < 0.05$).

Conclusion: Combining pCT-based radiomic and clinical attributes provided superior prognostication value regarding 5-year PFS in high-risk PCa patients following PORT. A large multi-centre study will potentially aid clinicians in implementing personalised treatment for this vulnerable subgroup in the future.

KEYWORDS

radiomic, high-risk, prostate cancer, prognosis, progression-free survival (PFS), radiation therapy, prostate-only radiotherapy, radiomic-clinical model

1 Introduction

Prostate cancer (PCa) ranks the second highest globally in terms of the prevalence of male malignancies, with more than 1.4 million new cases diagnosed in 2020 (1). High-risk PCa accounts for over one-third of the newly diagnosed PCa population, with a three-fold greater risk of developing distant metastasis compared to their low-risk counterparts. The management strategies of these two cohorts differ drastically. The low-risk PCa usually requires only active surveillance, while high-risk ones require combined modality therapy such as surgery, radiotherapy, systemic chemotherapy or hormonal therapy (2). Optimising treatment strategy for the high-risk is challenging.

Clinically undetectable occult pelvic nodal metastasis is commonly present in up to 40% of high-risk PCa patients (3). However, reliable detection of occult pelvic lymph node (PLN) metastasis is yet available for clinical use (4). It remains as an unresolved clinical challenge as to whether PLN should be prophylactically treated. The survival benefits and toxicity profiles of prostate-only radiotherapy (PORT), or prophylactic whole-pelvic radiotherapy (WPRT) were vigorously investigated in large randomised controlled trials (e.g. RTOG-9413), national database analysis and retrospective studies among the western population (5–9). Hence, the trade-off between better survival with WPRT and reduced toxicities with PORT is still highly debated.

Although the 5-year survival of high-risk PCa patients drastically increased by 23% over the years with greater emphasis on health-related quality of life (HRQoL) (10, 11), over 50% of high-risk PCa patients receiving PORT experienced recurrence, which was far higher than the 12.5% recurrence from the WPRT cohort (6). It is evident that a more refined subgrouping is necessary to predict which high-risk patient receiving PORT would experience recurrence within 5 years to support the clinical decision. Two commonly used conventional risk stratification tools are the National Institute for Health and Care Excellence (NICE) guideline and the Roach formula. The NICE guideline stratified patients into low, intermediate and high risk by clinical (c)T stage, prostate-specific antigen (PSA) serum concentration and Gleason score (GS) (12). Although all are prognostic markers (13–15), the cT stage is determined by digital rectal examination (DRE) that is subjected to high interobserver variability because (16) only a small portion of the prostate is palpable (17). The Roach score (RS) is also commonly used for risk stratification, based on the PSA and GS (18). A score of ≥15% is considered high-risk. A recent study reported that the RS has statistically significantly higher predictive power than the NICE guideline, with a concordance index of 0.724 and 0.715 respectively (13). However, the RS tends to overestimate the risk of occult PLN disease by 2.5 to 4 times among high-risk patients. This would result in the over-treatment of patients and compromise the therapeutic index (19, 20). Therefore, both NICE and RS may not be sufficiently effective in the era of precision medicine. There is a growing demand for developing a more refined, personalised risk stratification method for predicting treatment outcomes of high-risk PCa patients.

Recent advancement in artificial intelligence and radiomics accelerates the development of precision and personalised medicine. Radiomics adopts high-throughput methods to extract high-dimensional radiological features, transforming them into imaging biomarkers to improve clinical decisions (21). Magnetic resonance imaging (MRI) has been extensively studied, employing derived radiomic features for diagnosis or risk prediction of PCa. They showed promising classification performance on clinical endpoints such as GS or biochemical recurrence (BCR) (22–26). By contrast, very few investigations were conducted on the prognostic value of imaging biomarkers derived from the pCT of high-risk PCa patients, despite that the prognostic power of CT-

based radiomics has been widely reported in other types of primary solid tumours such as non-small cell lung cancer, nasopharyngeal carcinoma and renal cell carcinoma (27–30). Franzese et al. (31) was the only study employing pCT-derived radiomic features to predict metastasis-free survival in PCa patients treated by external beam radiotherapy (EBRT). However, the included patients in their study were treated with various kinds of treatment, including trans-urethral resection of the prostate, high-intensity focused ultrasound, and EBRT. The prognostic power of their model specifically on PORT-treated high-risk PCa patients remains to be explored.

To our best knowledge, this is the first study to investigate the feasibility of utilising pCT-derived radiomic features and clinical attributes to predict 5-year progression-free survival (PFS) in high-risk localised PCa patients following PORT. Recently, a systematic review in prostate radiomics suggested that incorporating clinical features into a radiomic model may improve its clinical utility (32). Given the inherently heterogeneous nature of the disease, conventional clinical factors may provide additional prognostic value (33). The success of this study may provide insightful findings for clinicians to optimise treatment strategies for managing high-risk PCa patients.

2 Methods and materials

2.1 Patients

2.1.1 Patient source

The present study was approved by the Human Subjects Ethics Sub-committee of the Hong Kong Polytechnic University (Reference: HSEARS20220406011) and Kowloon West Cluster Research Ethics Committee (KWC-REC) of the Hong Kong Hospital Authority (Reference: KW/EX-21-155 (165–05)). The requirement for individual informed consent was waived due to the retrospective nature of this study. One hundred and seventy-six biopsy-proven PCa patients who underwent definitive PORT at the Princess Margaret Hospital (PMH) in Hong Kong between February 2011 and December 2016 were retrospectively screened for eligibility. Following the inclusion and exclusion criteria (IEC) shown in Figure 1, 100 patients with localised (cT1-3, N0, M0) disease, with RS ≥ 15% (i.e. high-risk PCa) were included in this study.

2.1.2 Patient data

Clinical information such as the age at diagnosis, PORT start date and disease characteristics (clinical tumour (T), nodal (N) and distant metastatic (M) staging, histology, PSA serum concentration, GS, RS); treatment information (prescription and period of PORT and hormonal therapy, treatment techniques and organ contours); imaging information (pCT registered with organ contours); and clinical outcome (status of biochemical failure, regional and distant metastasis) were collected retrospectively.

2.1.3 Treatment approach and clinical endpoint

All patients were treated with PORT using intensity-modulated radiotherapy (IMRT), to a total of 70 or 74Gy. The treatment regimen also included neoadjuvant and concurrent antiandrogen and/or luteinising hormone-releasing hormone analogue (LHRHa) for 8-12 weeks, and 3 years of adjuvant LHRHa.

For this study, the clinical endpoint was the 5-year PFS status. Patients with disease progression manifested as biochemical recurrence, regional or distant metastasis, or death (34) were labelled “PFS-1”, with the others labelled as “PFS-0”. The Phoenix criteria of biochemical recurrence, defined as > 2 ng/mL rise from nadir PSA (35), was adopted in this study.

2.1.4 Patient stratification

The enrolled patients with treatment commenced on or before the date of 08/11/2016 were allocated to a training dataset (n = 75), and the remaining ones were assigned to an independent validation dataset (n = 25). The PFS-1 to PFS-0 ratio between the training and independent validation cohort was set at 6:4, referencing a similar work adopting temporal stratification (36). This patient

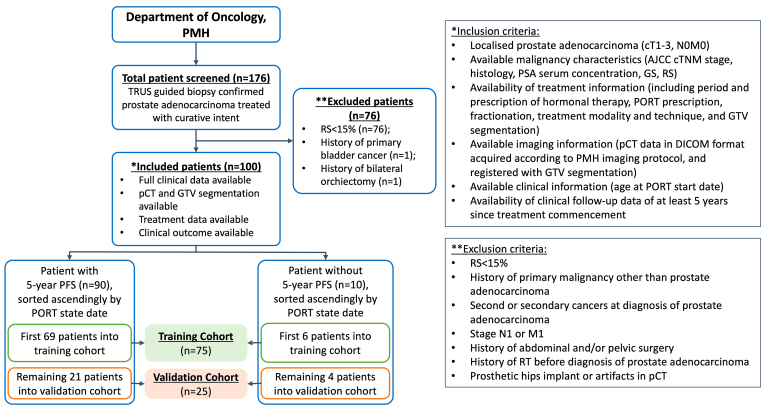

FIGURE 1
Patient stratification and inclusion-exclusion criteria. PMH, Princess Margaret Hospital; n denotes number of patients; TRUS, transrectal ultrasound; RS, Roach Score; pCT, planning computed tomography; GTV, gross tumour volume; PORT, prostate-only radiotherapy; AJCC, American Joint Committee on Cancer; PSA, prostate specific antigen; GS, Gleason score.

stratification approach has been widely adopted in similar studies (36–38), which complies with the recommendation provided in the Transparent Reporting of a Multivariable Prediction Model for Individual Prognosis or Diagnosis (TRIPOD) type-2b classification (39).

2.2 Planning CT acquisition and volume-of-interest segmentation

Patients underwent iodinated contrast-enhanced (intravenous injection of 120mL Omnipaque 300 mg/dL at 3 mL/second with 75 seconds scan delay) on one of the two CT scanners: 16-slice GE LightSpeed RT16 or GE BrightSpeed (GE Medical Systems, WI, USA). The pCT acquisition parameters included: X-ray tube voltage 120 kVp or 140 kVp; X-ray tube current 114-376 mA; field-of-view 500-650 mm; body filter; standard convolution kernel; matrix size 512x512; pixel spacing 0.98-1.27 mm; and reconstruction thickness 2.5 mm. The pCT scans were acquired 24 (range, 6-47) days on average before PORT commencement. All pCT scans were stored in Picture Archiving and Communication System (PACS) in Digital Imaging and Communications in Medicine (DICOM) format. All pCTs scans were registered with GTV segmentation, which was the VOI for radiomic feature extraction and modelling in this study. The GTV of all patients were segmented by experienced oncologists on the Eclipse ARIA system (version 8.6.15 or 13.0.26, Varian Medical System). The delineation of VOI is performed according to the ESTRO ACROP consensus guideline (40). A team of oncologists with expertise in prostate cancer radiotherapy delineated the ROI. To address the inter-observer variabilities, the contours were all reviewed and approved by a Consultant Oncologist before use. Calcification, necrosis, nor artifacts due to fiducial markers were not found in all the included cases in this study. The GTV segmentation of a representative patient is illustrated in Figure 2.

2.3 CT image pre-processing

All pCT images were pre-processed before radiomic feature extraction, in compliance with the recommendations provided in the internationally accepted Image Biomarker Standardisation Initiative (IBSI) guideline (41). All steps were implemented by an in-house developed pipeline (IhDP) which used an open-source Pyradiomics v2.2.0 with SimpleITK v1.2.4 package on Python v3.7.3 platform. pCT was first resampled to 1 mm isotropic voxels by B-spline interpolation to account for voxel spacing variation while avoiding longitudinal image oversampling (41). Resampled pCT were discretized to 10-Hounsfield unit (HU) bins to homogenise intensity resolution (42). The GTV was re-segmented by HU thresholding, bounded by -150 and 180 HU (43). Six kernel sizes of Laplacian of Gaussian (LoG) filters, 0.5, 1, 2, 3, 4 and 5 mm, were used to reconstruct the image, facilitating fine and coarse texture feature extraction at different resolutions (44).

FIGURE 2
Representative example of a GTV segmentation on contrast-enhanced pCT of a high-risk prostate cancer patient.

2.4 Feature extraction & feature normalization

A total of 665 radiomic features from the GTV were extracted using the IhDP. Types of the extracted features of both unfiltered and LoG-filtered images included shape (n = 14), first-order intensity (n = 108) and texture (n = 543). Details of the extracted features classes and their distributions are shown in Supplementary Material.

Before analysis, all radiomic features were normalised by using z-score transformation using R software (version 4.1.3). Specifically, features were centred and scaled firstly in the training cohort in which each feature had a mean of 0 and a standard deviation of 1. The normalisation factors obtained in the training cohort were then used to perform feature normalisation in the independent validation cohort.

2.5 Feature selection & model development

Relevant feature selection processes including the Spearman correlation coefficient (SCC) and Mann-Whitney U test were performed on the training cohort before the use of Ridge regression algorithms (44–46). The independent validation cohort was adopted for independent model validation. All model training and validation were performed using the R software.

For the radiomic model development, the SCC was first calculated for each pair of radiomic features in the training cohort using the R package "caret". When the absolute correlation coefficient (r) was ≥ 0.6 in any of the feature pairs, the feature with a higher mean absolute correlation was removed from the original feature set to minimise the likelihood of multicollinearity and model overfitting (21). The clinical significance of the remaining features was assessed by using a two-sided, unpaired Mann-Whitney U test in the training cohort by executing the "wilcox.test' function in the R software, while features with $p > 0.1$ were removed. A L2 regularisation was performed using ridge regression in the R package "glmnet". Ridge regression penalises regression coefficients through hyperparameter (λ) tuning in a grid search. The λ yielding a minimum cross-validation error was then chosen. The objective function was optimised through cyclical coordinate descent in the R package "glmnet".

For the clinical model development, clinical features including PSA serum concentration, GS, RS and GTV volume formed the initial feature set. PSA was categorised into< 10, 10-20 and > 20 ng/mL while GS was classified into five groups (14). RS was divided into 4 categories: 15-25%, > 25-35%, > 35%-45% and > 45% (18). All clinical features were tested for correlation using the SCC test in the training cohort. The same correlation threshold of r ≥ 0.6 as in the R model was applied. Ridge regression was also performed.

To develop the radiomic-clinical (RC) combined model, all selected radiomic and clinical features were combined and fitted into the ridge regression. A 5-fold cross-validation was employed with 100 iterations to obtain the average predictive performance model. The model score was calculated as

$$Model \quad Score = (Coefficient) \times (Feature \quad Value) + Intercept$$

Three model scores were calculated for each patient: R (R-score), C (C-score) and RC combined (RC-score) models. The R package "cvAUC" and "PRROC" were used to compute the averaged area under the receiver-operating characteristics (ROC-AUC) curves and precision-recall curve (PRC). Other performance indicators including sensitivity, specificity, accuracy and the Youden index (YI) were calculated by the R package "pROC". The optimal cut-off in each model was determined using the Youden method (47).

2.6 Statistical analysis

All continuous variables have been verified for conformity by the Shapiro-Wilk test. Statistical differences of continuous clinical and demographic variables were evaluated by the Mann-Whitney U test, while categorical variables were assessed by Chi's square or Fisher-exact test as appropriate. Performance of the R, C and RC combined models were compared using the Delong test, based on their averaged ROC-AUC in both training and independent validation cohorts. The correlations between RC-score, radiomic and clinical variables were evaluated by SCC to reveal any dominant features in the model that contribute heavily to the RC-score. SCC was also used to assess inter-feature correlation in the training cohort for feature screening. All statistical tests were two-sided with a value of p< 0.05 considered statistically significant.

3 Results

3.1 Patient characteristics

Among 176 patients screened for eligibility, 100 cases met the inclusion criteria. 10 included patients who experienced disease progression were labelled as "PFS-1", in which 6 (8%) and 4 (16%) were allocated to the training and independent validation cohorts respectively. Table 1 summarises the characteristics of the enrolled patients.

No statistically significant difference was detected in the distribution of age, PSA serum concentration, GS, RS, GTV volume, neoadjuvant hormonal therapy (NHT), concurrent hormonal therapy (CHT) and adjuvant hormonal therapy (AHT) regimen between training and independent validation cohorts, except for the PORT dose scheme (p< 0.001). Furthermore, PSA, GS, RS and GTV volumes were not significantly different between PFS-1 and PFS-0 patients in both cohorts, except for the CHT regime.

3.2 Model development

A simplified modelling workflow is illustrated in Figure 3. In the R model, 40 features with high independence (r< 0.6) shown in the correlation map (Supplementary Material) underwent further elimination. Among them, the unfiltered-shape-flatness and LoG-1mm-filtered root-mean-square (RMS) features were chosen for the development of the R model. In the C model, the Spearman correlations between PSA, GS, RS and GTV volume were less than 0.6 (Supplementary Material). Therefore, all 4 clinical features were used for modelling. The R and C models consisted of 2 radiomic and 4 clinical features respectively, while these 6 features were combined in the RC model.

Table 2 lists the intercepts and coefficients of all three models. Patients with model scores higher than the optimal cut-off were classified as high-risk of having disease progression within 5 years since the commencement of treatment, or vice versa.

3.3 Model evaluation

The performance of each model in both the training and independent validation cohorts is summarised in Table 3. The ROC and PR curves are shown in Figure 4. Boxplots of the model scores are presented in Figure 5.

The RC combined model yielded the highest ROC-AUC (0.797, 95%CI = 0.786-0.826) in the independent validation cohort compared to the R (0.795, 95%CI = 0.774-0.816) and C (0.625, 95%CI = 0.585-0.665) models. The DeLong test showed that the RC combined model had a ROC-AUC significantly higher than the C model in both training (0.747 vs. 0.554, p< 0.001) and independent validation (0.797 vs. 0.625, p< 0.001) cohorts. A similar finding was also observed with the RC model demonstrating a higher ROC-AUC than the R model in the independent validation cohort (0.797 vs. 0.795, p<.001). Moreover, the RC combined model had the highest PR-AUC, accuracy and YI compared to R and C models in the independent validation cohort. The RC combined model also attained a relatively high sensitivity and specificity of 0.808 and 0.722 in the training cohort and 0.793 and 0.653 in the independent validation cohort, respectively.

Of note, the RC combined model was the only model that resulted in a significantly different RC-score between PFS-1 and PFS-0 patients in both the training (median: -2.428 vs. -2.447, p = 0.01) and independent validation cohorts (median: -2.411 vs. -2.451, p = 0.03). On the other hand, the R model failed to render a significantly different R-score in the independent validation cohort (median: -2.368 vs. -2.491, p = 0.08). Similarly, the C model did not yield any significant difference in C-score for

TABLE 1 Patient characteristics.

Patient Characteristics	Whole Cohort	Training Cohort				Validation Cohort				p**
		All	PFS-1	PFS-0	p*	All	PFS-1	PFS-0	p*	
Patients, n	100	75	6	69	–	25	4	21	–	–
Age at PORT start date, median (range)	72 (52–86)	72 (55-84)	70 (58-78)	72 (55-84)	0.66	70 (52-86)	69 (52-86)	73.5 (68-82)	0.32	0.93
PSA before PORT, ng/mL, n (%)					0.37				0.80	0.11
< 10	10 (10)	6 (8)	0 (0)	6 (8.7)		4 (16)	1 (25)	3 (14.3)		
10-20	29 (29)	19 (25.3)	3 (50)	16 (23.2)		10 (40)	1 (25)	9 (42.9)		
> 20	61 (61)	50 (66.7)	3 (50)	47 (68.1)		11 (44)	2 (50)	9 (42.9)		
GS grade group, n (%)					0.75				0.64	0.11
GS ≤ 6	11 (11)	11 (14.7)	0 (0)	11 (15.9)		0 (0)	0 (0)	0 (0)		
GS = 3 + 4	21 (21)	14 (18.7)	2 (33.3)	12 (17.4)		7 (28)	1 (25)	6 (28.6)		
GS = 4 + 3	17 (17)	13 (17.3)	1 (16.7)	12 (17.4)		4 (16)	0 (0)	4 (19.0)		
GS = 8	24 (24)	20 (26.7)	1 (16.7)	19 (27.5)		4 (16)	0 (0)	4 (19.0)		
GS = 9-10	27 (27)	17 (22.7)	2 (33.3)	15 (21.7)		10 (40)	3 (75)	7 (33.3)		
RS, n (%)					0.94				0.61	0.71
15-25%	29 (29)	22 (29.3)	1 (16.7)	21 (30.4)		7 (28)	0 (0)	7 (33.3)		
> 25-35%	19 (19)	16 (21.3)	2 (33.3)	14 (20.3)		3 (12)	0 (0)	3 (14.3)		
> 35-45%	22 (22)	15 (20)	1 (16.7)	14 (20.3)		7 (28)	2 (50)	5 (23.8)		
> 45%	30 (30)	22 (29.3)	2 (33.3)	20 (29.0)		8 (32)	2 (50)	6 (28.6)		
GTV volume, cm^3, median (range)	42.7 (15.7-170.6)	43.5 (15.7-170.6)	40.9 (24.9-86.8)	43.5 (15.7-170.6)	0.52	35.6 (18.1-100.4)	34.1 (22.5-63.7)	41.7 (18.1-100.4)	0.92	0.10
PORT dose/fractionation, n (%)					0.29				0.16	< 0.001
70Gy/35fr	31 (31)	31 (41.3)	4 (66.7)	27 (39.1)		0 (0)	0 (0)	0 (0)		
74Gy/35fr	67 (67)	43 (57.3)	2 (33.3)	41 (59.4)		24 (96)	3 (75)	21 (30.4)		
74Gy/37fr	2 (2)	1 (1.3)	0 (0)	1 (1.4)		1 (4)	1 (25)	0 (0)		
NHT, n (%)					> 0.99				0.42	0.18
Antiandrogen only	4 (4)	2 (2.7)	0 (0)	2 (2.9)		2 (8)	1 (25)	1 (4.8)		
Antiandrogen with LHRHa	94 (94)	72 (96)	6 (100)	66 (95.7)		22 (88)	3 (75)	19 (90.5)		
LHRHa only	1 (1)	0 (0)	0 (0)	0 (0)		1 (4)	0 (0)	1 (4.8)		
None	1 (1)	1 (1.3)	0 (0)	1 (1.4)		0 (0)	0 (0)	0 (0)		
CHT, n (%)					0.71				0.003	0.88
Antiandrogen only	18 (18)	12 (16)	1 (16.7)	11 (15.9)		6 (24)	3 (75)	3 (14.3)		
Antiandrogen with LHRHa	59 (59)	45 (60)	5 (83.3)	40 (58)		14 (56)	0 (0)	14 (66.7)		
LHRHa only	18 (18)	14 (18.7)	0 (0)	14 (20.3)		4 (16)	0 (0)	4 (19)		
None	5 (5)	4 (5.3)	0 (0)	4 (5.8)		1 (4)	1 (25)	0 (0)		
AHT, n (%)					0.11				0.11	0.80
Antiandrogen only	2 (2)	1 (1.3)	0 (0)	1 (1.4)		1 (4)	1 (25)	0 (0)		
Antiandrogen with LHRHa	7 (7)	5 (6.7)	1 (16.7)	4 (5.8)		2 (8)	1 (25)	1 (4.8)		

(Continued)

TABLE 1 Continued

Patient Characteristics	Whole Cohort	Training Cohort				Validation Cohort				p**
		All	PFS-1	PFS-0	p*	All	PFS-1	PFS-0	p*	
LHRHa only	81 (81)	61 (81.3)	3 (50)	58 (84.1)		20 (80)	2 (50)	18 (85.7)		
None	10 (10)	8 (10.7)	2 (33.3)	6 (8.7)		2 (8)	0 (0)	2 (9.5)		

PORT, prostate-only radiotherapy; PSA, prostate specific antigen; GS, Gleason score; RS, Roach score; GTV, gross tumour volume; NHT, neoadjuvant hormonal therapy; CHT, concurrent hormonal therapy; AHT, adjuvant hormonal therapy; LHRHa, luteinizing hormone-releasing hormone analogue; n denotes the number of patients; PFS, progression-free survival, *refers to p derived from univariate analysis on association of each patient characteristics with the status of 5-year PFS, **refers to p derived from patient characteristics comparison between the training and validation cohorts.

either the training (median: -2.405 vs. -2.440) or independent validation cohort (-2.383 vs. -2.425).

3.4 Correlation analysis among RC-scores, radiomic and clinical features

The average absolute SCC (r) of R features with RC-scores (r = 0.603) was ~2.6 times higher than that of C features with RC-scores (r = 0.235). Among radiomic features, LoG-1mm-filtered RMS had the highest correlation with the RC-score (r = 0.797), followed by the unfiltered-shape-flatness (r = 0.409). The clinical features with the highest and lowest correlation with RC-score were GS (r = 0.411) and GTV volume (r = 0.105) respectively. Between radiomic and clinical features, unfiltered-shape-flatness and LoG-1mm-filtered RMS had the highest correlation with RS (r = 0.372) and GTV volume (r = 0.228), respectively. The correlation matrix (Supplementary Material) described in detail the correlation between RC-scores of patients in the independent validation cohort and their corresponding R and C features.

4 Discussion

For the first time, we demonstrated that combining CT-based radiomic (unfiltered-shape-flatness, LoG-1mm-filtered RMS) and clinical attributes (PSA, GS group, RS group and GTV volume) provided superior prognostic value for 5-year PFS in high-risk PCa patients following PORT. The DeLong test revealed that the ROC-AUC of the RC combined model was significantly higher than those of the R and C models in the independent validation cohort. The RC model had the highest overall accuracy and YI. Only the RC model score significantly classified patients into "progression" (PFS-1) and "progression-free" (PFS-0) groups according to their 5-year PFS in both training and independent validation cohorts (both $p < 0.05$). These findings suggested the potential of the RC combined model in supporting clinicians to implement personalized treatment for this vulnerable patient subgroup in the future. For instance, if a patient is classified into the "progression" (PFS-1) group ahead of the commencement of the PORT treatment, clinicians may consider a more aggressive therapy (e.g., WPRT) for improving the prognosis of the given patient.

The two identified radiomic features (unfiltered-shape-flatness and LoG-1mm-filtered RMS) are in line with previous studies using CT images (27, 28, 48, 49). Unfiltered-shape-flatness is a shape feature calculated by the square root of the least axis length divided by the major axis length (48). A value closer to zero indicates the tumour is flatter. This feature was reported in another CT radiomic model for predicting tumour response in lung cancer patients receiving EBRT (49). Additionally, the RC-score was negatively

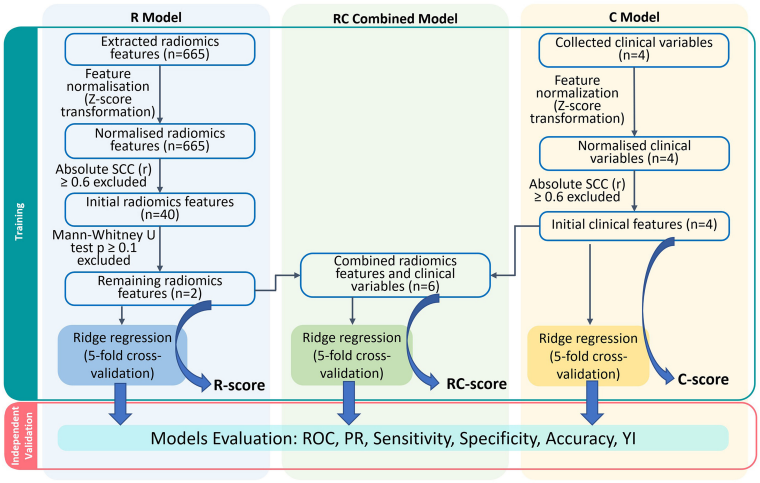

FIGURE 3
Models construction workflow. R, Radiomics; RC, Radiomic-clinical; C, clinical; n denotes number of features; ROC, receiver-operating characteristic; PR, precision-recall; YI, Youden index.

TABLE 2 Intercepts and selected radiomic and/or clinical features of the R, C and RC combined models.

Intercept and Coefficients	Values of Intercept and Coefficients of Each Model		
	R Model	C Model	RC Combined Model
Intercept	-2.463	-2.450	-2.445
Raw_shape_flatness	-0.052	—	-0.010
LoG_1mm_first-order_root-mean-square	-0.101	—	-0.017
PSA	—	-0.032	-0.005
GS	—	0.015	0.004
RS	—	0.033	0.004
GTV volume	—	-0.044	-0.006

R, radiomics; C, clinical; RC, radiomic-clinical; LoG, Laplacian of Gaussian; PSA, prostate specific antigen; GS, Gleason score; GTV, gross tumour volume.
—, feature absent.

correlated to the flatness, with a lower flatness value indicating a poorer prognosis. Such a finding is consistent with Khodabakhshi's study, which predicted the OS of patients with renal cell carcinoma (27). The feature LoG-1 mm-filtered RMS is calculated by the mean of all squared intensity values in LoG-1mm-filtered ROI (48). Similar to flatness, it is negatively correlated to the RC-score. The RMS has been reported in a CT radiomic model study for lung adenocarcinoma, in which a lower value was associated with poorer PFS and OS (28). The prognostic implications of these features have not been reported for PCa, and the association between the selected pCT radiomic features and biological properties remains unclear. Indeed, the RC model was dominated by the R features since the absolute SCC of R features with RC-score was ~2.6 times higher than those of clinical features (Supplementary Material). Further investigation is needed to explore the biological mechanism of radiomic features.

Another notable finding is the lack of textural features in the RC combined model. It may be attributed to the intrinsic property of pCT images and the clinical endpoint of our study. Most prostate radiomic studies use MRI-derived features for prognostic prediction (22–24, 50). In a study using T2-weighted MRI, features with the highest predictive value originated from the gray-level run-length matrix (GLRLM) texture feature class (23). Another two studies using apparent diffusion coefficient (ADC) MRI for radiomics modelling (23, 24) suggested that the gray-level co-occurrence matrix (GLCM) texture feature class contained the most predictive features. However, in a prostate radiomic study (51) exploring interfraction cone-beam CT, both shape and first-order features have excellent capability in predicting patient outcomes, which was similar to our study. In addition, these two features were also found to be capable of predicting PFS in both nasopharyngeal carcinoma (NPC) and NSCLC (29, 30). Meanwhile, texture features dominate in MRI-based NPC radiomic studies (52, 53). These observations suggested that the feature class selected for PFS prediction could be influenced by the choice of imaging modality. This may be explained by the inherently lower soft-tissue contrast characteristic in CT than in MRI, resulting in less prominent texture features that may be relevant to the PFS. Texture features in CT and MRI have been regarded as the manifestation of tumour heterogeneity. Hence, the dominant feature class may vary according to different clinical endpoints. For instance, texture features are often selected in both CT and MRI prostate radiomic studies when GS is chosen as the clinical endpoint (25, 42). It is not surprising since GS is the gold standard for characterising prostate heterogeneity, while texture features measure the same physical property. The current study demonstrated that both shape (unfiltered-shape-flatness) and first-order features (LoG-1mm-filtered RMS) have similar predictive performance compared to MRI radiomic studies (23, 24, 50). Nonetheless, a further study involving a larger external validation cohort is needed to validate

TABLE 3 Predictive performance of the R, C and RC combined models.

Model	Training Cohort							Validation Cohort						
	ROC-AUC, Mean (95% CI)	PR-AUC, Mean	Sens.	Spec.	Acc.	YI	p*	ROC-AUC, Mean (95%CI)	PR-AUC, Mean	Sens.	Spec.	Acc.	YI	p*
R	0.798 (0.788-0.809)	0.177	0.998	0.658	0.685	0.656	0.005	0.795 (0.774-0.816)	0.357	0.825	0.605	0.640	0.430	< 0.001
C	0.554 (0.521-0.587)	0.097	0.353	0.764	0.731	0.117	< 0.001	0.625 (0.585-0.665)	0.230	0.530	0.676	0.652	0.206	< 0.001
RC combined	0.747 (0.726-0.767)	0.172	0.808	0.722	0.729	0.530	(Ref.)	0.797 (0.768-0.826)	0.371	0.793	0.653	0.676	0.446	(Ref.)

R, radiomics; C, clinical; RC, radiomic-clinical; ROC, receiver-operating characteristic; AUC, area-under-curve; CI, confidence interval; PR, precision-recall; YI, Youden index (Sensitivity + specificity -1); Sens., sensitivity; Spec., specificity; Acc., accuracy; Ref., reference, *refers to statistical significance of ROC-AUC differences between R and RC combined model and that between C and RC combined model in each cohort

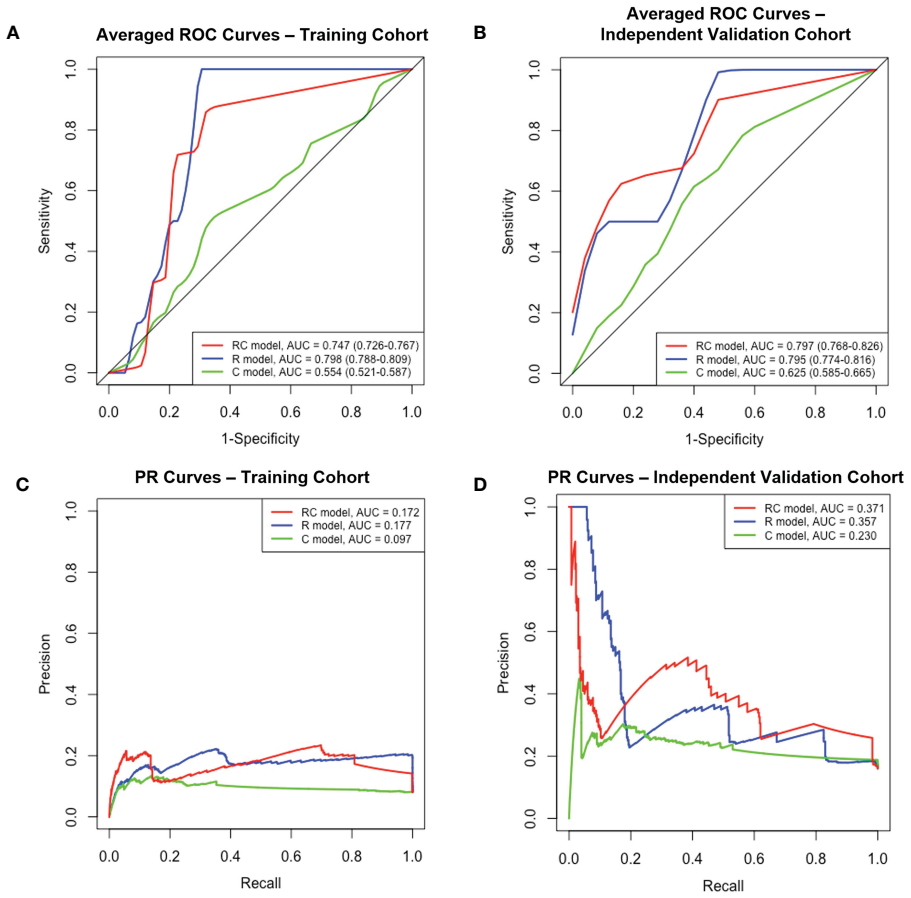

FIGURE 4
The ROC and PR curves of R, C and RC combined models. Boxplots **(A, B)** Averaged ROC curves of the training and independent validation cohort. Boxplots **(C, D)** The PR curves of both cohorts. ROC, receiver-operating characteristic; PR, precision-recall; R, radiomic; C, clinical; RC, radiomic-clinical; AUC, area under curve.

the performance of these two feature classes in predicting the PFS of high-risk PCa patients.

The C model constructed based on clinical factors had the poorest performance. Univariate analysis did not show any statistical significance of these clinical features between PFS-1 and PFS-0 patients in both cohorts. The most probable explanation is that these clinical features are homogeneous within the high-risk subgroup of PCa patients (32). Thus, using the C model alone would lead to the poorest prediction performance. Statistically, the C model also failed to differentiate the 5-year PFS status in both cohorts. These findings are in line with those reported by Fernandes et al. (23) and Bourbonne et al. (26), who have also incorporated PSA and GS in their clinical models. They also retrospectively investigated the clinical predictive model for high-risk PCa patients treated by EBRT (23) and radical prostatectomy during a 5-year follow-up (26). The sensitivity and specificity of the C model were also comparable to those reported by Bourbonne et al. (26) (Sensitivity: 0.53 vs 0.68; Specificity: 0.53 vs. 0.59). These clinical features, however, are not without predictive values when combined with the R model. It is demonstrated by the increase in overall accuracy in both the training and independent validation cohorts after combining R with C models. The potential complementary role between R and C features for prognosis warrants future investigation (54).

Overall, this study explored the potential of combining pCT-derived radiomic and clinical features in the prognostic prediction of high-risk PCa patients receiving PORT. Our study has demonstrated that the classification performance of the combined RC model was comparable to the combined MRI-derived radiomic and clinical models. Among all included features, the shape and first-order features are considered more intuitive than other complex features when interpreting the classifier in predicting 5-year PFS of high-risk patients in the clinical setting (51). Our patient stratification methodology is highly standardised by adopting a temporal validation as in type-2b study according to the TRIPOD guideline (39). Moreover, the use of pCT is preferable due to its higher standardisation, repeatability and calibration of CT over diagnostic MRI (33). For instance, HU in pCT directly quantifies the electron density of the tissue while the pixel value in MR is arbitrarily allocated.

This study has several limitations. First, the sample size is relatively small. This can be attributed to the strict inclusion and exclusion criteria enforced to ensure high-quality radiomics and clinical data. Nonetheless, numerous studies have also contributed

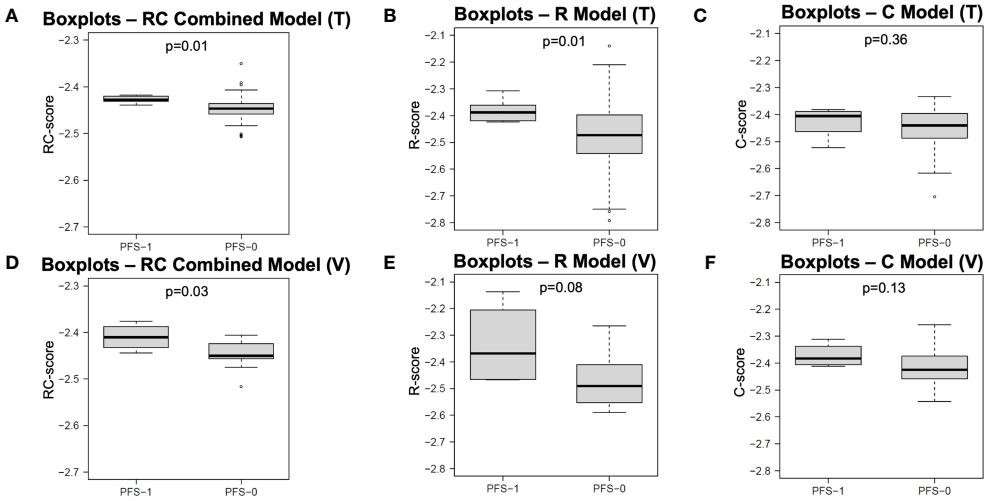

FIGURE 5
Boxplots of model scores of R, C and RC combined models. The boxplots in first **(A–C)** and second rows **(D–F)** display the distribution of model scores calculated by different models in training and validation cohorts, respectively. R, Radiomics; C, clinical; RC, Radiomic-clinical; T, training cohort; V, validation cohort; PFS, progression-free survival.

insightful findings to the community with a similar sample size as our work (32, 55–57). Second, this work only performed modelling based on data from a single centre as COVID-19 has restricted the research team from conducting data collection from multiple centres. Third, owing to the small sample size and temporal stratification, a class imbalance exists in which only 10% are PFS-1 patients. Although a similar situation was observed in Bosetti's (2020) work analysing cone-beam CT performance for predicting prostate cancer clinical progression, further study with a larger sample size and proportion of PFS-1 patients would be beneficial to minimise modelling and evaluation bias. Minority class-boosting techniques should also be implemented if appropriate. Fourth, an external testing set was not employed. This would be essential to demonstrate satisfying model generalisability in a multi-centre study before actual clinical application (58). Moreover, Ridge regression, which was a relatively straightforward modelling strategy, was adopted in this work for demonstrating the proposed feasibility of using radiomic-clincial factors to predict patient outcomes. To render the model fit for clinical application, more robust modelling methodologies such as non-linear machine learning techniques and random oversampling should be incorporated when processing multi-centre data sets.

5 Conclusion

This study demonstrated the feasibility and potential of using pCT-derived radiomic and clinical features for predicting 5-year PFS in high-risk PCa patients receiving PORT, which is an important clinical research gap that previously lacks investigation The RC combined model provided statistically superior predictive performance than both R and C models in the independent temporal validation cohort. These findings lay the ground for the future development of a combined radiomic-clinical model involving robust modelling techniques, multicentre data and external validation. We hope that this work will bring attention to the academic community and encourage future work to address this on a larger scale towards clinical implementation. Ultimately, it could potentially act as a supportive decision tool predicting the outcome of different treatment regimens to facilitate personalised management of high-risk PCa patients.

Data availability statement

The raw data supporting the conclusions of this article will be made available by the authors, without undue reservation.

Ethics statement

The studies involving human participants were reviewed and approved by Human Subjects Ethics Sub-committee of The Hong Kong Polytechnic University and Kowloon West Cluster Research Ethics Committee of the Hong Kong Hospital Authority. Written informed consent for participation was not required for this study in accordance with the national legislation and the institutional requirements.

Author contributions

JCC, SL, WSL and SWL contributed to the study design, methodology development, results interpretation, and manuscript review. WL offered administrative and material support for data collection. JCC, AOL, and JCK collected patients' clinical and imaging data. JCC, SL and AOL contributed to image pre-processing and feature extraction. JCC, SL, CCL, AOL and JCK constructed the models. JCC wrote the manuscript. WSL co-

supervised the study. SWL supervised the study. All authors contributed to the article and approved the submitted version.

Acknowledgments

The authors would like to express their appreciation to Mr. Jiang Zhang and Mr. Alex Nicol for their expert advice on computation modelling. Mr. Jiang Zhang is the developer of the in-house developed pipeline for fast feature extraction. Finally, our team also thanks staff of the Department of Oncology, Princess Margaret Hospital, Hong Kong for their logistical support on data collection.

Conflict of interest

The authors declare that the research was conducted in the absence of any commercial or financial relationships that could be construed as a potential conflict of interest.

Publisher's note

Supplementary material

The Supplementary Material for this article can be found online at: https://www.frontiersin.org/articles/10.3389/fonc.2023.1060687/full#supplementary-material

References

1. Sung H, Ferlay J, Siegel RL, Laversanne M, Soerjomataram I, Jemal A, et al. Global cancer statistics 2020: GLOBOCAN estimates of incidence and mortality worldwide for 36 cancers in 185 countries. *CA Cancer J Clin* (2021) 71:209–49. doi: 10.3322/caac.21660

2. Roy S, Morgan SC. Who dies from prostate cancer? an analysis of the surveillance, epidemiology and end results database. *Clin Oncol (R Coll Radiol)* (2019) 31:630–36. doi: 10.1016/j.clon.2019.04.012

3. Dirix P, Joniau S, Van den Bergh L, Isebaert S, Oyen R, Deroose CM, et al. The role of elective pelvic radiotherapy in clinically node-negative prostate cancer: a systematic review. *Radiother Oncol* (2014) 110:45–54. doi: 10.1016/j.radonc.2013.06.046

4. Muteganya R, Goldman S, Aoun F, Roumeguère T, Albisinni S. Current imaging techniques for lymph node staging in prostate cancer: a review. *Front Surg* (2018) 5:74. doi: 10.3389/fsurg.2018.00074

5. Roach M, Moughan J, Lawton CAF, Dicker AP, Zeitzer KL, Gore EM, et al. Sequence of hormonal therapy and radiotherapy field size in unfavourable, localised prostate cancer (NRG/RTOG 9413): long-term results of a randomised, phase 3 trial. *Lancet Oncol* (2018) 19:1504–15. doi: 10.1016/S1470-2045(18)30528-X

6. Murthy V, Maitre P, Kannan S, Panigrahi G, Krishnatry R, Bakshi G, et al. Prostate-only versus whole-pelvic radiation therapy in high-risk and very high-risk prostate cancer (POP-RT): outcomes from phase III randomized controlled trial. *J Clin Oncol* (2021) 39:1234–42. doi: 10.1200/JCO.20.03282

7. Amini A, Jones BL, Yeh N, Rusthoven CG, Armstrong H, Kavanagh BD. Survival outcomes of whole-pelvic versus prostate-only radiation therapy for high-risk prostate cancer patients with use of the national cancer data base. *Int J Radiat Oncol Biol Phys* (2015) 93:1052–63. doi: 10.1016/j.ijrobp.2015.09.006

8. Pommier P, Chabaud S, Lagrange J-L, Richaud P, Le Prise E, Wagner J-P, et al. Is there a role for pelvic irradiation in localized prostate adenocarcinoma? update of the long-term survival results of the GETUG-01 randomized study. *Int J Radiat Oncol Biol Phys* (2016) 96:759–69. doi: 10.1016/j.ijrobp.2016.06.2455

9. Aizer AA, Yu JB, McKeon AM, Decker RH, Colberg JW, Peschel RE. Whole pelvic radiotherapy versus prostate only radiotherapy in the management of locally advanced or aggressive prostate adenocarcinoma. *Int J Radiat Oncol Biol Phys* (2009) 75:1344–9. doi: 10.1016/j.ijrobp.2008.12.082

10. Kim MM, Hoffman KE, Levy LB, Frank SJ, Pugh TJ, Choi S, et al. Improvement in prostate cancer survival over time: a 20-year analysis. *Cancer J* (2012) 18:1–8. doi: 10.1097/ppo.0b013e3182467419

11. Wang S, Tang W, Luo H, Jin F, Wang Y. Efficacy and toxicity of whole pelvic radiotherapy versus prostate-only radiotherapy in localized prostate cancer: a systematic review and meta-analysis. *Front Oncol* (2021) 11:796907. doi: 10.3389/fonc.2021.796907

12. *Prostate cancer: diagnosis and management NICE guideline. org.uk* (2021). Available at: https://www.nice.org.uk/guidance/ng131/resources/%20prostate-cancer-%20diagnosis-and-management-pdf-66141714312133 (Accessed March 18, 2021).

13. Chan MFT, Lam QYN, Lee VHF, Ho PPY, Sze HCK, Siu SWK, et al. Using the roach formula to stratify patients with localised prostate cancer treated with intensity-modulated radiotherapy. *Hong Kong J Radiol* (2017) 20:103–9. doi: 10.12809/hkjr1715378

14. Joniau S, Briganti A, Gontero P, Gandaglia G, Tosco L, Fieuws S, et al. Stratification of high-risk prostate cancer into prognostic categories: a European multi-institutional study. *Eur Urol* (2015) 67:157–64. doi: 10.1016/j.eururo.2014.01.020

15. Rodrigues G, Warde P, Pickles T, Crook J, Brundage M, Souhami L, et al. Pre-treatment risk stratification of prostate cancer patients: a critical review. *Can Urol Assoc J* (2012) 6:121–7. doi: 10.5489/cuaj.11085

16. Gosselaar C, Kranse R, Roobol MJ, Roemeling S, Schröder FH. The interobserver variability of digital rectal examination in a large randomized trial for the screening of prostate cancer. *Prostate* (2008) 68:985–93. doi: 10.1002/pros.20759

17. Koulikov D, Mamber A, Fridmans A, Abu Arafeh W, Shenfeld OZ. Why I cannot find the prostate? behind the subjectivity of rectal exam. *ISRN Urol* (2012) 2012:456821. doi: 10.5402/2012/456821

18. Morikawa LK, Roach M3rd. Pelvic nodal radiotherapy in patients with unfavorable intermediate and high-risk prostate cancer: evidence, rationale, and future directions. *Int J Radiat Oncol Biol Phys* (2011) 80:6–16. doi: 10.1016/j.ijrobp.2010.11.074

19. Rahman S, Cosmatos H, Dave G, Williams S, Tome M. Predicting pelvic lymph node involvement in current-era prostate cancer. *Int J Radiat Oncol Biol Phys* (2012) 82:906–10. doi: 10.1016/j.ijrobp.2010.11.053

20. Nguyen PL, Chen MH, Hoffman KE, Katz MS, D'Amico AV. Predicting the risk of pelvic node involvement among men with prostate cancer in the contemporary era. *Int J Radiat Oncol Biol Phys* (2009) 74:104–9. doi: 10.1016/j.ijrobp.2008.07.053

21. Lambin P, Leijenaar RTH, Deist TM, Peerlings J, de Jong EEC, van Timmeren J, et al. Radiomics: the bridge between medical imaging and personalized medicine. *Nat Rev Clin Oncol* (2017) 14:749–62. doi: 10.1038/nrclinonc.2017.141

22. Gnep K, Fargeas A, Gutiérrez-Carvajal RE, Commandeur F, Mathieu R, Ospina JD, et al. Haralick textural features onT2-weighted MRI are associated with biochemical recurrence following radiotherapy for peripheral zone prostate cancer: impact of MRI in prostate cancer. *J Magn Reson Imaging* (2017) 45:103–17. doi: 10.1002/jmri.25335

23. Dinis Fernandes C, Dinh CV, Walraven I, Heijmink SW, Smolic M, van Griethuysen JJM, et al. Biochemical recurrence prediction after radiotherapy for prostate cancer with T2w magnetic resonance imaging radiomic features. *Phys Imaging Radiat Oncol* (2018) 7:9–15. doi: 10.1016/j.phro.2018.06.005

24. Shiradkar R, Ghose S, Jambor I, Taimen P, Ettala O, Purysko AS, et al. Radiomic features from pretreatment biparametric MRI predict prostate cancer biochemical recurrence: preliminary findings. *J Magn Reson Imaging* (2018) 48:1626–36. doi: 10.1002/jmri.26178

25. Toivonen J, Montoya Perez I, Movahedi P, Merisaari H, Pesola M, Taimen P, et al. Radiomics and machine learning of multisequence multiparametric prostate MRI: towards improved non-invasive prostate cancer characterization. *PloS One* (2019) 14:e0217702. doi: 10.1371/journal.pone.0217702

26. Bourbonne V, Fournier G, Vallières M, Lucia F, Doucet L, Tissot V, et al. External validation of an MRI-derived radiomics model to predict biochemical recurrence after surgery for high-risk prostate cancer. *Cancers (Basel)* (2020) 12:814. doi: 10.3390/cancers12040814

27. Khodabakhshi Z, Amini M, Mostafaei S, Haddadi Avval A, Nazari M, Oveisi M, et al. Overall survival prediction in renal cell carcinoma patients using computed

tomography radiomic and clinical information. *J Digit Imaging* (2021) 34:1086–98. doi: 10.1007/s10278-021-00500-y

28. Pérez-Morales J, Tunali I, Stringfield O, Eschrich SA, Balagurunathan Y, Gillies RJ, et al. Peritumoral and intratumoral radiomic features predict survival outcomes among patients diagnosed in lung cancer screening. *Sci Rep* (2020) 10:10528. doi: 10.1038/s41598-020-67378-8

29. Intarak S, Chongpison Y, Vimolnoch M, Oonsiri S, Kitpanit S, Prayongrat A, et al. Tumor prognostic prediction of nasopharyngeal carcinoma using CT-based radiomics in non-Chinese patients. *Front Oncol* (2022) 12:775248. doi: 10.3389/fonc.2022.775248

30. Forouzannezhad P, Maes D, Hippe DS, Thammasorn P, Iranzad R, Han J, et al. Multitask learning radiomics on longitudinal imaging to predict survival outcomes following risk-adaptive chemoradiation for non-small cell lung cancer. *Cancers (Basel)* (2022) 14:1228. doi: 10.3390/cancers14051228

31. Franzese C, Cozzi L, Badalamenti M, Baldaccini D, D'Agostino G, Fogliata A, et al. Radiomics-based prognosis classification for high-risk prostate cancer treated with radiotherapy. *Strahlenther Onkol* (2022) 198:710–8. doi: 10.1007/s00066-021-01886-y

32. Ghezzo S, Bezzi C, Presotto L, Mapelli P, Bettinardi V, Savi A, et al. State of the art of radiomic analysis in the clinical management of prostate cancer: a systematic review. *Crit Rev Oncol Hematol* (2022) 169:103544. doi: 10.1016/j.critrevonc.2021.103544

33. Delgadillo R, Ford JC, Abramowitz MC, Dal Pra A, Pollack A, Stoyanova R. The role of radiomics in prostate cancer radiotherapy. *Strahlenther Onkol* (2020) 196:900–12. doi: 10.1007/s00066-020-01679-9

34. Halabi S, Vogelzang NJ, Ou SS, Owzar K, Archer L, Small EJ. Progression-free survival as a predictor of overall survival in men with castrate-resistant prostate cancer. *J Clin Oncol* (2009) 27:2766–71. doi: 10.1200/JCO.2008.18.9159

35. Roach M3rd, Hanks G, Thames HJr, Schellhammer P, Shipley WU, Sokol GH, et al. Defining biochemical failure following radiotherapy with or without hormonal therapy in men with clinically localized prostate cancer: recommendations of the RTOG-ASTRO phoenix consensus conference. *Int J Radiat Oncol Biol Phys* (2006) 65:965–74. doi: 10.1016/j.ijrobp.2006.04.029

36. He L, Huang Y, Yan L, Zheng J, Liang C, Liu Z. Radiomics-based predictive risk score: a scoring system for preoperatively predicting risk of lymph node metastasis in patients with resectable non-small cell lung cancer. *Chin J Cancer Res* (2019) 31:641–52. doi: 10.21147/j.issn.1000-9604.2019.04.08

37. Feng XL, Wang SZ, Chen HH, Huang YX, Xin YK, Zhang T, et al. Optimizing the radiomics-machine-learning model based on non-contrast enhanced CT for the simplified risk categorization of thymic epithelial tumors: a large cohort retrospective study. *Lung Cancer* (2022) 166:150–60. doi: 10.1016/j.lungcan.2022.03.007

38. Dikaios N, Alkalbani J, Sidhu HS, Fujiwara T, Abd-Alazeez M, Kirkham A, et al. Logistic regression model for diagnosis of transition zone prostate cancer on multi-parametric MRI. *Eur Radiol* (2015) 25:523–32. doi: 10.1007/s00330-014-3386-4

39. Collins GS, Reitsma JB, Altman DG, Moons KGM. Transparent reporting of a multivariable prediction model for individual prognosis or diagnosis (TRIPOD): the TRIPOD statement. *Eur Urol* (2015) 67:1142–51. doi: 10.1016/j.eururo.2014.11.025

40. Harris VA, Staffurth J, Naismith O, Esmail A, Gulliford S, Khoo V, et al. Consensus guidelines and contouring atlas for pelvic node delineation in prostate and pelvic node intensity modulated radiation therapy. *Int J Radiat Oncol Biol Phys* (2015) 92(4):874–83. doi: 10.1016/j.ijrobp.2015.03.021

41. Zwanenburg A. EP-1677: multicentre initiative for standardisation of image biomarkers. *Radiother Oncol* (2017) 123:S914–5. doi: 10.1016/s0167-8140(17)32209-0

42. Osman SOS, Leijenaar RTH, Cole AJ, Lyons CA, Hounsell AR, Prise KM, et al. Computed tomography-based radiomics for risk stratification in prostate cancer. *Int J Radiat Oncol Biol Phys* (2019) 105:448–56. doi: 10.1016/j.ijrobp.2019.06.2504

43. Tanadini-Lang S, Bogowicz M, Veit-Haibach P, Huellner M, Pauli C, Shukla V, et al. Exploratory Radiomics in Computed Tomography Perfusion of Prostate Cancer. *Anticancer Res* (2017) 38(2):685–90. doi: 10.21873/anticanres.12273

44. Sun J, Liu K, Tong H, Liu H, Li X, Luo Y, et al. CT texture analysis for differentiating bronchiolar adenoma, adenocarcinoma in situ, and minimally invasive adenocarcinoma of the lung. *Front Oncol* (2021) 26:634564(11). doi: 10.3389/fonc.2021.634564

45. Jiang X, Jia H, Zhang Z, Wei C, Wang C, Dong J. The feasibility of combining ADC value with texture analysis of T2WI, DWI and CE-T1WI to preoperatively predict the expression levels of ki-67 and p53 of endometrial carcinoma. *Front Oncol* (2021) 11:805545. doi: 10.3389/fonc.2021.805545

46. Chen H, Deng X, Pan Y, Chen J, Liu Y, Chen W, et al. Pancreatic serous cystic neoplasms and mucinous cystic neoplasms: differential diagnosis by combining imaging features and enhanced CT texture analysis. *Front Oncol* (2021) 11:745001. doi: 10.3389/fonc.2021.745001

47. Youden WJ. Index for rating diagnostic tests. *Cancer* (1950) 3:32–5. doi: 10.1002/1097-0142(1950)3:1<32::aid-cncr2820030106>3.0.co;2-3

48. van Griethuysen JJM, Fedorov A, Parmar C, Hosny A, Aucoin N, Narayan V, et al. Computational radiomics system to decode the radiographic phenotype. *Cancer Res* (2017) 77:e104–7. doi: 10.1158/0008-5472.can-17-0339

49. Yan M, Wang W. Radiomic analysis of CT predicts tumor response in human lung cancer with radiotherapy. *J Digit Imaging* (2020) 33:1401–3. doi: 10.1007/s10278-020-00385-3

50. Zhong QZ, Long LH, Liu A, Li CM, Xiu X, Hou XY, et al. Radiomics of multiparametric MRI to predict biochemical recurrence of localized prostate cancer after radiation therapy. *Front Oncol* (2020) 10:731. doi: 10.3389/fonc.2020.00731

51. Bosetti DG, Ruinelli L, Piliero MA, van der Gaag LC, Pesce GA, Valli M, et al. Cone-beam computed tomography-based radiomics in prostate cancer: a mono-institutional study. *Strahlenther Onkol* (2020) 196:943–51. doi: 10.1007/s00066-020-01677-x

52. Shen H, Wang Y, Liu D, Lv R, Huang Y, Peng C, et al. Predicting progression-free survival using MRI-based radiomics for patients with nonmetastatic nasopharyngeal carcinoma. *Front Oncol* (2020) 10:618. doi: 10.3389/fonc.2020.00618

53. Zhang B, Ouyang F, Gu D, Dong Y, Zhang L, Mo X, et al. Advanced nasopharyngeal carcinoma: pre-treatment prediction of progression based on multi-parametric MRI radiomics. *Oncotarget* (2017) 8:72457–65. doi: 10.18632/oncotarget.19799

54. Kittler J, Hatef M, Duin RPW, Matas J. On combining classifiers. *IEEE Trans Pattern Anal Mach Intell* (1998) 20:226–39. doi: 10.1109/34.667881

55. Zhu C, Huang H, Liu X, Chen H, Jiang H, Liao C, et al. A clinical-radiomics nomogram based on computed tomography for predicting risk of local recurrence after radiotherapy in nasopharyngeal carcinoma. *Front Oncol* (2021) 11:637687. doi: 10.3389/fonc.2021.637687

56. Lam SK, Zhang J, Zhang YP, Li B, Ni RY, Zhou T, et al. A multi-center study of CT-based neck nodal radiomics for predicting an adaptive radiotherapy trigger of ill-fitted thermoplastic masks in patients with nasopharyngeal carcinoma. *Life* (2022) 12(2):241. doi: 10.3390/life12020241

57. Yang L, Chu W, Li M, Xu P, Wang M, Peng M, et al. Radiomics in gastric cancer: first clinical investigation to predict lymph vascular invasion and survival outcome using 18 f-FDG PET/CT images. *Front Oncol* (2022) 12:836098. doi: 10.3389/fonc.2022.836098

58. Ramspek CL, Jager KJ, Dekker FW, Zoccali C, van Diepen M. External validation of prognostic models: what, why, how, when and where? *Clin Kidney J* (2021) 14:49–58. doi: 10.1093/ckj/sfaa188

Frontiers in Oncology

Advances knowledge of carcinogenesis and tumor progression for better treatment and management

The third most-cited oncology journal, which highlights research in carcinogenesis and tumor progression, bridging the gap between basic research and applications to imrpove diagnosis, therapeutics and management strategies.

Discover the latest Research Topics

See more →

Frontiers

Avenue du Tribunal-Fédéral 34
1005 Lausanne, Switzerland
frontiersin.org

Contact us

+41 (0)21 510 17 00
frontiersin.org/about/contact